



UNIVERSITAT^{DE}
BARCELONA

Production of Solar Fuels by Photoelectrochemical Conversion of Carbon Dioxide

Ibrahim Erdem Irtem

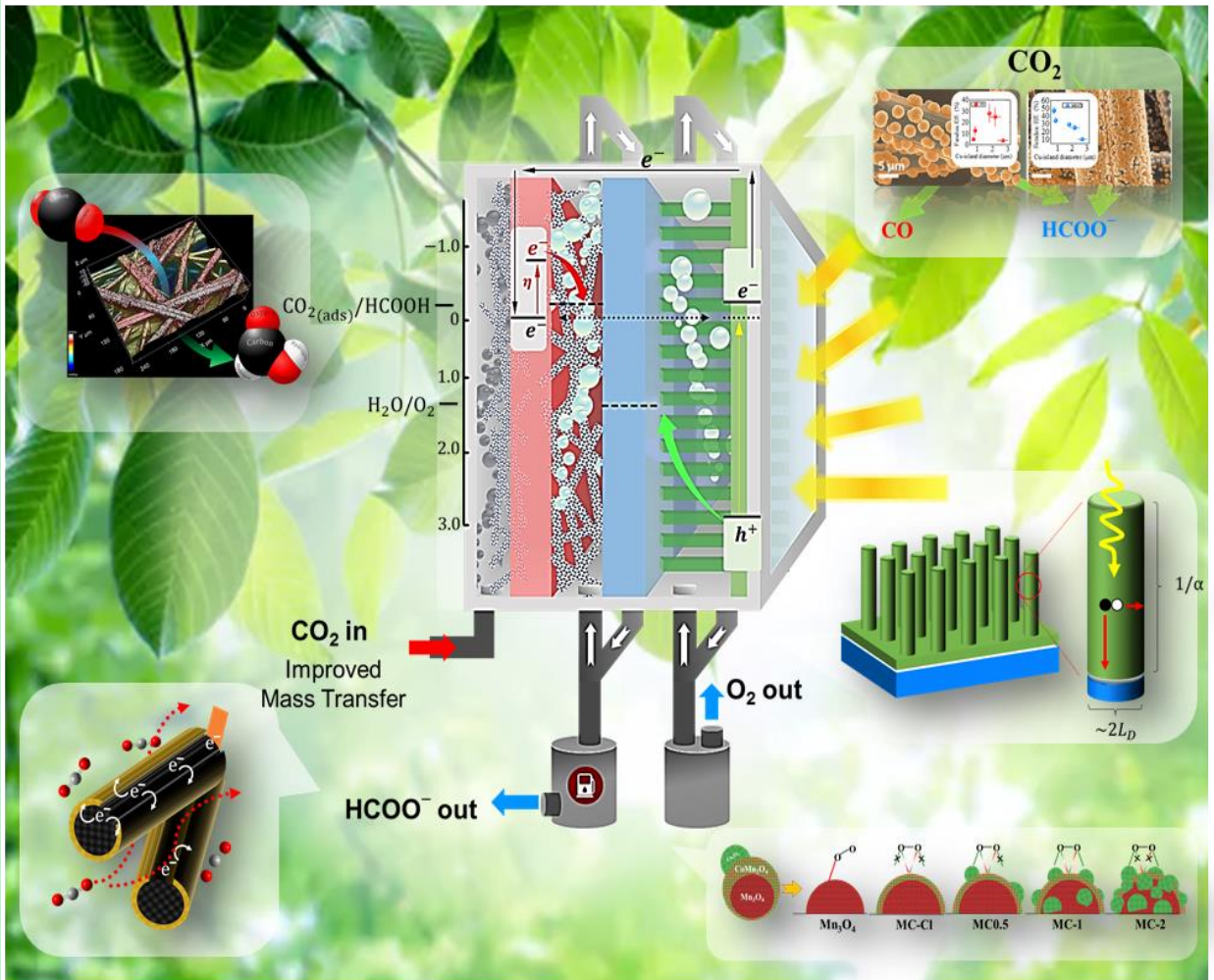
ADVERTIMENT. La consulta d'aquesta tesi queda condicionada a l'acceptació de les següents condicions d'ús: La difusió d'aquesta tesi per mitjà del servei TDX (www.tdx.cat) i a través del Dipòsit Digital de la UB (diposit.ub.edu) ha estat autoritzada pels titulars dels drets de propietat intel·lectual únicament per a usos privats emmarcats en activitats d'investigació i docència. No s'autoritza la seva reproducció amb finalitats de lucre ni la seva difusió i posada a disposició des d'un lloc aliè al servei TDX ni al Dipòsit Digital de la UB. No s'autoritza la presentació del seu contingut en una finestra o marc aliè a TDX o al Dipòsit Digital de la UB (framing). Aquesta reserva de drets afecta tant al resum de presentació de la tesi com als seus continguts. En la utilització o cita de parts de la tesi és obligat indicar el nom de la persona autora.

ADVERTENCIA. La consulta de esta tesis queda condicionada a la aceptación de las siguientes condiciones de uso: La difusión de esta tesis por medio del servicio TDR (www.tdx.cat) y a través del Repositorio Digital de la UB (diposit.ub.edu) ha sido autorizada por los titulares de los derechos de propiedad intelectual únicamente para usos privados enmarcados en actividades de investigación y docencia. No se autoriza su reproducción con finalidades de lucro ni su difusión y puesta a disposición desde un sitio ajeno al servicio TDR o al Repositorio Digital de la UB. No se autoriza la presentación de su contenido en una ventana o marco ajeno a TDR o al Repositorio Digital de la UB (framing). Esta reserva de derechos afecta tanto al resumen de presentación de la tesis como a sus contenidos. En la utilización o cita de partes de la tesis es obligado indicar el nombre de la persona autora.

WARNING. On having consulted this thesis you're accepting the following use conditions: Spreading this thesis by the TDX (www.tdx.cat) service and by the UB Digital Repository (diposit.ub.edu) has been authorized by the titular of the intellectual property rights only for private uses placed in investigation and teaching activities. Reproduction with lucrative aims is not authorized nor its spreading and availability from a site foreign to the TDX service or to the UB Digital Repository. Introducing its content in a window or frame foreign to the TDX service or to the UB Digital Repository is not authorized (framing). Those rights affect to the presentation summary of the thesis as well as to its contents. In the using or citation of parts of the thesis it's obliged to indicate the name of the author.

Production of Solar Fuels by Photoelectrochemical Conversion of CO₂

Ibrahim Erdem Irtem



Thesis submitted to apply for the degree of Doctor, in the Nanoscience Program of
the University of Barcelona.

Departament d'Enginyeries: Secció d'Electrònica, Facultat de Física

PRODUCTION OF SOLAR FUELS BY PHOTOELECTROCHEMICAL CONVERSION OF CARBON DIOXIDE

Ibrahim Erdem Irtem, M.Sc., B.Eng.

Supervisors

Dra. Teresa Andreu Arbella

Institut de Recerca en Energia de Catalunya

Departament de Ciència dels Materials i Química Física: Secció de Ciència i
Enginyeria de Materials, Universitat de Barcelona

Prof. Dr. Joan Ramon Morante Lleonart

Institut de Recerca en Energia de Catalunya

Departament d'Enginyeries: Secció d'Electrònica, Universitat de Barcelona

Date of Submission: March 2017

La Dra. Teresa Andreu Arbella, investigadora del Institut de Recerca en Energia de Catalunya (IREC) y profesora asociada del Departamento de Ciencia de Materiales y Química Física de la Universidad de Barcelona, El Prof. Dr. Joan Ramon Morante Lleonart, investigador de Institut de Recerca en Energia de Catalunya (IREC) y Catedrático del Departamento de Ingenierías: Sección de Electrónica de la Universidad de Barcelona,

CERTIFICAN:

Que la memoria titulada “**Production of solar fuels by photoelectrochemical conversion of carbon dioxide**” presentada por Ibrahim Erdem Irtem para optar al grado de Doctor en el Programa de Nanociencias de la Universidad de Barcelona ha sido realizada bajo su dirección en el Institut de Recerca en Energia de Catalunya (IREC).

Barcelona, Marzo de 2017

Dra. Teresa Andreu Arbella

Prof. Dr. Joan Ramon Morante Lleonart

To my parents.

Ömer and Şükran IRTEM.

Abstract

Growing global emission of carbon dioxide gas (CO_2) reflects the world's energy dependence on fossil fuels. The conversion of CO_2 emission into value-added products, like fuels completes a circular CO_2 economy which requires a renewable energy conversion and storage system. Amongst a few, photo/electrochemistry has been particularly appealing thanks to its energy efficiency and enormous potential for industrial applications. Formic acid (HCOOH) production from CO_2 reduction appears as an alternative energy storage option based on the commercialization of this process. Herein, stable and selective catalysts working at low overpotential are needed to reduce CO_2 . Likewise, cell design is critical to have improved CO_2 mass transport for obtaining high conversion efficiencies and to achieve feasible production yields.

The initial work was conducted on the design and understanding of operational parameters of an electrochemical flow cell (ECf-cell) such as flow rates and electrode potentials. For CO_2 reduction at the cathode site, two different gas diffusion electrodes were produced by electrodeposition: Sn-GDE and Cu-GDE. An optimum potential range was established to control HCOOH selectivity. The complementing reaction at the anode site, oxygen evolution reaction (OER), was studied using Mn-Co oxide nanoparticles to replace expensive DSA: Ir-Ta oxide catalyst. Subsequent efforts were devoted on the assembly of a photoelectrochemical flow cell (PECf-cell) which enabled coupling of Sn-GDE as cathode vs. TiO_2 nanorods as photoanode. This led to nearly 1/3 reduction in overall cell voltage reaching an energy efficiency up to 70 %. The solar-to-fuel (STF) conversion efficiency was 0.25 % which was one of the highest efficiencies reported amongst the data obtained from a cell in device level. The results proved that optimized system efficiency could be achieved with a large bandgap photoanode having superior stability and a GDE cathode with improved CO_2 mass transfer.

The deployment of renewable energy sources will require new technologies to emerge. The photoelectrochemical flow cell developed in this work can store energy from intermittent electricity sources (i.e. wind and solar) in a sustainable manner. This may pave the way for commercialization of this process and moving towards a circular CO_2 economy.

Resumen

La creciente emisión mundial de dióxido de carbono (CO_2) refleja la dependencia energética mundial en los combustibles fósiles. La conversión de emisiones de CO_2 en productos de valor añadido, como los combustibles, completa una economía circular de CO_2 que requiere de un sistema de conversión y almacenamiento de energía renovable. Entre algunas opciones, la foto/electroquímica ha sido especialmente atractiva gracias a su eficiencia energética y su enorme potencial para aplicaciones industriales. La producción de ácido fórmico (HCOOH) a partir de la reducción de CO_2 aparece como un almacenamiento de energía alternativo para la comercialización de este proceso. Sin embargo, se requieren catalizadores estables y selectivos que puedan reducir el CO_2 a bajo sobre potencial. Además, el diseño de la celda es crítico para mejorar el transporte de masa de CO_2 y obtener elevadas eficiencias de conversión, alcanzando rendimientos de producción viables.

En este trabajo se centró en primer lugar en el diseño y la comprensión de los parámetros operativos de una celda de flujo electroquímica (ECf-cell), tales como caudales y potenciales de electrodo. Para la reducción de CO_2 sobre el cátodo, se emplearon dos electrodos de difusión de gas diferentes por electrodeposición: Sn-GDE y Cu-GDE. Se estableció un valor de operación óptimo para controlar la selectividad a HCOOH . Se estudió también la reacción de complementaria en el ánodo, reacción de evolución de oxígeno (OER), empleando nano partículas de óxido de Mn-Co para reemplazar el elevado coste del catalizador de óxido de DSA:Ir-Ta. Finalmente, los esfuerzos se dedicaron al montaje de una celda fotoelectroquímica de flujo (PECf-cell) que permitió el acoplamiento de Sn-GDE como cátodo frente a TiO_2 nanorods como fotoánodo. Esto condujo a cerca de 1/3 de reducción en el voltaje total de la celda alcanzando una eficiencia energética del 70 %. El rendimiento de la conversión de energía solar a combustible (STF) fue de 0,25%, siendo una de las eficiencias más altas registradas entre los datos obtenidos a partir de configuraciones de celda completas. Los resultados demuestran que se puede lograr una eficiencia optimizada del sistema con un fotoánodo de amplio ancho de banda que tiene una buena estabilidad y un cátodo GDE para favorecer la transferencia de masa de CO_2 .

El despliegue de fuentes de energía renovables requerirá la aparición de nuevas tecnologías. La celda de flujo fotoelectroquímica desarrollada pueden este trabajo permite almacenar energía de fuentes de electricidad intermitentes (por ejemplo, eólica y solar) de una manera sostenible. Esto podría ser una solución para la comercialización de este proceso y avanzar hacia una economía circular de CO_2 .

Table of Contents

Abstract	vii
Resumen	viii
Table of Contents	ix
1 Introduction	13
1.1 Key Figures of Sustainability	15
1.2 CO₂ Valorisation Methods	17
1.3 Electrochemical Methods	23
1.3.1 Fundamentals of electrochemistry.....	24
1.3.2 Fundamentals of photoelectrochemistry.....	43
1.4 Scope of this research	52
2 Experimental Methods	55
2.1 Electrode Preparation	57
2.1.1 Electrodes for CO ₂ reduction.....	57
2.1.2 Electrodes for H ₂ O oxidation.....	59
2.2 Test Methods	65
2.3 Product Analysis and Quantification	75
2.3.1 Gas phase analysis and product quantification.....	75
2.3.2 Liquid phase product quantification.....	79
3 Dark-CO₂RR: Sn-GDE in ECf-cell	89
3.1 Experimental Remarks	90
3.2 Results and Discussion	91
3.2.1 Sn electrodeposition & CO ₂ RR activity.....	91
3.2.2 CO ₂ reduction products and Tafel plot analysis.....	96
3.2.3 Effect of hydrodynamic conditions.....	99
3.2.4 Stability and feasibility of formate production.....	102
3.3 Conclusions	105

4	Dark-CO₂RR: Cu-GDE in ECf-cell	107
4.1	Experimental Remarks	108
4.2	Results and Discussion	110
4.2.1	Continuous electrodeposition of copper	110
4.2.2	Pulsed current electrodeposition of copper	115
4.2.3	Effect of electrodeposition in CO ₂ RR.....	119
4.2.4	Feasibility of formate production.....	123
4.3	Conclusion.....	126
5	Dark-OER: Co-Mn oxide NP in ECf-cell.....	127
5.1	Experimental Remarks	128
5.2	Results and Discussion	129
5.2.1	Effect of cobalt (II) chloride precursor: MC1-Cl NPs.....	129
5.2.2	Effect of cobalt (II) perchlorate precursor: MC _x NPs.....	130
5.2.3	Rotating disk electrode analysis of NPs for ORR & OER	132
5.2.4	DSA vs. NPs/CFS in ECf-cell	146
5.3	Conclusion.....	154
6	Light-CO₂RR & OER in PECf-cell.....	155
6.1	Experimental Remarks	156
6.2	Results and Discussion	156
6.2.1	Reaction at the anode side: OER	158
6.2.2	Energy balance of full cell: Sn-GDE vs. Ti ₂ O-NR	160
6.2.3	PECf system efficiency	166
6.3	Conclusions.....	170
7	Conclusion & Perspectives.....	171
7.1	Conclusions.....	172
7.2	Future Perspectives.....	175
8	Secondment Reports.....	177
8.1	INRS, Montreal – CANADA.....	177
8.1.1	Introduction	177
8.1.2	Objective	177
8.1.3	Experimental Activities	178
8.1.4	Results & Discussion.....	181
8.1.5	Conclusions.....	185
8.2	ETH Zurich, Hönggerberg - SWITZERLAND	186
8.2.1	Introduction	186

8.2.2	Objective	186
8.2.3	Experimental Activities	186
8.2.4	Results and Discussion	187
8.2.5	Conclusion.....	194

Bibliography.....	195
--------------------------	------------

Annexes	I
----------------------	----------

Glossary	XVII
-----------------------	-------------

List of Figures	XXI
------------------------------	------------

List of Tables.....	XXXI
----------------------------	-------------

List of Scientific Activities.....	XXXIII
---	---------------

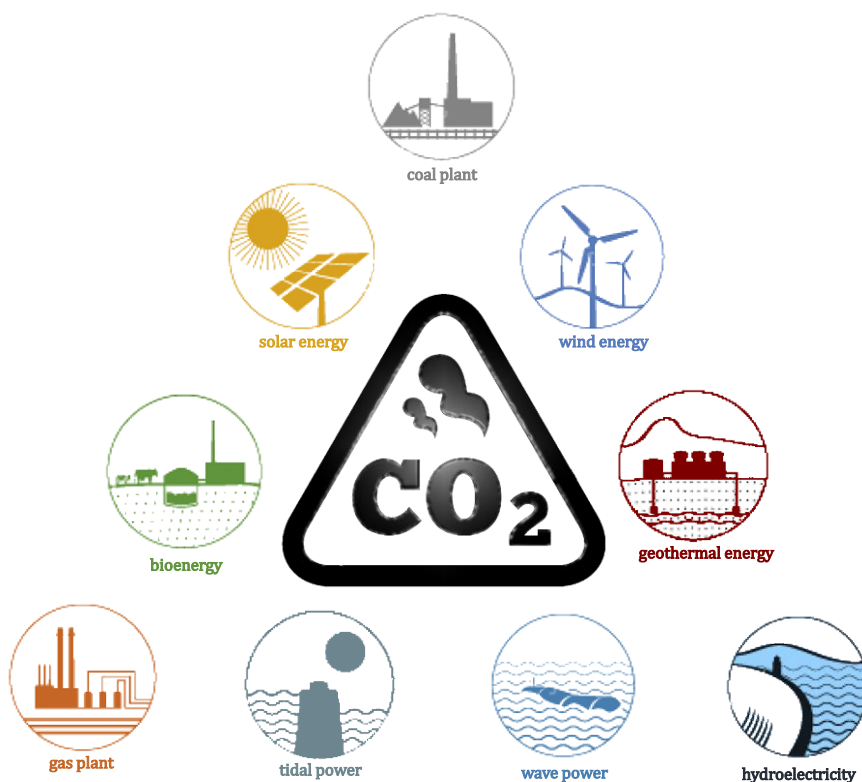
Acknowledgments.....	XXXV
-----------------------------	-------------

Financial Support	XXXVII
--------------------------------	---------------

Curriculum vitae.....	XXXIX
------------------------------	--------------

CHAPTER 1

Introduction



In this chapter, the key numbers of CO₂ economy were described initially. Most of the figures were obtained from international agencies and their latest reports on the climate and energy issues accessible to public. Later, CO₂ capture, use and conversion methods were explained with an emphasis on catalysis technologies. The electrocatalyst technologies mainly used in the frame of this work were highlighted including photo-assisted methods. The chapter was concluded with the scope of the research.

1.1 Key Figures of Sustainability

A part of heat delivered by solar irradiation is adsorbed on earth's crust; a part in our earth's atmosphere by greenhouse gases, while the rest is released to space. This balance keeps the planet warm enough to live comfortably. However growing amount of greenhouse gases, such as carbon dioxide (CO₂), methane (CH₄), nitrous oxide (N₂O) etc., trap too much heat which lead to climate change also known as "global warming". This imbalance causes a break down in planet's ecosystem such as extreme weather changes, desertification, ocean acidification, etc. which makes life difficult for living beings – or impossible in the future. Figure 1-1 shows a recent global temperature update by Hansen et. al.¹ showing the frequency of local June-July-August temperature anomalies (relative to 1951-1980 mean) for Northern Hemisphere land in units of local standard deviation (horizontal axis). Temperature anomalies in 1951-1980 match closely the normal distribution (green curve), which is used to define cold (blue), typical (white) and hot (red) seasons, each with probability of 33.3%. The observational data show that the frequency of unusually warm anomalies has been increasing over the past three decades. Global surface temperature measured in 2012 was +0.56 °C warmer than the 1951-1980 base period average. In their review, the authors associated the long-term warming trend, including continual warming since the mid-1970s, with the human-made greenhouse gases which began to grow substantially early in the 20th century.

Another figure often mentioned is the concentration of CO₂ by parts per million (ppm) in the atmosphere and usually compared to the period before industrial

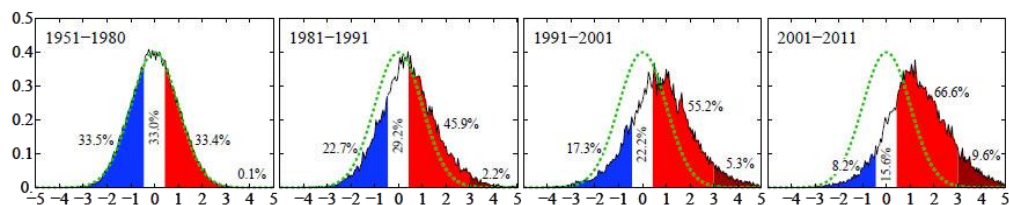


Figure 1-1. The shifting distribution of summer temperature anomalies adopted from Ref [1]

revolution¹ with a concentration of 270 ppm that elevated to 400 ppm today². Global surface temperature compared to that era raised nearly +2 °C.³ Proceeding on this issue, the world leaders have held a session in Paris, France for 2015 United Nations Climate Change Conference following the 1997 Kyoto Protocol⁴. The main objective was to set an international action to prevent global warming less than 2 °C till 2050 by undertaking rapid reductions for anthropogenic greenhouse gas emissions. However, the results from a recent study of McGlade et. al.² showed that globally, 1/3 of oil reserves, 1/2 of gas reserves and over 80 % of current coal reserves should remain unused from 2010 to 2050 in order to meet the target of 2 °C. Nevertheless, the fast development of the economy and rapid growth of the population create a continuous increase of energy demand leading to an aggravated energy crisis. This demand must be supplied by non-fossil fuels, e.g. renewable energies.

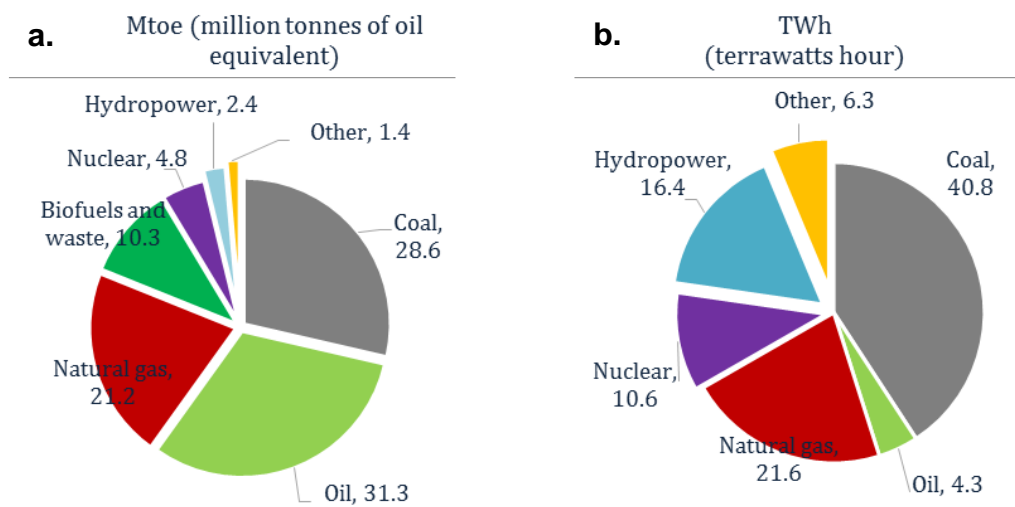


Figure 1-2. (a) Shares of world total primary energy supply till 2014. 100 % corresponds to 13,699 Mtoe (million tonnes of oil equivalent) **(b)** Shares of world electricity generation till 2014. 100 % corresponds to 23,816 TWh (terawatt hour) *Other includes geothermal, solar, wind, heat and etc. Adopted from “2016 Key world energy statistics” report pg. 6, from International Energy Agency (IEA) Ref.[5]

According to International Energy Agency (IEA) 2016 report, the world relied on renewable sources for almost 14 % (10.3 % biofuels, 2.4 % hydropower and 1.4 % other alternatives) of the primary energy total ~14K Mtoe (million tonnes of oil

¹ The transition to new manufacturing processes in the period from about 1760 to sometime between 1820 and 1840.

equivalent) by the year 2014, Figure 1-2 (a). This number is the sum of the energy equivalent of wind power, solar power (thermal, photovoltaic and concentrated), hydroelectric power, tidal power, geothermal energy, biofuels and the renewable waste in Mtoe unit. The total energy produced in terms of terawatts hour (TWh) shows a different aspect of the energy distribution where renewables accounted for almost 23 % (16.4 % hydropower and 6.3 % other alternatives) of the total world electricity generation, ~24K TWh, Figure 1-2 (b). These plots effectively summarize our dependence on oil in transportation, e.g. land, marine and aviation, and coal in residential or industrial purposes. In both categories, natural gas is the second alternative, to be used in manufacturing, heating/cooling and transport, with nearly $\frac{1}{4}$ of the total share. Considering the excessive depletion of fossil fuels and their high carbon footprint, alternative energies are inevitable for the future of our ecosystem. Since a report on all the alternative solutions are beyond the scope of this work, further reading on the low carbon footprint solutions (carbon capture and storage, nuclear power, energy efficiency and renewable energy sources) could be found elsewhere⁶.

1.2 CO₂ Valorisation Methods

From a materials science point of view, numerous advancements in catalysis⁷, solar energy⁸, batteries, fuel cells and supercapacitors⁹ have been conducted to create alternatives towards the aforementioned problems on energy. Increasing rate of renewable energy projects^{10 11} is a promising start but the share of renewable sources in total energy production is still low (~6 % excluding hydropower). Besides these are intermittent energy sources which are dependent on geographical site and season so energy conversion and storage technologies must be concerned. Pumped hydro, for example, is perhaps the least expensive large-scale energy storage system but is very site specific¹². Large scale batteries¹³ are another option to level the electricity output and there are several successful projects on site¹⁴. But their high cost of raw materials vs. low energy density is still a limiting factor, for instance, the storage of electricity with batteries have an energy density by volume (or even by mass) ranging from 0.3 to 2.8 GJ·m⁻³, depending on the kind of battery considered (the most efficient ones are Li-ion batteries). Figure 1-3 gives a comparison of chemical energy conversion methods with batteries and carbon

derived fuels. Chemicals such as methanol or gasoline have an energy density that is from 10 to even 100 times higher than that of batteries^{7b}. Therefore, a direct and effective action should be applied on the reduction of atmospheric CO₂ and industrial CO₂ emissions.

The first question in mind would be “How much useful could CO₂ be for the industry in its initial form?” In general, CO₂ is used as refrigerant for food preservation, beverage carbonation agent, inert medium (such as fire extinguisher), pressurizing agent, supercritical solvent, chemical reactant (urea, polymeric materials, carbonates etc.). But for all those applications to increase the value of CO₂, its purity is of importance.

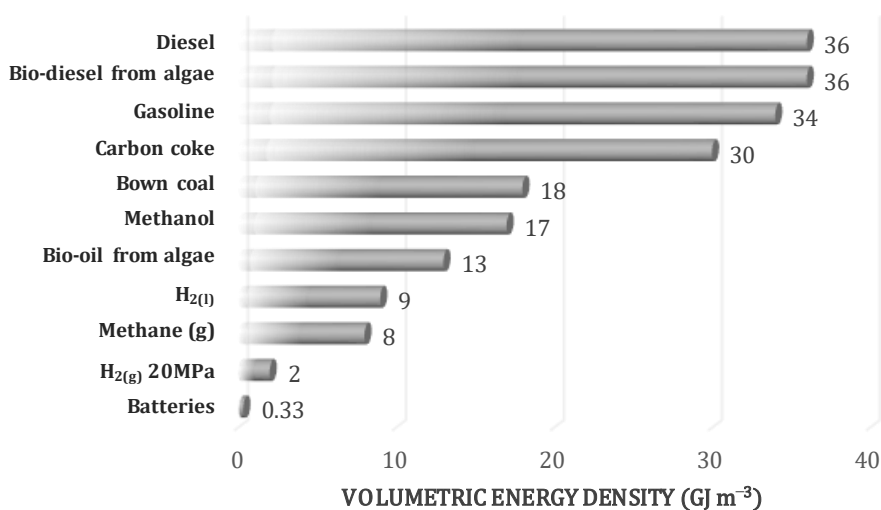


Figure 1-3. Volume energy density of batteries compared to that of different classes of chemicals. Image reproduced from Ref [7^b] Copyright 2013, American Chemical Society.

The second question would be “Is it possible to valorise CO₂ emissions by their conversion to another form?” There are two main challenges in its valorisation; separation/capture and conversion. **The first challenge** (separation and capture) is capturing CO₂ from flue gasses to produce a pure stream of CO₂ from natural gas or industrial processes for use in food processing and chemical industries. The main limitation is the quality of CO₂ gas because the attractiveness of CO₂ capture from a source depends on its volume, concentration and partial pressure. Most the emission sources have concentrations of CO₂ lower than 15 % by volume. However, a small proportion of the CO₂ emitting industry (less than 2%) have concentrations

that exceed 95 %, making them more suitable for CO₂ capture¹⁵. The data of selected worldwide large CO₂ stationary sources emitting more than 0.1 Mt CO₂ per year are given in Table 1.1. For example, effluents from power stations (coal, natural gas, fuel oil etc.) are the largest source of CO₂ emission ~10⁴ Mt CO₂ equivalent to ~79 %. Unfortunately, low partial pressures and concentration of CO₂ require a separation of oxygen from air after fossil fuel combustion. In that respect, valorisation of CO₂ emissions from petrochemical industry seems more attractive.

Table 1.1. Profile of worldwide large CO₂ stationary sources emitting more than 0.1 Mt CO₂ per year, adapted from Ref [15 7b]

Process	CO ₂ % vol. in gas stream	Emissions (MtCO ₂ /yr.)
Power		
Coal	12 – 15	7084
Natural gas	3 – 10	752 – 759
Fuel oil	3 – 8	326 – 654
Cement production	20	932 – 1000
Refineries (crude oil)	3 – 13	798 – 900
Iron and steel industry	15	630 – 900
Petrochemical industry		
Ethylene	12	155 – 300
Ammonia: process	100	113 – 160
Ammonia: fuel combustion	8	5
Ethylene oxide	100	3
CO₂ from Biomass		
Bioenergy	3 – 8	73
Fermentation	100	17.6

After its separation from the flue gases, **the second challenge** arises which is the conversion of CO₂. It is a linear molecule with the carbon at highest oxidation state (+4) making it a very stable molecule ($\Delta G_{\text{formation}}^{\circ} = -396 \text{ kJ} \cdot \text{mol}^{-1}$). Its conversion into oxidation state +2 or lower values requires a large amount of energy. In other means, it is an energy-demanding process when CO₂ is used as a single reactant. In some processes, energy requirements are thermodynamically smaller when CO₂ used with a co-reactant e.g. H₂.



At this point, there are several methods for reduction of CO_2 including electrochemical, photochemical, biochemical and thermochemical methods, which has been intensively studied^{7c,16}. Figure 1-4 (adapted from Centi et. al.^{7c}) illustrates the reaction routes for CO_2 conversion on the basis of desired end-product. The first expectation is the renewable energies that could be used directly to produce syngas and other low carbon species, e.g. solar thermal or photoelectrochemical routes.

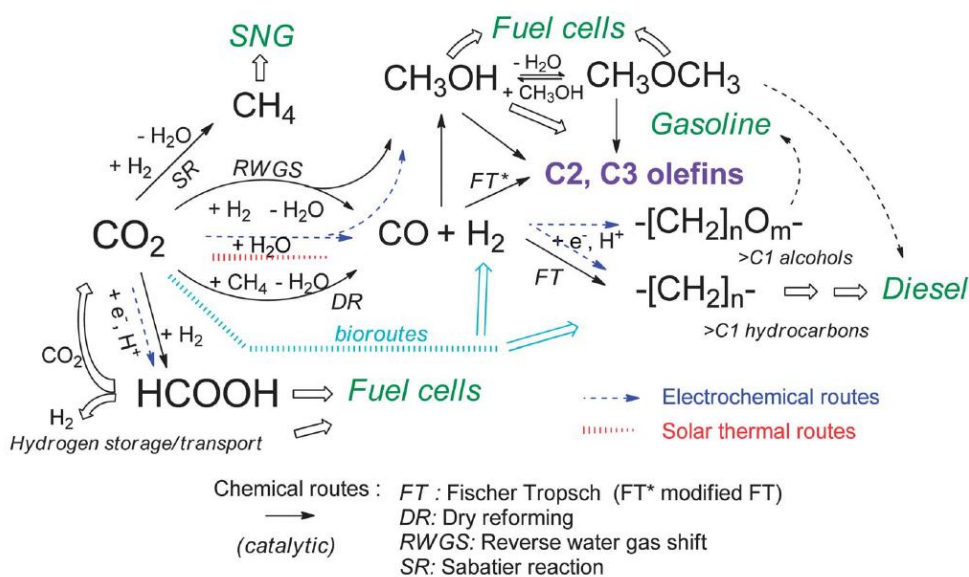


Figure 1-4. Schematic overview of the CO_2 conversion routes to including renewable energy routes. Image taken from Ref [7c] Copyright 2013, Royal Society of Chemistry.

In some specific conditions, those methods could produce C_2 hydrocarbons but with very low yield and poor catalyst stability. On the other side, indirect methods can be considered to integrate renewable routes to present technologies. For instance, production of sustainable H_2 and streaming to the following process such as reverse water gas shift could be an option to reach high value hydrocarbons. Here, hydrogen is one of the main co-reactant in many different steps shown in Figure 1-4 so production of H_2 from renewable energy can be a key point to decrease the carbon footprint of the overall system. Additionally, H_2O in vapour or liquid form is generally the product of the reaction except for solar thermal and

photo/electrochemical routes where water is used as a reactant for protonation of CO₂ species.

It is evident that renewable routes e.g. biochemical, electrochemical, photochemical routes, are limited to low carbon end-products such as O/C and H/C ratio is below 4. On the other hand, thermo-chemical routes (often with a catalyst) are the main routes to reach larger hydrocarbons which have higher economic values such as ethanol (C₂H₅OH), n-propanol (C₃H₇OH), octane (a constituent of gasoline with formula of C₈H₁₈) etc. In that respect, Aresta et. al.^{7b} classify the CO₂ conversion reactions in two categories which require low or high energy. In the low energy processes, CO₂ maintains its +4 oxidation state forming various organic molecules (urea, carbonates, polycarbonates, polyurethanes, carboxylates etc.) by homogenous reactions. In the high-energy processes, CO₂ goes down to oxidation states +2 or below to form hydrocarbons and alcohols. The former category mainly constitutes organics for the chemical industry and the latter is the fuel derivatives.^{7b} Syngas and short-chain carbons (C₂–C₃) are the main fuel derivatives for petrochemistry and have a market size ca. 12–14 times larger than that of the former thus suited targets for the conversion of large volumes of CO₂. Figure 1-5 shows an example of a plant producing fuels from flue gases using solar energy – carbon capture – CO₂ conversion system, in other terms solar fuel production. The modules in the imagined solar refinery operate for,

1. Harvesting sunlight
2. Capturing, purifying and releasing CO₂
3. Direct solar-driven CO₂ reduction by H₂O into fuels
4. Solar activation of CO₂/H₂O to CO/H₂, respectively, and
5. Catalytic conversion to fuels via traditional processing (i.e. methanol synthesis, hydrogenation, water gas shift or Fischer-Tropsch).

The goal for solar fuel production would be exploiting photocatalytic or photoelectrochemical routes in ambient conditions (unit-3, Figure 1-5). If the energy of the photons reaching the reactor would be the only input power then secondary solar electricity/heat units could be omitted (solar heat and solar electricity in unit-1, Figure 1-5). This could be realized by the design of an

electrochemical reactor which can operate with direct solar illumination which is the core of this study and discussed further in the next chapters.

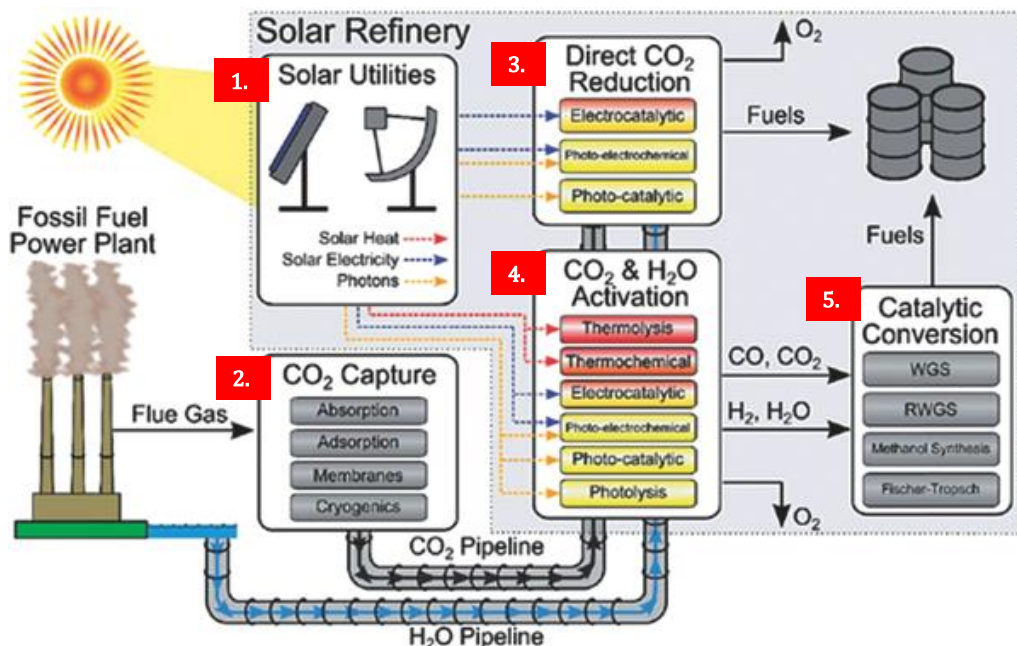


Figure 1-5. Schematic that illustrates the constitution and operation of a solar refinery for on-site capturing and transformation of solar fuel feedstocks (CO₂, H₂O, sunlight) into conventional fuels by: (1) Solar utilities, (2) CO₂ capturing, (3) Direct CO₂ reduction, (4) CO₂ & H₂O activation, (5) Catalytic conversion. The approximate temperature requirements for the solar-driven conversion processes are color-coded with red and yellow for high and ambient temperature, respectively. Reproduced with permission of Ref [17] Copyright 2015, Royal Society of Chemistry.

In brief, water splitting cells with direct semiconductor/liquid contacts are attractive because they avoid significant fabrication and systems costs involved with the use of separate electrolyzers wired to p-n junction solar cells. If catalyst selectivity and conversion yield is great enough to produce high value fuels such as methane, methanol or ethanol; catalytic conversion step (unit-5) can be bypassed as well. Such system would be similar to plant's photosynthesis where a positive change in the Gibbs free energy is accompanied by solar illumination and a catalyst loop producing sugar and oxygen¹⁸. In fact photosynthesis is a very complex mechanism with five integrated, membrane-bound assemblies involving thousands of atoms bound in thylakoid membrane of chloroplasts and is coupled with the Calvin cycle for CO₂ reduction^{18b}. Plants and some living organisms (algae and bacteria) do photosynthesis since a billion year and it is an inspiration to valorise excess CO₂ but it has a low efficiency (below 1 %)¹⁹. Thanks to intensive research,

this value has been improving for solar water splitting exceeding 10 % solar-to-hydrogen conversion efficiencies using multi-junction semiconductors integrated in a photoelectrochemical cell, besides photovoltaic-electrolysers systems have been pushing the limits even further²⁰. Although H₂ is an important fuel and chemical feedstock, a desirable alternative is to target the direct production of carbon-based fuels. In terms of energy efficiency in solar-to-fuel conversion from CO₂ gas, the values are much lower $\leq 1\%$ ²¹ for C1-products –except some works published in the last three years, $\sim 4.5\%$ ^{22 23} and 10% ²⁴ for formic acid and 6.5% ²⁵ for carbon monoxide. Hence the results show that solar powered CO₂ reduction is currently lagging far behind solar driven H₂O splitting and more research is needed to improve the activity of the catalysts and design novel reactors to increase the overall system efficiency. For instance, recent analysis by Herron et. al.¹⁷ on CO₂ conversion into methanol (CH₃OH, a high value fuel) showed the gap between photocatalytic reaction and commercial production rates. The photocatalytic reaction rates are $\sim 0.1 - 10 \mu\text{mol}_{\text{product}} \cdot \text{g}_{\text{cat}}^{-1} \cdot \text{h}^{-1}$ while commercial CH₃OH synthesis rates by hydrogenationⁱⁱ with Cu/Zn/Al₂O₃ catalyst are 7800-39000 $\mu\text{mol}_{\text{product}} \cdot \text{g}_{\text{cat}}^{-1} \cdot \text{h}^{-1}$. This is nearly 4-fold higher rate in comparison. Thus, the use of solar energy may lower the carbon footprint but the cost of the required catalyst and electrode area is quite significant ($>10^4$) with today's catalysts. In that respect, catalyst (or electrode) formation and reactor design are the two key points for energy conversion reactions in electrocatalysis which are CO₂ reduction and O₂ evolution. Next sections provide the general principles and results of the state-of-art in that fields.

1.3 Electrochemical Methods

Two approaches of electrochemistry have been realized:

- electrocatalysis in dark conditions (e.g. electrolysis cell)
- photo-assisted electrocatalysis under light illumination (e.g. photoelectrolysis cell).

ⁱⁱ 498 K, 50 bar, gas hourly space velocity at 10K range from 0.3-1.5 kgmethanol · Lcat⁻¹ · h⁻¹ using a bulk catalyst density of 1.2 g·cm⁻³

Next sections would expand the fundamentals of electrochemical and photoelectrochemical catalysis. Additionally, a general overview of the state-of-the-art in photo/electrocatalysis field are included.

1.3.1 Fundamentals of electrochemistry

Electrochemistry is the study of chemical reactions occur where the charge transfer and adsorption/desorption of species take place between the boundary of an electrode (conducting or semiconducting solid) and an electrolyte (ionically conducting phase).

Potential and Thermodynamic of the Cell. In order for a reaction to happen, the reaction must be energetically feasible and thermodynamically favourable²⁶. This depends on the energy balance of the reaction. For a chemical reaction that is thermodynamically favourable, the Gibbs free energy must be negative $\Delta G^0 < 0$. In an electrolyte, such a reaction would imply an electron transfer between electrodes so the free energy could be used (in the form of electricity). For a chemical reaction that is thermodynamically unfavourable, the Gibbs free energy is positive ($\Delta G^0 > 0$). The energy difference needs to be supplied to start the reaction or shift it towards the desired side of the equilibrium, Figure 1-6. If there is no change in Gibbs energy ($\Delta G^0 = 0$), the reaction is either not happening or the reaction is in a chemical equilibrium, i.e. the reaction occurs in both direction at the same rate.²⁶ The Gibbs free energy can be expressed in terms of kilojoules per mole ($\text{kJ}\cdot\text{mol}^{-1}$) and converted to the cell voltage. The relationship between the Gibbs Energy and the equilibrium cell potential is given by,

$$\Delta G_{\text{eq}}^0 = -n \cdot F \cdot E_{\text{eq}}^0 \quad (1.3)$$

where n is the number of transferred electrons per mol of the reactant in the reaction, F is the Faraday constant ($96485 \text{ Coulombs}\cdot\text{mol}^{-1}$) and E_{eq}^0 is the thermodynamic potential at equilibrium.

A typical reaction in an electrochemical cell consists of two half-cell reactions where an oxidation process taking place at the anode and a reduction process at the cathode. The electron is transferred from the anode to the cathode through an electrical wire while the cell balance is maintained by the ionic charge transfer with

the electroactive specie through the solution i.e. the electroactive species is oxidized/reduced by the electron transfer at anode/cathode, respectively.

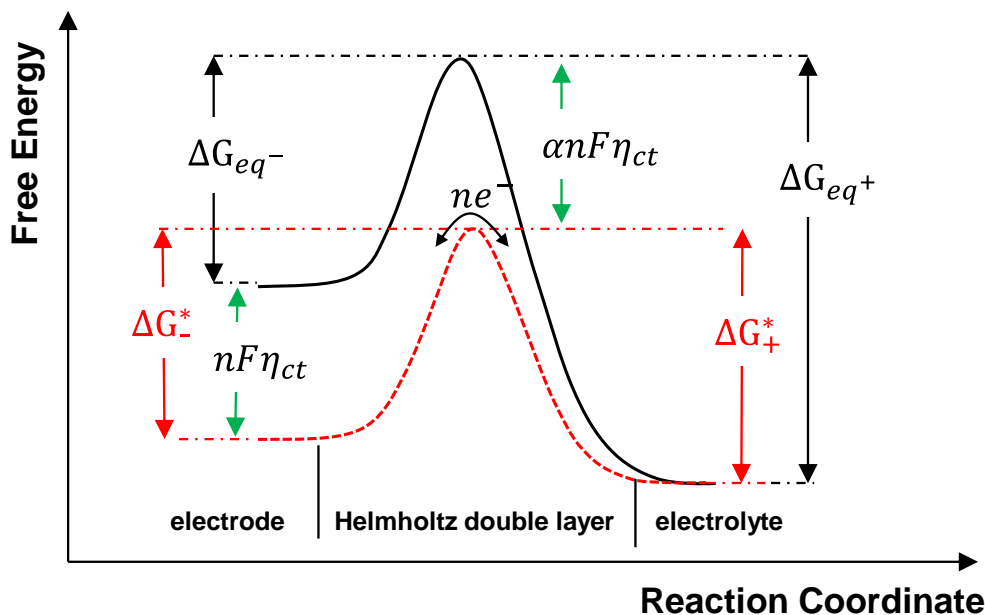
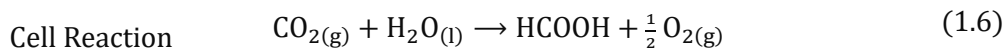
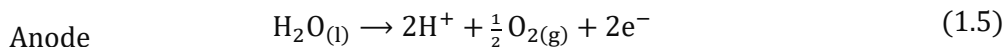
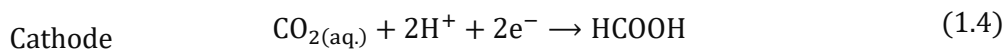


Figure 1-6. Free energy of redox system at the electrode-electrolyte interface where the redox system is at equilibrium (black) and at polarized state (red curve). ΔG_{eq}^- and ΔG_{eq}^+ denote the activation energies for the cathodic and anodic reactions, respectively under equilibrium. ΔG_{-}^* and ΔG_{+}^* denote the activation energies for the cathodic and anodic reactions, respectively, for applied bias conditions. α is the transfer coefficient and η_{ct} is the overpotential for charge transfer. The figure is adapted from Ref. [27]

The product of the reactions can be liquid or gaseous and leave the surface or it can be solid and deposit on the surface. The reactions at both electrodes are interconnected and contribute to the overall cell reaction of the electrochemical cell. The oxidation of water (H_2O) and reduction of carbon dioxide (CO_2) could be an example for such reaction couple. For instance, CO_2 would be converted into formic acid ($HCOOH$) with uptake of two electrons and protons at the cathode (CO_2RR) whereas water oxidation to O_2 gas takes place at the anode supplying the electrons (OER). The half-cell reactions and the cell reaction would be written by,



Now considering the full cell reaction, most electrochemical reactions operate at potentials well above the thermodynamic equilibrium potential as calculated by Eq.(1.3), due to various losses in the electrochemical cell. A certain current passing through a conductor faces a certain resistance of the conductor so a slightly higher potential must be applied to overcome this resistance. The same accounts for the electrolyte resistance, where the conductivity of the electrolyte is the main factor. Additionally the electrolyte conductance depends on the cell geometry (area and distance between electrodes) and molarity and type of ions, the solution viscosity, the operating temperature etc. Consequently, the total cell voltage for a given current density (j) is the sum of thermodynamic equilibrium potentials E^0 of cathode and anode reactions, including their kinetic overpotentials $\eta_{\text{cathode or anode}}(j)$, and the cell polarization losses $\Delta\phi_{(j)}$, which are a factor of the operational current density. This equation is given by,

$$E_{\text{cell}}(j) = E_{\text{anode}}^0 - E_{\text{cathode}}^0 + \eta_{\text{anode}}(j) - \eta_{\text{cathode}}(j) + \Delta\phi_{\text{ionic}}(j) + \Delta\phi_{\text{elect.}(j)} \quad (1.7)$$

Kinetics of Electrode Reactions. Eq. (1.7) shows that the current is a major factor in final cell potential. The factors effecting the current density should be considered while designing an electrochemical system. At low overpotentials, the current density is controlled by electrical charge transfer defined as the activation limitation region and given by Butler-Volmer and Tafel equations²⁸

$$j_i = j_i^0 \cdot \exp\left[\frac{\alpha_i \cdot z_i \cdot F}{R \cdot T} (E - E_i^0)\right] \quad (1.8)$$

where "i" stands for products of anode (or cathode) reaction, j_i^0 and α_i is the exchange current density and charge transfer coefficient for reaction product "i", respectively. R is the universal gas constant ($8.314 \text{ J mol}^{-1}\text{K}^{-1}$) and T stands for absolute temperature (298 K). E is the potential established at the electrode under equilibrium and E_i^0 is the thermodynamic equilibrium potential of "i". By taking the logarithm of Eq.(1.8), once can obtain the Tafel equation²⁸ given by,

$$E - E_i^0 = \eta_i = b \cdot \log\left(\frac{j_i}{j_i^0}\right) \quad (1.9)$$

Table 1.2 shows the charge transfer coefficients calculated from a series of Tafel slope values. Usually, cyclic (or linear sweep) voltammetry curves are plot in current versus applied potential, $j = f(E)$. On the other hand, Tafel slopes are presented in form of $E = f(j)$ that correspond to the overvoltage required for one decade increment of current (or current density).

Table 1.2. Selected Tafel slope values calculated from Eq.(1.8) for a direct 1, 2 and 4 electron transfer at the rate determining step (RDS), $R = 8.314 \text{ J mol}^{-1}\text{K}^{-1}$ and $T = 298 \text{ K}$.

$\text{mV}^{-1} \cdot \text{dec}$ $j = f(E)$	Tafel slope $\text{mV} \cdot \text{dec}^{-1}$ $E = f(j)$	α (charge transfer coefficient)		
		#e ⁻ at RDS		
		1 e ⁻	2 e ⁻	4 e ⁻
4	250	0.24	0.12	0.06
5.0	200	0.3	0.15	0.07
8.5	118	0.5	0.25	0.13
16.9	59	1.0	0.5	0.2
33	30	-	1.0	0.5

The lessening of Tafel slope value indicates a faster reaction kinetic due to the firm current response by a small overvoltage increment. A representative Tafel plot is given in Figure 1-7.

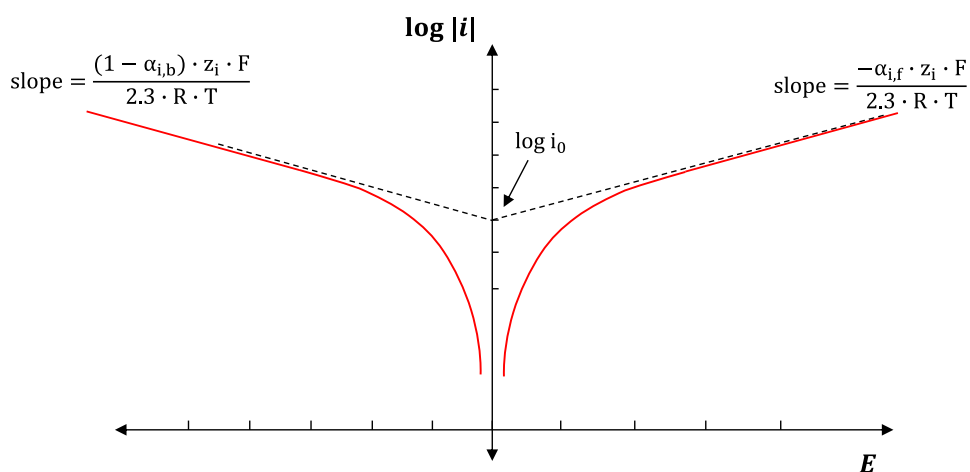


Figure 1-7. Representative Tafel plots for anodic and cathodic branches of a logarithmic current versus potential curve

The unit of the slope value is mV per decade, which contains information about the kinetics of the reaction mechanism. In general, low Tafel values ($<60 \text{ mV} \cdot \text{dec}^{-1}$) are

correlated with fast electron transfer where the reaction is limited by another phenomenon, i.e. a rate determining step such as re-organization of the molecule or uptake of an ion such as protonation. Figure 1-8 (a) shows a model²⁹ of current versus electrode potential curves for an ideal system driven from Eq.(1.9) where both half-cell reactions (CO₂RR and OER) exhibit fast reaction kinetics and do not limited with mass transport. The half-cell reactions are given in Eq.(1.4) ($E_{\text{CO}_2\text{RR}}^0 = -0.225 V_{\text{RHE}}$) and Eq.(1.5) ($E_{\text{OER}}^0 = 1.23 V_{\text{RHE}}$), respectively. Consequently, the equilibrium cell voltage would be 1.45 V and exponentially increase with the required current value according to Eq. (1.8). In Figure 1-8(a), the point-lines present the standard redox potentials, E^0 . The dashed-curves show an example of overpotentials (η) required for each reaction to continue respect to the Butler-Volmer parameters given in Figure 1-8 comments. It is evident that α and i_0 (or current density, j_0) are the main factors of the overpotential. For instance, to reach 10 mA·cm⁻² current density over 10 cm² geometrical surface area, the cathodic and anodic voltage would be -0.825 and $1.407 V_{\text{RHE}}$, respectively, corresponding to a cell voltage of 2.23 V according to an ideal model shown in Figure 1-8. Only the contributions of kinetic losses from both electrodes are nearly 800 mV, an overvoltage to the standard value for Eq.(1.6).

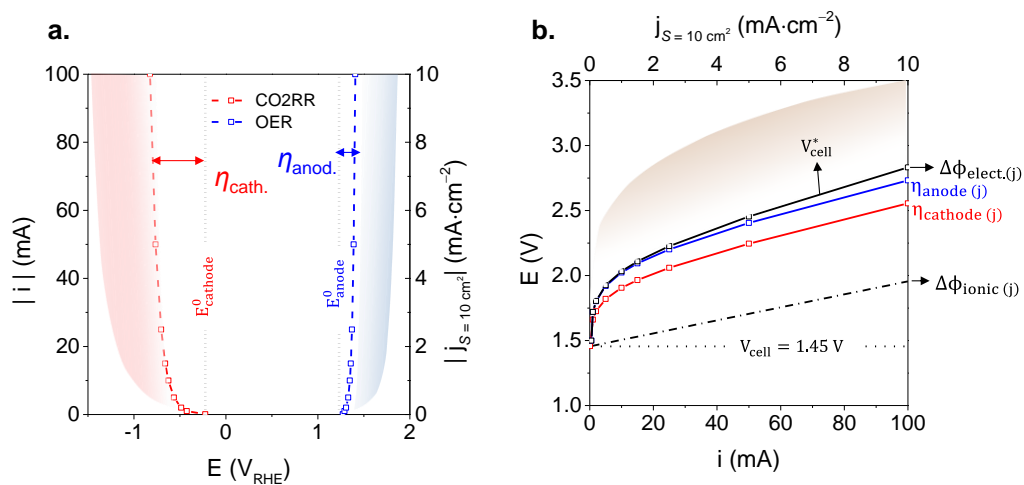


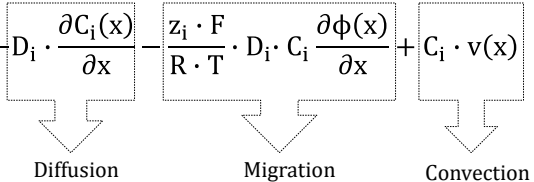
Figure 1-8. (a) Current versus applied voltage modelled²⁹ for half-cell reactions: an ideal anode for OER in a 0.1 M KOH solution ($\alpha = 1.0$ or $60 \text{ mV}\cdot\text{dec}^{-1}$ and $i_0 = 0.1 \text{ mA}$) versus a hypothetical cathode with 100 % CO₂RR conversion efficiency in 0.1 M KHCO₃ solution ($\alpha = 0.29$ or $200 \text{ mV}\cdot\text{dec}^{-1}$ and $i_0 = 0.1 \text{ mA}$) (b) Electrochemical load curve of the full-cell showing the contributions of ionic and electronic losses; 5 and 2 Ω , respectively.

Figure 1-8(b) shows the corresponding electrochemical load curve of the full cell including ohmic losses from the electrolyte and contacts i.e. ionic and electronic contributions, respectively. The largest contribution is derived from the mass transfer limitations and ionic resistance which depends on the type of the supporting electrolyte and its concentration. This effect is more noticeable in large cells that operate at larger currents (>100 mA). Therefore, industrial cells utilize highly concentrated electrolytes (1-3 M) contrary to laboratory cells (0.1-1 M). Additionally, the kinetic losses due to the cathodic and anodic overvoltage is a major product on the overall cell voltage, which is highlighted with shaded areas in Figure 1-8(a-b).

Mass Transfer Limitations. The electrochemical reactions are dependent on the concentration of the electroactive species which are in molecular distance to the electrode surface, thus transport processes close to the solid/liquid boundary must be considered. In order to have a continuous reaction in a cell, the species participating in the reactions must be continuously absorbed on the electrode's surface, therefore the mass transport in the electrolyte cell is of importance. Meanwhile, reactants must be supplied to the surface and the products would be removed from it simultaneously. Therefore three modes of mass transfer must be revised which are; diffusion, convection and migration.²⁶

Diffusion is the movement of a species due to a concentration gradient. If the species reacts on the surface leading to a decrease of their concentration at the vicinity of the electrode, there is an unequal concentration which leads to a mass transport of reactant towards the electrode. However, diffusion is a rather slow process which might lead to mass transport problems especially at large overpotentials. *Convection* is the movement of a molecule due to density or temperature differences within the electrolyte. It arises either from external forces in the electrochemical cell like vibrations, flushing the solution with a gas or a mechanical stirrer. *Migration* is the movement of charged molecules in the electrolyte due to potential gradients. The electrons flow from the anode to the cathode and accumulate at the electrode/electrolyte junction. In the meantime, negatively (or positively) charged ions (dissociated in the electrolyte) are attracted towards the anode (or cathode) which creates a potential difference in the solution between the

cathode and anode. This overall mass transfer to an electrode is explained by the Nernst-Planck equation²⁶, written for one-dimensional mass transfer along the x-axis as,

$$j_i(x) = -D_i \cdot \frac{\partial C_i(x)}{\partial x} - \frac{z_i \cdot F}{R \cdot T} \cdot D_i \cdot C_i \frac{\partial \phi(x)}{\partial x} + C_i \cdot v(x) \quad (1.10)$$


Diffusion Migration Convection

where $j_i(x)$ is the flux of species "i" ($\text{mol} \cdot \text{s}^{-1} \cdot \text{cm}^{-2}$) at distance x from the surface, D_i is the diffusion coefficient ($\text{cm}^2 \cdot \text{s}^{-1}$), $\partial C_i(x)/\partial x$ is the concentration gradient at distance x , $\partial \phi(x)/\partial x$ is the potential gradient, z_i is the charge (dimensionless) and C_i is concentration ($\text{mol} \cdot \text{cm}^{-3}$) of species "i" and ϕ is the electric field. Finally, $v(x)$ is the velocity ($\text{cm} \cdot \text{s}^{-1}$) with which a volume element in solution moves along the x-axis.

Considering a redox reaction such as Eq.(1.4) ($E_{\text{CO}_2\text{RR}}^0 = -0.225 V_{\text{RHE}}$) and Eq. (1.5) ($E_{\text{OER}}^0 = 1.23 V_{\text{RHE}}$), Nernst equation is often used to provide a linkage between electrode potential, E and the concentration of participants in the electrode process by,

$$E = E^0 + \frac{R \cdot T}{n \cdot F} \cdot \ln \left(\frac{C_{ox}}{C_{red}} \right) \quad (1.11)$$

where C_{ox} can be CO_2 specie which gains electrons, and would be reduced according to Eq.(1.4). Considering the reverse reaction, C_{red} can be HCOOH specie which loses two electrons and is oxidized back to CO_2 . The same relation can be done with $\text{O}_2/\text{H}_2\text{O}$ couple as oxidant/reductant according to Eq. (1.5). If a system follows the Nernst equation or an equation derived from it, the electrode reaction is often said to be thermodynamically or electrochemically reversible (or Nernstian).³⁰

Whether a process appears reversible or not, it depends on one's ability to detect the signs of disequilibrium²⁶. To detect this difference, some components of the reactions would be omitted so that the system can attain equilibrium rapidly enough compared to measuring time. In that respect, electrochemical systems are frequently designed so that one or more of the contributions to mass transfer are negligible³¹. For example, the migration component can be reduced to negligible

levels by addition of an inert electrolyte (a supporting electrolyte) at a concentration much larger than that of the electroactive speciesⁱⁱⁱ. Convection can be avoided by preventing stirring and vibrations in the electrochemical cell²⁶. Under these circumstances, the rate of the reaction will be determined by the diffusion of the species and the current density is limited by the diffusion of the reactants to the electrode surface. This mode of mass-transfer condition can be written by a simplified form of Fick's law²⁶

$$j_{\text{lim},i} = \frac{z_i \cdot F \cdot D_i}{\delta} \cdot C_i \quad (1.12)$$

where $j_{\text{lim},i}$ is the limiting current density, D_i is the diffusion coefficient, δ is the diffusion layer thickness. This section would be expanded in Rotating Disk Electrode section which was used in Chapter 5 for O_2 reduction reaction with Mn-Co nanoparticles. Throughout this study, we will be concerned with the interface between an electrode (electronic conductor) and an electrolyte (an ionic conductor) studied with electrochemical cells. These systems are designed mostly in two or three electrode configurations as illustrated in Figure 1-9(a) and (b), respectively. The electrode potentials are controlled with a potentiostat which can alter the direction and the rate of charge transfer according to the reactions of interest. In general, for two electrode cells, the focus is the overall cell performance, e.g. cell potential, current and stability. For instance, Figure 1-9(a) illustrates a water splitting reaction where hydrogen evolution (HER) and oxygen evolution reactions (OER) occur at the cathode and anode, respectively. If the individual cell potentials or a reaction mechanism would be investigated, three electrode cells can be used which employs a reference electrode placed at the vicinity of the working electrode. The reaction of interest is studied at this electrode and its potential is followed by reference electrode which has a stable potential throughout the experiment. Figure 1-9(b) demonstrates a similar three electrode set-up but particularly design for electrocatalysis of CO_2 where its reduction (CO_2RR) occurs at the cathode.

ⁱⁱⁱ e.g. potassium pyrophosphate in electrodeposition of tin as in Chapter 3 or sodium bicarbonate ions in CO_2RR experiments as in Chapter 3 & 4 or potassium hydroxide in OER experiments as in Chapter 5.

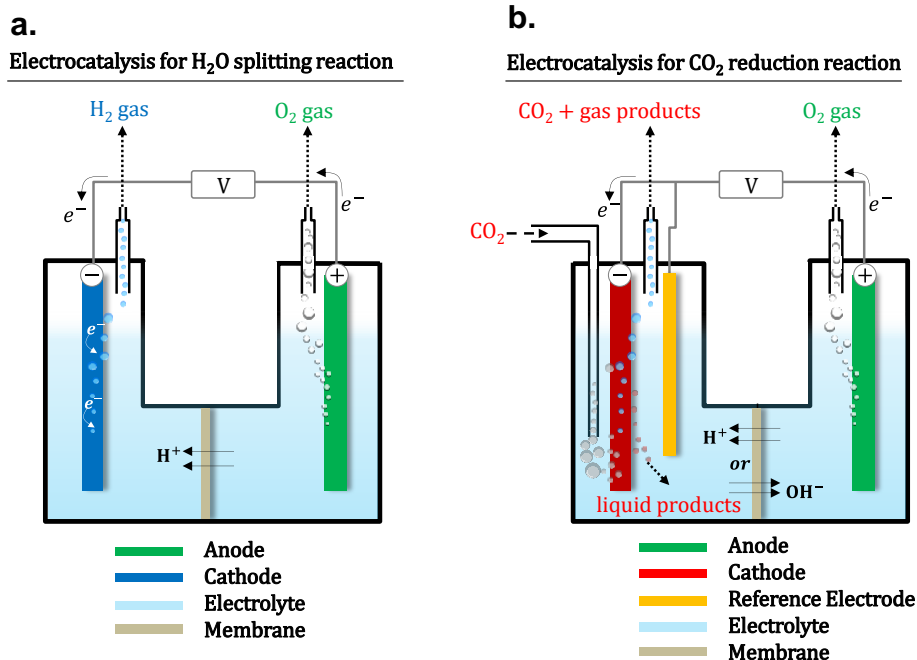


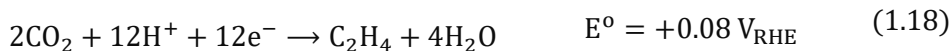
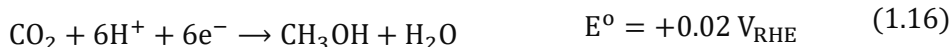
Figure 1-9. (a) Two electrode cell separated with a proton exchange membrane. HER and OER occurs at cathode and anode, respectively. (b) Three electrode cell separated with either cation or anion exchange membrane. CO₂RR and OER occurs at cathode and anode, respectively. Electrons flow from anode to cathode direction and “V” is the symbolic voltage reading at the potentiostat that controls the direction and rate of electron transfer. CO₂ is continuously bubbled before and during the electrocatalysis reactions.

The electrolyte solution is bubbled with CO₂ before and during the experiments so the maximum saturation of the gas in the electrolyte could be maintained. The end-products of the cathode reaction could be either in the gas form (CO, CH₄, C₂H₄ etc.) leaving the cell with unreacted CO₂ or they could be in liquid form (HCOOH, CH₃OH etc.) to be analysed later by taking samples from the catholyte. The complementary reaction, O₂ evolution reaction (OER) at the anode, would be the sink of electrons. The electrons flow through a wire between anode and cathode and electron exchange must be compensated with the ion exchange through the solution. Often, the alkali metal salts are added to increase its ionic conductivity of the electrolyte. An ion exchange membrane separates both compartments to prevent re-oxidation of CO₂ end-products and their dilution by the counter reaction products, i.e. O₂. Those membranes are made of a polymeric material attached to a charged ion group that could be selective to cations (H⁺) or anions (OH⁻) depending on the mobility of the functional group³². To achieve large-scale electrolysis in an efficient manner; abundant, stable and active catalyst materials should be developed. In addition to

those requirements, the overall system design is critical to decrease the energy losses such as ohmic drop due to ionic and electronic resistance of the electrolyte and electrode contacts, respectively. The following sections provide general insights and a summary of the results for the both side of the reactions, CO₂RR at the cathode and OER at the anode.

Cathode Reaction: CO₂ reduction reaction

The electrocatalytic reduction of CO₂ is a multistep reaction that requires electrons (>2) and simultaneous proton uptake. The potential values of the half reactions involved in the CO₂RR are given by,



On several occasions carbon-carbon coupling is necessary to form larger hydrocarbons such as ethylene (C₂H₄) and ethanol (C₂H₄OH). To perform these tasks, a catalyst must be able to absorb and stabilize intermediate species, transfer the electrons, cleave C–O bonds and/or form C–H bonds. Additionally, reduced species must be able to desorb from the catalyst surface without further blocking/poisoning those active sites. Hence it is clear that a catalyst with a high electrical conductivity and surface energy is necessary to perform those tasks. The metals are the initial candidates which have been studied for many years³³. A pioneer in this field is Hori and his coworkers³⁴ that classified metal electrodes into four categories in accordance with the product selectivity shown in Figure 1-10.

The 1st group metals include Pb, Hg, In, Sn, Cd, Tl, and Bi which have high H₂ overvoltage, negligible CO adsorption properties, and high overvoltage for the initial electron uptake of CO₂ to form CO₂^{•-} radical. The weak stabilization of CO₂^{•-}

radical give formate ion, HCOO^- (or formic acid, HCOOH in acidic media) as the major product³⁵.

The 2nd group metals include Au, Ag, Zn, Pd, and Ga. They have medium H_2 overvoltage and weak CO adsorption properties. They can cleave the C–O bond and allow CO desorption so their major product is CO .

The 3rd group metals include Cu (and in some studies ruthenium as well). Cu is unique for production of CO_2 reduction CH_4 , C_2H_4 , alcohols and aldehydes in quantitatively reproducible amounts by its ability to stabilize and react CO to more reduced species.

The 4th group metals do not practically give product from CO_2 reduction continuously^{34d}, but H_2 evolution occurs in water. They can be divided into two sub-groups as semi-inert and inert. The former sub-group include Ni, Fe, Pt, and Ti, which do not exhibit useful catalytic properties under typical reaction conditions however, this situation can change when the conditions are modified e.g. high pressure or organic electrolytes/ionic liquids. The latter sub-group include Ta, Mn, and Al which heavily form H_2 even if the reaction conditions are altered.³⁶

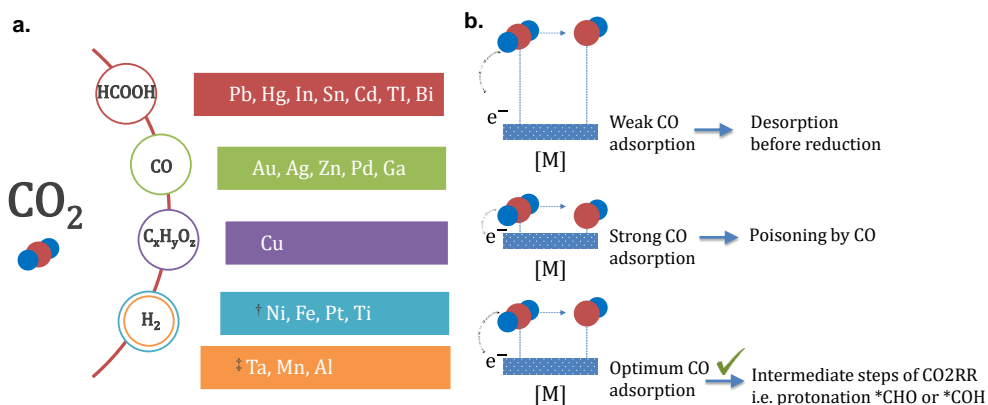


Figure 1-10. (a) Electrode materials and their selectivity in accordance to reaction products of CO_2 reduction^{36 37 34d 35 38} (\dagger semi-inert because modified conditions such as high pressure or in ionic liquids showed CO_2RR activity³⁶ \ddagger inert because even if the reactions conditions are modified no CO_2RR activity was found.) (b) Schematic illustration of metal and surface bound CO_2 and CO interactions. The first one is weak CO bonding leading to desorption before its further reaction, second is strong CO adsorption leading to surface poisoning and the last figure is the optimum CO adsorption for further electron and proton uptake to form intermediates species.

At this point, a choice should be made for the selection of the catalyst to be work with. As discussed earlier, the total conversion efficiency (yield) of CO_2 is 4-fold

lower than the commercial methods today. In a simpler meaning, from 100 unit of CO₂ gas entering to an electrochemical system, broadly 0.1 unit of CO₂ gas could be converted with electrocatalysis while the rest 99.9 is the unreacted CO₂ –in comparison to hydrogenation. This is mainly the result of the charge density devoted to CO₂ end-product. If we would design a system to electrochemically reduce CO₂ in one-pass, all the gas entering to the system should be converted to obtain a feasible gaseous end-product. However, the recovery of the accumulated liquid products at the electrolyte beaker would be more feasible if one builds up a closed CO₂ gas loop which circulates continuously to obtain liquid end-products instead of a gas product which is highly diluted with unreacted CO₂. Therefore, a catalyst choice in Figure 1-10 leads us to 1st and 3rd group metals. Cu is the only choice in the 3rd group while there are several alternatives in the 1st. There are numerous studies that use either pure metals or their alloys of the 1st group which could give >90 % faradaic efficiency³⁹ but there are concerns for an electrolysis set-up regarding its sustainability.

Table 1.3. Selected properties of some post-transition metals with high H₂ overpotential.

Property	Sn	Bi	In	Pb	Hg
Appearance at ambient conditions	Silver solid metal	Silver solid metal	Silvery-white solid metal	Silvery-grey solid metal	Silver liquid metal
Density (g/cm ³)	6.99	9.8	7.31	11.34	13.55
Hazards under GHS*	Not	Not	Not	Slight	Acute
Exposure Limit under NIOSH IDLH, TWA** (mg/m ³)	2	5	0.1	0.05	0.025
Price low-high (\$/kg)	13-21	15-27	720-745	1.56-2.11	2.9-8.7

GHS: Globally Harmonized System of Classification and Labelling of Chemicals

TWA: A threshold exposure limit (used in the workplace) measuring the average exposure to a substance over an 8-hour work day or a 40-hour work week.

NIOSH IDLH: The National Institute for Occupational Safety and Health Immediately Dangerous to Life or Health

Firstly, Pb and Hg are environmentally more toxic than Sn metal and secondly, the cost of those metals are higher. So far, Sn metal has proven a good faradaic efficiency for HCOOH ($\approx 70\%$)⁴⁰ which is the only liquid phase product. For instance,

compared to Cu, Sn metal facilitates post-valorisation of the electrosynthesis because only water and formic acid would be separated in the steam boiler. Selected properties of those metals are given in Table 1.3 for comparison.

Sn-based electrocatalysis of CO₂

An early effort on formic acid production through CO₂RR was performed with a fixed reactor providing 90% formic acid efficiency but following a decrease of faradaic efficiency to 30% due to re-oxidation of formic acid ⁴¹. Authors in essential used an ion exchange membrane to separate two redox reactions preventing re-oxidation of products. Li & Oloman ⁴² used Sn deposited on Cu mesh electrodes having 50 – 86 % HCOOH conversion at a high expense of –4 to –5.8 V reactor voltages. The low catalytic stability in their former work (catalyst deteriorating after about 20 min operation) was related to the loss of Sn from the mesh surface. Their latter work showed the significant effect of reactor design reaching up to 3 hours operational stability which may be attributed to the lower reactor voltages –2.7 to 4.3 V. Wu et al. made noteworthy contributions ⁴³ achieving 72 % HCOOH conversion efficiency on Sn sprayed on GDE with 20 wt. % Nafion which was found to be the percolation threshold for binder loading. The decrease of faradaic efficiency (above 20 wt. % Nafion loading) was attributed to “a blockage of catalyst” sites reducing gas permeation[‡]. Along with a statistical analysis, another valuable report by Alvarez et. al.⁴⁴ was 70.5 % HCOOH efficiency with a Sn catalytic ink again including Nafion, with a binder to water ratio (1:1) resulting in 90 min of operational stability. A recent study reported by Wang et. al. ⁴⁵ also utilized Sn catalyst ink with 50% wt. Nafion sprayed on GDE and obtained 72.9 % HCOOH conversion efficiency over CO₂ for 30 min of operation time. The most similar approach to our study was made by Lee & Machunda. They also utilized Sn deposited on GDE as working electrode to reduce humidified CO₂ gas realizing an electrolyte free reactor. A low formic acid faradaic efficiency with 12 % was obtained at -2 mA.cm⁻² with -1.6V as the cell voltage while H₂ gas fed to the Pt counter electrode.

Cu-based electrocatalysis of CO₂

The electroreduction of CO₂ on copper (Cu) metal and its oxide derivatives (Cu₂O and CuO) is one of the most attractive research areas due to their abundancy, non-

toxicity and unique ability to produce a large variety of hydrocarbons. Previous studies tried to highlight which parameters govern the activity and selectivity of the copper metal by using experimental and/or computational methods⁴⁶. A summary of that extensive study of the pioneers in the field is given in Table 1.4 in Chapter 1. Despite many ambiguities to explain the mechanism towards its unique catalytic property, main assumptions generally accepted so far by the community are:

- (i) initial electron transfer ($\text{CO}_2^\bullet -$ radical) is the initial rate determining step (RDS)
- (ii) CO and HCOOH originated from different pathways ^{46d, 46e, 46g}
- (iii) CO is assumed to be the key intermediate for hydrocarbon production^{34a, 47} e.g. C2-C3 derivatives, and
- (iv) proton concentration (or local pH disturbed by side product: OH^-) at the electrode surface has a great influence on selectivity⁴⁸ i.e. higher hydrocarbons promoted by protonation and particularly for copper oxides.

The most of the authors in Table 1.4 indicated that active sites for reaction intermediates play a key role to selective CO_2RR .

Table 1.4. Mechanistic pathway for CO_2RR /CORR on Cu proposed by different authors. The asterisk “*” indicates that this compound is adsorbed at the surface. Underlined arrows ($\underline{\rightarrow}$) indicates the RDS – rate determining step.

	Hori	Petersson & Durant & Norskov	Schouten & Koper
	1997-2016 ^{34a, 34b, 34d, 47a, 49} experimental	2010-2012 ^{46b, 46c} experimental / computational	2011-2013 ^{46d, 50} experimental
HCOOH	$\text{CO}_2 \underline{\rightarrow} \text{CO}_2^\bullet - + \text{H}^+ / \text{ads} \rightarrow \text{HCOOH}$	$\text{CO}_2 \rightarrow \text{CO}_2^\bullet - \rightarrow \text{COOH}^* (-\text{F})$ $\text{CO}_2 \rightarrow \text{CO}_2^\bullet - \rightarrow \text{OCHO}^* (-\text{C})$	$\text{CO}_2 \underline{\rightarrow} \text{CO}_2^\bullet - + \text{H}^+ / \text{ads} \rightarrow \text{HCOOH}$
CO	$\text{CO}_2 \underline{\rightarrow} \text{CO}_2^\bullet - + \text{H}^+ / \text{ads} \rightarrow \text{CO} + \text{OH}^-$	$\text{COOH}^* \rightarrow \text{CO}^* - \text{OH} \rightarrow \text{CO}^* (-\text{C})$	$\text{CO}_2 \underline{\rightarrow} \text{CO}_2^\bullet - + \text{H}^+ / \text{ads} \rightarrow \text{CO} + \text{OH}^-$
C₂H₄	$\text{CO} \underline{\rightarrow} \text{CO}^* \rightarrow \text{C-OH} + \text{H}^+ \rightarrow \text{CH}_2\text{-CO}$	$\text{COOH}^* \rightarrow \text{CO}^* \rightarrow \text{CHO}^* (-\text{C})$	$\text{CO} \underline{\rightarrow} \text{CO}^* \rightarrow \text{C-O} \rightarrow \text{C}_2$
CH₄	$\text{CO} \underline{\rightarrow} \text{COH}^* \rightarrow (\text{COH})^- (\text{pH})$	$\text{CO}^* \underline{\rightarrow} \text{CHO}^* \rightarrow \text{CH}_2\text{O}^* \rightarrow \text{CH}_3\text{O}^*$	$\text{CO} \underline{\rightarrow} \text{C-O} + \text{H} \rightarrow \text{CHO}^* (\text{C1})$

$\text{CO}_2^\bullet -$, radical anion of CO_2 ; $-\text{HCO}^*$, surface-bound formyl; $-\text{COH}^*$, surface-bound formyl; $-\text{CH}_2^*$, surface-bound methylene; $-\text{CH}_2\text{O}^*$, surface-bound methoxide; -F, formate and -C, carboxyl intermediate pathways;

Therefore formation and stabilization of key intermediates are shown to be more favourable on particles with rough surfaces having defects⁵¹ and/or step sites⁵². Particularly defect sites such as grain boundaries are invoked as catalytic sites that can stabilize CO₂RR intermediates^{46e}.

Gas diffusion electrodes

The products and rates of CO₂RR are influenced also by the electrode formation^{39b, 43a, 53} (catalyst loading, its conductive additives and electrode support). The conventional practice is to form a catalyst ink to deposit onto a conductive substrate. The vacuum deposition methods can also be used to grow metallic films i.e. sputtering, evaporation, and physical or chemical vapour deposition. On the other hand, electrodeposition could be a good alternative providing simpler operational conditions.⁵⁴ This is due to the fact that porous electrodes are preferred rather than flat electrodes in catalysis reactions which can provide larger amount of active sites, e.g. fuel cells⁵⁵, supercapacitors⁵⁶, redox flow batteries⁵⁷ and electrocatalysis³⁶⁻³⁷.

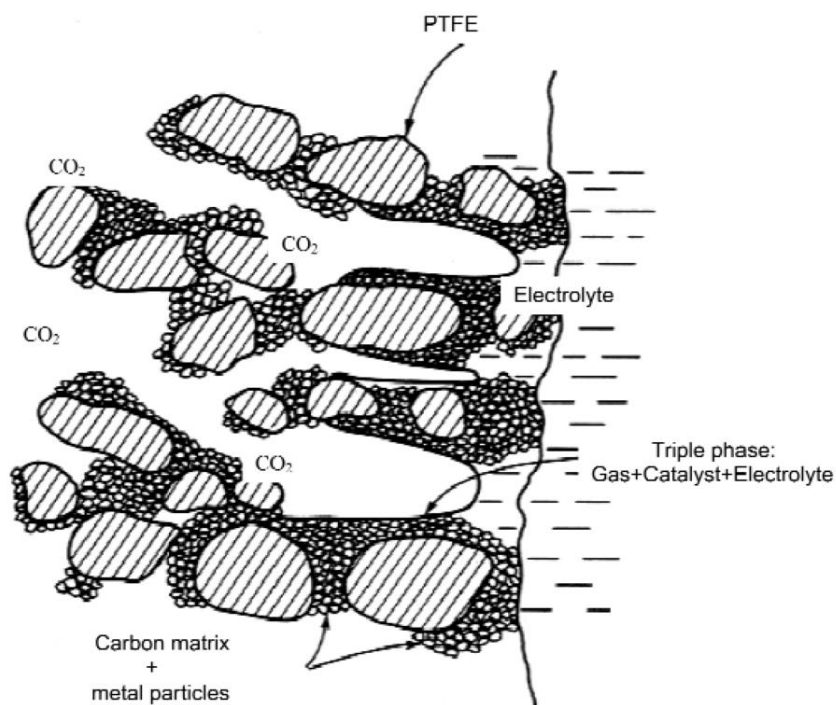


Figure 1-11. Schematic diagram of a gas-diffusion electrode active layer adapted from Ref[36] Copyright 2001, International Union of Pure and Applied Chemistry.

The motive of using gas diffusion electrodes (porosity > 75 %) are more significant due to sluggish kinetics of CO₂RR vs. HER. In CO₂RR, the aqueous electrolyte salts are generally used as a proton source, and for the motivation of overall process feasibility i.e. electrolysis at ambient conditions, non-flammable and abundant^{7c, 34b, 34d, 48}. Therefore it is essential to promote CO₂RR over competing HER in aqueous electrolytes. In this context, low CO₂ solubility (0.034 M) is the limiting factor which requires a gas diffusion electrode (GDE) with disperse catalyst immobilized at its backbone. Such approach would minimize the mass transport limitation and improve the availability of the three phase interfaces (TPI) which would be the meeting point of CO₂ gas – liquid electrolyte – electrode for CO₂RR to take place as illustrated in Figure 1-11. By this way, high density of active sites would be available in a three-dimensional net of conductive supporting material allowing simultaneously; diffusion CO₂ gas and transfer of the electrical charge. Recent efforts and approaches^{39b, 39c, 39h, 43a, 44-45, 58} have been paid on the implementation of GDE for CO₂RR. The obtained results of faradaic efficiency for C1-carbons are ranging between 65 to 73 % using inks prepared with Sn–Nafion and/or carbon additive mixed with binders and deposited on gas diffusion layers^{39b, 43-45}. Likewise, more recently, catalyst layer consisted of commercial Sn or SnO₂ powder⁵⁹ mixed with additives (such as Nafion solution and powder of either carbon black⁶⁰ or carbon nanotubes⁶¹ or graphene⁶²) sprayed on a gas diffusion layers enhanced faradaic efficiency due to the use of nano-sized electrocatalyst/additives although overall energy consumption and stability remains to be solved. Consequently, an important effort is still needed for simultaneously improve endurance against degradation, maintain high faradaic efficiencies and final concentration. In parallel the overall energy of spent should be closer to theoretical values to reduce energy consumption. All these conditions must be fulfilled to satisfy the minimum requirements for its industrial applicability foresight^{39c, 63} considering the final concentration of the liquid end-products in the electrolyte.

Anode Reaction: O₂ evolution reaction

The electrocatalytic oxidation of H₂O could be performed in acid or basic solutions. It is a 4e⁻ reaction to form one O₂ molecule and it is an inherently sluggish process.



The acidic electrolytes ($1 < \text{pH} < 7$) are advantageous for proton exchange membrane electrolyzers that works above room temperature ($\sim 90^\circ\text{C}$)⁶⁴ thanks to high electrolyte conductivity and superior kinetics of HER at the counter side. However the challenge is to find an anodic OER catalyst with fast kinetics and good stability in low pH values.⁶⁵ On the other hand, the use of basic electrolytes for electrocatalytic oxidation of H_2O (or OH^- oxidation for $7 < \text{pH} < 14$) is kinetically easier owing to dissociated form of water into hydroxide ion according to Pourbaix diagram⁶⁶. Besides a large variety of metals could be used due to their high corrosion stability at this pH. Over the years, extensive investigations have been performed to find an active, non-toxic and earth-abundant catalyst for O_2 evolution reaction (OER) that could work efficiently in aqueous electrolytes⁶⁷. Bifunctional property^{iv} is essential in rechargeable metal-air batteries and regenerative low temperature fuel cells, but specific activity towards OER is critical for electrolysis cells dedicated to produce solar fuels, i.e. water splitting to produce O_2 at the anode.

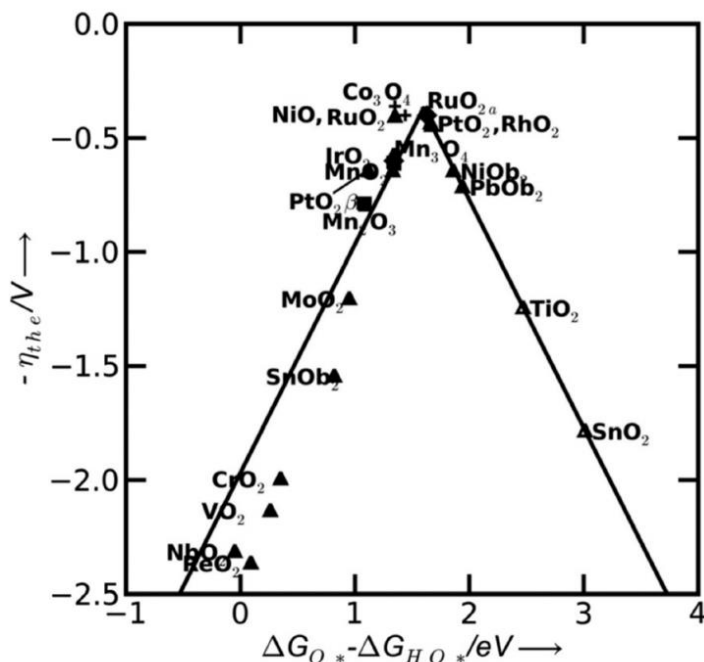


Figure 1-12. Volcano plot; Theoretical overpotential for OER vs. the difference between the standard free energy of two subsequent intermediates ($\Delta G_{\text{O}^*} - \Delta G_{\text{HO}^*}$) in electron volts for various binary oxides adapted from Ref^[68] Copyright 2014, Royal Society of Chemistry.

^{iv} O_2 evolution and reduction reactions; OER and ORR

Several predictions on the intrinsic OER activity have been proposed to understand its slow reaction kinetics and reactions mechanism^{28b, 69 70}. The generally accepted theory is the Sabatier principle⁷¹ that the interaction energy between the metal and surface bond oxide should be neither too weak nor too strong. According to DFT calculations by Man and coworkers⁷², in the case of surfaces that bind oxygen too weakly, intermediates cannot easily react and the potential is limited by the oxidation ($-HO = e^- + -HO^*$). In the opposite case of strong oxygen bonding, the intermediate states and the adsorbed products are quite stable and the potential is limited by the formation of HOO^* species ($-O^* + -HO = e^- + -HOO^*$). The optimum case is therefore a mean bonding strength concluded by Man, Jaramillo, Norskov and Rossmeisl et. al.⁷³ with Figure 1-12. Here, we would highlight the most promising catalysts for basic electrolytes in terms of their performance and abundancy for a sustainable energy conversion and storage system. These can be group by the type of metal/metal oxide:

- (i) Rare-earth metals/metal oxides
 - a. IrO_x or RuO_x based catalyst
 - b. Perovskite (mixed oxide) based catalyst
- (ii) Earth-abundant metals
 - a. Co-based catalyst
 - b. Ni-based catalyst
 - c. Mn-based catalyst
 - d. Fe-based catalyst

Rare-earth metals for water oxidation reaction

The best materials known so far to offer a stable catalytic activity at a low overvoltage respect to Eq. (1.20) are based on a mixture of Ir-, Ru- and Ta-oxides coated on titanium or nickel/stainless steel mesh electrodes for OER⁷⁰. These precious transition metal oxides are able to oxidize H_2O with onset potentials as low as of 1.44 V and 1.34 V, respectively, and Tafel slopes of $40 \text{ mV} \cdot \text{dec}^{-1}$ ⁷⁴. The use of scarce and pricy rare-earth metal catalyst represents a severe cost constraint that strongly limits the large-scale deployment of water splitting electrolyzers.

The perovskites are ABO_3 structures where A is the larger cation such as lanthanide or strontium (or an alkali metal dopant such as sodium or calcium) and B is the

smaller cation usually a transition metal such as nickel, iron or cobalt surrounded by six oxygen atoms forming an octahedral, BO_6 . There are many discrepancies between the studies about the role of perovskite in OER which generally suggest the essential role of oxygen vacancy in BO_6 octahedral contributing to B-OH bond strength⁶⁵ and higher number of d-electrons at the B metal improving the charge transfer.^{67f}

Earth-abundant metals for water oxidation reaction

Earth-abundant metals have been shown¹⁻⁹ as promising candidates for both ORR/OER in alkaline media associated with their multiple possible oxidation states, off-stoichiometric compositions, defects and vacancies. The most promising transition metals can be found in the 4th row of the periodic table (the so-called 3d elements) especially Mn, Fe, Co and Ni. Among them, the most accepted catalytic activity trend is reported as $\text{Ni} > \text{Co} > \text{Fe} > \text{Mn}$.⁶⁵ Most of those metals form an oxide-oxyhydroxide layer in alkaline media. Upon cycling they form a layer of $\text{M}(\text{OH})_2$ with several phases (e.g. α -, β - and γ -) on top of MO layer and increase in thickness by time. A huge spectrum of Tafel slope values have been reported from about 40 to 130 $\text{mV}\cdot\text{dec}^{-1}$ with overpotentials higher than 0.3 V.⁶⁵ The thickness of the hydroxide layer is time-dependent and its type is strongly linked to the material processing (synthesis, post-treatment and cycling potential). For nickel, β -NiOOH reported to be the optimal phase for OER which is formed by the oxidation of β -Ni(OH)₂.^{75 76 77} The alloying of Ni with Fe showed increased OER activity and Tafel slopes lower than 60 $\text{mV}\cdot\text{dec}^{-1}$ have been reported for Fe content varying from 5 to 40 mole %.⁶⁵ The cobalt based catalysts undergoes several oxidation steps; Co^{+2} , Co^{+3} and even mixed state $\text{Co}^{+3/+4}$ before OER. The most reported Tafel slope at low overpotentials is around 42 $\text{mV}\cdot\text{dec}^{-1}$.⁶⁵ For Fe-catalyst, Joiret et. al.⁷⁸ showed Fe_3O_4 phased at the surface which γ -FeOOH and γ - Fe_2O_3 grows onto at higher OER potentials. Another study showed that⁷⁹ alloying with Co- and Cr- enhances Tafel slope values as low as 40 $\text{mV}\cdot\text{dec}^{-1}$. Manganese based catalyst performances towards OER vary depending on the synthesis methods as well. Dau et.al.⁸⁰ and Jaramillo et. al.⁸¹ reported MnO_x deposition by cyclic voltammetry being more stable versus constant potential deposition (MnO_2 ; Mn^{+4}) and they linked Mn^{+3} valence for improved OER activity. Chemically prepared Mn-phases by Dismukes et. al.⁸² and electrochemically deposited Mn-oxides by Nocera et. al.⁸³ supported this

perspective that oxides contain Mn^{+3} and Mn^{+2} mixed states showing the highest OER performance. The reported values for Mn-oxides vary from 77.5 to 160 $mV \cdot dec^{-1}$ depending on the substrate, preparation method, type of the electrolyte salt and operating potentials.^{67d, 67h, 84} The recent studies showed that spinel structures formed by Co addition to Mn ($Mn_{3-x}Co_xO_4$; $0 < x < 2$) greatly improve the reaction kinetics and stability in alkaline media that can improve Tafel slope values 55^{67b} 67^{67g}, 81⁸⁵ and 85^{67e} $mV \cdot dec^{-1}$ with overpotentials between 0.3 and 0.55 V vs. standard potential of OER.

1.3.2 Fundamentals of photoelectrochemistry

Photoelectrocatalysis follows similar principles as electrocatalysis with the aim of supplying the required energy directly from sunlight. For this physical phenomenon, a material that can respond to an external excitation e.g. photons from sun irradiation must be used, such as semiconductors. In general, the electrons are restricted by atomic forces to just a few bands of energy. The alignment of those bands and their electron occupancy levels give rise to three class of materials; metals, semiconductors, and insulators shown in Figure 1-13.

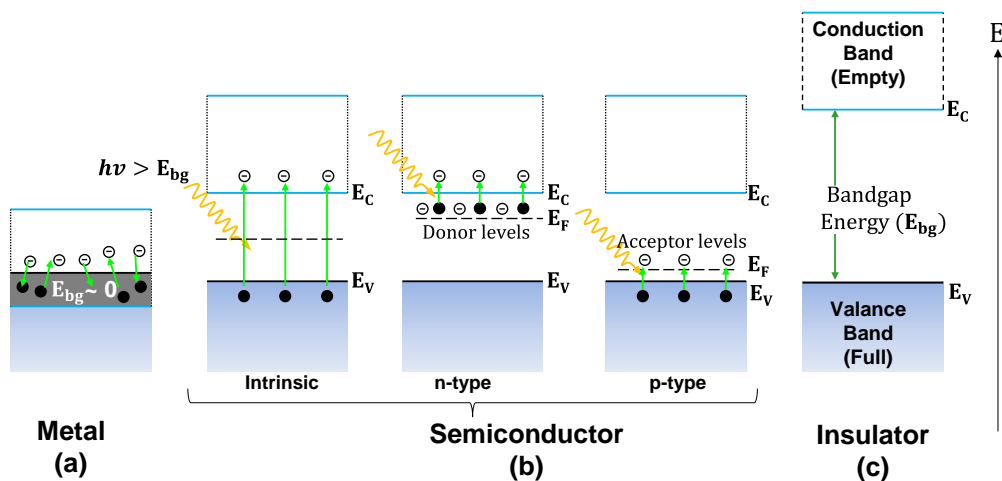


Figure 1-13. The schematic electron occupancy of allowed energy bands for a conductor, semiconductor and insulator. The shaded areas indicate the regions filled with electrons. The upper edge of the valence band is marked by E_V and lower edge of the conduction band by E_C . E_{bg} , is the bandgap energy expressed in electron volts (eV).

In metals, the valence and conduction bands overlap each other so electrons can move freely in the lattice. In semiconductors and insulators an energy gap called “band gap” exists between the lowest point of the conduction band and the highest

point of the valence band. If the bandgap energy is small enough (≤ 3.0 electron-volts, eV), the energy of the incoming photon from solar irradiance can bridge the gap for a small fraction of charge carriers i.e. electrons or holes. This behaviour of semiconductors relies on the photoelectric effect^v that an excited electron (from the valence band) can be transferred into a higher energy state (to the conduction band) by absorbing a "photon" (by solar light) within at least the band gap energy.⁸⁶ The excitation of the electrons into the conduction band is balanced with the equal number of holes generation at the valence band. The Fermi level position is related to the concentration of the generated electrons and holes, $c_{h^+} = c_{e^-}$, so the Fermi level^{vi} of an intrinsic semiconductor is located approximately in the middle of the energy gap illustrated in Figure 1-13.⁸⁶ Intrinsic semiconductors (such as Si) can be doped with a different element having more or fewer valence electrons (such as phosphorus or boron, respectively) than the atoms they replace in the intrinsic semiconductor. The donor or acceptor doped semiconductors are called extrinsic semiconductors respectively and given in Table 1.5.

Table 1.5. Charge carriers in intrinsic and extrinsic semiconductors

	intrinsic	n-type	p-type
Doped with	-	Donor impurity	Acceptor impurity
Majority carriers	-	e^-	h^+
Minority carriers	-	h^+	e^-
Example	Si, Ge GaAs, GaN	P (group V) Se, Te	B, As (group III) Be, Zn, Cd

The effect of n and p doping is to change the concentration of the charge carriers so the Fermi level would shift toward the conduction or valence band edges, respectively. The dominant charge carriers for n-type semiconductors are the electrons (donor doped), alternatively those where the holes make the majority are

^v The main distinction is that the term photoelectric effect is now usually used when the electron is ejected out of the material (usually into a vacuum) and photovoltaic/photoelectrochemical effect used when the excited charge carrier is still contained within the material. ⁸⁶Kittel, C., *Introduction to solid state*. John Wiley & Sons: 1966.

^{vi} The electrochemical potential of the electrons from the energy of the top most filled level at absolute zero. ⁸⁶ *Ibid.*

referred to as p-type semiconductors (acceptor doped). In Figure 1-14(a), the oxidation states of a redox couple in solution are schematically represented as strongly fluctuating energy levels. The levels reflect either the tendency of that specie to release electrons (from occupied level) or to accept electrons (to unoccupied level) when it gets in contact with the electrode. The species which prefer to donate an electron are called reducing species (E_{red}), those which prefer to accept an electron are called oxidizing species (E_{ox}). E_{ox} and E_{red} are the ionic energy levels for the ideal case of a non-oscillating solvent. For a single redox system with equal concentrations of oxidizing and reducing species, the redox energy level (E°_{redox}) in solution is at half-way between the energy level of the oxidizing and reducing agent.

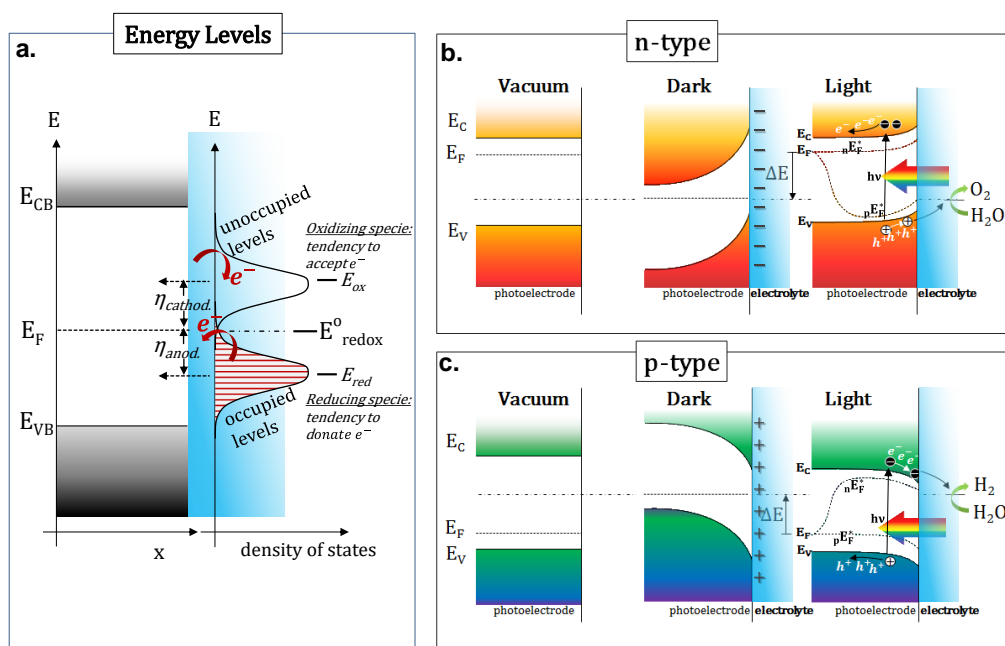


Figure 1-14. Schematic illustration of (a) energy levels in an intrinsic semiconductor and an electrolyte containing a redox couple shown on a vacuum reference scale. (b) The position of band levels for an n-type semiconductor before contacting an electrolyte, in contact at equilibrium under dark and light conditions (c) same as in (b) but for a p-type semiconductor

Figure 1-14(b-c) illustrates a schematic of the electronic energy levels at the interface of n and p type photoelectrode in vacuum and after inside an electrolyte containing a redox couple under dark and light condition. When the photoelectrode is brought in contact with redox electrolyte, the charge transfer takes place directly across the interface. E_{redox} is below E_F of the photoelectrode so the electrons will be

transferred to the oxidized species in solution. The band bending occurs until the equilibrium is reached and Fermi energy of the electrons in the solid (E_F) is equal to the redox potential of the electrolyte (E_{redox}). This region where the charge distribution differs from the bulk is called space-charge layer or depletion layer. Under illumination, the system departs from equilibrium due to the change of the concentration of the electrons and holes at the surface and their chemical potentials become different from each other if the energy of the photons are sufficient. Photons with energy less than E_{bg} , will not separate electron-hole pairs and simply pass through the photoelectrode. Photons with higher energy than E_{bg} generates an electron-hole pair. For n-type materials, holes migrate to the surface where they oxidize H_2O to O_2 . The electrons drift through the bulk to the back contact where they would travel to counter electrode by the external circuit. A similar condition may apply for p-type materials where electrons migrate to the surface reducing H_2O to H_2 , and holes drift to the back contact. The use of either n or p-type electrodes in an aqueous electrolyte could mimic photosynthesis if specific conditions are met which are explained from now on.

The foremost example of a light driven catalysis is the photosynthesis performed by plants, fungi, algae etc. One approach to mimic plant photosynthesis is called “photocatalysis” and has been proven with the use of colloidal semiconductor particles⁸⁷. This simplifies the overall set-up since OER and HER occur at the surface of same photocatalyst material which is dispersed in water. However, an electron or a hole scavenger is often required for a better charge separation and to avoid reverse reactions. On the other hand, the separation of evolved H_2 and O_2 in the same container is problematic. A second approach is called “photoelectrochemical catalysis” where the anode or cathode (explained in electrocatalysis part previously) would be instead made of a semiconductor material for light induced oxidation or reduction (and rephrased as photoanode or photocathode respectively).

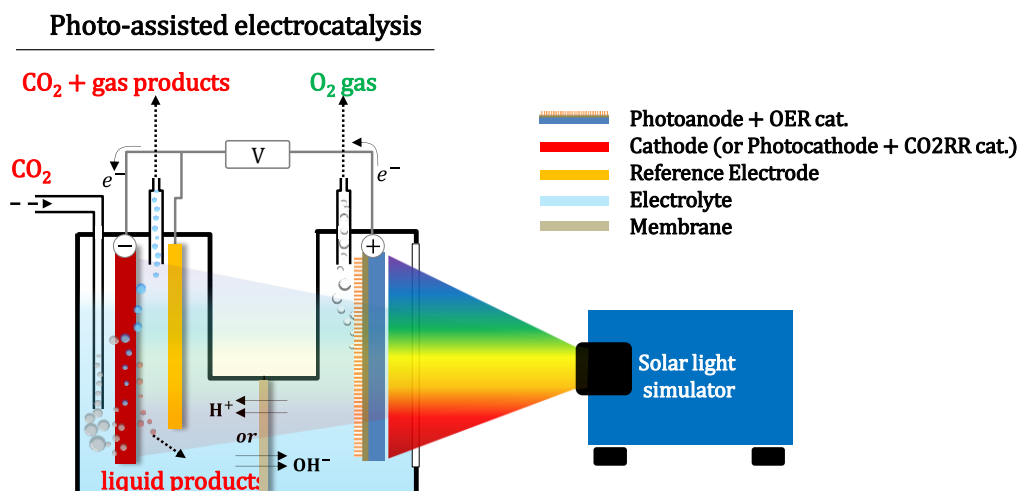


Figure 1-15. Schematic illustration of photoelectrochemical cell with a photoanode for OER against a metal cathode used for CO₂RR. The reference electrode is placed near metal cathode and CO₂ was bubbled through the solution during the tests.

Many distinct tandem cell configurations for water splitting and artificial photosynthesis are possible and have been discussed recently⁸⁷. The schematic given in Figure 1-15(a) is an example of an n-type photoelectrode used as photoanode for OER versus a metal cathode used for CO₂RR. Likewise, metal cathode could be replaced with a p-type electrode decorated with a catalyst active for CO₂RR to construct a photocathode. There are many successful designs with the implementation of both semiconductor types for water splitting reaction^{20c} [OER + HER] whereas real artificial photosynthesis [OER + CO₂RR] is challenging because a stable photocathode providing low on-set potential and high photocurrent density for CO₂RR has not been revealed yet. Figure 1-16(a) shows the theoretical on-set potentials for OER (1.23 V_{RHE}) and CO₂ reduction to HCOOH (−0.225 V_{RHE}) for pH~0. The broken lines represent the catalysis in dark conditions with a catalyst on the electrodes. The full lines show the shift of the on-set potentials for photoelectrodes under solar light illumination. The point where the two photoelectrodes cross each other is called “zero-bias” where the full cell can provide a current density without an external voltage.

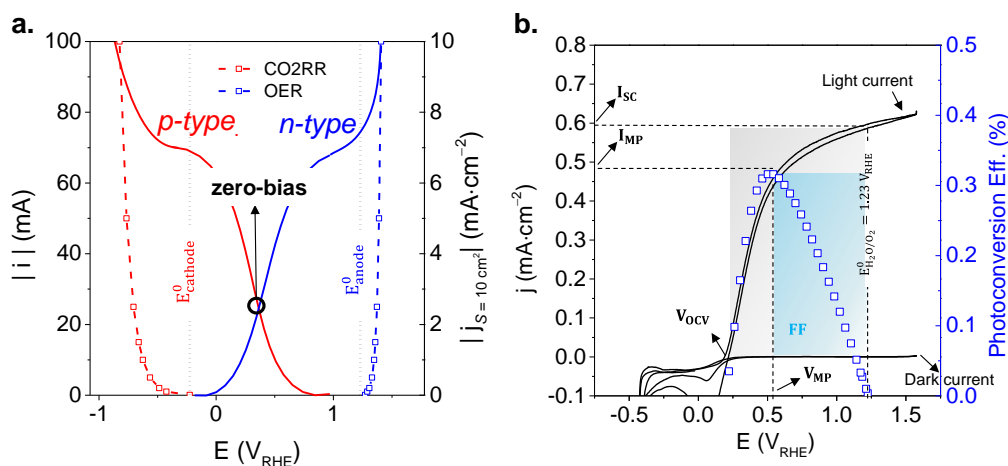


Figure 1-16. (a) j - E plot of a hypothetical n - and p -type semiconductor under AM 1.5G solar light illumination in an aqueous electrolyte to catalyse OER and CO_2RR . Rest of the curves are plotted with the parameters of Figure 1-8. (b) j - E plot and photoconversion efficiency of n -type semiconductor (TiO_2 nanorods in 0.1 M KOH) under AM 1.5G solar light illumination employed for OER.

The semiconductors with the right set of properties, i.e. bandgap, catalytic activity, stability and etc., can be employed as photoelectrodes (as cathode or anode or both) in an aqueous electrolyte under sunlight irradiation⁸⁸, as shown in Figure 1-16(a). In this line, the photon energy can be converted to chemical energy, and the solar energy would be stored in chemical bonds as a more stable reserve, for example the reduction of CO_2 into hydrocarbons. This is a very sustainable form of energy storage and conversion like plant photosynthesis, but careful calculations are necessary due to its complexity.

During the study of half-cell reactions (photocathode or photoanode studies), the first important parameter representing the quality of photoexcitation is the “fill factor” or FF. The FF determines the maximum power of the semiconductor (Figure 1-16(b)), indicating how severely voltage will change beyond the maximum usable potential under current loading given by,

$$\text{FF \%} = \frac{I_{\text{MP}} \cdot V_{\text{MP}}}{I_{\text{SC}} \cdot V_{\text{OCV}}} \cdot 100 \quad (1.21)$$

where I_{MP} and V_{MP} are the maximum point for current and voltage, V_{OCV} and I_{SC} are the short circuit current and open circuit voltage. The second parameter that needs

to be calculated in half-cell reactions is the photoconversion efficiency (η %) of the photoelectrode given by,

$$\eta \% = j_p \frac{E_{\text{rev}}^0 - |E_{\text{app}}|}{I_0} \cdot 100 \quad (1.22)$$

and,

$$E_{\text{app}} = E_{\text{meas}} - E_{\text{OCV}} \quad (1.23)$$

where j_p is the photocurrent density ($\text{mA}\cdot\text{cm}^{-2}$), E_{rev}^0 is the standard reversible potential ($E_{\text{rev}}^0 = 1.23 \text{ V}$ for Eq.(1.5)) and E_{app} is the applied potential. E_{meas} is the working electrode potential vs. reference electrode measured under illumination (I_0 in $\text{mW}\cdot\text{cm}^{-2}$) and E_{OCV} is the electrode potential vs. reference electrode under open circuit conditions, under the same illumination and in the same electrolyte.

In full cell reactions, the main figure-of-merit to consider is the solar to fuel efficiency (STF). This would be referred as solar to hydrogen efficiency (STH), if water splitting reaction is under study and H_2 is the main target for sustainable fuel production. STF efficiency describes the overall efficiency of a photoelectrochemical cell exposed to solar light (Air Mass 1.5 Global illumination, abbreviated as AM 1.5G) under zero-bias condition. Zero-bias means that there is no applied voltage between the working electrode (WE) and counter electrode (CE), and all of the energy in process is being supplied by sunlight⁸⁸. Eventually STF efficiency is the ratio of chemical energy of the produced fuel divided by the solar energy input from AM 1.5G solar light given by,

$$\text{STF} (\%) = \left[\frac{\dot{r}_{\text{FUEL}} (\text{mmol} \cdot \text{s}^{-1}) \cdot \Delta H_{\text{Fuel}}^0 (\text{J} \cdot \text{mol}^{-1})}{[P_{\text{solar flux}} (\text{mW} \cdot \text{cm}^{-2})] \cdot \text{Area} (\text{cm}^2)} \right]_{\text{AM 1.5G}} \quad (1.24)$$

where ΔH_{Fuel}^0 is the free energy of enthalpy per mol of the produced fuel (e.g. H_2 , HCOOH , CO or CH_3OH), $P_{\text{solar flux}}$ is the power generated by the solar light simulator, e.g. $100 \text{ mW}\cdot\text{cm}^{-2}$. Eq.(1.24) calculates the power output (at the numerator) based on the direct measurement of the true fuel production measured by a gas or liquid chromatography method.

On occasions that the photovoltage provided by the semiconductor is not enough to drive the electrochemical reaction so an extra bias should be applied. The

application of a bias generally increases the current drawn from the device providing insight into the functionality and limitations of a material/device. This term is called Applied Bias Photon-to-Current Efficiency (ABPE) and its equation is given by,

$$\text{ABPE (\%)} = \frac{|j \text{ (mA} \cdot \text{cm}^{-2})| \times [E^0 - |E_{\text{bias}}| \text{ (V)}]}{[P_{\text{solar flux}} \text{ (mW} \cdot \text{cm}^{-2})]} \times \eta_{\text{HCOO}^-} \text{ (\%)} \quad (1.25)$$

where j is the photocurrent density obtained under applied bias, E_{bias} . E^0 would be overall cell voltage.

To underline, the lack of proper photocathodes for CO_2RR obliges us to use metal electrodes and in that condition, the full cell system requires an external voltage called as “bias voltage” – that is around 1 V in this theoretical example. Under operation of such system (photoanode vs. metal cathode), the photogenerated electrons diffuse to the back contact and travel to the metal cathode for CO_2RR while the remainder charge carriers, holes, would flow to the surface for OER. One other possibility could be to utilize a photoanode providing a very large on-set voltage (>2 V) so that current-voltage curve (blue full line) of the photoanode could cross the metal electrode current-voltage curve (red dashed line) in Figure 1-15(b). Overall single junction photoelectrodes are not able to generate such photovoltage and harvest the full solar spectrum at the same time. Therefore, using a single semiconductor wired to a metallic cathode would require an external bias (V_{bias}) for solar fuel production. The photovoltage required for a cell generating simultaneously CO_2RR and OER, a theoretical minimum is around 1.5 V (1.23 V - -0.225 V) but due to the sluggish kinetic reactions larger than 2.0 V is needed, practically.⁸⁹ A list of semiconductors are shown in Figure 1-17 according to their band positions. The colour codes present the downsides when they are used in aqueous solutions. In theory, n- and p-type photoelectrodes could be wired to convert solar energy into fuels i.e. H_2 or $\text{C}_x\text{H}_y\text{O}_z$ if they can sustain some specific set of properties. Those are firstly, an electronic band gap that will be narrow enough for an efficient photon collection from the solar spectrum ($<2.2\text{eV}$) with correct position of the valence and conduction bands to oxidize H_2O and reduce CO_2 .

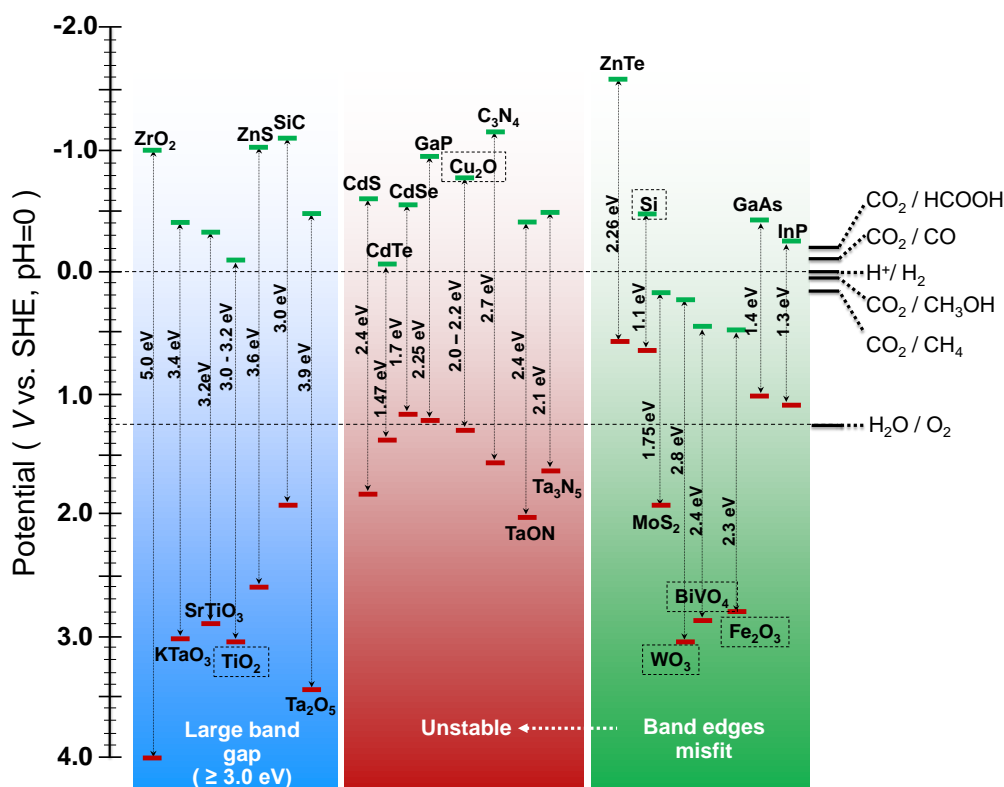


Figure 1-17. The band positions of several semiconductor materials in contact with aqueous electrolyte respect to pH ~0. The red and green lines represent the upper edge of the valence band and lower edge of the conduction band, respectively. The standard potentials of CO₂RR, HER and OER are adjusted to RHE scale.

Meanwhile, the materials must be stable and resistant to photocorrosion. Such requirements restrict the list of available semiconductor materials to a few – Si, Fe₂O₃, WO₃, BiVO₄, Cu₂O etc. Amongst them, titanium dioxide (TiO₂) is one of the most extensively investigated for photovoltaic cells for solar electricity generation^{vii} and photoelectrochemical cells for sunlight driven water splitting reaction. The first report dates to 1968 by Boddy et. al.⁹⁰ with rutile-TiO₂ but most of the work today would be related to the discovery of Fujishima and Honda⁹¹ in 1972 revealing TiO₂ as a stable semiconductor demonstrating water splitting with solar light. Its stability has been one of the strongest points however its large bandgap and activity to only UV-part of the solar spectra limits its applicability. A huge effort was devoted to increase its solar to electricity/fuel conversion efficiency by introducing dopants

^{vii} Such as dye sensitized solar cells, DSSC.

in the form of metals during synthesis⁹² or in the form of gas during post-treatment/calcination⁹³.

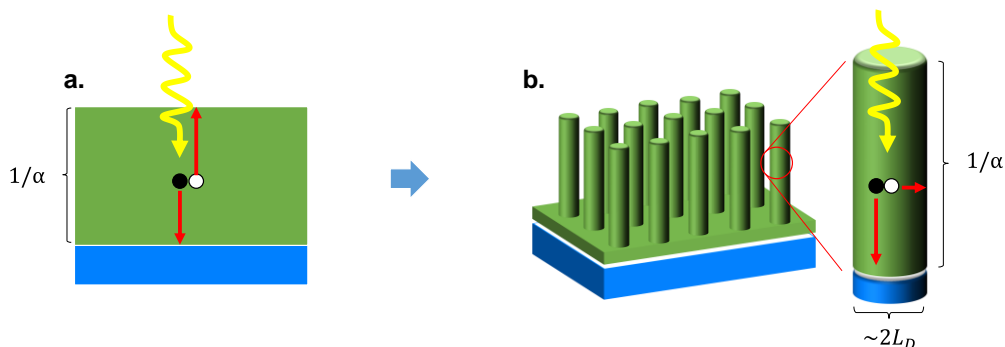


Figure 1-18. (a) In a planar device, photogenerated carriers must traverse the entire thickness of the cell $\sim 1/\alpha$ (where α is the absorption coefficient), before collection. (b) In a 2D-array structure, carriers must only reach the rod surface before recombination. L_D is the diffusion length of the photogenerated minority carrier (open circle).

Additionally, the most appealing strategy would be the use of nano-structuring to improve charge separation and to avoid recombination during charge transfer, as illustrated in Figure 1-18 – a planar and two-dimensional array structure. Two dimensional structuring (2-D) could be obtained by different methods such as sol-gel and vacuum deposition methods⁹² but a good control and aspect ratio were reported by many groups⁹⁴ using hydrothermal synthesis. The results showed that⁹⁵ photo-induced charge separation occurs on a length scale of a few nanometres, so higher levels of defects and impurities can be tolerated for 2-D structures than in planar devices, where the minority carriers are required to diffuse several microns.^{viii}

1.4 Scope of this research

The scope of this dissertation is the optimization of both components of the photoelectrochemical (PEC) cells; CO_2 reduction and H_2O oxidation reactions as well as on the optimization of the whole device.

From a **research** point of view for catalysis: In one hand, the optimisation of the electrocatalytic carbon dioxide reduction process (CO_2RR) focusing on the reduction of the overpotential is needed at a faradaic efficiency near unity. On the

^{viii} See Chapter 6 for further details.

other hand, the optimisation of the photoanode (and anode) towards oxygen evolution reaction (OER), is required in the same manner since this complementary reaction is the sink of electrons to the cathode to carry out the electroreduction. After developing a know-how for both reactions, the focus is to design catalysts in a cost-effective manner which can be up-scalable and applicable to different substrates, e.g. by electrodeposition. The optimized catalyst with such method must be selective and stable during CO₂RR.

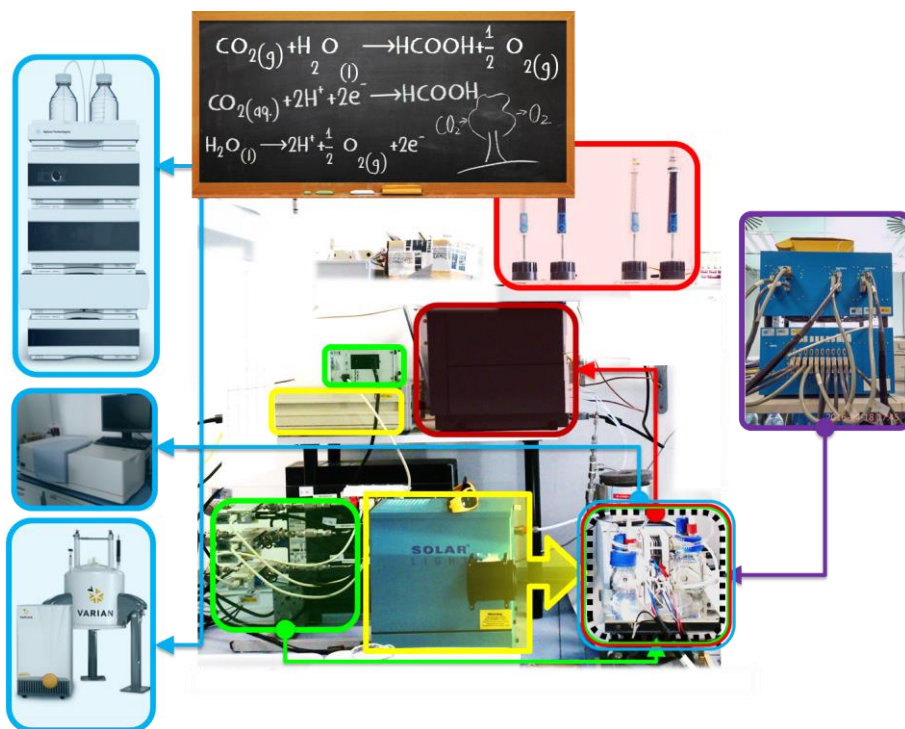
From a **development** point of view for electrolyser: In plant's photosynthesis, both reactions occur at different sites simultaneously, i.e. Photosystem I-II in light reactions for OER and Calvin cycle to convert CO₂ into sucrose and starch. Therefore, the steps need to be achieved are:

1. the physical separation of the water photo-dissociation from CO₂ reduction stages via photoelectrochemical (PEC) approach,
2. integration of gas and liquid flow to overcome mass transport limitation caused by low CO₂ solubility in aqueous solutions (0.033 mol·L⁻¹) and to minimize pH gradient at the vicinity of the electrodes
3. employment of a filter press stack cell design having a large photoelectrode incorporation (~10 cm²) to establish a greater electrode/electrolyte area to decrease ohmic losses and boost the overall energy efficiency

Finally, the techno-economic analysis of the whole process and evaluation of the benefits for using PEC flow cell is looked-for.

CHAPTER 2

Experimental Methods



This chapter can be divided into three parts which provides a general explanation for (i) electrode preparation techniques, (ii) electrochemical methods used and (iii) gas and liquid product characterisation for CO₂ reduction. The first part describes the methods to produce electrodes active for CO₂ reduction and H₂O oxidation reactions. The second part provides the electrochemical methodology and basic principles of electrochemistry including formulas, calculations and methods used in this work. Besides, details on the assembly of the filter-press flow cell for dark and light-assisted conditions were given in this part. The third part of this chapter outlines details about the detection and quantification of products from CO₂ reduction reaction to determine the faradaic efficiency of the process.

2.1 Electrode Preparation

In first section, electrodes realized for carbon dioxide reduction reaction (CO₂RR) are described. The electrodeposition of Sn and Cu metal on gas diffusion electrode are explained to give insights on the “cathodes”, used in Chapter 3, 4 and 6.

The second section, metal oxides for either anodes or photoanodes for water oxidation reaction to evolve O₂ gas (OER) are described. Mn-Co oxide nanoparticle synthesis and ink preparation are expanded to be tested on “glassy carbon disk” for RDE tests and as “anodes” for ECf-cell experiments in Chapter 5. Next, the hydrothermal synthesis of TiO₂ nanorods on a conductive glass substrate is explained which termed as “photoanode” (Chapter 6).

2.1.1 Electrodes for CO₂ reduction

Cathode: Sn on gas diffusion electrode

Set-up. Tin gas diffusion electrodes (Sn-GDE) were obtained by direct current electrodeposition using conventional three electrode cell configurations, Figure 2-1(a). A sheet of carbon paper (Toray® carbon paper, TGP-H-60) with a size of 30 x 34 mm was used as catalyst support (working electrode), the counter electrode was 40 x 40 mm graphite foil (0.5mm thick, 99.8%, Alfa Aesar) and Ag/AgCl/KCl (3M) ($E^\circ = 0.205 V_{SHE}$) was used as a reference electrode. The electrodeposition was carried out using a Biologic SP-150 potentiostat working under galvanostatic mode, applying a current density of 15 mA·cm⁻² during 5 minutes at room temperature. After electrodeposition, each electrode was thoroughly rinsed with deionized water and dried in vacuum oven (25 Torr, Ar atmosphere) at 70°C for 2 h. The digital pictures of GDE with different dimensions (10, 5, 2, and 1 cm²) were cut after electrodeposition shown in Figure 2-1(b).

Electrolyte. A pyrophosphate bath⁹⁶ containing three reactants was used as electrolyte for tin electrodeposition. 0.40 M potassium pyrophosphate (K₄P₂O₇), 0.09 M tin pyrophosphate (Sn₂P₂O₇) and 0.05 M tartaric acid (C₄H₆O₆) were mixed together in a glass beaker with 250 mL Milli-Q deionized water (18.2 MΩ·cm at 25 °C) under vigorous stirring, giving a final pH value about 8.3. To enhance mass transport and prevent side reactions such as oxygen reduction reaction (ORR), Ar gas was continuously bubbled during the plating process.

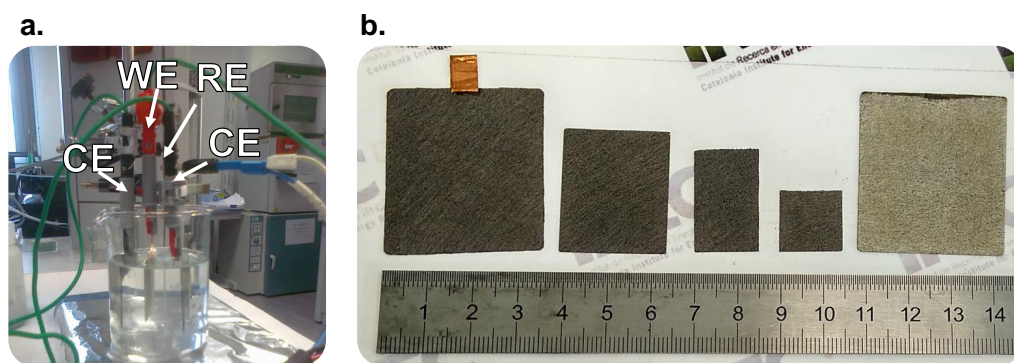


Figure 2-1. (a) 3-electrode set-up of tin pyrophosphate batch, Toray® carbon paper (GDE) is working electrode (WE), two short-circuited pieces of graphite foils are counter electrodes (CE) and Ag/AgCl/KCl(3M) is the reference electrode (RE) (b) Different GDE dimensions (10, 5, 2 and 1 cm²) before and after (10 cm²) electrodeposition of tin catalyst.

Cathode: Cu on gas diffusion electrode

Set-up. Copper deposited gas diffusion electrodes were obtained by means of direct current (Cu-DE) and pulsed current electrodeposition (Cu-PCE) technique from an electrolyte of CuSO₄ using a conventional three electrode cell set-up, similar to Figure 2-1(a). A sheet of carbon paper (Toray® carbon paper, TGP-H-60) was used as catalyst support (working electrode) to form a gas diffusion electrode (GDE). The geometrical dimensions of GDE was 1.5 cm x 2.3 cm, and its area was 6.9 cm² taking into account both sides in contact with the deposition solution. Figure 2-2 shows the digital pictures taken before and after electrodeposition on small and larger GDE supports. The counter electrode was 40 x 30 mm copper foil (0.5 mm thick, 99.9%, Alfa Aesar) to maintain the copper ion concentration inside the bath during electrodeposition. The reference electrode for all the deposition experiments were Ag/AgCl/KCl (3M) ($E^{\circ} = 0.205 V_{SHE}$) and tests performed using a Biologic SP-150 potentiostat.

Electrolyte. Before the preparation of the deposition bath, DI-H₂O was de-aerated with Ar gas for 30 min to remove dissolved O₂. 100 mL electrolyte volume of was prepared by first dissolving 50 g·L⁻¹ of ammonium sulphate ((NH₄)₂.SO₄, Reagent Plus®, ≥99.0% Sigma-Aldrich) in de-aerated DI-H₂O. After vigorous stirring for 5 minutes, 40 g·L⁻¹ of copper (II) sulphate pentahydrate (CuSO₄.5H₂O, 99.995% trace metals basis, Sigma-Aldrich) was added slowly during stirring. Subsequently, 30

$\text{g}\cdot\text{L}^{-1}$ of citric acid (ACS Reagent $\geq 99.5\%$ Sigma-Aldrich) was added gradually also during stirring of the solution, giving a final pH value about 2.17.

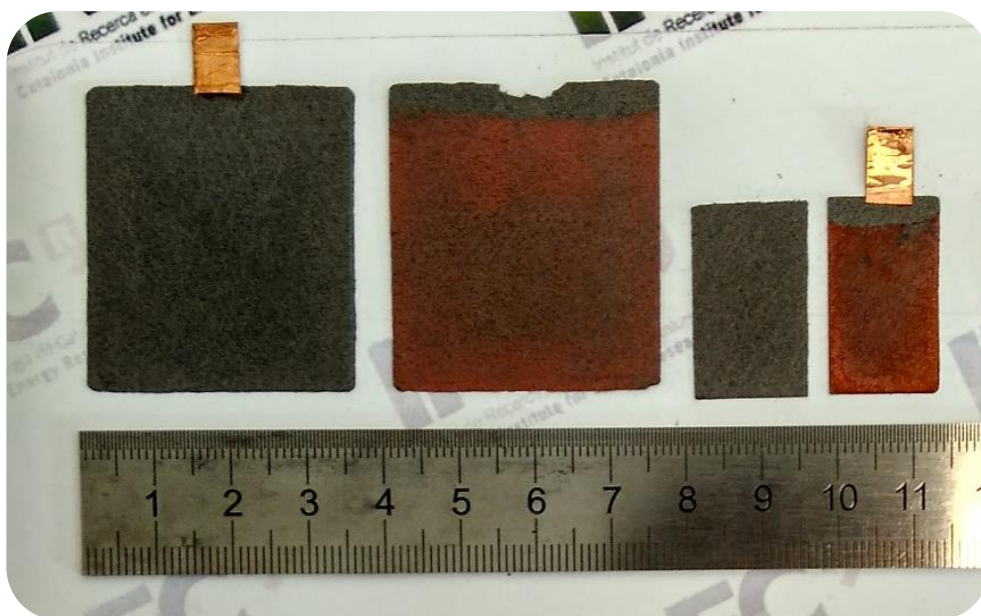


Figure 2-2. Different GDE dimensions (10 and 2 cm^2) before and after electrodeposition of copper catalyst. 3-electrode set-up is similar to **Figure 2-1 (a)** except that counter electrode (CE) was a copper foil.

2.1.2 Electrodes for H_2O oxidation

Anode: Mn-Co oxide nanoparticles

Synthesis. The synthesis scheme was illustrated in Figure 2-3(a). Mn_3O_4 NPs were produced by decomposing 1 mmol manganese (II) acetate ($\text{Mn}(\text{OAc})_2$) in the presence of xylene (15 mL), oleylamine (0.82 mL, OLA) and oleic acid (0.16 mL, OA) in a 50 mL three-neck flask. Under air conditions, this solution was heated to 90 °C with a rate of 5 °C/min, temperature at which deionized water (1 mL) was injected and the reaction mixture was maintained at 90 °C for 100 min to form Mn_3O_4 NPs.

Mn–Co oxide heterostructured (MC) NPs, were formed when 1 ml aqueous solution of $0.5 < x < 2$ M cobalt (II) perchlorate ($\text{Co}(\text{ClO}_4)_2 \cdot 6\text{H}_2\text{O}$) was used as a second-step process. The *core-shell* type NPs (MC-Cl) were formed when 1.0 M of cobalt (II) chloride ($\text{CoCl}_2 \cdot 6\text{H}_2\text{O}$) was used instead of cobalt (II) perchlorate. Both reactions were continued for additional 300 min.

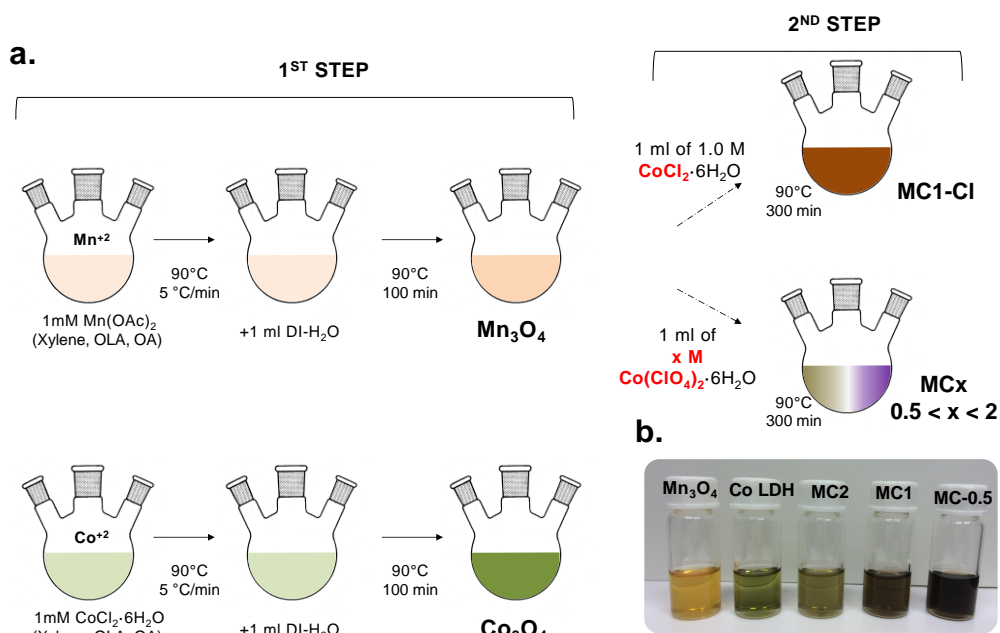


Figure 2-3. (a) Schematic illustration of the controlled synthesis of Mn_3O_4 , and Co_3O_4 in 1st step, MC_x and MC-CI NPs synthesized in the 2nd step (b) Digital pictures of the NPs dissolved in xylene, oleylamine, oleic acid mixture at the end of 300 minutes aging.

The pictures of solutions with dissolved NPs at the end of the aging after 300 minutes are shown in Figure 2-3(b). As an initial observation, it was presumed that the cation exchange between cobalt and manganese was successful owing to their colour change. Finally, the solutions were cooled to room temperature and NPs were purified by multiple precipitation/re-dispersion steps using toluene as solvent and ethanol as the non-solvent.

Ink preparation and nanoparticle immobilization. The as-synthesized nanoparticles were mixed with carbon powder (Vulcan XC-72) with a weight ratio of 30% through sonication of NPs and carbon in chloroform and ethanol mixture (1:1) to form a nanoparticle-carbon composite before the ink preparation. The NP+VC composite was washed several times with chloroform or acetone for later to be treated under air atmosphere at 180 °C for 5 h to remove surface organic ligands.² The catalyst ink for electrochemical measurements was prepared by two steps sonication. First, 5 mg of NP+VC, 0.5 mL of deionized water and 0.5 mL of isopropanol (IPO) were sonicated for 20 minutes. After, 17.5 μL 5 wt. % of Nafion solution were added in the

second step^{ix}. The sonication was continued for 10 minutes more to form the final catalyst ink, Figure 2-4(a). A thin-film was obtained by drop casting a suspension of the electrocatalysts ink onto an inverted glassy carbon disk electrode followed by the rotational drying, Figure 2-4(b). The centrifugal force during rotational drying causes the ink to spread evenly from the centre to edge of the substrate producing a uniform electrocatalyst thin-film free of “coffee rings” which has a great effect on electrochemical performance and reproducibility of RDE measurements.³ Later on, catalyst loaded electrodes were left in Ar flushed low vacuum oven (25 mbar) at 40 °C for 1 hour for complete desorption of surface groups left from the ink, e.g. organic groups from the solvents used. Glassy carbon electrode was introduced to RDE rotator and set at various rates, i.e., 400, 900, 1200, 1600, and 2000 rpm to study ORR activity. The voltage window of the tests was tuned to obtain a well-defined, quasi-steady state mass transport regime at a scan rate of 5 mV·s⁻¹. NPs were investigated in 0.1 M KOH electrolyte pre-saturated with Ar or O₂ at least 30 min before each test (pH = 13.3). OER tests were conducted at a scan rate of 10 mV·s⁻¹ under 1600 rpm rotation speed because it rapidly eliminated O₂ bubbles formed during water oxidation.

Figure 2-4(c) shows the illustration of the protocol for two step spin coating of nanoparticles on a carbon fibre substrate (CFS). 1 mL of the catalyst ink was pipetted on CFS which was fixed with a double-sided tape at the tip of the rotator. The first spin was conducted at 500 rotation per minute (rpm) for 30 seconds and the auto-control program instantly switched to the second spin step which was for 15 seconds at 2000 rpm. Then, the samples were soft-baked at 80°C for 5 minutes on a hot-plate inside the fume hood –ambient conditions. This corresponds to spin coating of nanoparticles for 1 layer. The repetition of this protocol for 2 and 5 times were labelled as 2 and 5 layers, respectively. A darker colour for NPs-CFS (due to the Vulcan carbon additive) was observed with increasing number of layers which is an initial confirmation for the higher amount of particle loading. Next diagram shows the integration of the NPs-CFS, in the ECf cell assembly. A platinumized titanium

^{ix} Two steps sonication was shown to minimize particle agglomeration by trials.

plate (Pt/Ti, DSA/H₂, Electrocell S/A) was used as counter electrode which was for hydrogen evolution reaction, (HER).

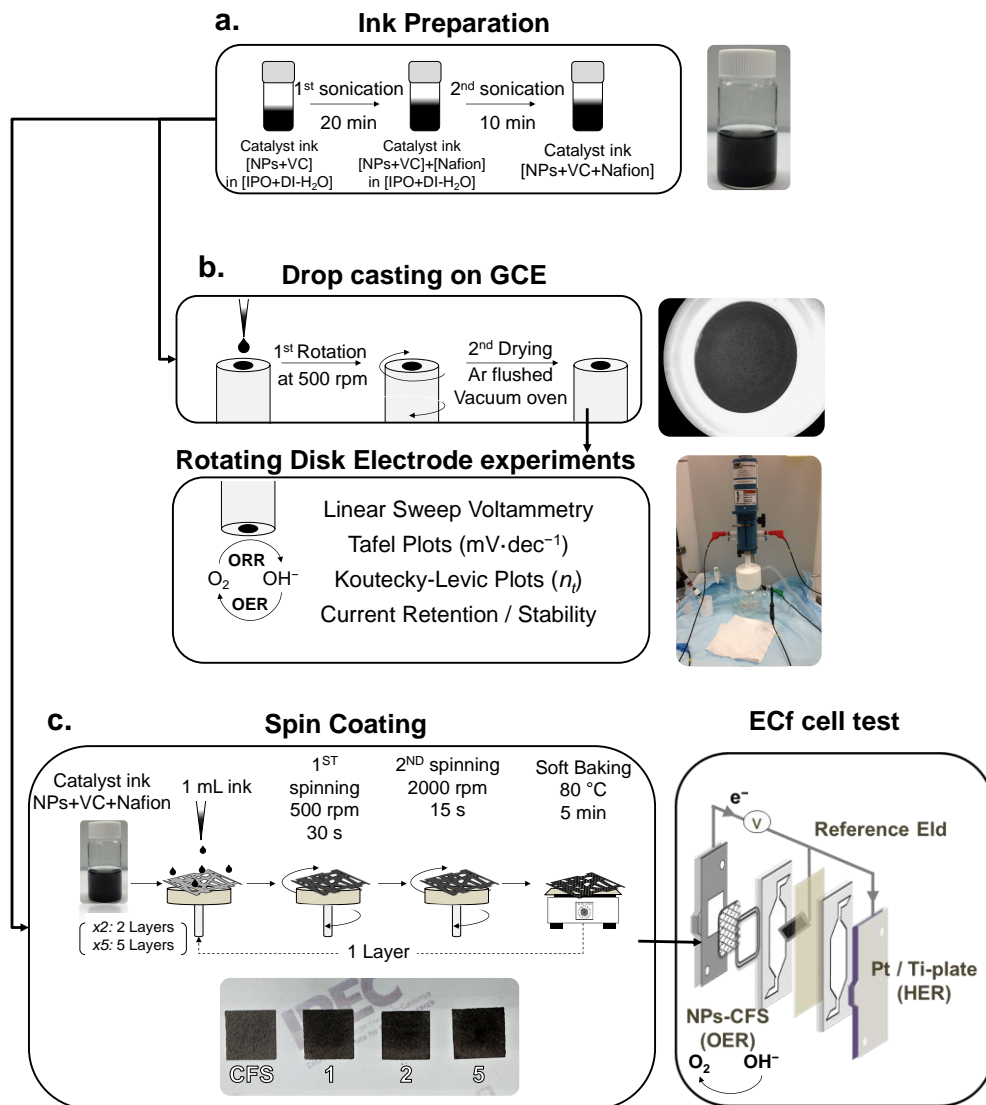


Figure 2-4. Protocol for the (a) two steps of ink [NPs:VC:Nafion] preparation of NPs (b) Schematic illustration of drops casting on GCE and RDE experiments (c) two steps of spin coating of ink on carbon fibre substrate (CFS) following its assembly in EC-flow cell.

Photoanode: TiO₂ nanorods

Titania nanorods (TiO₂ NRs) have been directly grown over an FTO substrate (35 x 40 mm², SnO₂/F coated glass slide ~8 Ω·sq.⁻¹, Sigma-Aldrich Co.) shown in Figure 2-5(a) by using a hydrothermal reaction synthesis following by calcination.

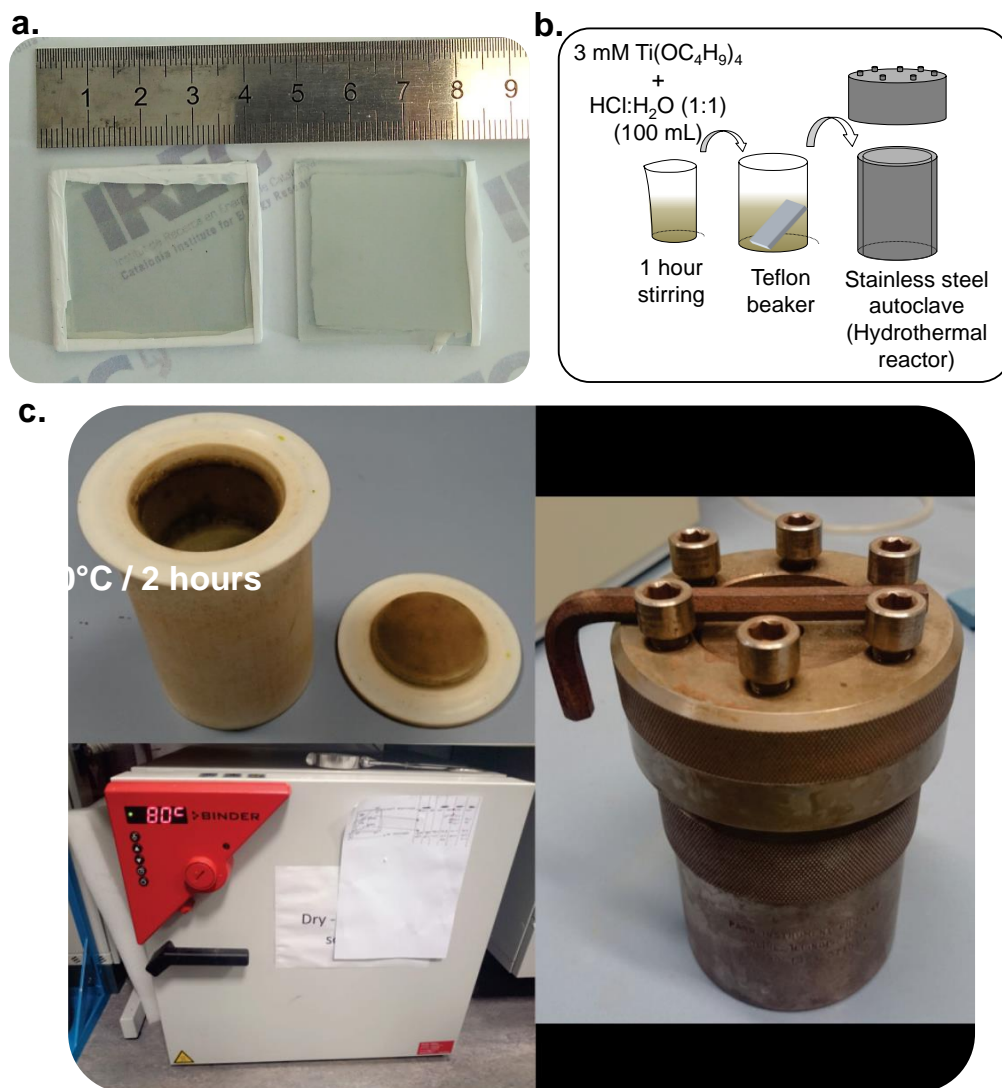


Figure 2-5. (a) Digital pictures of FTO-glass with Teflon® sealing at the edges, before (left) and after (right) the hydrothermal synthesis. (b) Schematic illustration of the protocol for the hydrothermal synthesis (c) Digital pictures of the Teflon® beaker, stainless steel autoclave and electrical furnace.

Hydrothermal synthesis. The steps of hydrothermal synthesis are illustrated in Figure 2-5(b). FTO substrate was dipped in a Teflon® beaker with a liquid having active reactants and the beaker was placed in a metal sealing case. Next, the metal case was held inside a furnace, Figure 2-5(c), for a constant time and temperature creating a pressure higher than ambient condition. Eventually, the reactant within the liquid would activate and react with the substrate surface to form a nanostructured deposit.

The reactor (Teflon® beaker with stainless steel cased autoclave, 125 mL, Parr Instrument Co.) was filled with 100 mL of solution which was prepared as follows⁹⁷: 50 mL of HCl solution (Hydrochloric acid, ACS reagent 37 %, Panreac) was added drop wise to 50 mL Milli-Q deionized water (18.2 M Ω ·cm at 25 °C) under vigorous stirring. After an hour stirring, 3 mL of titanium butoxide (Ti(OC₄H₉)₄, Fluka) was introduced to this solution as Titania precursor. The reaction was carried out on FTO glass slide masked with Teflon® tape at the edges for electrical wiring, to prevent TiO₂ nanorod growth at the contact sites, Figure 2-5(a). The conductive glass substrate was facing down with a 45° angle to favour nanorod formation on FTO site only. Hydrothermal reaction was performed in an electrical furnace at 200°C for 2 hours. A controlled cooling process to room temperature was held by using a water bath.

Post annealing. As-synthesized samples were cleaned by sonication in water and dried under nitrogen stream. Then, a thermal treatment for 1 hour at 450°C in air (20% O₂, 80% N₂) was applied to remove any residues from the prior synthetic procedure. These samples were labelled as TiO₂-O₂ photoanodes due to their post annealing under air atmosphere. Another set of samples were prepared from as-synthesized TiO₂ NRs by thermal treatment under reductive hydrogen atmosphere (10% H₂, 90% N₂) at 450 °C for 1 hour, and labelled as TiO₂-H₂ photoanodes.

2.2 Test Methods

Conventional three electrode cell

A simple electrochemical cell consists of three electrodes and an electrolyte. An ionically conductive electrolyte is needed to complete the inner circuit and balance the electrons passed by the external electrical circuit. The first of the three electrodes are the indicating electrode also known *working electrode*. This is the electrode at which the electrochemical phenomena (reduction or oxidation) being investigated. The second functional electrode is the *counter electrode* which serves as a source or sink for electrons to complete the charge balance. The final functional electrode is the *reference electrode*. This is the electrode whose potential is constant enough that it can be taken as the reference standard against which the potentials of the other electrodes present in the cell can be measured. Commonly used reference electrodes are the silver-silver chloride electrode (Ag/AgCl/KCl (3M), $E = 0.205 V_{SHE}$) or the calomel electrode (Hg/HgCl/KCl (satd.), $E = 0.242 V_{SHE}$).

The standard material for cell construction is a Pyrex glass for reasons both of visibility and general chemical inertness. The image in Figure 2-6 shows the conventional three electrode cells used during this thesis work. Figure 2-6(a) is a three-electrode cell displaying the working electrode (right, Sn-GDE), reference electrode (left, Ag/AgCl/KCl (3M)) and the counter electrode (behind facing the working electrode, a Platinum wire). The cell lid is made from resistant PTFE plastic. A gas line for bubbling the solution with CO₂ or Ar is also evident. Figure 2-6(b) is an undivided photoelectrochemical cell in three electrode configuration, made of Quartz glass in order to minimize absorption of solar illumination since Pyrex is a glass made of silica sand with higher mineral impurities such as CaO and Na₂O.⁸⁸ In order to characterize the state of the electrode surface and its electrochemical behaviour of the reactant, voltammetric experiments were initially carried out in such undivided conventional three electrode cells.

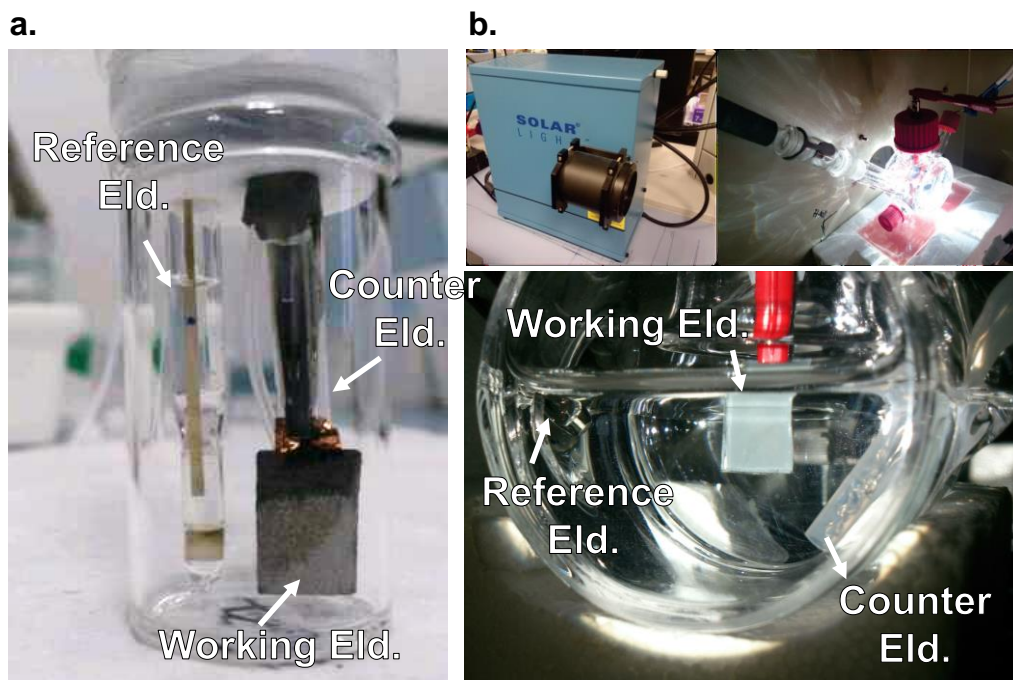


Figure 2-6. (a) Three electrode cell to study CO₂RR of cathodes and (b) photoelectrochemical three electrode cell to study OER of TiO₂ photoanodes. The counter electrode for both cells is a Pt wire and the reference electrode is a silver-silver chloride electrode (Ag/AgCl/KCl (3M)). Both cells have a separate inlet for gas bubbling during the test, e.g. CO₂, Ar or O₂.

Rotating disk electrode

The rotating disk electrode (RDE), illustrated in Figure 2-7, is an example of a device that can be used to obtain an electrochemical reaction in a quasi-steady state. This condition corresponds to a state where the system reach a current-voltage point that does not change with time⁹⁸,

$$\text{for } \forall i; \frac{\partial C_i}{\partial t} = 0 \text{ but possibly, } \frac{\partial C_i}{\partial x} \neq 0 \quad (2.1)$$

Eq.(2.1) explains that the concentration of species “i” do not change with time for an electrochemical system at “steady state”. But there could be a concentration gradient throughout the electrolyte and for a practical point of view^x, one should use the more accurate term of “quasi-steady state”⁹⁸. This notion is different than the notion of “equilibrium”. In other words, the system could be; either in a quasi-steady state where the current-voltage curves are steady throughout the duration

^x This phenomenon is illustrated in Figure 9-2 in the section of Koutecky-Levich plots where a quasi-steady state mass transfer is attained.

of the experiment with a concentration gradient in space; or in a constant state where the overall net current is zero and there is not concentration gradient varying with time (t) and space (x) e.g. equilibrium at open circuit voltage. To secure a quasi-steady state, two conditions are important,

- (i) The electrolyte volume must be large enough to ensure overall electrolyte composition be kept practically unchanged,
- (ii) A dynamic motion of electrolyte that the reactants are continuously fed and products are being simultaneously evacuated.

Figure 2-7 presents the main steps for RDE experiments which are; preparation of an ink, drop casting of the ink on a glassy carbon disc and RDE testing.

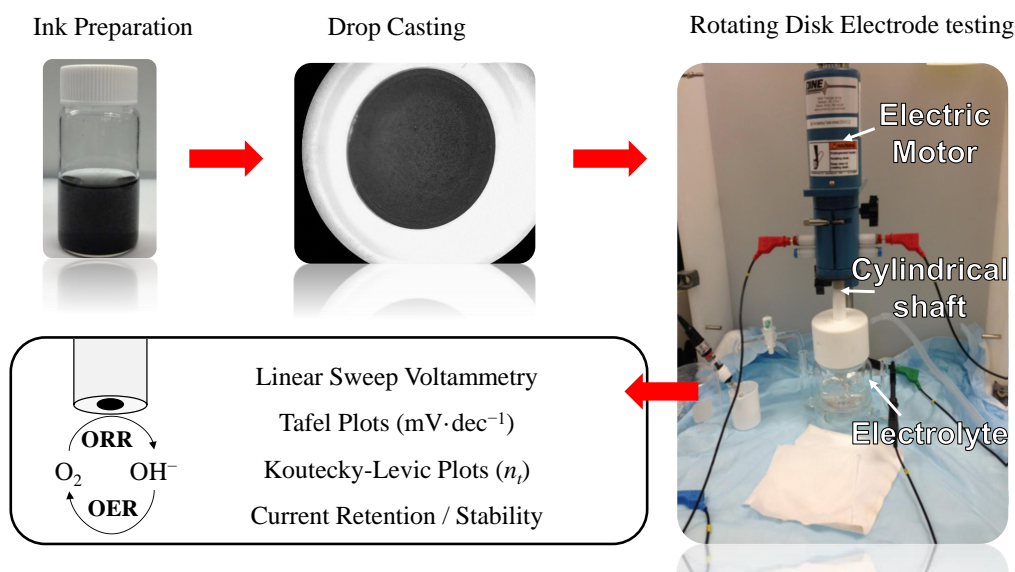


Figure 2-7. Main steps for an electrochemical study with Rotating Disk Electrode set-up; (i) Ink Preparation (ii) Drop casting of the ink to the glassy carbon (iii) Rotating disk electrode testing (iv) Data to be exploited for an electrochemical reaction such as O_2 reduction reaction (ORR) and O_2 evolution reaction (OER)

Briefly, RDE is a hydrodynamic working electrode used in a three-electrode system. It has a cylindrical shaft at one end which is attached to an electric motor ensuring the rotation of the electrode around its axis. The only metallic part in contact with the electrolyte is the glassy carbon disc section. With the rotation of the electrode around its axis, some of the solution (reactants) flows up, perpendicular to the electrode, from the bulk to replace the boundary layer and then flings the solution (products) away from the centre of the electrode. The sum result is a laminar flow

of solution towards and across the electrode. The rate of the solution flow can be controlled by the electrode's angular velocity (ω) and modelled mathematically. This flow can quickly achieve conditions in which the quasi-steady state current (convective-diffusion) is controlled by the solution flow rather than only diffusion. O_2 reduction reaction (ORR) and O_2 evolution reaction (OER) are often studied with RDE set-ups. In these experiments, aqueous solution contains an excess of supporting electrolyte (e.g. 0.1 M KOH) so the ionic migration component in Eq.(2.1) can be neglected^{xi}. The mathematical models employed mainly in Chapter 5 are explained in Annex 2.

Filter-press photo/electrochemical fow cell

Carbon dioxide electroreduction (CO_2RR) experiments were carried out in a filter-press type electrochemical cell (Micro Flow Cell, Electrocell A/S) which comprises different individual units stacked to form a complete cell. It operates with the use of a porous electrode (e.g. gas diffusion electrode) as cathode; under continuous recirculation of electrolytes, gaseous CO_2 and resulting products from CO_2RR .

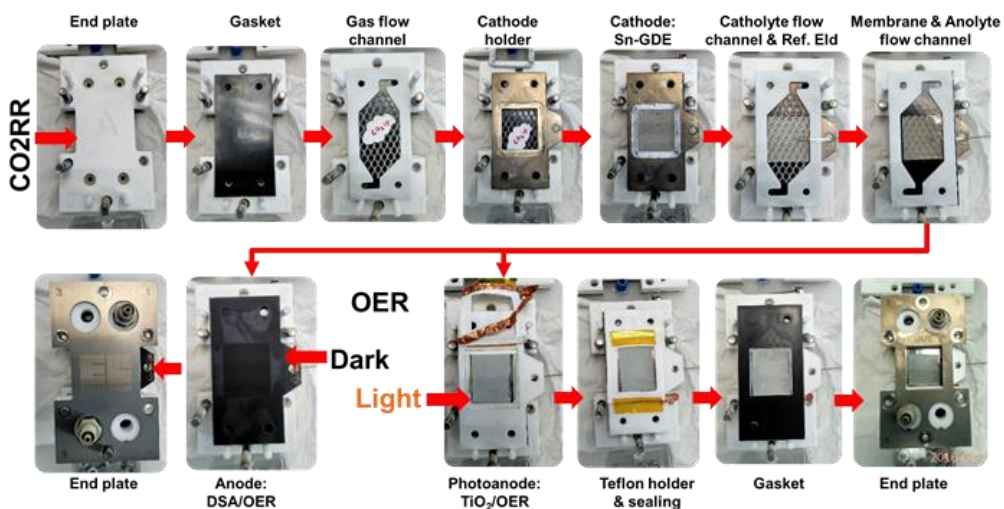


Figure 2-8. Digital pictures showing the stacking of the filter-press photo/electrochemical cell end to end order from cathode to anode compartments. CO_2RR occurs at the cathode compartment and OER at the anode. Ecf cell employs a DSA as anode whereas PECf cell operates with TiO_2 nanorods as a photoanode.

^{xi} The natural convection of the species to the concentration gradient can be neglected in dilute concentrations: CO_2 and O_2 dissolved in aqueous solutions are 3.3×10^{-3} and 1.2×10^{-3} M, respectively

ECf cell refers to operations under dark conditions when a dimensionally stable anode plate ($\text{IrO}_2\text{-Ta}_2\text{O}_5/\text{Ti}$, DSA/ O_2 , Electrocell S/A) was used as anode. PECf cell refers to operations under light conditions when a photoelectrode (e.g. TiO_2 nanorods) was used as anode and activated by back illumination. The stacking of layers is shown in Figure 2-8. Both electrodes had a geometric surface area of 10.2 cm^2 except in Chapter 6 where anode and cathode electrodes have a surface area ratio comprised from 1:1 to 1:0.1.

Dark: Electrochemical flow cell (ECf-cell).

Figure 2-9 shows a schematic illustration of electrochemical flow cell (ECf cell) set-up. The cathodic compartment was equipped with at least two distributor frames dedicated for gas and liquid flow, along with a cathode holder made of titanium metal (Ti, ASTM Grade 1) to place GDE in. The anodic compartment was equipped with one fluid distributor frame and a dimensionally stable anode plate. An ionic transport membrane (Nafion® 117 or Selemion®, AEM) divided the cell two separate compartments. A leak-free Ag/AgCl/KCl (3M) reference electrode (Warner Instruments) was assembled in a polytetrafluoroethylene (PTFE) frame of the cell, placed very close to the cathode surface.

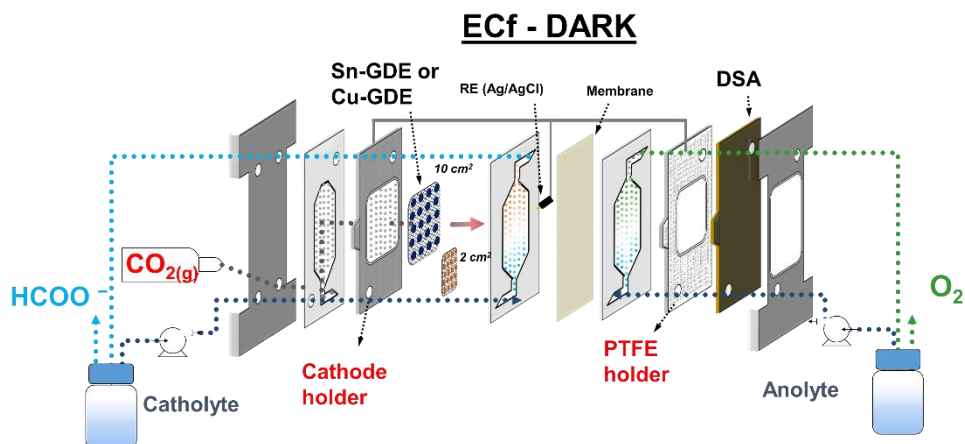


Figure 2-9. Scheme of ECf cell where cathode is a porous gas diffusion electrode with an electrodeposited metal (M-GDE) for CO_2RR and anode is a Dimensionally Stable Anode for OER. Anode and cathode compartments were separated with an ion exchange membrane. The liquid electrolyte was continuously circulated with electrical pumps at a flow rate of $10\text{ mL}\cdot\text{min}^{-1}$. CO_2 gas flow was controlled with a mass flow controller at a flow rate of $10\text{ mL}\cdot\text{min}^{-1}$ unless otherwise specified.

Ethylene propylene diene monomer (EPDM) gaskets were placed between each piece and at lateral ends of the compartments to prevent the gas and liquid leakage. Electrolytes (anolyte and catholyte) were kept in two separated tanks and recirculated continuously to the cell by a dual peristaltic pump (Major Science, MU-D02) to accumulate liquid products. A mass flow controller (Bronkhorst F-201CV) was used to control CO₂ flow rate entering the system, measured downstream by a volumetric digital flowmeter (Agilent ADM 2000). The flow of CO₂ gas and electrolytes were kept at 10 mL min⁻¹ unless otherwise specified (gas-to-liquid ratio of 1). Once assembled, the cell was closed and fitted with 2 Nm torque with 6 bolts and screws to assure mechanical robustness and fluidic watertight.

Light: Photoelectrochemical flow cell (PECf-cell)

Figure 2-10 shows a schematic illustration of photoelectrochemical flow cell (PECf cell) set-up. The cathodic compartment of PECf cell was the same as ECf cell except for the study in Chapter 6 where the cathode size was re-adjusted to compensate the energy demand of CO₂RR as much as possible from the sun light illumination. On the other hand, the anodic compartment comprised anode to cathode ratio from 1:1 to 1:0.1

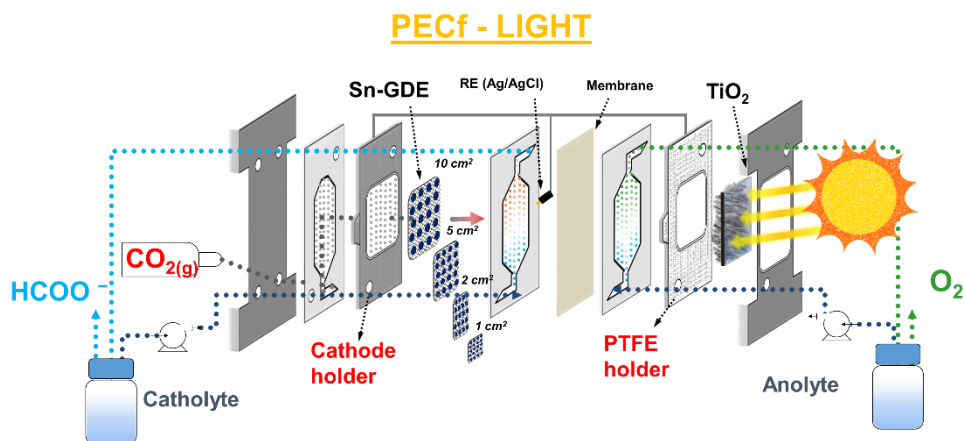


Figure 2-10. Scheme of PECf cell where cathode is a porous gas diffusion electrode with an electrodeposited metal (M-GDE) for CO₂RR and anode is an n-type semiconductor (TiO₂ nanorods) for OER. Anode and cathode compartments were separated with an ion exchange membrane. The liquid electrolyte was continuously circulated with electrical pumps at a flow rate of 10 mL·min⁻¹. CO₂ gas flow was controlled with a mass flow controller at a flow rate of 10 mL·min⁻¹ unless otherwise specified.

In the previous digital pictures given in Figure 2-8, the anode compartment was redesigned to replace DSA/OER anode with an n-type semiconductor active towards OER. At this part of the study, there were several parameters to engineer:

1. Illumination: Solar light illumination must enter from the back site of the anodic compartment of the cell.
2. Electrical contact: In one hand, a good electrical contact must be maintained with FTO part of the glass support to minimize contact losses. On the other hand, the liquid must not penetrate and contact to electrical circuit.
3. Ionic contact: The electrolyte must flow through smoothly and be in full contact with TiO_2 nanorod layer so that there will not be any dead-zone for photoelectrochemical reaction.
4. Mechanical Stability: The photoactive layer (TiO_2 nanorods) was grown on a glass substrate to allow solar irradiance enter from the back site. The glass support is extremely fragile if it is under a small and imbalanced stress.

To overcome those challenges, a series of modifications were engineered. At first, we used a Cu conductive tape (0.07mm, 0.005 ohm, 3M™ 1181 Tape) which is flexible and sturdy. The use of Cu tape, solely, was not successful due to electrolyte leakage corroding Cu tape which brings copper ions into the electrolyte. Later, a gold contact (Au) was utilized owing to its good stability against corrosion and dissolution. A fine Au wire (0.1 mm in diameter, 99%, Sigma Aldrich) was placed in between FTO and PTFE holder for electrical contact. Although PTFE has a fair flexibility to sustain a fine Au wire, the electrolyte leakage could not be prevented at a cell assembly pressure of 2 N·m. At higher pressures to tighten up the cell (2.5 or 3 Nm), the photoanode (FTO-glass) would break.

Finally, we have used a sandwich of several layers to maintain the electrical contact and at same time prevent electrolyte leakage which was an effective but cumbersome solution:

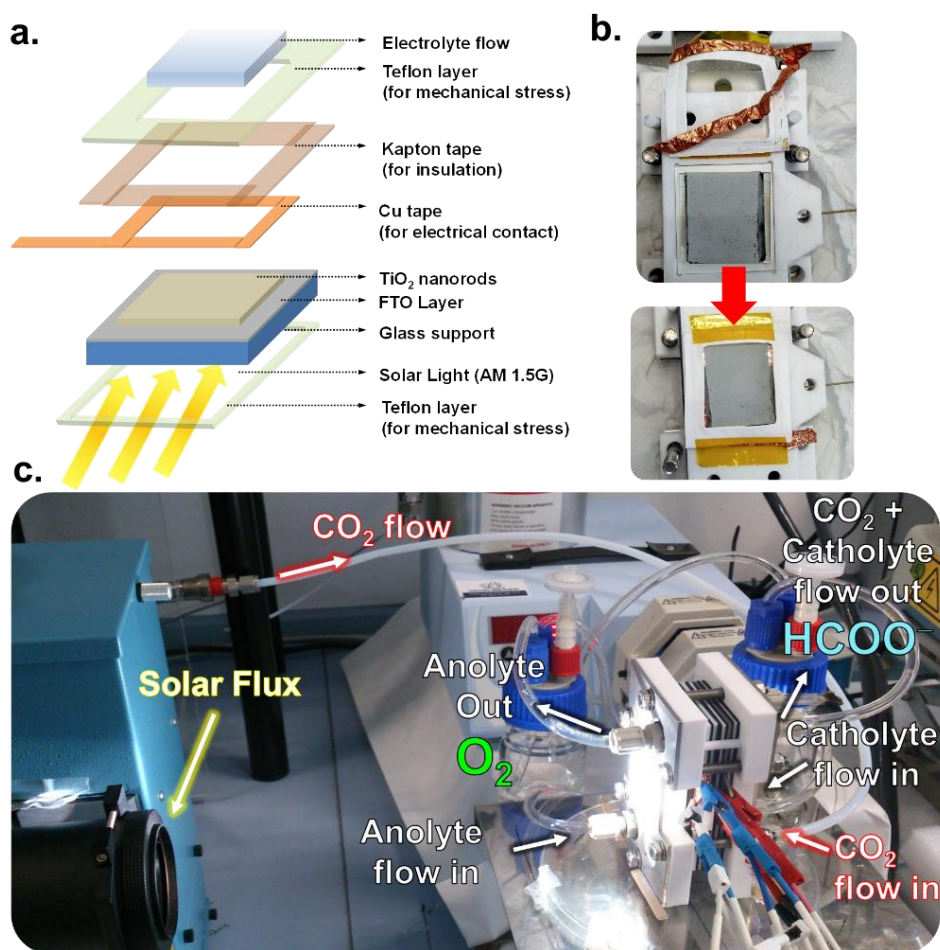


Figure 2-11. PECf flow cell set-up under continuous flow and illumination. The flow directions of the gas, catholyte and anolyte are highlighted. The experiment run with two channels of the potentiostat in *master-slave* configuration.

1. Cu adhesive tape was first attached to the FTO contact sites with a specific distance to TiO_2 layer
2. A polyimide film (DuPont™ Kapton®) was put on top of Cu tape for sealing from strong alkaline electrolyte and humidity in PECf cell.
3. A Teflon® frame was cut with the same dimensions of that contact site and placed on top of Kapton® film
4. Another Teflon® frame was cut and placed at the rear-side of FTO-glass to sustain the cell assembly pressures and prevent the breaking of FTO-glass

Figure 2-11(a) shows an illustration of the sandwich layers engineered to have a good electrical contact and mechanical stability along with isolation of the contacts from corrosion by leakage/humidity. The digital pictures of the layers' assembly are

given in Figure 2-11(b). The contact sites were completely dry after a long-term test. The PECf cell set-up under operation is also shown in Figure 2-11(c). Cu tape did not show any colour change, so it was evident that Cu-tape was not in contact with the anolyte or not affected by the humidity.

Electrolysis method

The term “Chronoamperometry” was used when an electrochemical test conducted under a fixed potential (E_{appl}) where the current or current density versus elapsed time ($j = f(t)$) was investigated. The term “Chronopotentiometry” was used when the experiment was under a fixed current control (I_{appl}) and the change of the potential ($E = f(t)$) was investigated.

The tests were carried out with chronoamperometry mode in two-electrode configuration, applying a voltage between anode and cathode, using a potentiostat/galvanostat Biologic VMP3 (Channel 1: *master channel*). A second potentiostat/galvanostat Biologic VMP3 channel was set to open circuit voltage (OCV) mode in three-electrode configuration to monitor the voltage of each electrode versus the Ag/AgCl reference electrode (Channel 2: *slave channel*). For the sake of clarity, potential was transformed to the reversible hydrogen electrode (RHE) scale given by,

$$E(V_{\text{RHE}}) = E(V_{\text{Ag/AgCl}}) + 0.0592 \cdot \text{pH} + 0.203 \quad (2.2)$$

Pre-electrolysis

The pre-electrolysis is critical to decrease the amount of trace metals of the electrolyte which could poison the catalyst and decrease the catalyst stability.⁶³ Therefore, anolyte (0.5M NaOH or 0.1M KOH, Panreac, >98%) and catholyte (0.5M NaHCO₃, 0.5M KHCO₃ or 0.1M KHCO₃ Merck >99.9%) were pre-electrolysed at -2 V under nitrogen bubbling to remove metal impurities by using two platinum meshes (as anode and cathode). The Pt electrodes were pre-cleaned with 0.1 M HCl following rinsing in triple deionized water. The glass beaker used in pre-electrolysis was pre-cleaned with 0.1 M HCl and rinsed with triple deionized water.

Solar light simulator, calibration and bench set-up

All photoelectrochemical experiments were conducted using a solar simulator (16S-150-002, Solar Light® Co.) equipped with a 150 W Xenon Arc lamp and AM.

1.5 G filter, in Figure 2-12(a). The single output produces full spectrum sunlight of Air Mass 1.5 Global illumination (AM. 1.5G). The calibration of the solar light intensity ($100 \text{ mW}\cdot\text{cm}^{-2}$) was conducted with a power detector shown in Figure 2-12(b) (UP19K-15S-H5-D0, Gentec-EO) which operates with an array of thermocouples connected in series to increase the sensitivity⁹⁹.

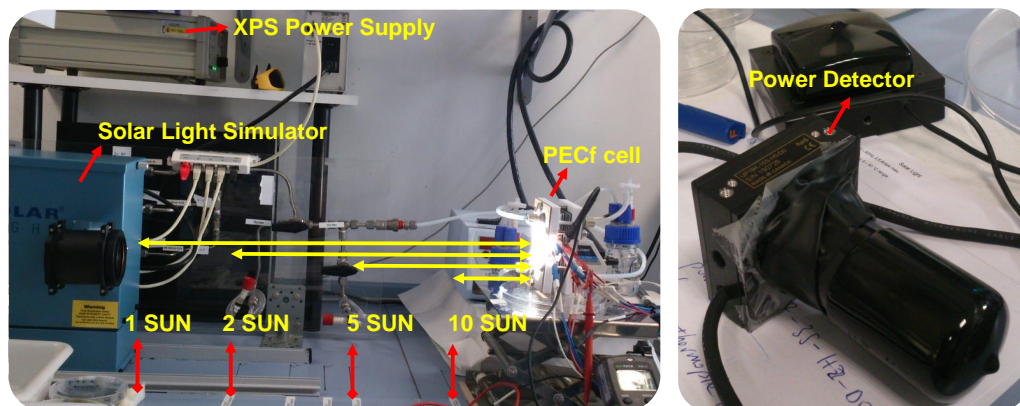


Figure 2-12. (a) Solar light simulator, XPS power supply and bench set-up during PECf cell test under illumination. The positions to increase the solar light power (1 sun to 10 suns) was calibrated with power detector before each test. (b) The digital picture of the power detector used to calibrate the intensity of the solar light for the exact position of PECf-cell.

The solar light radiation heats the absorber in the centre and creates a temperature difference between the centre and the edge. The thermocouples generate a voltage corresponding to this difference. The voltage response is converted to incoming power by a Gentec-EO monitor. The 150 W lamp is ignited at the touch of a switch on the power supply (300 W XPS Power Supply) and after a 10 minute “warm-up” period, the source is ready to use. The spot size is 5.7 cm in diameter with 1 sun output intensity. Additionally, the position of the solar simulator was brought closer to PECf set-up shown in Figure 2-11(a). By doing so, we were able to accumulate the light irradiance and increase the sun power from 100 to $1000 \text{ mW}\cdot\text{cm}^{-2}$ (abbreviated as 1 and 10 Sun). The effect of this modification (solar light concentration) is expanded in Chapter 6.

2.3 Product Analysis and Quantification

In this part, analytical instruments that could be used to measure the content of CO₂ reduction products are described. Since CO₂ can be reduced to several products (HCOO⁻, CO, CH₄, C₂H₄ and etc.) while simultaneous H₂O reduction is the competing reaction producing H₂ gas. In order to evaluate the performance of a catalyst owing to the various end-products in gas and liquid phase, the faradaic efficiency of each specie was obtained by converting the molar concentrations taking into account the number of transferred electrons required for that specie. In general, the electrical energy spent during the electrocatalysis must be equal to chemical energy of formation for that chemical specie "i" which is given by,

$$\text{Faradaic efficiency of R, \%} = \frac{n \cdot F \cdot [n_i]}{I \cdot t} \quad (2.3)$$

where n is the number of electron exchanged to produce "i", F is the Faraday's constant (charge in coulombs of one mole of electrons), n_i is the number of moles for "i" species, I is the net current flux of the reaction in amperes and t is time of electrocatalysis in seconds.

2.3.1 Gas phase analysis and product quantification

One of the challenges to tackle for CO₂ electroreduction reaction is the experimental difficulty in studying the reaction because of the need to quantify each product by multiple analysis methods. In comparison to water splitting reaction where only two products are formed (H₂ and O₂ gas), CO₂ electroreduction reaction can generate several carbon derivatives (C_x-H_y-O_z) in gas and liquid form, simultaneously. Hence, apart from electrochemical analysis (current or potential controlled methods), we used on-line gas chromatography where directly attached to the gas outlet of the catholyte beaker. While the catholyte circulates through the cell, CO₂ gas meets with the liquid phase at the cathode surface, flowing back to the beaker, shown in Figure 2-13(a-c). When GC loop begins, a certain amount of gas sample is allowed to enter inside the pre-chamber to be analysed during the course of the electrolysis for the detection and quantification of any gas phase product, i.e. CO, CH₄, C₂H₄ and C₂H₆.

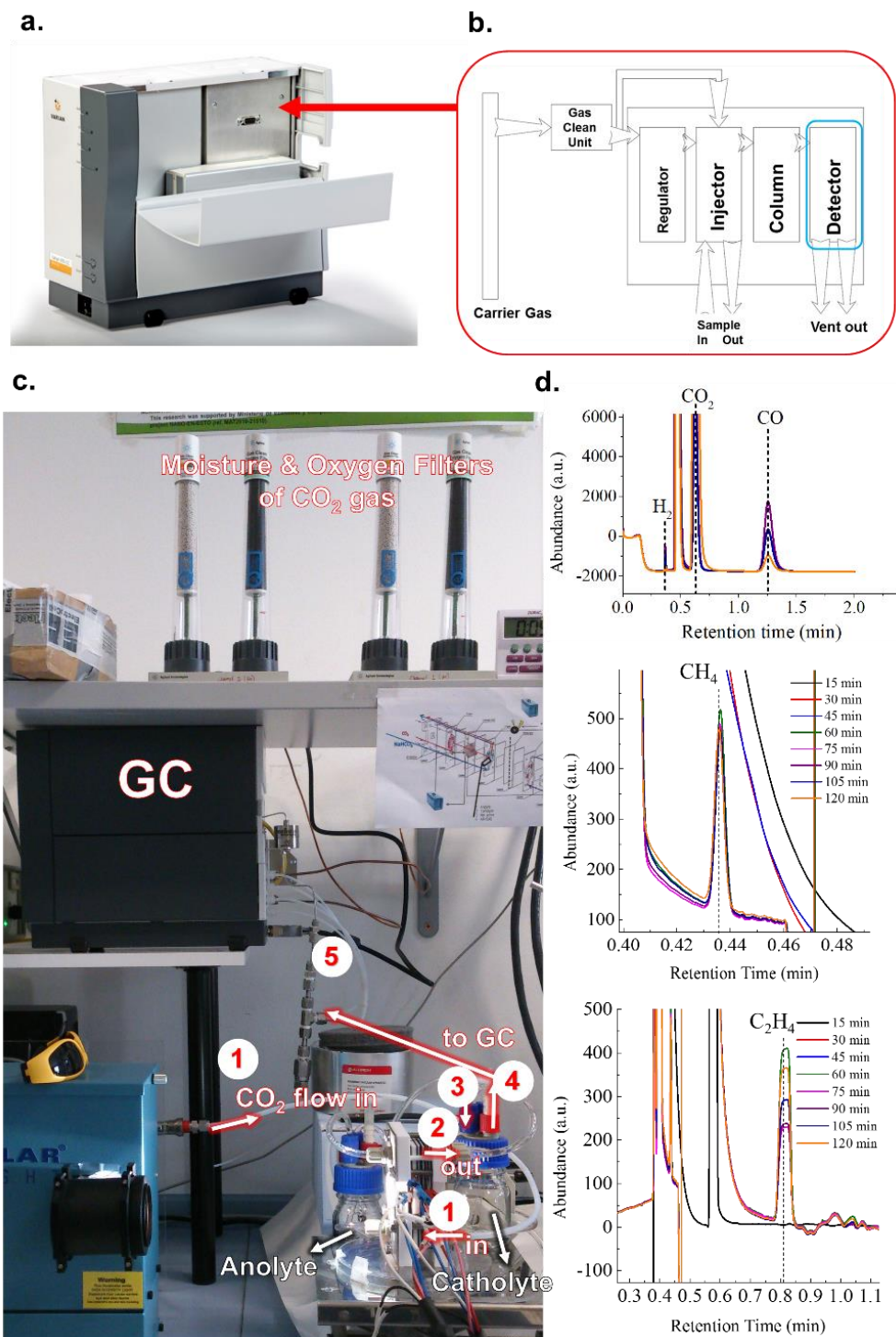


Figure 2-13. (a) Digital picture of Micro-GC 490 from Varian Instruments (b) The segments of the gas chromatogram in working order (c) Digital picture of PECf cell coupled to Gas Chromatogram for on-line product analysis from CO_2 reduction reaction. (d) The examples of gas chromatograms presents the peaks detected for H_2 , CO_2 , CO in the first GC machine (shown in the picture), CH_4 and C_2H_4 in the second GC machine (not shown here).

The fundamental of gas chromatogram depends on adsorption. According to the working order where the injected sample flow through, the segments of the gas chromatogram is shown in Figure 2-13(b). The gas flow directions is;

1. CO₂ mass flow controller outlet → PECf cell inlet
2. PECf cell inlet (CO₂ reactant) → PECf cell outlet (CO₂RR products)
3. PECf cell outlet → Gas-tight Catholyte beaker
4. Gas-tight Catholyte beaker → Gas Chromatogram

which is shown with markers and arrows in Figure 2-13(c). Once a known volume of an effluent is injected into the column, the carrier gas sweeps the molecules of the sample through the column. The adsorption of the molecules at the column walls or packing material cause a retention time for specific to that molecule. A thermal conductivity detector (TCD) analyses the molecules at the end of the column. TCD is a universal detector which is based on detecting differences in thermal conductivity of a gas stream and compares it to the thermal conductivity of a reference gas, as in our case argon and helium. The thermal conductivity is dependent on the temperature and thus temperature of the detector must be well adjusted. For instance, thermal conductivity of CO vs. Ar and H₂ vs. He at 400° K differ greatly, thus column #1 was used to detect CO and column #2 used for H₂ gas. The selected parameters are given in Table 2.1. Nevertheless, different detectors can be used to analyse gaseous molecules such as instance flame ionization detector (FID) which is limited to detection of flammable products. The output signal of a GC chromatogram shows the detector resonance on the x-axis and the time on the y-axis, as in Figure 2-13(d). The time corresponds to the retention time of the gas in the column system.

Table 2.1. Thermal conductivity (κ) of selected gases at 400° Kelvin

Compound	Formula	κ (mW·mK ⁻¹)	Column	Detection
Argon ¹⁰⁰	Ar	22.6	#1, Ar	CO
Helium ¹⁰⁰	He	190.6	#2, He	H ₂
Hydrogen ¹⁰¹	H ₂	230.4		
Carbon monoxide ¹⁰²	CO	32.2		

Analysis. A Teflon® pipe was attached to the top of the gas tight beaker and the pipe was connected to GC inlet. An automated sample loop injected aliquots every 15 minutes (14th, 29th, 44th and 59th mins and so forth) during the electrolysis experiments. Once a sampling ended, the gas stream continues to flow from the back-outlet of the gas chromatograph. Two types of equipment were used in this thesis. The first one was a multichannel Agilent 490 Micro-GC with two columns (Molsieve 5Å-8m, (M5Å_BF) Ar/He, Agilent Technologies Co.). The first column works with Ar and the second one with He as the carrier gas with a TCD detector. This machine was used for experiments when Sn-GDE was used as cathode, which evolved mainly H₂, CO. The second equipment was a multichannel Varian 490 Micro-GC with three columns and only helium as the carrier gas using a TCD detector as well. This equipment was used for experiments when Cu-GDE was used as cathode which produce C2-C3 type of hydrocarbons. Its first column was also a Molsieve type similar to the previous machine but the second column was PPQ column (PoraPLOT Q-10m, PPQ Agilent Technologies Co.) which is able to detect C2-type hydrocarbons. The third column was (CP-Sil 5 CB-6m, Agilent Technologies Co.) which is able to detect C3-type hydrocarbons and alcohols, nevertheless we used only the first two channels because the on-line experiments were conducted at room temperature ~25 °C where most alcohols are in liquid phase.

Quantification. Both GCs were calibrated to quantify H₂, CO, short chain hydrocarbons (CH₄, C₂H₄ and C₂H₆) from some reference gas bottles (Abelló-Linde). The concentrations of the reference bottles were <1% for all of them except H₂. 1% and 3 % for CO and H₂ bottle were also used to increase the calibration range. For CH₄, 20% bottle in He was used for the large range of concentrations.

The faradaic (current) efficiency of a CO₂ reduction product “R” was calculated from the GC peak area given by,

$$FE \% = \frac{\left[\left(\frac{i_{\text{peak area}}}{\zeta \left(\frac{\text{calb. area}}{\text{ppm}} \right)} \times \frac{10^{-6} L_{\text{red}}}{\mu L_{\text{red}}} \right), \frac{L_i}{L_{\text{mix}}} \times \left(\frac{P}{RT}, \frac{\text{mol}_{\text{red}}}{L_{\text{red}}} \right) \right] \times \left(\frac{n e^-}{\text{mol}} \right) \times (F, A \cdot s)}{(I_{\text{avg. at sampling time}}, A) \times \left(\frac{1}{\text{flow rate, } \frac{L_{\text{mix}}}{s}} \right)} \quad (2.4)$$

where ζ is the conversion factor obtained from the calibration curves, P is the ambient pressure (1 atm), R is the gas constant ($0.082 \text{ L}\cdot\text{atm}\cdot\text{mol}^{-1}\cdot\text{K}^{-1}$), T is the temperature (273.15 K), n_e are the electrons involved to obtain the product "R", F is Faraday's constant (96485 C or $\text{A}\cdot\text{s}$) and flow rate is the gas flow injected into the electrochemical cell in $\text{L}\cdot\text{s}^{-1}$.

2.3.2 Liquid phase product quantification

The liquid phase products were detected and quantified by three different methods depending on the catalyst employed. When Sn-GDE was used, the main product was formic acid dissolved in the electrolyte which can be detected by UV-visible-near infrared spectroscopy method (UV-Vis). When necessary, high pressure liquid chromatography (HPLC) was used owing to higher precision at ppm levels below 100. In case of copper catalyst nuclear magnetic resonance (NMR) method, which is a more extensive procedure, was followed due to the diversity of possible products containing C, O and H. Henceforth, sample preparation and the internal calibration of those methods are explained.

Diffuse Reflectance Ultraviolet – Visible Spectroscopy

Analysis. The electrons in a molecule interact in three types: namely σ (single bond), π (multiple-bond), or non-bonding (n- caused by lone pairs).¹⁰³ These electrons, when imparted with energy in the form of light radiation, get excited from the highest occupied molecular orbital (HOMO) to the lowest unoccupied molecular orbital (LUMO). The resulting species is in the excited state or anti-bonding state, Figure 2-14(a). Between the different electronic energy levels are the vibrational energy levels caused due to vibrational changes within the system. UV-visible light can excite molecular vibrational levels and as a result of this phenomenon, there is not one sharp peak obtained in the UV-Visible spectra, but rather a smooth curve shaped peak for absorption is obtained in recorded charts.¹⁰⁴ The ultraviolet-visible spectroscopy instrument used in this study was UV-1800, Shimadzu Spectrophotometer shown in Figure 2-14(b). It works with the principle of the intensity of light passing through a sample, and compares it to the intensity of light from a blank measurement.

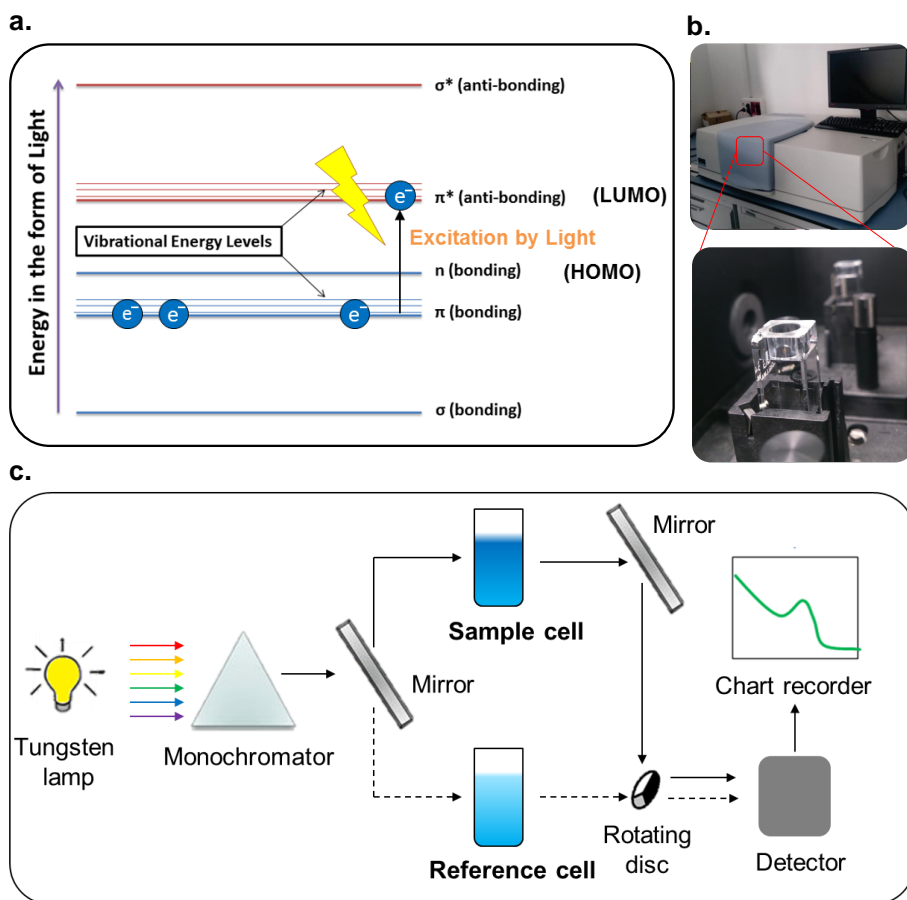


Figure 2-14. (a) Transitions between the bonding and anti-bonding electronic states when light energy is absorbed in UV-Visible Spectroscopy. Vibrational energy levels cause ultraviolet-visible spectra to be smooth and not sharp peaks. (b) Digital pictures of UV-Visible Spectroscopy machine, sample and reference cuvettes (c) Illustration of working principle for UV-Visible Spectroscopy analysis

The Beer-Lambert Law¹⁰³ states that the concentration of a substance in solution is directly proportional to the absorbance (A) of the solution when monochromatic radiation passes through a homogeneous solution in a cell given by,

$$A = k \cdot C \cdot L = \log_{10}(I_0/I) \quad (2.5)$$

where L is the thickness of the sample's path that light pass through, C is the concentration of the solution and k is the extinction coefficient- a constant dependent only on the nature of the molecule and the wavelength of the radiation. I_0 is the intensity of the incident light at a given wavelength, I is the transmitted intensity. The law is only true for monochromatic light and the physical or chemical state of the substance does not change with concentration. The ratio I/I_0 is called

transmittance. This is sometimes expressed as a percentage and referred to as transmittance (%T) given by,

$$A = \log_{10}(100/T) \quad (2.6)$$

The working principle of UV-Vis spectroscopy is illustrated in Figure 2-14(c). In a double-beam instrument, the light is split into two beams before it reaches the sample. One beam is used as the reference; the other beam passes through the sample. The reference beam intensity is taken as 100% T (or 0 A), and the measurement displayed is the ratio of the two beam intensities. The presence of a molecule such as formic acid (HCOOH) can give a response to be proportional to its concentration. For accurate results, the instrument's response to the sample should be compared with the response to a standard by the use of calibration curves.

Quantification. The initial quantification method of HCOOH concentration was conducted with UV-Vis spectroscopy (UV-1800, Shimadzu). 5 mL sample was collected at the end of each electrolysis and 500 μ L of an internal sulfuric acid solution (4M H₂SO₄) was added to convert formate ions (pH \sim 7.4) into formic acid (pH \sim 2). Next, the samples were sonicated for 20 minutes to reduce the background contributions of dissolved CO₂. Figure 2-15(a) presents an example of the UV-Vis absorption spectra for samples taken from Cu-GDE after 2 hours of electrolysis, from Chapter 4. The pristine electrolyte solution, 0 mM HCOOH (acidified 0.1 M KHCO₃) is given to show the difference (black dotted curve). Figure 2-15(b) shows UV-Vis absorption spectra for different concentrations of commercial formic mixed in 0.1 M KHCO₃. The dashed arrow is the selected wavelength at 215 nm to represent HCOOH maxima. Additionally, two more calibration curves (at 210 and 220 nm) are given in Figure 2-15(c) to calculate the standard deviation, Figure 2-15(d). The faradaic (current) efficiency of HCOOH can be calculated once its amount is found from UV-Vis spectroscopy analysis given by,

$$\text{Faradaic eff. of HCOOH, \%} = \frac{\left[\left(\text{HCOOH, } \frac{\text{mM}}{10^3} \right) \times (V_{\text{ely.}}, L) \right] \times \left(\frac{n \text{ e}^-}{\text{mol}} \right) \times (F, A \cdot s)}{(I, A) \times (t_{\text{electrolysis}}, s)} \quad (2.7)$$

where the number of electrons, n , is taken as two for electroreduction of CO₂ into HCOOH and rest of the symbols and units are identical to Eq.(2.4)

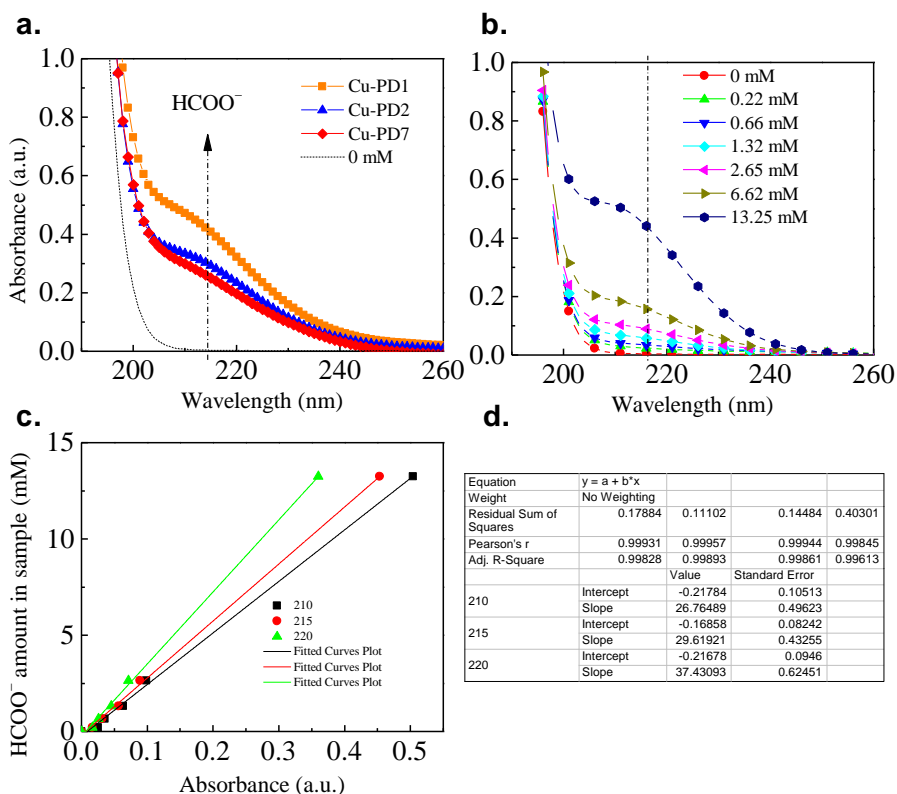


Figure 2-15. Quantification procedure of formic acid by UV-Vis spectroscopy. **(a)** UV-Vis absorption spectra for samples taken from Cu-GDE after 2 hours of electrolysis **(b)** UV-Vis absorption spectra for different concentrations of commercial formic acid and **(c)** its calibration curve for three different representative wavelength **(d)** for calculation of the standard deviation (220, 215 and 210 nm)

High Pressure Liquid Chromatography (HPLC)

Analysis. High Pressure Liquid Chromatography (HPLC) is relatively slower in terms of analysis time (several hours) compared to UV-Vis spectroscopy (several minutes). However, the accuracy (or sensitivity) of HPLC is significantly higher due to the high pressure used to generate the flow through a packed column resulting in species retention.

To explain briefly, the liquid phase is pumped at a constant rate to the column packed with the stationary phase i.e. small spherical silica particles around 5 μm in diameter, Figure 2-16(a). Before entering the column, the analysis sample is injected into the carrier stream. Inside the column, the sample components are selectively retained based on physico-chemical interactions between the mobile phase with solvent molecules and the stationary phase, Figure 2-16(b). Molecules

must freely enter and exit into the pores to be separated. Largest molecules elute first, followed by intermediate size molecules and finally the smallest molecules elute. Figure 2-16(c) shows the working principle of HPLC analysis where the eluted species are detected by a UV-detector similar to the principle in the previous section.

The mobile phase moving at a steady rate and the molecules in the solvent elute, causing a retention time for each specie based on the operating conditions such as,

- ❖ the pressure used (because that affects the flow rate of the solvent)
- ❖ the nature of the stationary phase (not only what material it is made of, but also its particle size)
- ❖ the exact composition of the solvent
- ❖ the temperature of the column

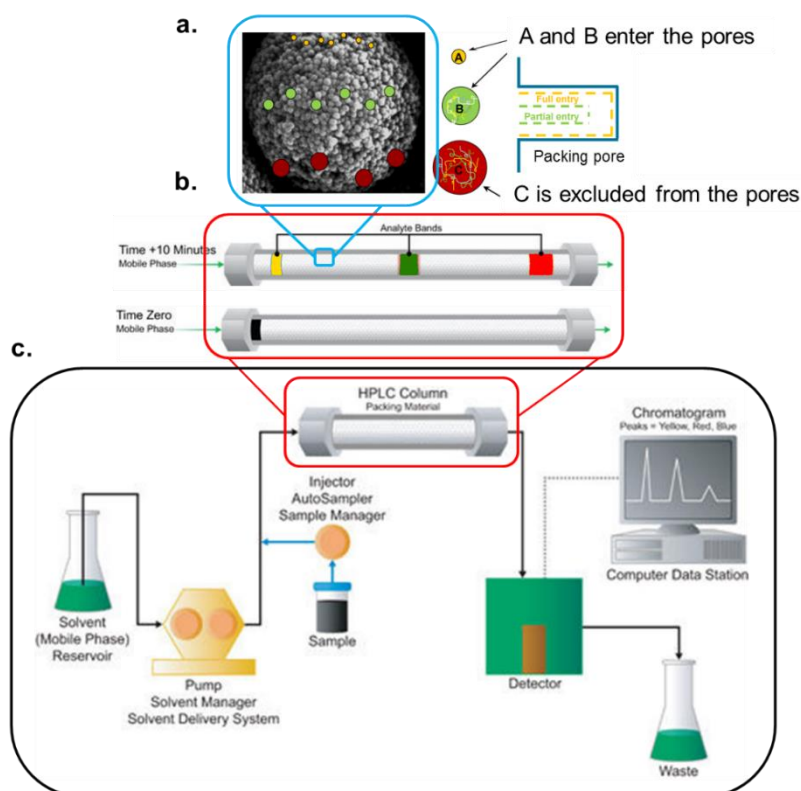


Figure 2-16. (a) An electron microscope image of silica particles and depiction of species retention due to the particle size vs. pore size relation (b) Illustration of the species entering the column with the flow of the mobile phase at time zero and after 10 minutes (c) The scheme of working principle for HPLC system. The images are taken from Ref [105]

A good separation prevents the interference of solvent molecules (i.e. bicarbonate ions), grants a lower background noise giving better peak shapes.

Quantification. 5 mL sample was collected at the end of each electrolysis and 500 μL of an internal sulfuric acid solution (4M H_2SO_4) was added to convert formate ions (pH ~ 7.4) into formic acid (pH ~ 2). Next, the samples were sonicated for 20 minutes to reduce the background contributions of dissolved CO_2 . The HPLC system used in this study was a Perkin Elmer Flexar SQ300MS equipped with a Rezex ROA-Organic Acid H+ (8%) column (300 x 7.8 mm, Phenomenex), with an isocratic pump (2.5 mM H_2SO_4 , 6 mL min^{-1}) and a UV Detector set at 210 nm. The result of HPLC chromatograms for HCOOH analysis is presented in Figure 2-17.

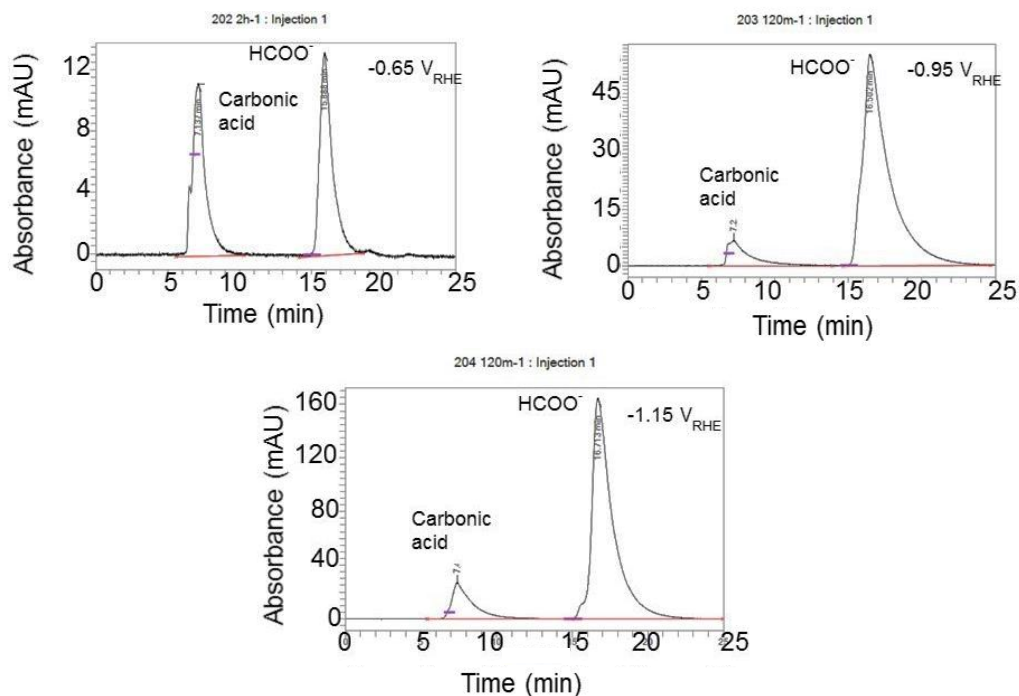


Figure 2-17. HPLC product analysis results of liquid phase samples generated from electrochemical CO_2 reduction. Carbonic acid and HCOOH were observed with retention time of 7.86 and 14.9 respectively.

The carbonic acid peak starts to elute at 7th minute and its peak height vary between 10 – 20 mAU. The formic acid peak has a higher retention time near 15 minutes and its peak height is in good correlation with the electrolysis conditions. Once the amount of HCOOH is found from HPLC analysis, the faradaic efficiency can be calculated from the same formula in Eq.(2.7).

Nuclear Magnetic Resonance (NMR)

NMR was proven^{46e} to be a very useful detection method for a variety of C1 – C3 products, despite the challenges of strong water peak coming from the aqueous electrolyte. One advantage is that analysis can be performed directly on the electrolyte and the peaks of different products and the reference molecule for internal calibration can be seen in the one spectrum. To avoid problems arising from the aqueous electrolyte sample giving a strong proton peak, *solvent suppression technique* could be applied to decrease the size of the proton peak which could be over 1000 times stronger than the signal of interest. It is a common technique for NMR realized by mixing the aqueous sample with heavy water (deuterium oxide, D₂O) i.e. samples usually dissolve in 90% H₂O / 10% D₂O solution instead of 100% H₂O.

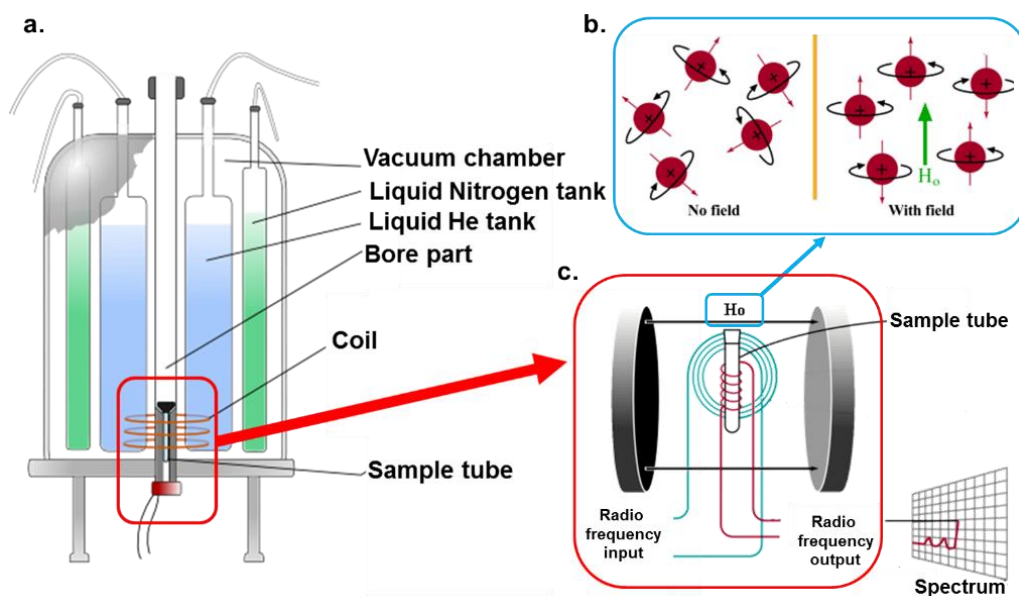


Figure 2-18. (a) The illustration of NMR system (b) spin polarization of nuclei under an applied magnetic field (c) sample position between the magnetic coils. The images are taken from Ref^[106]

In NMR test, the sample is positioned in the magnetic field in the bore part, shown in Figure 2-18(a). When the sample is under a magnetic field and is subjected to radio-frequency (RF radiation energy), nuclei in the sample can absorb the energy at the appropriate frequency. RF necessary for absorption depends on three things¹⁰⁷; (i) type of nucleus e.g., ¹H or ¹³C, (ii) chemical environment of the nucleus (iii) homogeneity of the magnetic field. In the absence of a magnetic field, nuclei are

randomly oriented but when a field is applied they line up parallel to the applied field, either spin aligned or spin opposed shown in Figure 2-18(b). Under magnetic field and the sample is excited by RF pulsations, Figure 2-18(c). The realignment of magnetic fields induces a radio signal in the output circuit which is used to generate the output signal. Fourier analysis of the complex output produces the actual spectrum. The pulse is repeated as many times as necessary to allow the signals to be identified from the background noise.

Analysis. 1D ^1H -NMR spectra was acquired by applying a hard pulse solvent pre-saturation pulse sequence with 2 second saturation delay, 2 second relaxation delay, 2.5 seconds acquisition time, and spectral window of 6400 Hertz. Typically, 8 scans were collected and the peak areas were integrated in order to calculate the concentration of the solutes by taking into account the difference in the number of protons in the reference compound with respect to that electrolysis product.

Quantification. The samples for NMR analysis were conducted on 700 μL samples of the electrolyte containing CO_2 reduction products after long electrolysis tests, i.e. 200 coulombs or minimum 2 hours. This sample was mixed with 40 μL of an internal standard solution to compare the peak areas for quantitative analysis. The internal standard solution is ~ 10 mM dimethyl sulfoxide (DMSO) and ~ 50 mM phenol in D_2O . The characteristic proton peaks of the selected standards, DMSO and Phenol, do not interfere with the products of CO_2RR and they are not volatile in ambient conditions. The internal standard solution (~ 5 mL) was stored inside a cold fridge to prevent any change in its concentration and used for the measurements throughout this study. Considering that only 40 μL from that 5 mL internal standard solution was used for each sample, ~ 125 samples could be tested by using the same internal standard solution. An example of the NMR spectra is shown in Figure 2-19 where internal standard solution and several commercial products were intentionally added to 0.1 M KHCO_3 to identify their peak locations.

In Figure 2-19, there is a shift of the baseline, due to the water peak appear at a frequency about 4.8 which is in the middle of the spectrum. Therefore, the product peak area at right side of the water peak was compared to the area of DMSO, and the areas at the left side of the water peak was compared to the area of Phenol to calculate the specific product concentration according to the standard formula,

$$\% R = \text{purity}_{\text{STD}} \times \frac{\text{mg}_{\text{STD}}}{\text{mg}_{\text{ELY}}} \times \frac{\#H^{\text{STD}}}{\#H^{\text{red}}} \times \frac{A^{\text{red}}}{A_{\text{STD}}} \times \frac{\text{MW}^{\text{red}}}{\text{MW}_{\text{STD}}} \times 100 \quad (2.8)$$

where “R” is the specie from CO₂RR, STD is the internal standard chosen (Phenol or DMSO), #H is the number of protons involved in NMR analysis (2 and 6 protons for Phenol and DMSO, respectively), A is the area of the peak and MW is the molecular weight in gram per mole.

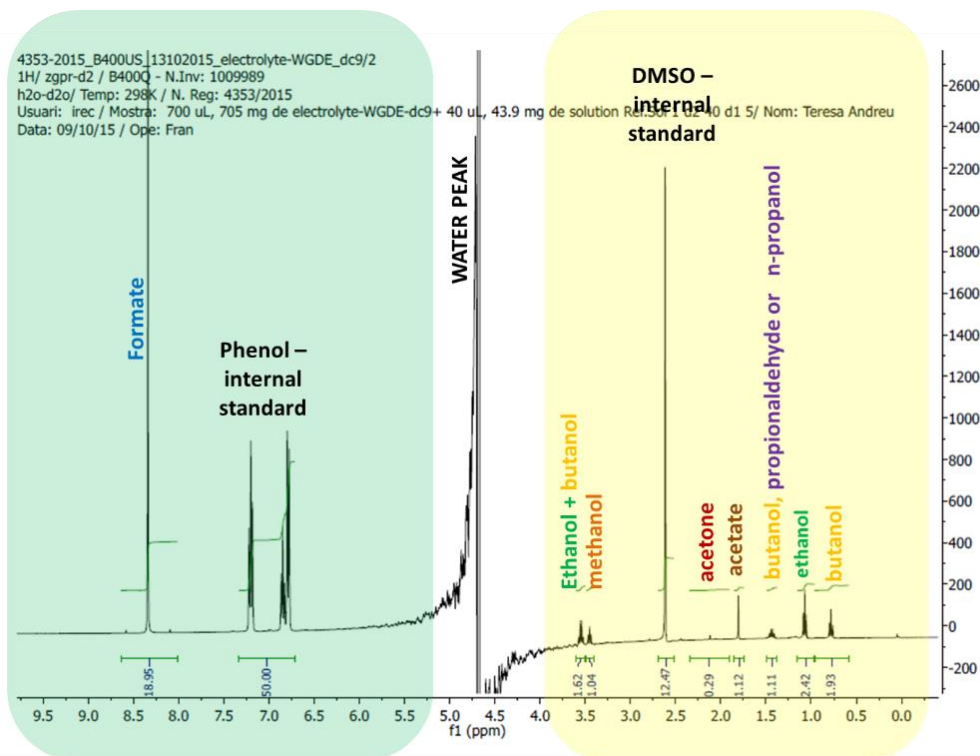


Figure 2-19. NMR spectra of known amount of commercial samples in 0.1 M KHCO₃ and internal standard solution containing Phenol and DMSO. Due to the shift in the baseline, Phenol and DMSO standards are used for left and right part of the water peak in the NMR spectra, respectively.

The coulombs needed to produce that concentration of each product was calculated and divided by the total coulombs passed at the end of the CO₂RR to determine the current efficiency.

Faradaic Eff, R %

$$= \frac{\left[(\% R), \frac{1 \text{ ppm}}{\% 10^{-4}} \times \frac{\text{mg/L}}{\text{ppm}} \times \frac{1}{\text{MW}} \times (V_{\text{ely}}, L) \right] \times \left(\frac{n e^-}{\text{mol}} \right) \times (F, A \cdot s)}{(I, A) \times (t_{\text{electrolysis}}, s)} \quad (2.9)$$

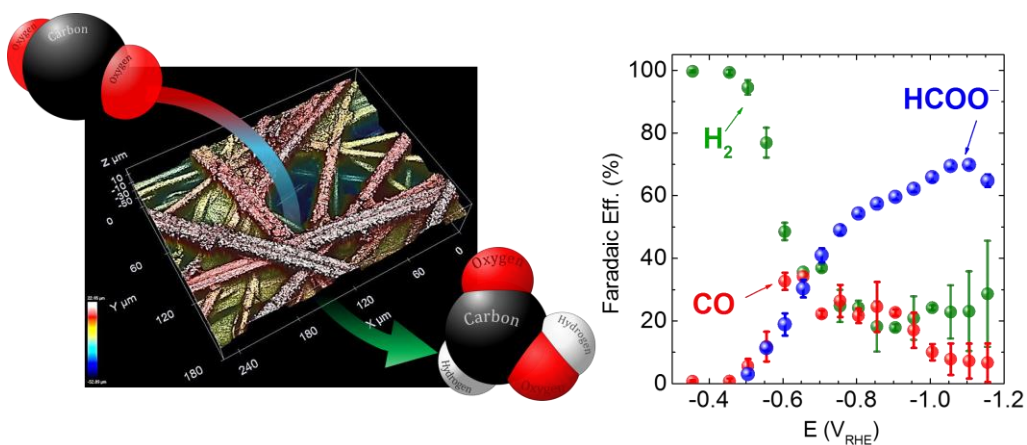
where the symbols and units are identical to Eq.(2.7) and the number of electrons, n , for electroreduction of CO_2 to "R" would be different for each species given in Table 2.2.

Table 2.2. Selected parameters of CO_2RR products and internal standards used in NMR measurements

Compound	Formula	Oxidation State	e^-	E SHE / pH = 0	Molar Mass g / mole
Formic Acid	CH_2O_2	2	2	-0.22	46.02
Methanol	CH_3OH	-2	6	0.03	32.04
Ethanol	$\text{C}_2\text{H}_5\text{OH}$ ($\text{CH}_3\text{CH}_2\text{OH}$)	-2	12	0.09	46.07
Acetone	$\text{C}_3\text{H}_6\text{O}$ ($\text{CH}_3\text{CH}_3\text{CO}$)	3	16	-0.14	58.08
n-Butanol	$\text{C}_4\text{H}_9\text{OH}$	-3, -2, -2, -1	24	0.18	74.12
Phenol	$\text{C}_6\text{H}_6\text{O}$	-	-	-	94.11
DMSO	$\text{C}_2\text{H}_6\text{OS}$	-	-	-	78.13

CHAPTER 3

Dark-CO₂RR: Sn-GDE in ECf-cell



This chapter focuses on the use of a gas diffusion electrode, based on carbon fibres decorated with electrodeposited submicron tin catalyst (Sn-GDE). This electrode was employed as cathode for electroreduction of CO₂ to formate (HCOO⁻) without incorporating, unlike other approaches, any additive or binder. Moreover, CO₂ gas and liquid electrolyte flow rates were studied parameters in this proposed electrochemical flow cell to define the ideal conditions. The system performance and the effective production yield over surface-time units were identified by mol·m⁻²·s⁻¹ and by supplied energy per mole of formate, Wh·mol⁻¹. The energy cost was reduced below 250 Wh·mol⁻¹ with formic acid faradaic efficiency as high as 71 ± 1.1 % being fully stable during 6 hours.

3.1 Experimental Remarks

The electrodeposition of tin on gas diffusion electrode (GDE) was conducted in a glass beaker with a three-electrode configuration as explained in Chapter 2. CO₂RR tests were performed in the electrochemical flow cell set-up (ECf-cell). As seen in Figure 3-1 the cell had three inputs (catholyte, anolyte and CO₂) and two outputs (catholyte+CO₂ and anolyte). 0.5 M NaOH as anolyte and 0.5 M NaHCO₃ as catholyte were kept in two separated tanks and recirculated continuously to the cell by a dual peristaltic pump. The gas and liquid phase enter to the cell from different inlets but they meet at GDE surface. The reference electrode was approximately 2 – 3 mm from the cathode electrode. Nafion membrane transfers Na⁺ ions and separates working and counter electrode compartments.

The faradaic efficiency to formate is the percentage of the total charge supplied that is used to produce formate. For its quantification, a total charge of 4 C·mL⁻¹ of catholyte (typical 50 mL) was employed for the electrolysis to assure a measurable quantity of formate at every potential. Analogously, carbon monoxide and hydrogen faradaic efficiencies were calculated using the analysis of the outlet gas by gas chromatography (GC).

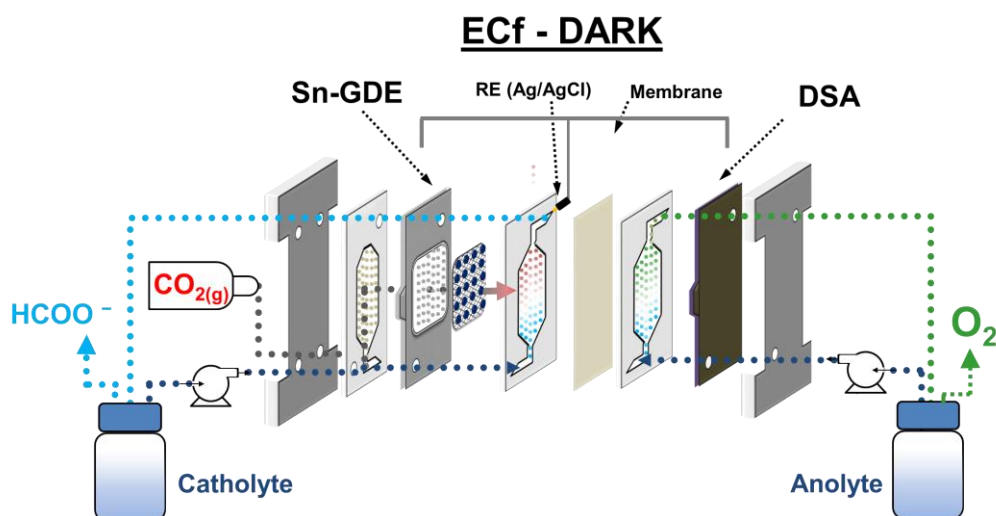


Figure 3-1 Sketch of the electrochemical flow cell and experimental setup used in CO₂RR tests, using a cathode formed by Sn electrodeposition on gas diffusion electrode. DSA is a commercial dimensionally stable anode for O₂ evolution reaction, IrO₂-Ta₂O₅ catalyst immobilized on Ti plate.

3.2 Results and Discussion

3.2.1 Sn electrodeposition & CO₂RR activity

Tin catalysts (Sn-GDE) were obtained by electrodeposition on carbon fibres using a pyrophosphate bath. One of the advantage of the pyrophosphate solution is its pH close to neutrality (pH = 8) and then tartaric acid additive as complexing agent^{54, 108} allows deposits to be obtained with a uniform morphology by favouring Sn metal reduction over hydrogen evolution (HER). As seen in the cyclic voltammometry in Figure 3-2(a), the reduction of Sn⁺² to Sn on carbon fibre electrode starts at -0.13 V_{RHE} close to its standard redox potential (-0.1375 V_{RHE})¹⁰⁹ while HER is significantly retarded.

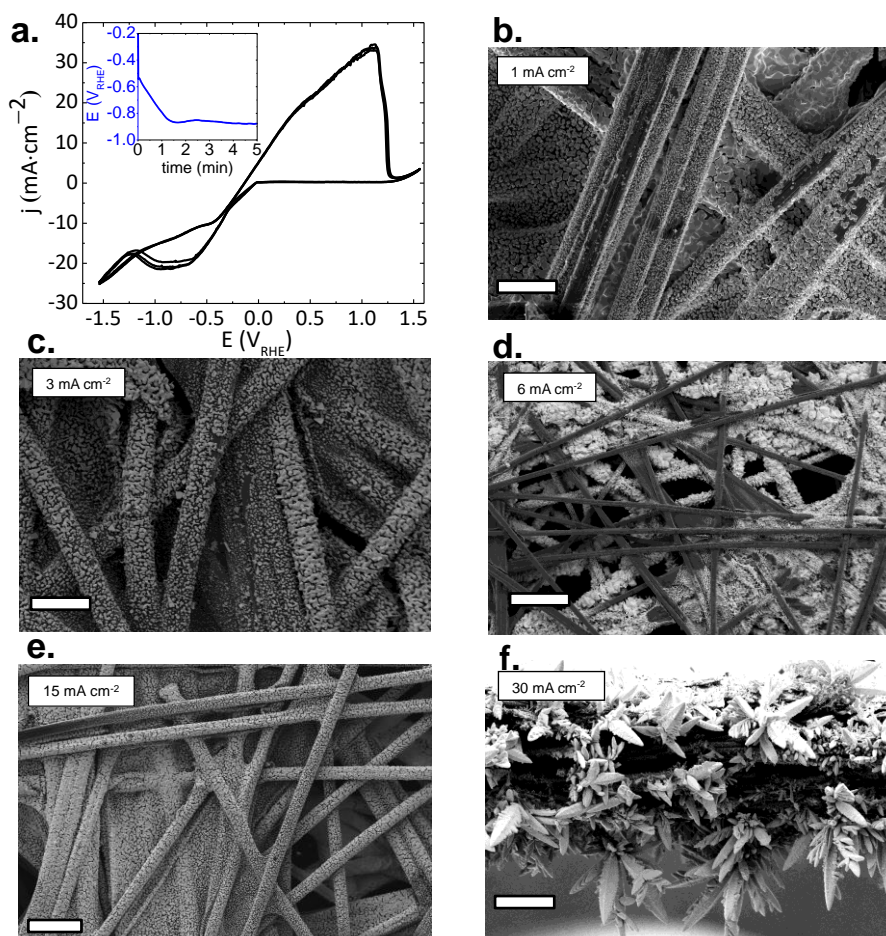


Figure 3-2 (a) Cyclic voltammogram recorded for Sn deposition and stripping on gas diffusion electrode in the pyrophosphate bath (pH 8.3) at a scan rate of 20 mV·s⁻¹ and (a)-(in-set) is the chronoamperometry test of Sn deposition at 15 mA·cm⁻² (b – f) FE-SEM images at different current densities from 1 – 30 mA cm⁻², respectively. Scale bars; (b – c) 20 μ m, (d) 40 μ m and (e – f) 100 μ m.

Cathodic scan of the cyclic voltammogram shows a plateau near $-20 \text{ mA}\cdot\text{cm}^{-2}$ because of tin reduction reaches a limiting current density. Later, a significant hydrogen formation was detected from $-1.32 V_{\text{RHE}}$.

In order to understand the deposition mechanism, we have applied five current values ranging from 1 to 30 mA cm^{-2} . For all deposited samples the charge density was kept constant ($4.5 \text{ C}\cdot\text{cm}^{-2}$). Depending on the used current densities, the nucleation and distribution of the layer deposited onto the carbon fibres changes as well as the depth of the achieved coverage. High current densities gave rise to coverage of the carbon fibres located mainly in the front part of GDE support. Due to the nucleation, growth and deposition rates, the procedure from 1 to 6 $\text{mA}\cdot\text{cm}^{-2}$ did not uniformly cover the fibres, Figure 3-2(c-e), and, complementarily, higher current densities than 30 $\text{mA}\cdot\text{cm}^{-2}$ gave rise to needle like Sn deposits with poor mechanical adherence due to concomitant hydrogen evolution Figure 3-2(f) (deposits peel off under N_2 gas stream and also when electrode was dipped inside a solution). In the range 10 to 30 $\text{mA}\cdot\text{cm}^{-2}$, 15 $\text{mA}\cdot\text{cm}^{-2}$ deposition was estimated to be the best current density for a uniform distribution over the carbon fibres, Figure 3-2(e). Under this condition, a thickness around 1 μm on a single carbon fibre was confirmed by FE-SEM image shown in Figure 3-3(a-b). This could be related to the advantages of the pyrophosphate solution mentioned earlier (near neutral pH and tartaric acid as complexing agent). The morphological analysis of 15 $\text{mA}\cdot\text{cm}^{-2}$ deposit conducted by FE-SEM showed compact and granular morphology with submicron size between 800 nm – 3 μm , Figure 3-3(c). The thickness of the deposit layer ($\sim 1\mu\text{m}$) was similar to the average size of individual grains which can be an evidence of an equilibrium between the rate of nucleation and grain growth. X-ray diffraction (XRD) pattern was performed right after the vacuum drying of Sn-GDE to prevent any modification of the film, Figure 3-3(d). In the XRD spectra, only detected phase was metallic tin in tetragonal structure. The (200) and (101) peaks were the strongest peaks observed for the polycrystalline film and all the other peaks well corresponded to the reference patterns.

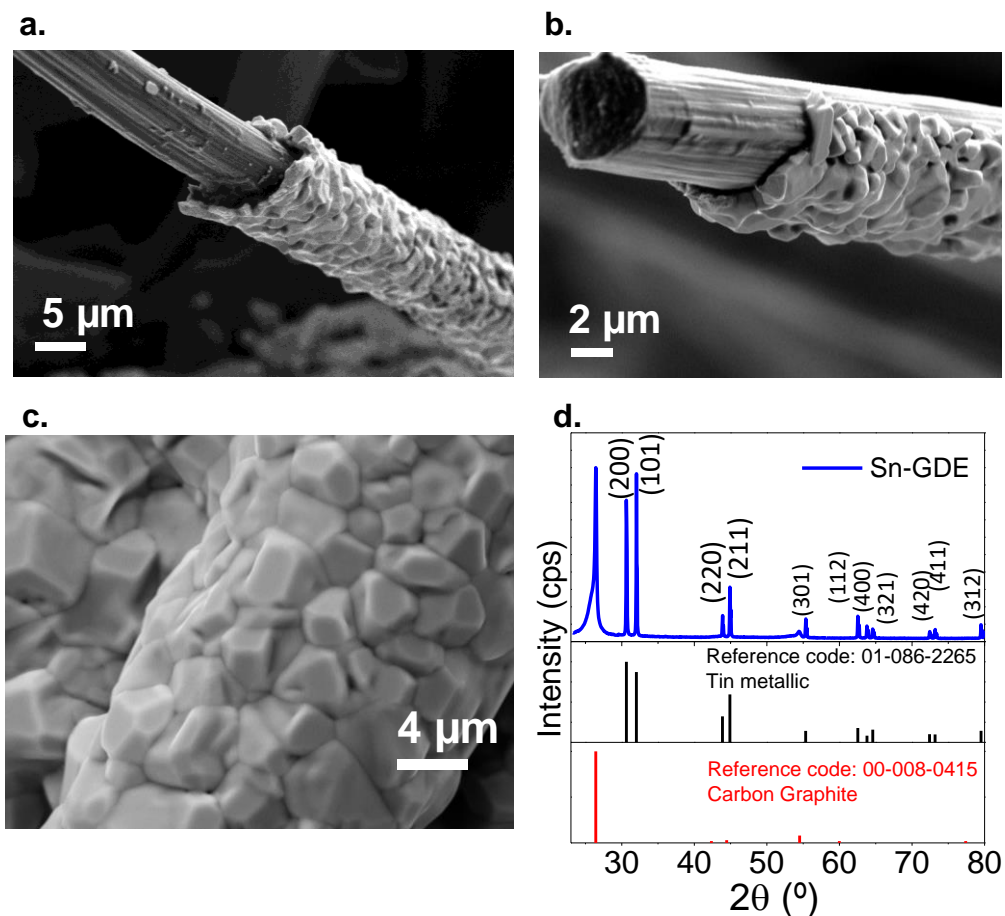


Figure 3-3. (a-b) FE-SEM images of carbon toray fibres of Sn-GDE. Images taken from different sites of Sn-GDE cross-section which shows a granular deposit with a thickness around 1 μm . (c) Top view of a fibre with Sn deposit displaying a compact and pore-free Sn grains (d) corresponding XRD pattern of β -Sn and graphite peaks –from the GDE support.

Line Profile Scanning (Figure 3-4) also confirmed that Sn film formation at 50 ± 5 μm inside the porous electrode (190 μm total electrode thickness) and indicated that nearly 1:3 in volume of the backbone was covered by catalyst film. Profile depth from top to down by 50 μm into the GDE by 3D Profilometer colour gradient confirmed the uniform distribution in FE-SEM, Figure 3-4(d). The average Sn loading on GDE measured by ultrasensitive microbalance weighting was 2.6 $\text{mg}\cdot\text{cm}^{-2}$ (by neglecting a fine SnO layer which is formed as soon as the deposit was taken out from the electrolyte). Consequently, the average faradaic efficiency of Sn electrodeposition was 94 %. The film thickness agreed well with the value calculated from the total coulombic charge passed ($4.5 \text{ C}\cdot\text{cm}^{-2}$).

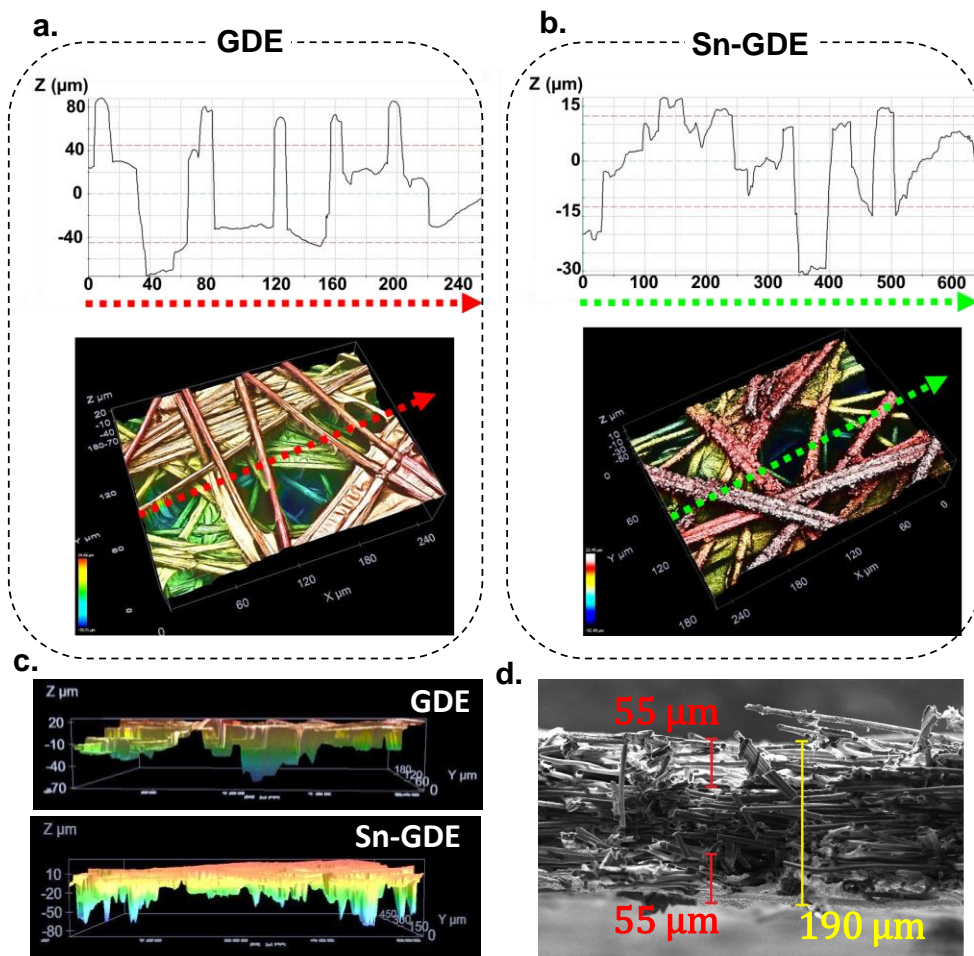


Figure 3-4. 3D Optical Profiler – Line Profile Scanning presenting the profile depth of (a) pristine GDE and (b) Sn-GDE and corresponding top view. Arrows indicate the direction of the line scan (c) Cross-section views of GDE and Sn-GDE (d) FE-SEM of Sn-GDE cross-section, mean GDE thickness was $150 \pm 15 \mu\text{m}$ and Sn coverage from top to bottom, $50 \pm 5 \mu\text{m}$.

Figure 3-5(a) presents a comparison of polarization curves for CV test conducted on glassy carbon (GC) electrode, pristine-GDE, and Sn-GDE in 0.5 M NaHCO_3 electrolyte buffer under Ar or CO_2 bubbling. The difference between GC and GDE in their current density verified the large and active surface area of porous electrode vs. a planar electrode. Next, nearly two times higher current density of Sn-GDE under Ar and CO_2 bubbling (grey and red line, respectively) was attributable to CO_2RR . The cathodic peak with an on-set voltage at $-0.13 \text{ V}_{\text{RHE}}$ in the 1st scan was in agreement with the reversible standard potential of Sn^{2+}/Sn (at $-0.1375 \text{ V}_{\text{RHE}}$).²⁶

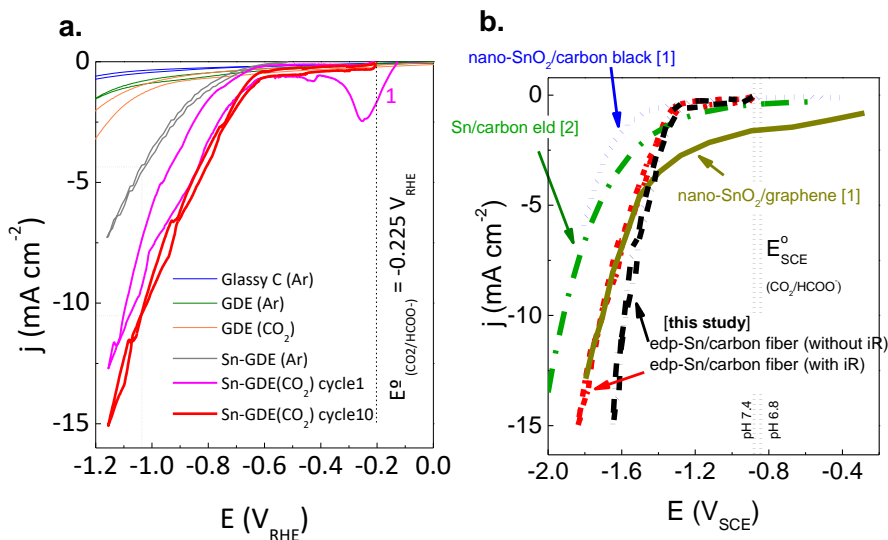
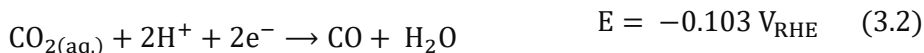
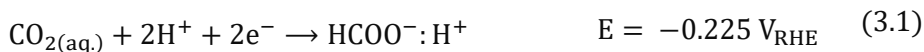


Figure 3-5. (a) Cyclic voltammogram on glassy carbon (GC), GDE and Sn-GDE under 10 mL·min⁻¹ Ar and CO₂ gas flow at scan rate 20 mV·s⁻¹ in 0.5 M NaHCO₃ electrolyte (only GC electrode was tested vs. Pt mesh in a glass beaker with 0.5 M NaHCO₃ electrolyte), (b) Current vs. potential curves for Sn-GDE compared to nanostructured SnO_x¹⁹ and Sn (5 nm) catalyst⁴⁶

The standard potential¹¹⁰ of CO₂ reduction to HCOOH (or HCOO⁻ for neutral pH) and CO are highlighted in Figure 3-5(a) and the half-reactions are given by,



Hence the overpotential of CO₂ reduction was only 400 and 490 mV for CO and HCOO⁻. In comparison to Ar saturated solution, the current density under CO₂ gas had increased by 3 times at an overpotential of only 0.8 V. Compared to a recent result with a 5 nm size Sn-catalyst, our Sn-GDE required 250 mV less energy regardless of up-scaling challenges to produce larger electrodes, Figure 3-5(b). The red line in the figure was in ECf-cell operated at 10 mL·min⁻¹ CO₂ gas flow through Sn-GDE having 10 cm² geometrical electrode area. The black line was after ohmic drop (iR) correction, $R = 1.24 \Omega$. Usually ohmic resistances between 1 and 5 Ω might not be very significant in a laboratory scale device however our ECf-cell was delivering a total current up to 0.1 A. It might be possible to reduce the overvoltage even further in an electrolyte with higher molarity than > 0.5 M as in industrial electrolyzers¹¹¹.

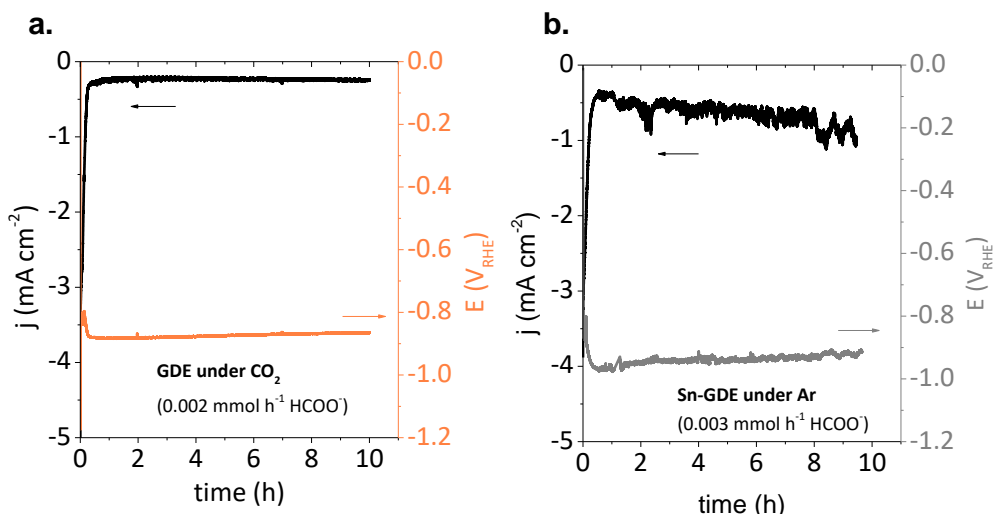


Figure 3-6. Chronoamperometry tests conducted at $-0.85 V_{RHE}$ to check the inertness of (a) GDE towards CO₂RR and (b) to verify that the CO₂ gas is the main product that is reduced.

Before going onto the targeted electrolysis experiments, we conducted further analysis on the inertness of carbon fibres and final product contribution of the carbonate buffer, Figure 3-6(a) and (b) respectively. Previous studies showed¹¹² that carbon surface alone (glassy carbon, activated carbon and etc.) could reduce CO₂ at sufficiently high potentials. Therefore, at first, chronoamperometry tests were conducted with similar flow cell CO₂RR conditions for 10 hours onto pristine GDE under 10 mL·min⁻¹ CO₂ gas flow at $-0.85 V_{RHE}$ to validate the inertness of GDE towards CO₂ electroreduction. Secondly, Sn-GDE were tested under the same conditions expect gas flow was changed to 10 mL·min⁻¹ Ar to confirm that CO₂ in gas form was the true reactant not only between liquid-electrode but also at the TPI (gas-liquid-solid; triple phase interface) sites. As shown in Figure 3-6, at the end of 10 hour experiments, 2 and 3 $\mu\text{mol}\cdot\text{h}^{-1}$ of HCOO⁻ was detected for GDE and Sn-GDE electrodes, respectively. Those values were equivalent of 24.8 and 36.6 ppm which were within the error limit of HPLC protocols towards formic acid detection (< 50 ppm). The blank test results confirmed that gaseous CO₂ was the reduced specie only in the existence of Sn-GDE.

3.2.2 CO₂ reduction products and Tafel plot analysis

Figure 3-7(a) shows the total faradaic efficiencies towards formation of HCOO⁻ and CO/H₂ as liquid and gaseous products, respectively.

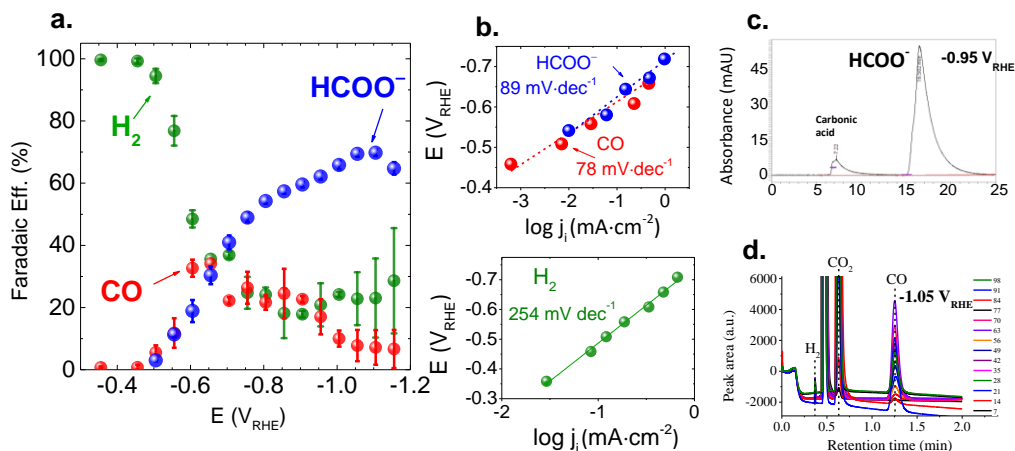
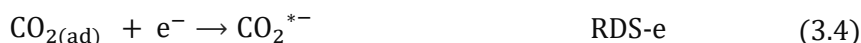


Figure 3-7. (a) Total faradaic efficiency of CO₂ reduction products at the end of 200 C charge passed from the external circuit and (b) corresponding Tafel plots for production of HCOO⁻, CO and H₂ (c) HPLC formic acid analysis: formic acid peak retention starts at 15th minute (d) CO and H₂ peak retention is after 0.3 and 1.15 minutes, respectively. In half an hour, accumulation of the gaseous products reaches to an equilibrium

The working electrode potential versus CO₂ conversion to CO or HCOO⁻ frequently produces an “elbow” shape¹¹³ which appeared in our results also. As discussed earlier by several authors^{41b, 43, 62, 110, 114}, this implies a critical limiting step within an aqueous system where the end products are being limited by formation of CO₂^{*-} radical and it is somewhat independent from the type of the metal catalyst. Most of those studies^{43b, 45, 115} revealed a Tafel slope value around 120 mV·dec⁻¹ which could be correlated to 1e⁻ transfer at the rate determining step (RDS-e) according to Butler-Volmer equation (Table 1.2 in Fundamentals of electrochemistry). Other studies found smaller Tafel slope values^{59 116}, e.g. between 70-90 mV·dec⁻¹, linking to a rapid transfer of the initial electron following chemical rate determining step of a concurrent proton–electron uptake (RDS-c). As a conclusion, they postulated a selectivity criteria by two competing RDS for HCOO or CO depending on protonation at C vs. O of CO₂^{*-} given by,



Tafel slopes of CO₂ reduction reactants were calculated from the similar data obtained by chronoamperometry tests until 200 Coulombs. Figure 3-7(b) shows the Tafel slope values of HCOO⁻ and CO giving 89 and 78 mV·dec⁻¹ at the low potential range, respectively. As expected, H₂ gave a higher Tafel slope value, 254 mV·dec⁻¹, which was due to the low adsorption capability of Sn towards H₂ resulting in higher overpotential and sluggish HER kinetics. Those findings were in good correlation with Tafel values of Kannan et. al.⁵⁹ which found 74 and 77 mV dec⁻¹ for HCOO⁻ and CO, respectively. Our slightly bigger value for HCOO⁻ reduction could be attributed to the quantification limitation of very low formic acid concentrations by our HPLC protocol. Nevertheless, our comparable findings of Tafel slope and on-set voltage were the indicator of a competing chemical rate determining step following to initial electron transfer to CO₂.^{59,117}

There was a (1:1:1) product ratio voltage zone at -0.65 V_{RHE} where Sn-GDE could convert CO₂ to HCOO⁻ by 30 ± 2.8 % and to CO by 32 ± 2.7 %, whereas the rest was H₂ detected by an online GC set-up. The highest faradaic efficiency for HCOO⁻ was 71 ± 1.1 % reaching to 82 ± 2.0 % of total CO₂ conversion including CO (6 ± 4.5 %).

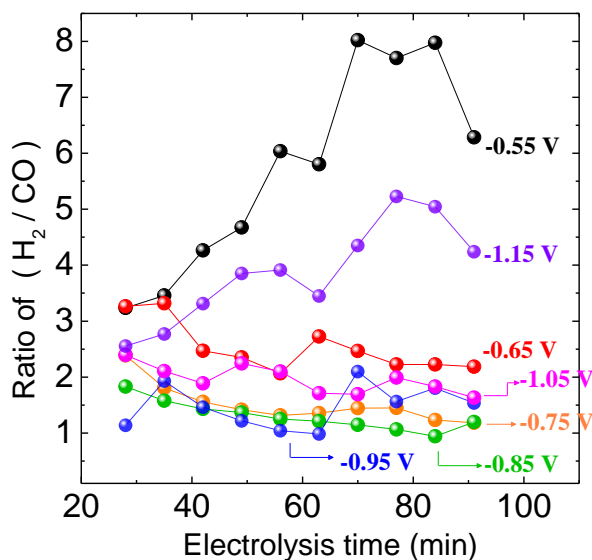


Figure 3-8. Conversion efficiency of CO₂ and H₂O into syngas (CO : H₂) in 0.5 M NaHCO₃ electrolyte solution and 10 mL·min⁻¹ CO₂ and electrolyte flow rate.

Beyond -1.2 V_{RHE} selectivity shifts towards H₂ production. Figure 3-8 highlighted the ratio control on syngas (CO : H₂) with a reliable stability for 2 hours at voltages

between -0.65 to $-0.105 V_{\text{RHE}}$. At extreme ends (very low or high overpotential) H_2 gas was the dominant product. This result also indicated that CO_2 adsorbed at the surface would be activated at a range of overpotential where an uptake of a proton and electron was favoured e.g. between -0.75 to $-0.105 V_{\text{RHE}}$. Once a stable catalytic response had been reached after the first 20 minutes, 1:1, 1:1.5 and 1:2 ratio of syngas could be obtained between -0.85 , -0.75 and $-0.65 V_{\text{RHE}}$, respectively. At $-1.15 V_{\text{RHE}}$, there was a few amounts of CO gas ($7.2 \pm 5.5 \%$) and most of the coulombs passed through the cell spent most likely for HCOO^- together with H_2 evolution, indicator of a favoured intermediate path, e.g. protonation at C site of CO_2^{-*} in Eq. (3.6).

3.2.3 Effect of hydrodynamic conditions

After verifying the catalytic performance of electrodeposited Sn on carbon fibre based gas diffusion electrode, next step was to take advantage of the possibility of tuning the flow system, i.e., ratio of gas and liquid flows, and observe how mass transport can affect CO_2 reduction. The influence of hydrodynamic conditions on mechanisms involved in the reaction intermediates has been well studied.³⁰ These conditions may occur where electrode itself is in motion respect to the solution, i.e. rotating disk electrode, and/or there is a forced solution flow passing through a stationary electrode, i.e. channel electrodes or bubbling electrodes.²⁶ The advantage is that; a steady state is attained very quickly meaning a diffusion layer would be formed at a certain distance from the electrode (diffusion layer, δ) by forced convection. In that state, the current can be related to flow rates, by means of flux of CO_2 gas and the electrolyte acts as proton source. Therefore, changes in formate production rate could take place by modifying hydrodynamic conditions (gas – liquid flow) and electronic energies (applied potential or current) if some of these parameters are limiting these processes.

Initially, cyclic voltammetry test was conducted at different CO_2 to Ar proportions, and CO_2 gas amount was increased from 0 to 100 %. A clear distinction can be seen in the current density vs. potential plots in Figure 3-9(a). The increment of CO_2 gas flow from 10 to 100 % resulted in one-fold higher current density (0.69 to $8.3 \text{ mA}\cdot\text{cm}^{-2}$) when the current generated under Ar was subtracted from CO_2 to obtain partial current devoted to CO_2 gas, as shown in Figure 3-9 (b). Furthermore, net

current density reached to $8.13 \text{ mA}\cdot\text{cm}^{-2}$ for pure CO_2 feed at $-1.1 \text{ V}_{\text{RHE}}$ once the gas and liquid flow rates were equal ($\text{g/L} = 1$). Next, liquid flow was fixed at $50 \text{ mL}\cdot\text{min}^{-1}$ and CO_2 flow was increased (100 and $200 \text{ mL}\cdot\text{min}^{-1}$) above the liquid flow rate ($\text{g/L} = 2$ and 4). This showed a minor increase in the current density, 8.47 and $8.58 \text{ mA}\cdot\text{cm}^{-2}$. These results proved that not only the increase of the CO_2 gas but also g/L flow was essential to promote higher current densities. Here, the conversion of CO_2 into HCOO^- must be in relation to the liquid flow because the electrolyte was the critical component for the protonation of the intermediate specie shown in Eq. (3.6).

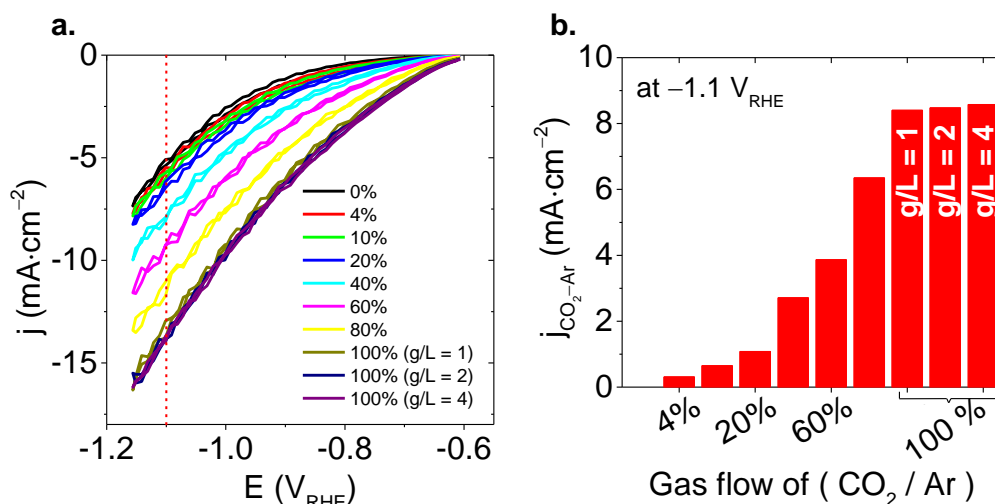


Figure 3-9. (a) Increasing the amount of gas by CO_2 percentage in Ar gas flow (total flow $50 \text{ mL}\cdot\text{min}^{-1}$). For G/L 2 and 4, 100 and $200 \text{ mL}\cdot\text{min}^{-1}$ of gas flow was used. Each CV scan was recorded at $20 \text{ mV}\cdot\text{s}^{-1}$ in ECf-cell in 0.5 M NaHCO_3 (electrolyte flow fixed at $50 \text{ mL}\cdot\text{min}^{-1}$) (b) Histogram of net current density for CO_2 reduction obtained by subtracting the current density value of Ar from CO_2 at $-1.1 \text{ V}_{\text{RHE}}$ in the CV scans.

For a further understanding, electrolysis tests of 200 C were conducted at different cell currents (1 , 5 and $10 \text{ mA}\cdot\text{cm}^{-2}$) and cathode potentials was recorded during electrolysis. Gas to liquid flow rate (g/L) were also adjusted systematically. For the selected current densities, we have explored 5 different g/L ratios by modifying volumetric flow of CO_2 gas and electrolyte from 5 to $50 \text{ mL}\cdot\text{min}^{-1}$ resulting in: 0.5 , 1 , 2 and 5 in terms of g/L flow ratio. A thorough product analysis by HPLC revealed a dependence of g/L ratio vs. electrode potential which was given in Figure 3-10. All the lines showed an arc shaped dependence of HCOO^- efficiency to electrode potential. The most significant effect could be seen for the red and black curve, 0.2

and 0.5 g/L ratio, that the amount of CO₂ gas was not sufficient for reaching the overpotential required to convert CO₂ into HCOO⁻.

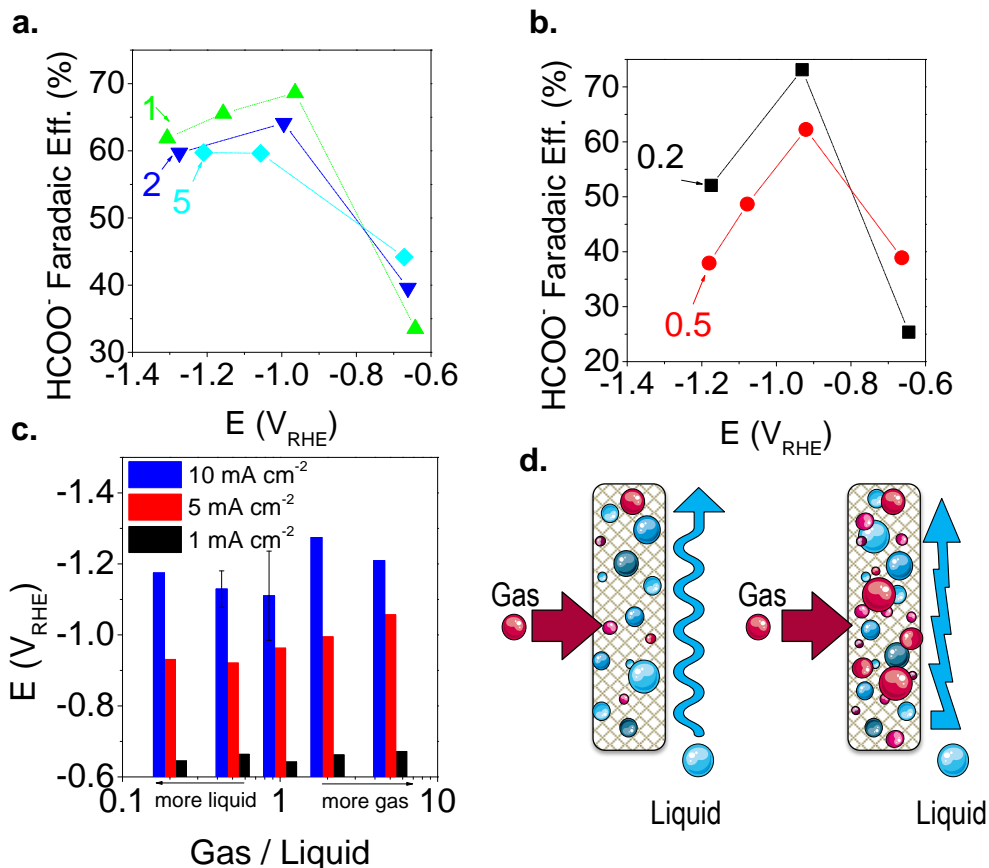


Figure 3-10. Faradaic efficiency of formate against Sn-GDE electrode potential in a full cell experiments for g/L ratio (a) higher and (b) lower than 1 – conducted under current densities of 1, 5 and 10 mA cm⁻² in 0.5 M NaHCO₃ for 200 C (c) CO₂ gas to 0.5M NaHCO₃ electrolyte flow ratio effect on Sn-GDE voltage (d) Schematic of gas and liquid flow through Sn-GDE, at flow ratio lower and higher than 1, left and right parts respectively.

While ratio of 1 provided higher current efficiency, still the reaction was under a rate control mechanism. The further increase of the gas to liquid ratio gave a lower faradaic efficiency for formate in a related trend: 1 > 2 > 5. This may be due to the shorter residence time at higher CO₂ flow rates affecting CO₂ absorption onto the active sites.¹¹⁸ Another remark should be given for the rising electrode potentials with the increment of g/L value, shown by a column plot in Figure 3-10 (c). It is well-known that, higher turbulence at the electrode-electrolyte interface hinders the complete utilization of the electrode surface. High amount bubbles most probably accumulated and locally blocked the active sites of the tin catalyst. With

excessive turbulence, some of the CO_2 molecules entering the reactor left without undergoing electrochemical reaction, leading to a low yield of formate at high flow rates. This could be supported with the increase of the electrode potential. Strong turbulence would contribute to the electrolyte resistance at the vicinity of the electrode depicted in Figure 3-10 (d). Lastly, the improvement in faradaic efficiency must be highlighted for 0.2 compared to 0.5. At low g/L flow ratio, where the liquid stream was superior to gas flow, there was sufficient time for the adsorption and stabilization of CO_2 at the electrode surface before the consecutive step of electron uptake. Also, several (experimental and computational) studies highlighted that protonation of CO_2^{*-} radical could be a rate determining step and the faradaic efficiency for producing formate was promoted by proton existence at the surface layer i.e. protonation at C of CO_2^{*-} , as shown previously in Eq. (3.3)–(3.7).^{41b, 43d, 117a}

3.2.4 Stability and feasibility of formate production

The catalytic activity of Sn deposit was tested for 6 hours and results were given in Figure 3-11 (a) where the dotted line corresponds to 100 % faradaic efficiency of formate conversion from CO_2 .

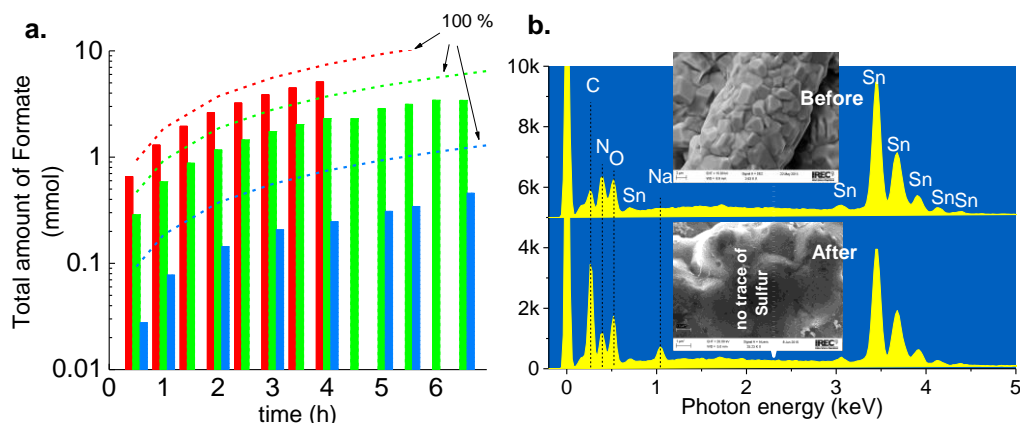


Figure 3-11. (a) Long term catalytic activity of SnGDE conducted under different current densities: 10, 5 and 1 $\text{mA}\cdot\text{cm}^{-2}$ (b) EDX scan and FE-SEM; images of Sn-GDE before and after electroreduction of CO_2 in EC flow cell at $-1.1 V_{\text{RHE}}$ in 0.5 M NaHCO_3 electrolyte while both gas and liquid were flowing at $10 \text{ mL}\cdot\text{min}^{-1}$.

A stable formate production yield was attained (at 1 to $10 \text{ mA}\cdot\text{cm}^{-2}$ applied current densities) during the whole experiment. Moreover, experiments at 1 and $5 \text{ mA}\cdot\text{cm}^{-2}$ were held to longer times to maintain the analytical protocol by preventing a high

product saturation altering the acidity of the electrolyte. The longstanding activity was attributed to the chosen deposition batch providing a catalyst coating free of impurities shown by the EDX scan in Figure 3-11(a-b) and compact catalyst film. There were not any sulphur traces usually reported to be originated from Nafion additives and linked to poisoning of the catalytic sites i.e. in PEMFC¹¹⁹. Also, we haven't observed any significant exfoliation of the catalyst from the backbone of GDE during the simultaneous flow of gas and liquid after the full cell test. Likewise, we haven't observed any significant catalyst losses in weight. It seems that there was not any internal stress at the grain boundaries of Sn deposit since no long crack formation was observed. The highest catalyst material loss was calculated to be less than 6.2% which was for the test conducted at 50 and 10 mL·min⁻¹ gas and liquid flow, respectively.

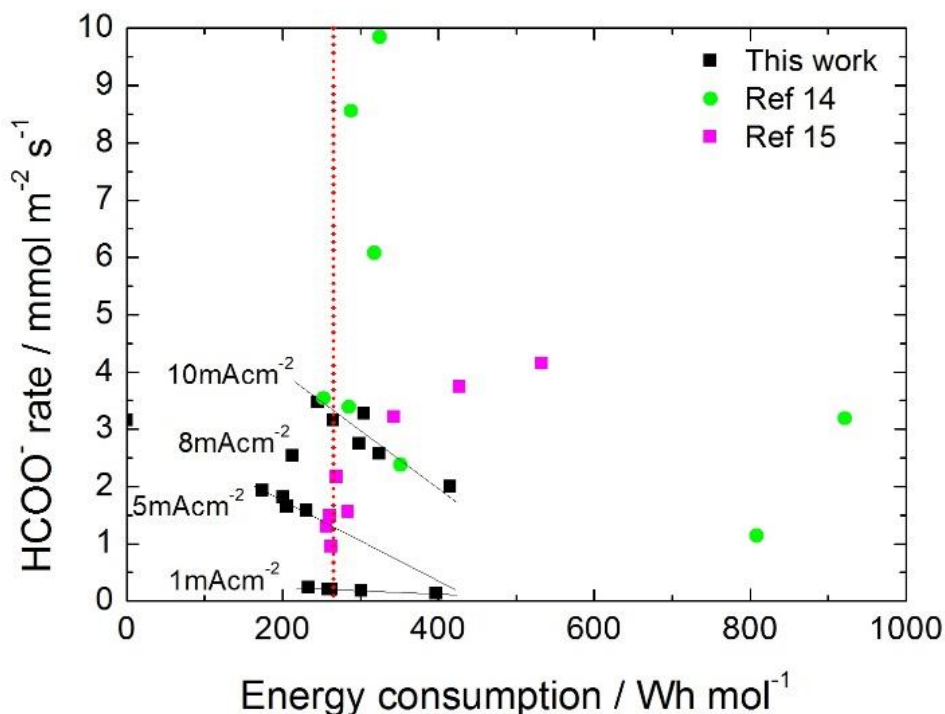


Figure 3-12. (a) Energy consumption of CO₂ reduction to HCOO⁻ using Sn-GDE in ECf-cell at different production rates. Data from this work and Ref. [39c, 58a].

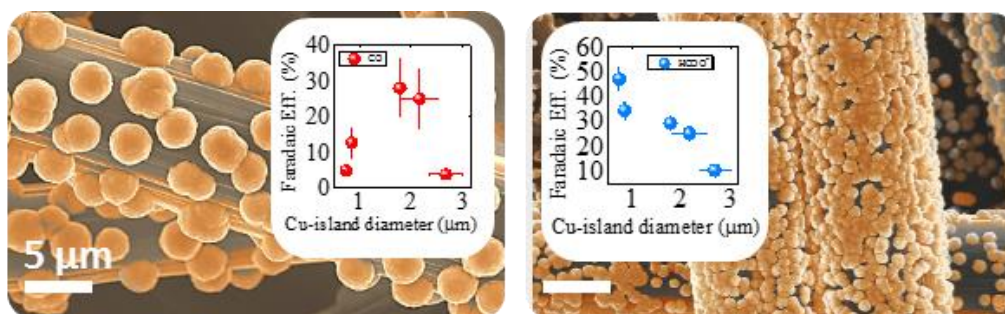
Among the different potential sub-products of CO₂RR, HCOOH has been receiving great industrial attention because of its versatility in various applications (e.g., direct formic acid fuel cells¹²⁰; leather, textile, chemical and food industries). Likewise, its synthesis from CO₂ appears as a powerful alternative if it can be obtained at high concentration with minimum energy consumption during electro-

synthesis. For the procedure of concentration after CO₂RR, the consumed energy at the distillation column would be in the form of steam in the reboiler to reach the background purity of a commercial formic acid at a target of typically 85% in weight¹²¹. This parameter is significantly important for the economic viability of the process. Moreover, to decrease investment costs further, the use of inexpensive electrode materials with high degradation endurance is necessary. HCOOH price for metric ton is currently around 1000 € with an estimated annual increase of about 2%. In this scenario, according to the existing literature^{39b, 39h, 44, 115b} nowadays, high faradaic efficiency values have been obtained with energy consumptions greater than 300 Wh·mol⁻¹ whereas its combustion energy under standard conditions is 254.6 kJ·mol⁻¹ (70.7 Wh·mol⁻¹). Accordingly, the final figure of merit to be highlighted is the energy efficiency of the process shown in Figure 3-12. Considering the combustion energy associated to formic acid (70.7 Wh·mol⁻¹), a threshold of 250 Wh·mol⁻¹ can be set, since the energy efficiency of the process would be 33%. The results of this work were compared with previous literature that use a similar cell configuration and a Sn-GDE obtained by spraying an ink (Sn nanoparticles + Nafion® solution) on C-Toray.¹²² As it has been shown that for the same applied current density, a wide range of values could be seen. Here, besides the current density, the faradaic efficiency of the process had a direct impact on the energy efficiency that, higher F.E. implies a higher HCOO⁻ rate and, consequently, lower energy consumption. Besides this, our binder free Sn-GDE electrode showed a lower resistance (1.2 Ω) resulting in a lower iR drop, whereas reported values range from 5 to 7 Ω using ink-based electrodes^{43a}. In our process, there was an optimum point in the range from 2 to 4 x 10⁻⁴ mol·m⁻²·s⁻¹ where the required energy can be lower than 200 Wh·mol⁻¹ (whereas results from the bibliography show higher production yields up to 1 mmol·m⁻²·s⁻¹ but were associated to an energy consumption higher than 250 Wh·mol⁻¹, which limits its practical application).

3.3 Conclusions

The electrodeposition of tin catalyst on carbon fibres, free of additives and up-scalable for gas diffusion electrodes, has been proved as a successful alternative methodology for preparing gas diffusion electrodes feasible for CO₂ electroreduction to HCOOH (or HCOO⁻ in neutral pH). The highest faradaic efficiency for HCOO⁻ detected by HPLC was 71 ± 1.1 %, being fully stable at least for 6 hours, reaching to 82 ± 2.0 % of total CO₂ conversion to C1-products (HCOO⁻ and CO). In the electrochemical flow cell, faradaic efficiencies were also dependent on the gas to liquid flow ratio, due to the turbulence promoted at the electrode by CO₂ gas flow. At low gas to liquid flow ratio; greater electrolyte flow provided higher faradaic efficiency ($0.2 > 0.5$) which could be due to the residence time of the adsorbed CO₂^{*-} intermediate specie. As this process demands high energy, it is relevant to equilibrate its production yield with the energy consumption. According to the reported data, by taken care of the electrocatalyst synthesis procedure on gas diffusion electrode, we obtained an energy consumption below 200 Wh·mol⁻¹. In the meantime, relatively high production yield was maintained (2-4 mmol·m⁻²·s⁻¹) which promotes the electroreduction method into a significant and competitive alternative for formate production while decreasing CO₂ emissions.

Dark-CO₂RR: Cu-GDE in ECf-cell



This chapter focuses on the effect of electrodeposition methods on CO₂RR with Cu-GDE. Cu-islands with nanocrystalline structure obtained by pulsed current electrodeposition (PCE) method. A correlation between the pulse sequence and particle size was obtained and PCE offered better coverage of porous GDE compared to continuous electrodeposition (CE). Additionally, a change in selectivity for CO₂RR was observed with PCE electrodes. Cu deposits with smaller diameter (~700 nm) promoted HCOO⁻ production (47 ± 4.7 % faradaic efficiency) while higher CO production (28 ± 8.1 %) was favoured with larger Cu-islands (~2 μm). Corroborated by the analysis FE-SEM images, selectivity difference of CO₂RR was attributed to preferential CO₂ binding sites between the perimeter and surface of Cu islands. This easily scalable catalysts immobilization method on porous GDEs (Cu-PCE) offered 21.7 % energy efficiency towards CO₂ conversion to HCOO⁻ which was 5 times higher than the value (4.2%) obtained with Cu-CE.

4.1 Experimental Remarks

Copper deposited electrodes were produced on gas diffusion electrode's carbon fibres by means of direct and pulsed electrodeposition technique as explained in Chapter 2. Electroplating bath parameters are given in Table 4.1.

Table 4.1. Summary of experimental data for electrolyte used to deposit copper catalyst

Experimental parameters		
pH	T [°C]	Hydrodynamic condition
2.1 (± 0.1)	40	mechanically stirred at 100 rpm
Bath composition †		
CuSO ₄	(NH ₄) ₂ SO ₄	Citric acid
40	50	30

† Amount of additives in the electrodeposition bath are given in g·L⁻¹

In continuous electrodeposition (CE), the driving force for producing a deposit is in the form of continuous potential or current applied to the electrode. The difference in pulsed-current electrodeposition (PCE) is creating pulses with a ratio between ON and OFF times during electrodeposition, known as “duty cycle” defined in percentage (%) given by,

$$\text{Duty Cycle} = \frac{t_{\text{ON}}}{t_{\text{ON}} + t_{\text{OFF}}} \times 100 \quad (4.1)$$

A duty cycle of 100 % corresponds to CE because OFF time is zero. In PCE, four variable parameters are central; peak current density during ON time (j_{ON}), average current density of one cycle (j_{AVG}), ON time (t_{ON}) and OFF time (t_{OFF}). The sum of ON and OFF times constitute one pulse cycle and the average current density under pulse deposition conditions defined as,

$$j_{\text{AVG}} = j_{\text{ON}} \times (\text{Duty Cycle}) \quad (4.2)$$

At first, a set of copper samples were prepared by continuous electrodeposition (Cu-CE) at potentials from -0.2 to -0.8 V vs Ag/AgCl until $2.7 \text{ C}\cdot\text{cm}^{-2}$ amount of charge was reached. Next, using the same plating bath, another set of electrodes was prepared by pulsed current electrodeposition (Cu-PCE) respecting the same amount of charge. PCE was carried out galvanostatically using cathodic current square wave pulses by turning the current off periodically. The ON-time was fixed to 0.02 s while OFF time was varied between 2 and 0.5 s. Table 4.2 shows a summary

of electrodeposition parameters which was performed in PCE method for duty cycles, 1, 2, 4 and 7 % and CE method for an applied potential of $-0.7 V_{\text{Ag|AgCl}}$.

Table 4.2. Experimental data for pulsed electrodeposition of copper for CO₂RR in the this study

Sample	Direct Electrodeposition Parameters (DE)						Catalyst	
	Q_{total} C	$j_{\text{AVG.}}$ mA·cm ⁻²	t_{ON} s	Duty %	Pulse	$E_{\text{appl.}}$ $V_{\text{Ag AgCl}}$	Morphology Granular film	
Cu-CE	20	-17.4	170	100%	1	-0.7	2–4 μm	
Sample	Pulsed Current Electrodeposition Parameters (PCE)							Catalyst
	Q_{total} C	$j_{\text{AVG.}}$ mA·cm ⁻²	$t_{\text{ON (1)}}$ s	$t_{\text{OFF (2)}}$ s	Duty %	Pulse	$j_{\text{ON (1)}}$ A·cm ⁻²	Morphology Island growth
Cu-PCE1	20	-4.35	0.02	2	1	330	0.43	740 nm
Cu-PCE2	20	-4.35	0.02	1	2	654	0.22	850 nm
Cu-PCE4	20	-4.35	0.02	0.5	4	1282	0.11	1.78 μm
Cu-PCE7	20	-4.35	0.02	0.25	7	2469	0.058	2.16 μm

The unit of time ($t_{\text{ON (1)}}$, $t_{\text{OFF (2)}}$ and t_{final}) is given in seconds. $j_{\text{AVG.}}$ is in mA·cm⁻²; $j_{\text{ON (1)}}$ is in A·cm⁻²; multiplication of the current applied during the ON period with duty cycle is equivalent to average current density of the electrodeposition. Electrode area, 6.9 cm² as described in experimental section previously.

Carbon dioxide electroreduction (CO₂RR) experiments were carried out in ECf-cell configuration, described in Chapter 2 except a different the ion selective membrane and GDE dimension was used. Once Cu-GDE (with 6.9 cm² geometrical area) was placed onto the titanium electrode holder in the cathode part of the ECf-cell, a top frame that fitted tightly onto the holder defining Cu-GDE surface area of 10 mm x 20 mm (2 cm² geometrical area). In the previous part (Chapter 3)⁴⁰, GDE area was 10 cm² so the cathode geometrical area would be five times smaller in this part of the thesis. There were two reasons of this alteration. First, current limit of our potentiostat was exceeded in pulsed-current electrodeposition tests^{xii} on larger electrodes, therefore a geometrical area of 2 cm² was used instead of 10 cm². Secondly, previous studies in our group showed that Cu plate or Cu mesh required a high energy (beyond 1 V overvoltage) to produce C2 – C3 hydrocarbons, affecting the counter electrode and so cell potential as well. Thus, smaller surface area would locally accumulate the total energy and provide better conversion efficiency. This

^{xii} GDE geometrical area >5 cm² required a pulse current around 1.25 A while current ranging of potentiostat was 10 μA to 800 mA

would lessen the rate of CO₂ conversion (mol per time) but was expected to increase the selectivity and energy efficiency of the complete cell.

In order to maintain electrode area to gas flow ratio as 1:1, CO₂ flow was adjusted to 2 mL·min⁻¹ for the active electrode geometrical area; 2 cm². The ion selective membrane, dividing the cell in two separated anodic and cathodic compartments, was Selemion AEM (styrene-divinylbenzene copolymer type anion-exchange membrane, 0.13 mm thickness: Asahi Glass Co. Ltd). Selemion® AEM allows the passage of OH⁻ ions so pH equilibrium was maintained at both sides at pH ~6.82. The electrolyte flow was kept at 10 mL·min⁻¹ while CO₂ gas stream was 2 mL·min⁻¹ to obtain a smooth flow. CO₂RR experiments were carried out under potentiostatic conditions applying a voltage between cathode and reference electrode during 2 hours using a potentiostat/galvanostat Biologic VMP3.

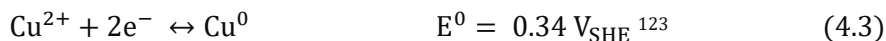
The gas products were detected and quantified by gas Chromatography and liquid products were analysed by NMR and UV-Vis spectroscopy. The details of the methods for CO₂RR products can be found in Chapter 2.

4.2 Results and Discussion

4.2.1 Continuous electrodeposition of copper

For electrochemical characterization of Cu formation, cyclic voltammetry (CV) test was conducted on glassy carbon electrode and gas diffusion electrode, as shown in Figure 4-1. In a CV experiment of electrodeposition, a significant concentration of the product, e.g. Cu⁰, would be generated near the electrode on the forward scan. When the scan direction was reversed, Cu⁰ would oxidize back to the original starting material (Cu⁰ → Cu²⁺ + 2e⁻) or go through a different electron transfer reaction (Cu⁰ → Cu⁺ + e⁻). Accordingly, the difference of CV profiles between the non-porous (flat) electrode (as glassy carbon) and highly porous electrode (as GDE) in citric-sulphate solution was noticeable. The calculation of the deposition and stripping efficiency of reactions from CV curves of glassy carbon and GDE gave 93.8 % and 54.7 %, respectively. For glassy carbon (black curve), the on-set potential of Cu deposition was at -0.05 V_{Ag|AgCl} and beyond this voltage, the cathodic current

started to increase by forming the peak current^{xiii} of $-23 \text{ mA}\cdot\text{cm}^{-2}$ at $-0.15 \text{ V}_{\text{Ag|AgCl}}$ followed by mass transport limitation. The reaction responsible for the peak current would be given by,



Nernst equation¹²³ from the mathematical expression in Eq. (1.11) can be written to recalculate the redox potential, ,

$$E = E^0 + 0.0592 \log[\text{Cu}^{2+}] \quad (4.4)$$

$$E = 0.34 + 0.0592 \log[0.16] \quad (4.5)$$

$$E = 0.293 \text{ V}_{\text{SHE}} \quad (4.6)$$

$$E = 0.293 - 0.205 = 0.087 \text{ V}_{\text{Ag|AgCl}} \quad (4.7)$$

The current density of electrodeposition on GDE (purple curve) showed a less steep reduction profile compared to glassy carbon. The transport time of Cu^{2+} species to the electrode surface would be the reason due to their diffusion through the pores of GDE. In the region between -0.2 to $-0.4 \text{ V}_{\text{Ag|AgCl}}$, Cu deposition on GDE was under mixed control (activation and mass transport) favourable for the nucleation and phase growth of Cu⁵⁴.

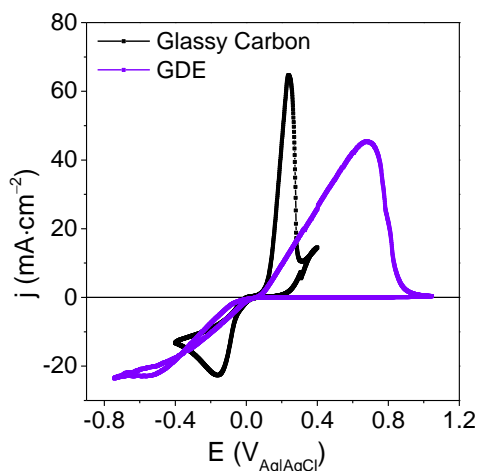


Figure 4-1. Cyclic voltammetry of glassy carbon and GDE in 0.16 M CuSO_4 , 0.15 M citric acid and 0.38 M ammonium sulphate solution. Scan rate is $20 \text{ mV}\cdot\text{s}^{-1}$

Between -0.4 and $-0.8 \text{ V}_{\text{Ag|AgCl}}$ was the region limited by the mass transport where deposit growth was related to ion diffusion through the electrode pores. Beyond

^{xiii} Current limited by the rate of formation of electroactive species which is Cu^{2+} ions in the solution obtained by dissolution of CuSO_4 in the aqueous electrolyte

$-0.8 V_{\text{Ag|AgCl}}$, water electrolysis (hydrogen evolution reaction) current prevailed which decreased the efficiency of the electrodeposition and created irregular deposits¹²⁴.

In order to examine the deposit morphology, we conducted chronoamperometry tests between -0.2 and $-0.8 V_{\text{Ag|AgCl}}$ until $2.7 \text{ C}\cdot\text{cm}^{-2}$ was reached. Figure 4-2(a) shows the current density (j) over time (t) for various voltages applied on GDE. It was evident that the current raised much faster at higher voltages and gave shorter electrodeposition times, between 3 to 10 minutes. The oscillation of the current density was due to the mild stirring (100 rpm), argon bubbling and continuous change of GDE surface area during the formation of Cu nanoparticles.

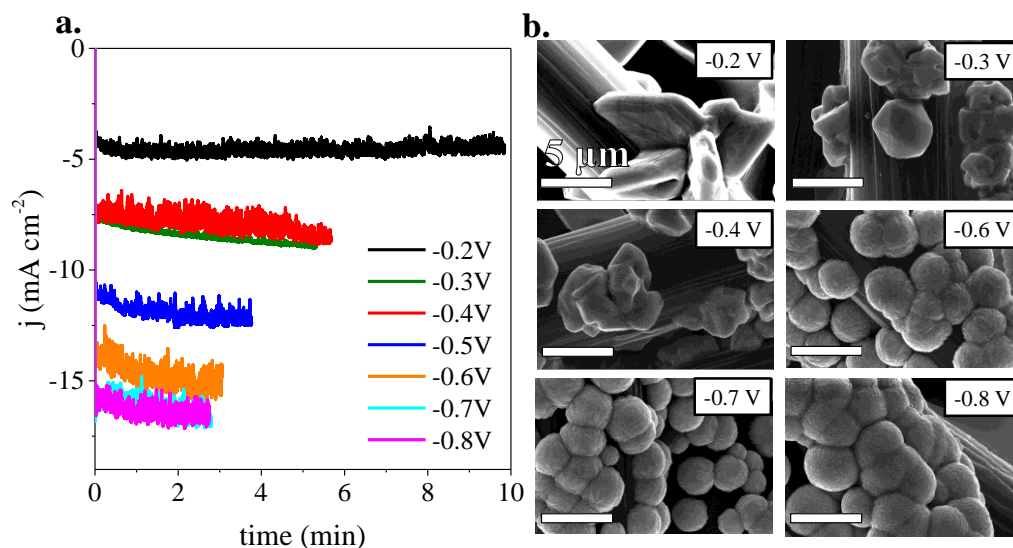


Figure 4-2. (a) Continuous electrodeposition of Cu at different potentials applied as a function of time –chronoamperometry. Total charge per unit area is $2.7 \text{ C}\cdot\text{cm}^{-2}$. In contrast to CV experiments, mild stirring (100 rpm) was applied during plating experiments to improve Cu ion diffusion into the GDE pores by convection. Additionally, N_2 gas was bubbled into the electrolyte beaker to eliminate the O_2 bubbles generated at the counter electrode. (b) FE-SEM images of Cu deposits formed on GDE at the end of the chronoamperometry tests

The current profile was linear for $-0.2 V_{\text{Ag|AgCl}}$ and beyond that potential, current density increased to a certain value and stabilized in 2-minutes; indication of a mass transport limitation expected from the cyclic voltammetry profile (limited current density region beyond $-0.4 V_{\text{Ag|AgCl}}$). At the end of the electrodeposition, Cu-GDE were rinsed with double ionized water ($\text{DI}\text{-H}_2\text{O}$) and dried under N_2 before their morphological analysis with FE-SEM, shown in Figure 4-2(b). At $-0.2 V_{\text{Ag|AgCl}}$, sparsely populated particles formed a rectangular shape with sharper edges. An

earlier study showed that, Cu deposits obtained at lower voltages showed a faceted particle formation indicating that surface diffusion plays a significant role influencing island morphology.¹²⁵ At -0.3 and -0.4 $V_{\text{Ag|AgCl}}$, a granular rocky particles were observed without a specific orientation. At potentials -0.5 $V_{\text{Ag|AgCl}}$ and beyond, the morphology was changed to spherical features forming overlapped nano-particles with populated grain boundaries between each other. These observations indicated that the deposition potential influenced Cu-island formation mechanism. At lower potentials, Cu ions were likely to reduce onto the pre-formed Cu-island by surface diffusion. At higher overvoltage, Cu nucleation and growth on GDE-carbon fibre would be promoted by the availability of higher electron density at the surface, illustrated in Table 4.2.

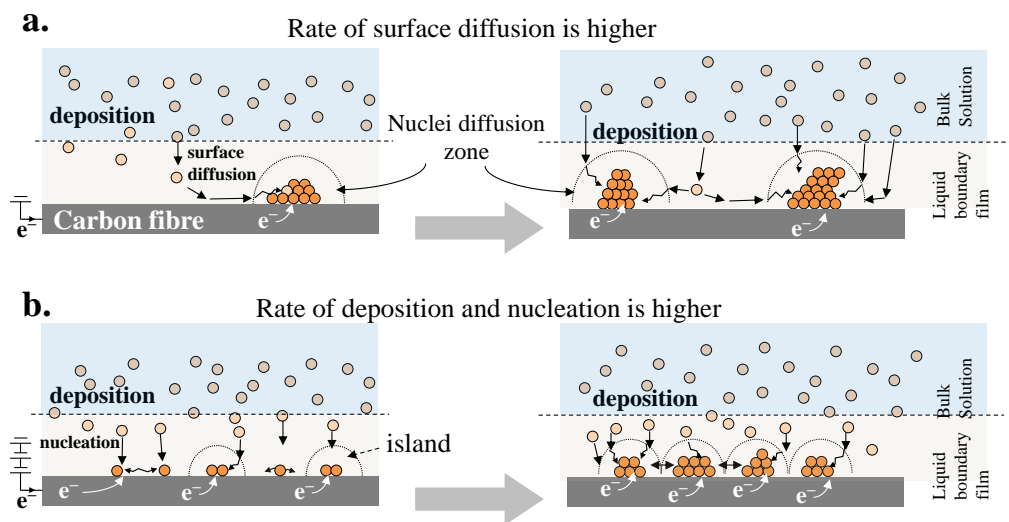


Figure 4-3. Illustration of the nuclei formation and grain growth of the deposits under (a) higher rate of surface diffusion at low deposition potentials and (b) higher rate of nucleation at higher deposition potentials.

To expand further, the growth mode for Cu deposition on carbon fibres followed an island growth mechanism similar to Volmer – Webber island growth which usually occurs in deposition of metals onto foreign substrates¹²⁶. The probability of a Cu ion to be reduced on Cu metal was greater due to the interaction energy between the “Cu-adatoms and the native-Cu” ($E_{\text{Cuads-Cu}}$) being larger than “Cu-adatoms and carbon fibres” ($E_{\text{Cuads-C}}$). For that reason, ($E_{\text{Cuads-Cu}} > E_{\text{Cuads-C}}$), the driving force of Cu-deposition was to segregate on the carbon surface where only sufficient nucleation energy was provided by the local electrons. Hence higher number of Cu-

islands were observed at greater deposition potentials with smaller sizes. In the opposite case ($E_{\text{Cu}_{\text{ads}}-\text{Cu}} < E_{\text{Cu}_{\text{ads}}-\text{C}}$), deposition would form a monolayer of Cu (underpotential deposition) at potentials positive to the equilibrium potential, i.e. observed in Cu deposition on Pt metal ($E_{\text{Cu}_{\text{ads}}-\text{Cu}} < E_{\text{Cu}_{\text{ads}}-\text{Pt}}$).

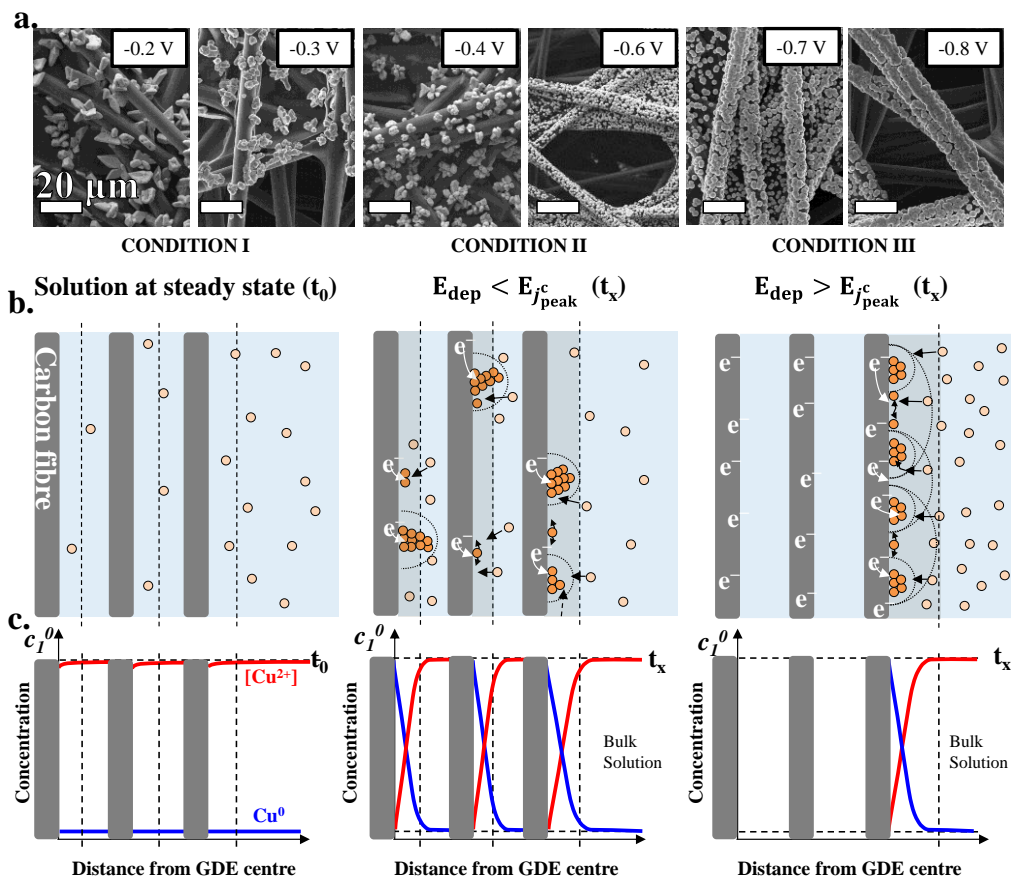


Figure 4-4. (a) Effect of electrodeposition potential on the particle distribution (analysed by FE-SEM) of deposited Cu at potentials from -0.2 to -0.8 $V_{\text{Ag}|_{\text{AgCl}}}$. Solution conditions: 0.16 M CuSO_4 , 0.15 M citric acid and 0.38 M ammonium sulphate; pH 2.1. Copper deposition equivalent to 2.7 $\text{C}\cdot\text{cm}^2$ (b) Schematic presentation of phenomena involved during Cu nucleation and growth on GDE by DE at a potential (E_{dep}) lower or higher than the peak potential ($E_{f_{\text{peak}}}^c$) (c) Representation of the boundary layer on the carbon fibres (dashed line) and concentration gradient of Cu particles between carbon fibre surface and bulk of solution. Red and blue curves represent the concentration gradient of Cu^{2+} ions and Cu adatoms/deposited metal, respectively.

Due to the mismatch between Cu-adatoms and GDE-carbon fibres, surface diffusion led Cu reduction to progress on the pre-formed Cu particles. This resulted in faceted morphology of Cu-islands at lower potentials and a granular island-like morphology at high potentials. In a previous study¹²⁵ with in-situ TEM of Cu deposition showed a change from a faceted particles to circular shaped islands which supports our

present definition. The distribution of Cu particles over a larger area of GDE obtained by CE is given in Figure 4-4(a). At potentials, lower than peak current value (-0.2 , -0.3 and -0.4 V_{Ag|AgCl}), Cu-deposition was governed by the nucleation rate and surface diffusion of the adsorbed ions since there had been sufficient amount of Cu ion to diffuse into GDE openings. Higher voltages (-0.6 , -0.7 and -0.8 V_{Ag|AgCl}) promoted the number of active sites for Cu deposition by local electron density at the carbon fibre surface. Low and high potential deposition conditions of CE were illustrated in Figure 4-4(b-c). The build-up of a diffusion zone at the front layer of GDE readily consume all Cu⁺² ions and generated a concentration gradient along the GDE. These results showed that the increase of deposition potential had a positive effect on nucleation density to obtain smaller and more compact particles. This was confirmed by Radisic et. al.¹²⁵ that Cu-island density increased exponentially for the potentials where deposition was in the diffusion limited regime. To promote smaller Cu particles, it was advantageous to apply higher energy (current or potential). However, CE was not suitable to apply higher potential or current in magnitude during electrodeposition on GDE. Because only front side of GDE was covered with Cu due to the concentration gradient and an extra effort would be required to control the particle size difference between the front site and inside of the GDE. Particularly, carbon fibre based GDE have >75 % porosity and the geometrical size of the electrode had relatively large area (geometrical area $\geq 6.9 \times 2$ cm²) contrary to the electrode size often used in the literature (≤ 1 cm²). Our aim was to increase electrode/electrolyte superficial contact area as much as possible in ECf-cell to react all the gaseous CO₂ entering to the cathode chamber and accumulate higher amount of CO₂RR product. Therefore, a full deposit coverage around the carbon fibres of a large GDE was essential while preserving the morphology, distribution and catalytic property of Cu deposit. To make complete use of GDE porosity and to activate these sites with Cu catalyst, we have conducted pulsed current electrodeposition (PCE) technique which is explained in the following section.

4.2.2 Pulsed current electrodeposition of copper

Compared to conventional deposition methods, pulsed current electrodeposition (PCE) has received great interest in electronics field for its feature filling capability i.e. for filling trenches and paths of silicon interconnectors and in automotive sector

for enhanced uniformity at complex three-dimensional parts with improved hardness i.e. engine components¹²⁷.

Table 4.3. Experimental data of the selected literature with pulsed current electrodeposition of Cu for CO₂RR

Year & Author	Method ‡	Parameters †			CO ₂ RR	Ref.
2016 Ren et. al.	PRC	$j_{(1)} = -5.8$ $j_{(2)} = 2.9$	$t_{(1)} = 0.1$ $t_{(2)} = 0.1$	50% duty 600 s	n-propanol 10.8 %	128
2016 Chung et. al.	SPC	$j_{(1)} = -2.0$ $j_{(2)} = -30$	$t_{(1)} = 0.25$ $t_{(2)} = 0.05$	16% duty 5 h	formic acid 28.6 %	129
2015 Chen et. al.	PRC	$j_{(1)} = -4.9$ $j_{(2)} = 2.4$	$t_{(1)} = 0.1$ $t_{(2)} = 0.1$	50% duty 3000 cycles	ethylene ≈15 %	52

† j in mA·cm⁻² and t in seconds.

‡ PRC and SPC stands for pulsed reversed current and superimposed pulsed current electrodeposition, respectively.

Herein, the plating parameters had a strong influence on the nanostructure of the deposit which would determine its physical and chemical property, e.g. hardness, conductivity or chemical stability. Recent studies of nanostructured Cu deposits formed by PCE technique was applied for catalysis of CO₂RR and gave promising results by varying deposition parameters, given in Table 4.3. The end-products vary between the studies but the conclusion of the authors was mainly focused towards the influence of defects sites formed by PCE.

Usually in PCE tests, j_{ON} is fixed and t_{ON}/t_{OFF} ratio can be altered. In this work, t_{ON} was fixed and j_{ON}/t_{OFF} was altered. As indicated previously, high current pulses were targeted for PCE tests because CE showed that a high energy (in the form of potential) would increase the nucleation rate and promote a smaller particle size. For that reason, higher current densities were set at t_{ON} period to achieve a higher nucleation rate. Simultaneously, t_{OFF} period was altered to keep j_{AVG} same for each sample (-4.35 mA·cm⁻²). Figure 4-5 shows the fixed t_{ON} as 0.02 seconds and the change in t_{OFF} amongst values of 0.25, 0.5, 1 and 2 seconds, giving duty cycles of 7, 4, 2 and 1 %, respectively. From these figures, it was observed that the size of Cu particles decreased at lower duty cycles. Because j_{ON} was increased during fixed t_{ON} for each sample, t_{OFF} time had to be adjusted. Thus, the increment of j_{ON} value resulted in larger potentials and promoted an increment of nucleation sites for copper.

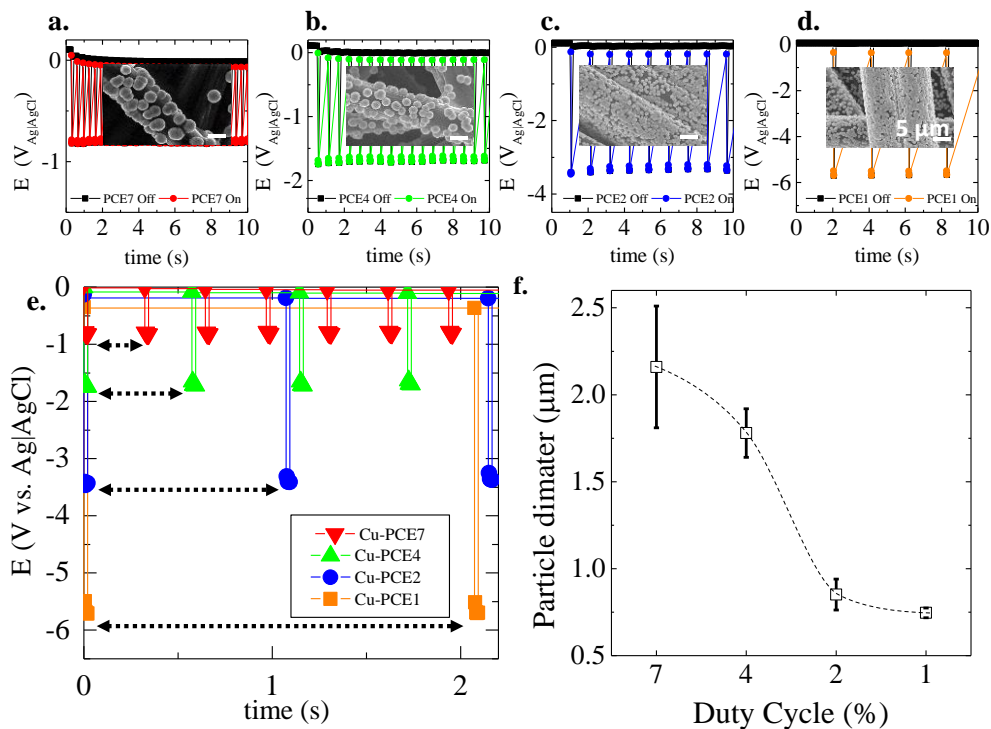


Figure 4-5. (a – b) Potential vs. time plot of the pulsed electrodeposition of copper at different duty cycles; 7, 4, 2 and 1 % respectively. The in-set picture is FE-SEM of a carbon fibre decorated with Cu-islands. (e) Potential vs. time plots of PD are overlapped in a single graph to highlight the increment of relaxation time, t_{OFF} in accordance to deposition potential driven by peak current density during t_{ON} period. (f) Particle diameter plotted as a function of duty cycle applied during pulsed electrodeposition. The effect of duty cycle shows an exponential profile on the Cu-island diameter.

PCE to obtain nanostructures would be associated with two important factors: (i) “nucleation rate” triggered by current density and (ii) the crystal growth affected by inhibiting molecules of the electrolyte¹³⁰. High rate of Cu deposition could be achieved by depleting all Cu^{+2} ions in t_{ON} period with a very high current which will be compensated in the following t_{OFF} period with bulk diffusion to the vicinity of the carbon fibres. This depends on the capacity of the pulse to give an effective diffusion layer which follows the micro-profile of the surface so closely that the resulting deposits could be regular and evenly distributed¹³¹. The microscopic investigation of the top layer and cross-section of Cu-PCE have shown a very good accordance to this behaviour. Figure 4-6 (a) shows FE-SEM images from the top and cross-section of GDEs. Their particle size distribution was calculated from over 200 particles collected from images taken from four different sites including the cross-section images.

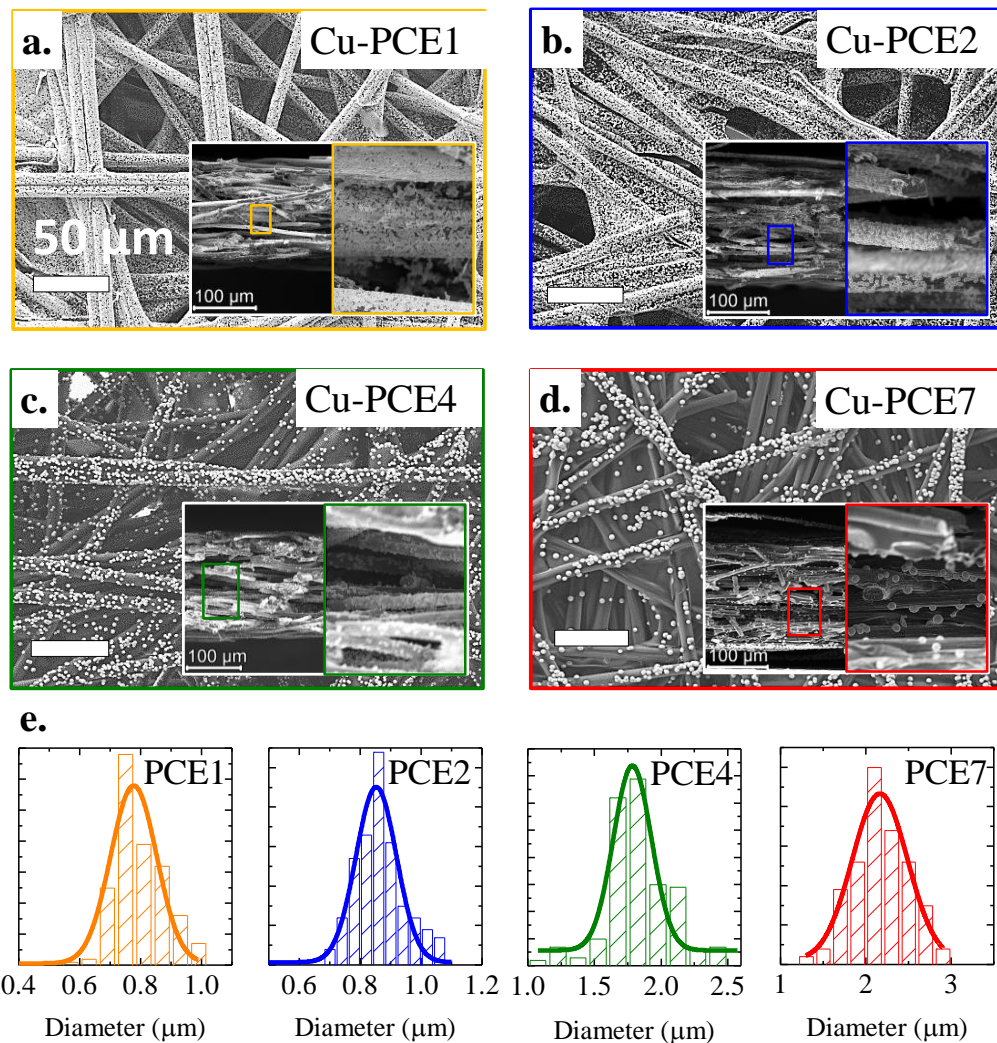


Figure 4-6. (a-d) FE-SEM images of copper deposit formed on carbon fibres at 1, 2, 4 and 7% duty cycle, respectively (all scale bars are 50 μm); (e) Particle size distribution calculated from FE-SEM images.

The mean radius of spherical Cu-islands decrease nearly three times, from 2.16 μm to 740 nm, when a larger current in amplitude was applied. (The calculations of Image-J graphic analysis were given in Annex 4.1). The morphology of Cu deposits followed Volmer – Webber island growth mechanism similar to the deposits in CE method. Conversely, it became possible to control the diameter and obtain a narrow particle size distribution of Cu islands throughout GDE. The particles at the front site of GDE were in the same size as the deposits formed in the interior porous sites. This also validates that a homogenous Cu catalyst distribution was achieved with PCE method exempt of concentration gradient limitation contrary to CE. Corresponding schematic presentation of the phenomena during PCE and the

boundary condition adjacent to the carbon fibre surface was illustrated in Figure 4-7. There were three different stages of PCE: steady state (I), pulsed (II) and relaxation period (III). At the beginning of electroreduction (Condition I), the electrolyte solution was at steady state having a constant concentration profile along GDE. When the electrode potential was driven to values below Cu²⁺/Cu redox potential, the number of Cu atoms deposited on the carbon fibre surface was a function of Cu²⁺ concentration available for adsorption and ability to form a nucleation centre. CE method showed that only front surface of GDE was covered, while the rest of the GDE stay intact –Figure 4-4. This region would be inert towards CO₂RR and prone to H₂ evolution reaction (HER). The catalytic activity of CO₂RR on Cu-CE and Cu-PCE samples were studied in the next section to investigate this claim.

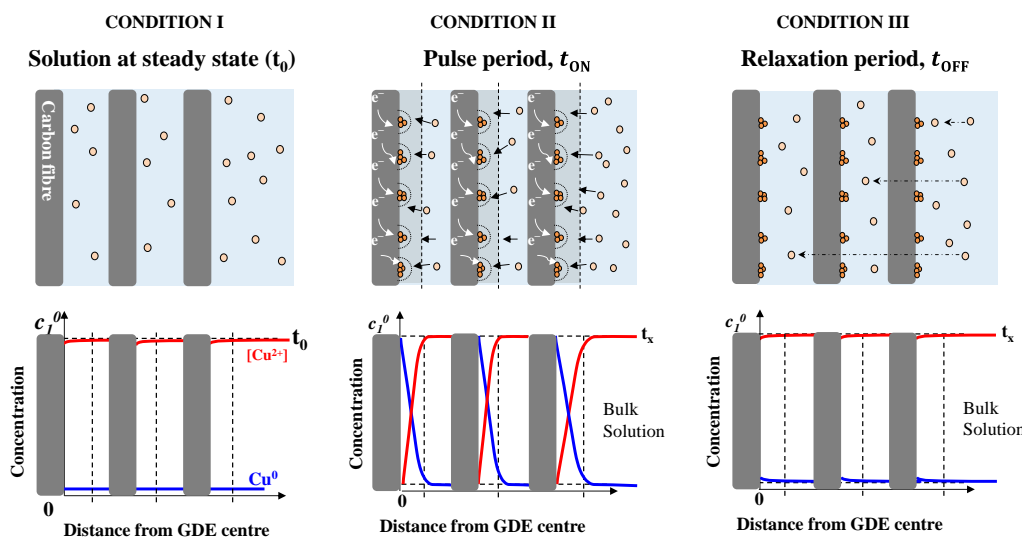


Figure 4-7. Schematic illustration of the phenomena during steady state, ON and OFF states and corresponding boundary condition between carbon fibre surface and bulk of the solution.

4.2.3 Effect of electrodeposition in CO₂RR

The effect of Cu-island morphology and distribution on CO₂RR was investigated in an ECf-cell operating with continuous gas and liquid flow. 0.1 M KHCO₃ was circulated at 10 ml·min⁻¹ and CO₂ gas flow was set to 2 ml·min⁻¹ for all the experiments to obtain a smooth flow through GDE geometric area (2 cm²). Figure 4-8(a-b) shows that the major products of CO₂RR at $-1.0 V_{RHE}$ on Cu-CE and Cu-PCEs were both CO and HCOO⁻ with a small contribution of higher carbon derivatives (C₂H₄ and CH₄), consistent with the results reported in the literature¹²⁴,

¹³². Cu-CE produced between 5 – 10.6 % HCOO⁻ faradaic efficiency at the end of 2-hour electrolysis. Nearly 15 % CO faradaic conversion was obtained at -0.8 V_{RHE} with increasing selectivity to ethylene (C₂H₄) at higher potentials, in a similar trend with the findings of Hori et. al.⁴⁸. Cu-PCEs provided nearly three times higher faradaic efficiency for CO and HCOO⁻ compared to Cu-CE at -1.0 V_{RHE}. This increment of CO₂RR products could be related to suppression of H₂ as a result of improved coverage carbon fibres prone to HER.

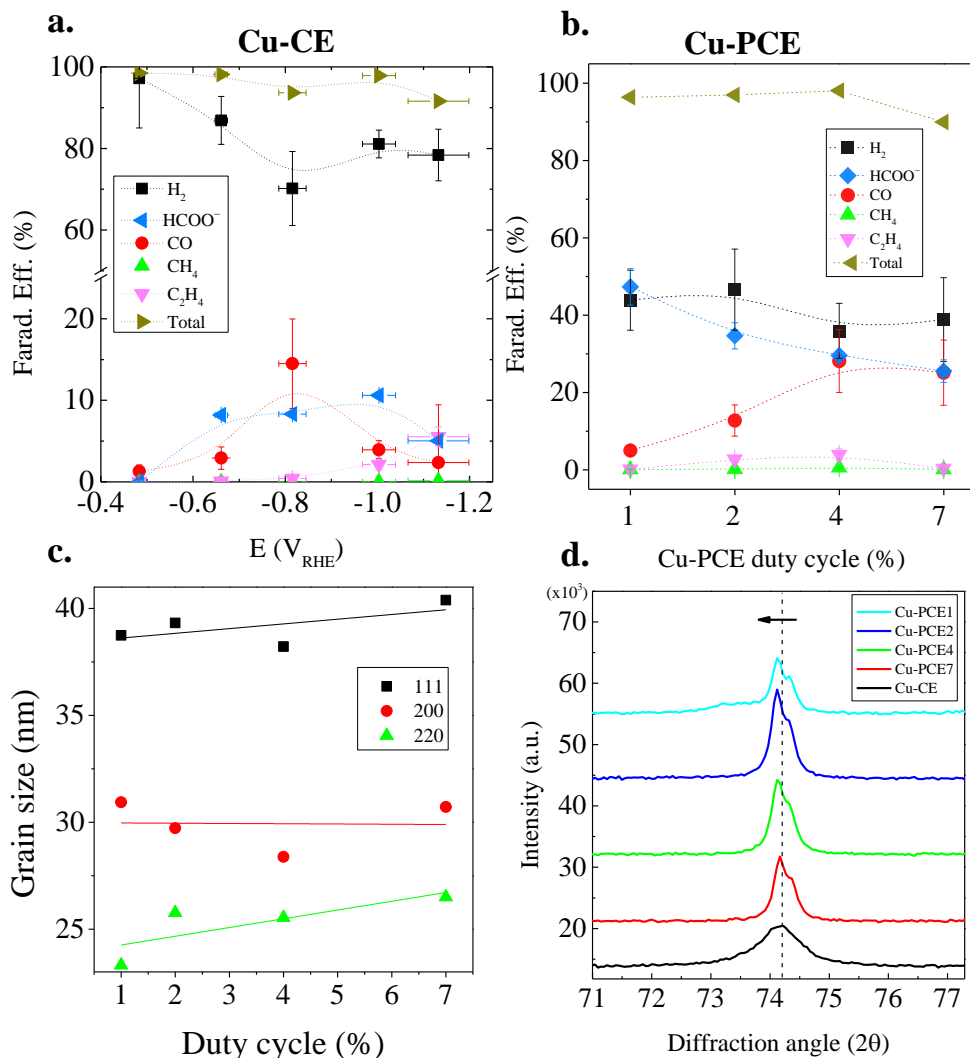


Figure 4-8. Faradaic efficiency of CO₂RR products for **(a)** Cu-CE samples tested at different potentials and **(b)** Cu-PCE tested at -1.0 V_{RHE} during 2 hours with 0.1M KHCO₃ electrolyte flow at 10 ml·min⁻¹ and 2 ml·min⁻¹ CO₂ gas bubbling through GDE **(d)** X-ray diffraction patterns (220-reflections) of Cu-CE and Cu-PCE samples.

Between Cu-PCE samples, higher selectivity towards HCOO⁻ production was also observed with smaller and more compact Cu-islands formed at smaller duty cycles.

Grain size of deposits were calculated from their X-ray diffraction peaks according to Scherrer equation¹³³

$$D_{hkl} = K \cdot \lambda / (B_{hkl} \cdot \cos \theta) \quad (4.8)$$

where “ D_{hkl} ” is the crystallite size in the direction perpendicular to the lattice planes, “hkl” are the Miller indices of the planes being analysed, “K” is a numerical factor frequently referred to as the crystallite-shape factor, “ λ ” is the wavelength of the X-rays, “ B_{hkl} ”, is the width (full-width at half-maximum) of the X-ray diffraction peak in radians and “ θ ” is the Bragg angle. Cu-PCE electrodes with smaller duty cycles had small and well-defined grains ranging from 25 to 40 nm ($220 < 200 < 111$). Peak shift was observed in lower duty cycles, noticeable in 220 crystallites. The most typical diffraction peak aberrations are shifts, broadening and asymmetries which occur due to the dislocations, stacking fault, twinning and grain boundaries, commonly known as strain sources¹³⁴. Stacking faults and twin boundaries primarily cause lattice parameter changes or shifts of Bragg reflection. This was the first evidence for creation of defect sites active towards CO₂ molecule. Previous studies in the literature has also confirmed the effect defect sites and surface roughness on CO₂RR. Sen et. al.¹²⁴ obtained nearly 40% formic acid, 5% CO and around 1.5% C₂H₄ by electrochemical reduction of CO₂ at moderate overpotentials with Cu-foams having hierarchical porosity. Li et. al.¹³⁵ prepared Cu₂O layers on Cu foil electrodes correlating high HCOO⁻ (38.8 %) and CO (41.4%) faradaic efficiency to active surface area distinct from the structures of high index facets.^{49a} The increment of overall CO₂ faradaic efficiency (CO+HCOO⁻) with PCE method might be linked to the nanocrystalline geometry with defect sites. Those high coordination sites such as grain and twin boundaries were invoked as catalytic sites for CO₂ absorption¹³⁶. These results may confirm that increased density of defect sites would be able to lower those barriers by their stronger adsorption energies.

In this line, HCOO⁻ selectivity vs. CO between different incremental duty cycles suggested that Cu-island size and its GDE coverage might play a critical role on the reaction pathway of CO₂. A model was developed from the area vs. perimeter calculations obtained from FE-SEM images of the samples given in Annex 3 and 4. The initial observation to support this phenomenon is presented in Figure 4-9(a). At first, it is important to mention that the first step in electrochemical reduction of

CO_2 is to form $\text{CO}_2^{\bullet-}$ radical which occurs at more negative voltages than the onset potential of CO_2 reduction¹¹⁰ which explains the requirement of a moderate potential. The electrocatalytic reaction concerning HCOO^- showed a dependence to the Cu-island perimeter. Conversely, CO selectivity was increased when the Cu-island surface was superior to its perimeter. Hence, a significant insight into this catalytic process could be outlined that two sites of the catalyst play a different role in CO_2RR . First, importance of the perimeter of Cu-islands for the catalyst process of HCOO^- would be the triple phase points where CO_2 -electron-proton would meet each other. Secondly, in respect to catalyst processes for CO and H_2 production from CO_2 and H_2O molecules, respectively, there might be a competition for an available active site. The importance of Cu-islands area for this behavior still needs further study to fully understand its origin. Nevertheless, Cu-CE samples showed that a large portion of current density spent for H_2 evolution where uncovered carbon fibers in those samples were the active site for HER.

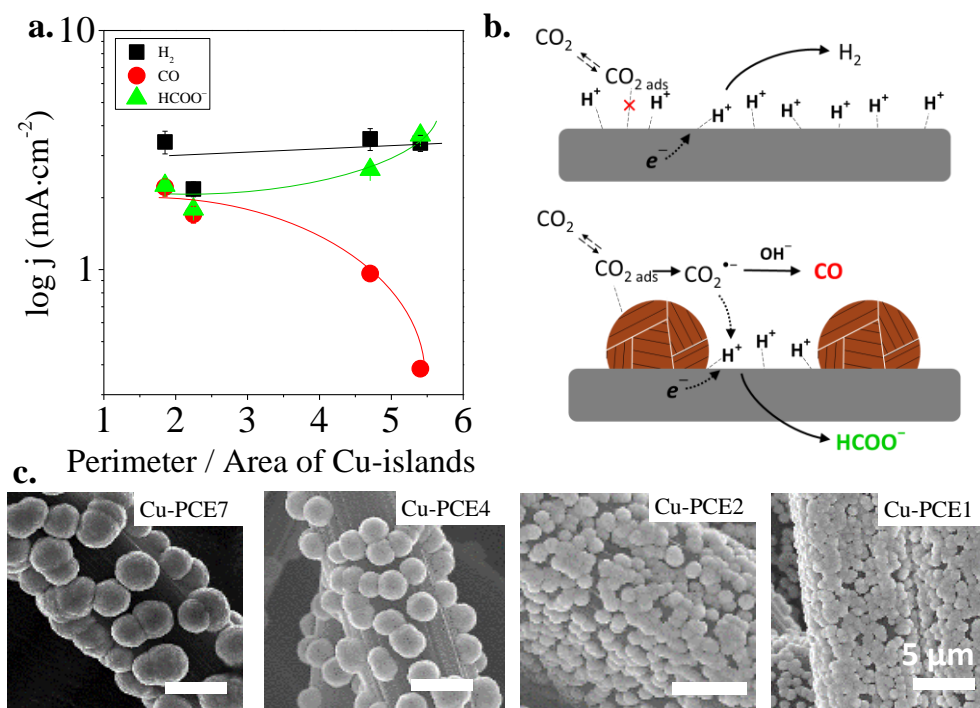


Figure 4-9 Faradaic efficiency of formate (a) and carbon monoxide (b) as a function of Cu-island diameter, and related pathways occurring on PCE1 and PCE7 for CO_2RR (c) through formate (F) intermediate and (d) carboxyl (C) intermediate

Meanwhile, well-covered carbon fibers richer in Cu-surface in Cu-PCE samples might be the evidence of active sites for CO . The theoretical calculations on $\text{CO}_2^{\bullet-}$

radical by several authors^{34b} showed that 84.3 % of unpaired electron occupancy would be on “C” site which influence the next reaction as the active site. The two possible pathways following this step are “C” site reacts with the surface of the catalyst as a proton attack on the “O” site prior to electron uptake to give CO and H₂O, or “C” site undergoes through a proton-coupled-electron-transfer mechanism towards HCOO⁻ pathway^{46g} as illustrated in Figure 4-9(b).

Moreover, traces amount of CH₄ and C₂H₄ was detected by gas chromatography. For higher hydrocarbons, residence and re-coordination period would be required for proton-coupled-electron-transfer (or dimerization). At this point, the effect of the dynamic flow on the reaction pathway must be considered. The earlier studies by Frese et. al. and Hori et. al.⁴⁸ showed that when the electrolyte was stirred, the weakly adsorbed CO desorbed easily from the surface giving higher CO % faradaic efficiency. at ambient conditions. Similarly, experiments of Sakata et. al.¹³⁷ affirmed enhanced yield of CO (30.4%) and HCOOH (43.8%) with stirring the solution, while trace amount of CO and 6.2% HCOO was obtained without stirring. As evidenced in the product results of Cu-CE and Cu-PCE, the amount of CO gas was clearly larger than C₂H₄ or CH₄. The formation of those hydrocarbons were the following pathways of CO with the additional proton and electron uptake or chemical dimerization step of CHO* proposed by several groups^{46b, 46c}. However, the continuous flow of gas (2 ml·min⁻¹) and liquid (10 ml·min⁻¹) phases might render this pathway at $-1.0 V_{RHE}$, giving higher FE % CO via improved CO desorption from the surface. In our previous work with Sn-GDEs, we found that the flow rate of the gas and liquid affected the residency time of the intermediate species and modified the reaction rate for HCOO⁻ production from CO₂RR. Our experimental observations in accordance with the previous results confirmed that mid-products of CO₂RR could be more liable to desorb under the influence of dynamic conditions, as was compatible with the moderate adsorption of CO on the electrode surface^{34d}. Consequently, flux of gas (CO₂) and electrolyte (0.1 M KHCO₃) may also be a factor to determine the product selectivity.

4.2.4 Feasibility of formate production

The increasing selectivity towards HCOO⁻ (PCE 4% < PCE 2% < PCE 1%) drastically reflected on their HCOO⁻ partial current density. Cu-CE exhibited a Tafel

plot value of $165 \text{ mV}\cdot\text{dec}^{-1}$ in accordance with the recent reports on CO_2RR with Cu metal given in Figure 4-10(a). Amongst the literature results, electrode selectivity usually shifted to a mixture of C_2 -hydrocarbons and H_2 at higher potentials which leads to an extra separation cost, impairing product value. In this study, the flow cell design enabled us to operate at larger currents without a compromise of extreme polarisation losses unlike conventional H-shaped electrochemical cells.

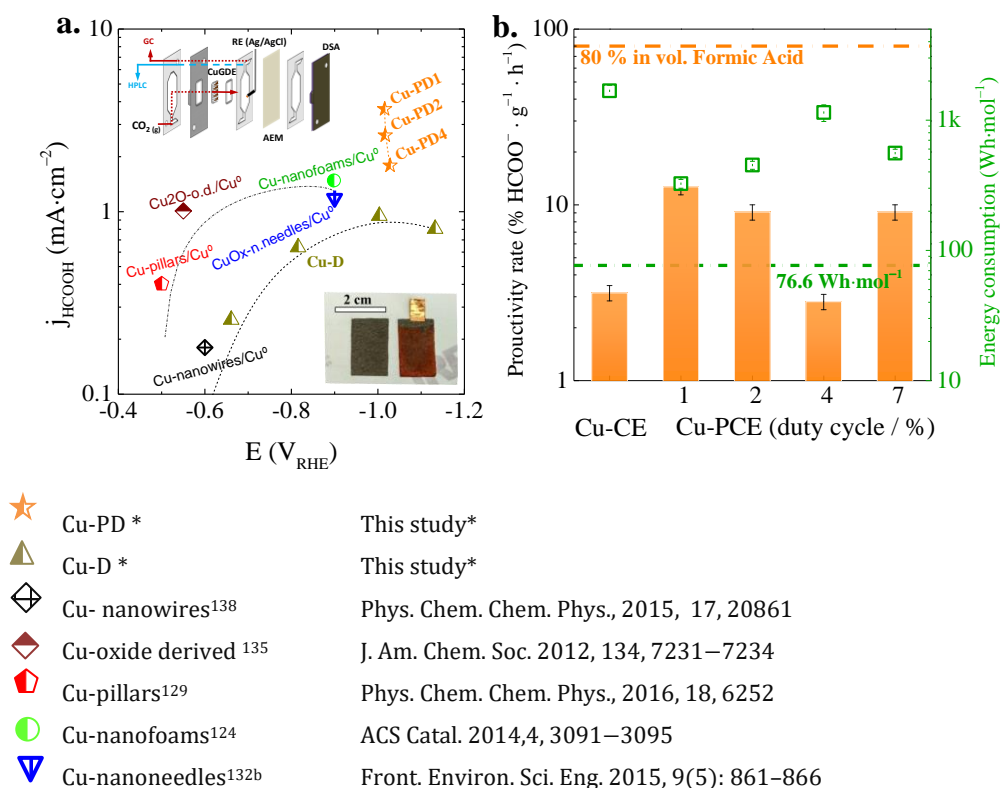


Figure 4-10. (a) Schematic illustration of the continuous electrochemical flow cell with the individual stacks of the cathode, membrane and anode parts are displayed from left to right, (RE: Reference Electrode, AEM: Anion Exchange Membrane, DSA: Dimensionally Stable Anode) (b) Digital image of pristine GDE and Cu-PCE1 sample (scale bar length is 20 mm). (c) The comparison of partial current density of HCOO^- (formate) obtained from this work vs. state-of-the-art for Cu-modified catalyst electrodes to reduce CO_2 into formate, 0.1M KHCO_3 (d) Amount of formate concentration accumulated at the catholyte per hour and same data taking into account the Cu-loading on GDE on the left axis. The dashed line corresponds to 80 % in vol. formate concentration. The right axis is the energy cost per hour for one mole of formate and dashed green line represents formic acid formation energy; $76.6 \text{ Wh}\cdot\text{mol}^{-1}$.

Eventually a higher current density increased the product rate and the final product concentration inside the beaker (catholyte compartment). Cu-PCE obtained with 1 % of duty cycle delivered $\sim 3.6 \text{ mA}\cdot\text{cm}^{-2}$ partial current density for HCOO^- at an expense of around $\sim 0.8 \text{ V}$ of overvoltage (2.6 and $1.8 \text{ mA}\cdot\text{cm}^{-2}$ for 2 and 4 % duty cycle, respectively).

The industrial realization of photoelectrochemical CO₂ conversion (artificial photosynthesis) demands high rate product formation as long as the selectivity is met. Once the side reactions (e.g. H₂ evolution and higher carbon production) was restrained as tackled here by an effective GDE coverage and particle control, the second objective was to raise the formate concentration. The product feasibility would be achieved if formate purity is near 80 % inside the beaker. Figure 4-10(b) shows the CO₂RR performance of Cu-PCE samples at $-1.0 V_{RHE}$ where the final concentration of HCOO⁻ was given (i) in unit time (hours) and (ii) per Cu-catalyst loading (grams) calculated according to Eq. (4.9)

$$\text{Productivity rate HCOO}^- = \frac{\left(\frac{\text{mol HCOO}^- \times \text{MW}_{\text{HCOO}^-}}{\rho_{\text{HCOO}^-} \times L_{\text{Ely.}}} \right)}{t \times m_{\text{Cu}}} \quad (4.9)$$

where MW is the molecular weight of formate, “ ρ ” is the density of formate, and L is the catholyte volume in the beaker. “t” is the time spent during electrolysis and m is the catalyst loading on GDE. Accordingly, the highest HCOO⁻ concentration reached was 0.02 % HCOO⁻·h⁻¹ and 12.6 % HCOO⁻·h⁻¹·g_{Cat}⁻¹ for Cu-PCE1 electrode. This value could be increased by higher current densities attained from a larger ratio of electrode-to-electrolyte superficial area. The effect of the catalyst loading was also a significant parameter since only 0.95 mg·cm² of catalyst was deposited on the GDE. Considering the unit price and toxicity of other catalyst that offer higher formate efficiency, such as In and Hg or Pb, our PCE method re-designing Cu metal seems to be a feasible and sustainable alternative. The cost of energy spent for HCOO⁻ production was calculated from the multiplication of cell voltage (in volts) with the amount of charge (in coulombs) passed from the cell (watts per hour, Wh).

$$\text{Energy} = V_{\text{CELL}} \times Q = V_{\text{CELL}} \times (I \times t) \quad (4.10)$$

The molar amount of formate measured by UV-Vis and NMR analysis was divided to that total energy.

$$\text{Cost of HCOO}^- = \frac{V_{\text{CELL}} \times I \times t}{\text{mol of HCOO}^-} \left(\frac{\text{Wh}}{\text{mol}} \right) \quad (4.11)$$

Only the energy spent on the full cell was taken into consideration, neglecting the energy consumption of the liquid pump and gas flow controller. The energy requirement between the samples were slightly different due to the small variations in their current density during 2 hour CO₂ electrolysis. Therefore, we normalized the product yield in terms of Wh per mole of HCOO⁻. As we discussed earlier in

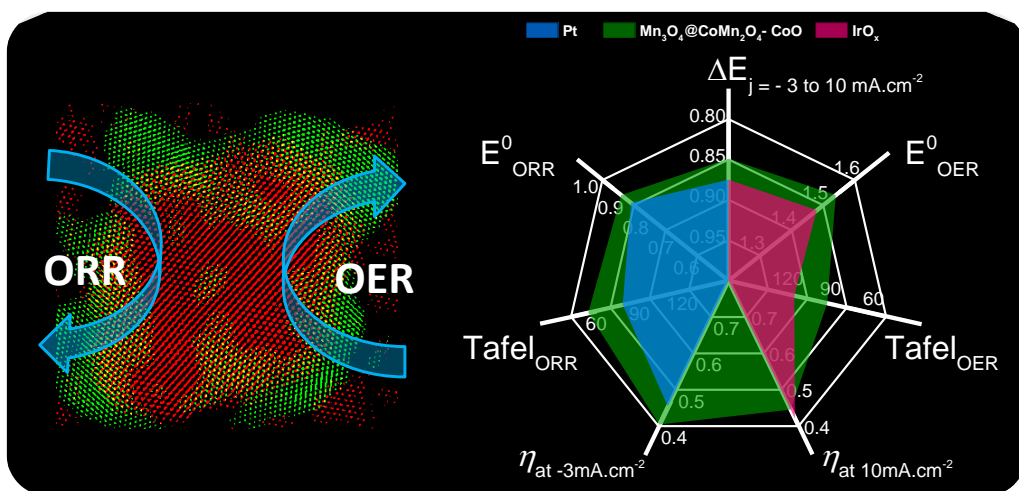
Chapter 3, we would set 100% process energy efficiency to formic acid formation energy; $70.7 \text{ Wh}\cdot\text{mol}^{-1}$. The lowest cost of formate production was with Cu-PCE1 electrode, $325 \text{ Wh}\cdot\text{mol}^{-1}$. This corresponds to 21.7 % energy efficiency towards CO_2 conversion to HCOO^- which is 5 times higher than the value (4.2%) obtained with Cu-CE.

4.3 Conclusion

The mechanism of continuous (CE) and pulsed-current electrodeposition (PCE) of Cu from a citric-sulphate based electrolyte was explained. The rest period (t_{OFF}) during PCE improved Cu ion diffusion to GDE pore openings resulting in an evenly distributed catalyst throughout carbon fibres with nearly three times smaller Cu-island deposits. CO_2RR tests revealed a morphology dependent selectivity between HCOO^- and CO for PCE samples. Smaller Cu-island deposits gave rise to a higher perimeter/area ratio favouring HCOO^- corresponding to 47 % Faradaic efficiency. There was a competition between CO and H_2 on Cu-island area. CO was promoted with coarser Cu-islands presumably facilitating OH^- uptake to form CO product – 28 % at a moderate potential where C_2H_4 and CH_4 were below 5 %. CO selectivity over C_2H_4 and CH_4 was correlated to improved desorption of CO under dynamic conditions of ECf-cell. Those results would suggest that it is crucial to evaluate the catalytic performance of CO_2RR in an industrial electrochemical flow cell which may affect the final product amount significantly.

CHAPTER 5

Dark-OER: Co-Mn oxide NP in ECf-cell



This chapter focuses on use of cobalt doped manganese oxide ($\text{Co-Mn}_3\text{O}_4$) nanoparticles as an alternative catalyst to replace dimensionally stable anode (DSA) for oxygen evolution reaction in our electrochemical flow cell. Two different nanoparticles were the main candidates; core/shell $\text{Mn}_3\text{O}_4@\text{CoMn}_2\text{O}_4$ and heterostructured $\text{Mn}_3\text{O}_4@\text{CoMn}_2\text{O}_4\text{-Co}_x\text{O}_y$. Initial characterization of their electrochemical performance was performed with rotating disk electrode (RDE) measurements. Heterostructured NPs with Co:Mn molar ratio of 1 (MC1), outperformed platinum (Pt) catalyst in oxygen reduction reaction (ORR) and iridium oxide (IrO_2) catalyst in oxygen evolution reaction (OER) in RDE experiments. Therefore, a catalyst ink of “MC1: Nafion: Vulcan Carbon” was immobilized on carbon fibre substrate (CFS). MC1-CFS can deliver a current density of $10 \text{ mA}\cdot\text{cm}^{-2}$ at $1.9 \text{ V}_{\text{RHE}}$ in 0.1 M KOH solution, which is similar in comparison to DSA electrode. 70% current retention in 1 hour under $10 \text{ mL}\cdot\text{min}^{-1}$ flow of 0.1 M KOH was correlated to de-attachment of nanoparticles from CFS under electrolyte flow.

5.1 Experimental Remarks

The anode (counter electrode) in experiments of Chapter 3 and 4 were performed with a state-of-the-art DSA; a commercial electrode formed by Ta₂O₅-IrO₂ immobilized on Ti-plate. This anode plate was custom design electrode by the cell manufacturer (Micro Flow Cell, Electrocell A/S) aligning with the gaskets and Teflon frames at the anodic compartment of ECf-cell assembly. DSA is a flat electrode limiting the full function of an electrochemical flow cell so we aimed to use a CFS loaded with an earth-abundant OER catalyst. The initial choice of this catalyst was from one of the nature's design in water splitting reaction. In some higher plants and bacteria^{18a} OER occurs in the oxygen-evolving complex of photosystem II (PS II) in the form of Mn₄CaO₅ complex. This Mn-based cluster is responsible for the catalytic water splitting reaction with different oxidation states and molecular binding features. In view of that, Co doping of Mn₃O₄ could create mixed oxide states of manganese (MC_x-NPs) by using different molar ratio of Co/Mn ($0 < x < 4$). A set of catalyst with different loadings and oxidation states could provide insight for ORR/OER mechanisms.

Mn-Co based nanoparticles were obtained from Andreu Cabot group. The electrochemical tests and characterization of nanoparticles were performed in our group. At first, MC_x-NPs was immobilized on a carbon fibre substrate to evaluate their oxygen reduction and evolution reaction (ORR and OER) catalytic properties against benchmark catalysts, Pt and IrO₂. A large focus was devoted to ORR to understand the kinetic properties of the catalyst, since common intermediates can play a key role for both OER and ORR. For example, surface adsorbed peroxide (HO₂⁻_{ads}) is an intermediate which has an oxidative property that can result oxidation of the catalyst and carbon support leading to their corrosion and dissolution.

After initial RDE test, NP catalyst with highest OER activity was selected and immobilized on CFS by spin coating to be tested as anode in EC-flow cell. The water splitting tests in EC-flow cell were conducted under both static (no electrolyte flow) and dynamic mode (electrolyte flow at 10 mL·min⁻¹).

5.2 Results and Discussion

5.2.1 Effect of cobalt (II) chloride precursor: MC1-Cl NPs

The synthesis of partial cation exchange is explained in Figure 2-3 in Chapter 2. Figure 5-1(a-b) shows transmission electron microscopy (TEM) micrographs of the initial Mn_3O_4 produced in the 1st step and MC1-Cl that produced after adding an equivalent molar amount of CoCl_2 in the 2nd step ($[\text{Co}]/[\text{Mn}]=1$; MC1-Cl).

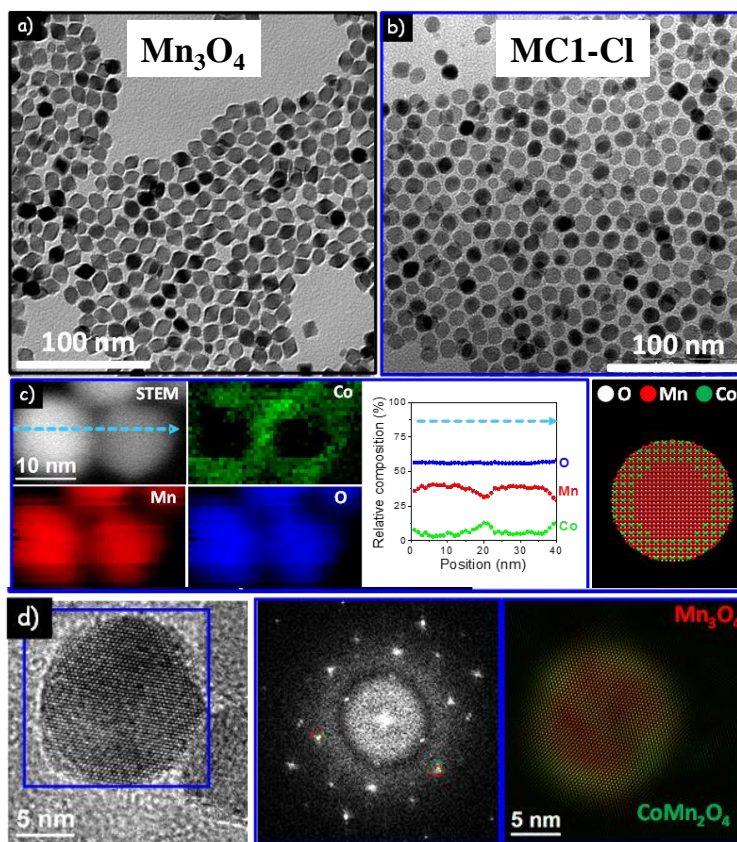


Figure 5-1. (a-b) TEM micrographs of Mn_3O_4 NPs (a) and MC1-Cl NPs (b). (c) ADF-STEM image and EELS elemental mapping of MC1-Cl NPs and compositional line profile of Mn, Co and O elements recorded along the blue arrow in the STEM images. (d) HRTEM micrograph of a MC1-Cl NP, power spectra of the blue squared region and colourful structural map showing the distribution of Mn_3O_4 (red) and CoMn_2O_4 (green) phases.

Upon Co addition, the initial octahedral-shaped Mn_3O_4 NPs were slightly rounded without undergoing significant growth even for $[\text{Co}]/[\text{Mn}]$ ratios up to 5. Annular dark field scanning TEM (ADF-STEM) in combination with electron energy loss spectroscopy (EELS) showed a core-shell type Co and Mn distribution with core and shell compositions compatible with Mn_3O_4 and CoMn_2O_4 stoichiometry – Figure 5-1(c-d). All Co concentrations with $[\text{Co}]/[\text{Mn}]$ ratios above one resulted in core-

shell type structures with similar shell thickness. High resolution TEM (HRTEM) analysis showed Bragg reflections from two body centred tetragonal Mn_3O_4 phases (space group = $I4_1/amd$) with close lattice parameters. Upon filtering, a crystallographic epitaxial core-shell distribution was preserved.

5.2.2 Effect of cobalt (II) perchlorate precursor: MCx NPs

Mn_3O_4 produced in the 1st step as explained previously and MCx was produced after adding an equivalent molar amount of cobalt perchlorate ($\text{Co}(\text{ClO}_4)_2 \cdot 6\text{H}_2\text{O}$) instead of chloride CoCl_2 in the 2nd step.

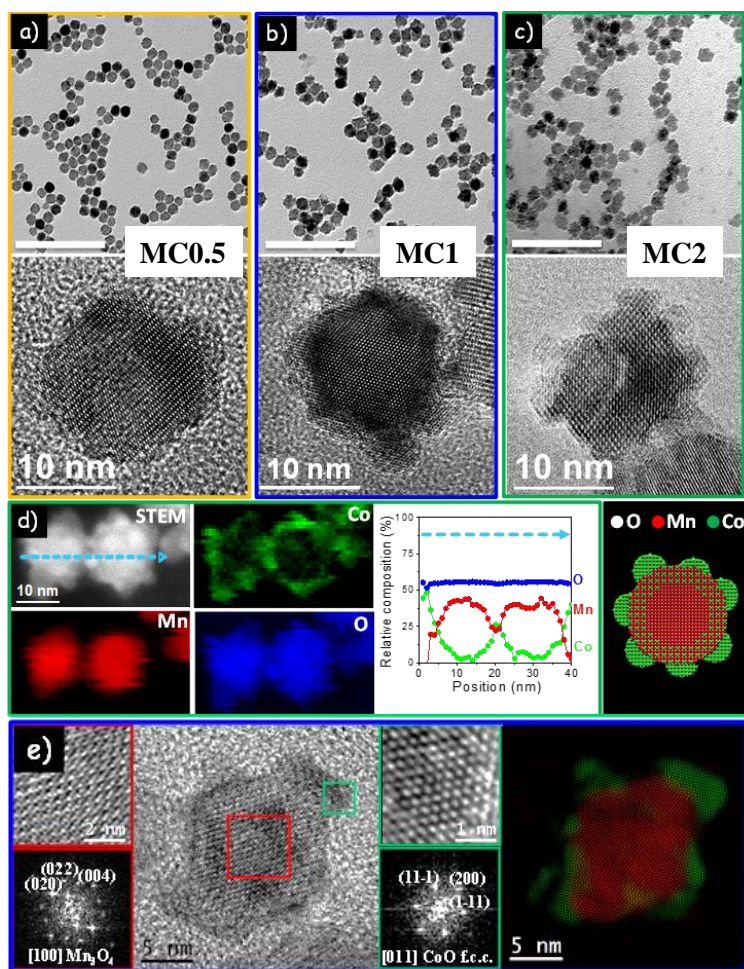


Figure 5-2. (a-c) HRTEM micrographs of MC0.5 (a), MC1 (b) and MC2 (c) NPs. TEM (scale bar = 100 nm) (d) ADF-STEM image and EELS elemental mapping of MC2 NPs and compositional line profile of Mn, Co and O elements recorded along the arrow in the STEM image. (e) HRTEM micrographs of a MC1 NP, details of the red and green squared regions with the corresponding power spectra, and colourful structural map showing the distribution of body centered tetragonal Mn_3O_4 (red) and face centered cubic CoO (green) phases.

This led to MC_x-NPs ($0 < x < 2$) with rougher surfaces shown in Figure 5-2 (a-c). Upon Co(ClO₄)₂ addition, a clear increase of the NP size was observed, with a final diameter depending on the amount of Co precursor used; 12.5, 13.5 and 15 nm for MC0.5, MC1 and MC2, respectively. In Figure 5-2 (d-e), HRTEM and EELS mapping displayed a clear core-shell type element distribution with a central core phase and composition consistent with Mn₃O₄ and a Co-rich shell. At the NP surface, several crystallites with a CoO phase were evidenced –Figure 5-2 (e). Figure 5-3 illustrates the particle formation mechanism concluded from the structural and chemical characterization. Both Co precursors tested (Co-chloride and Co-perchlorate), a partial cation exchange between Mn and Co takes place at the outer surfaces of Mn₃O₄ to form a CoMn₂O₄ shell.¹⁹ Besides, when compared with the Co-chloride, the lower coordination ability of the perchlorate promoted a relatively higher reactivity of the Co ions in solution, resulting in the nucleation of a cobalt oxide phase, identified as CoO, at the NP surface. On the other hand, the lower reactivity of Co²⁺ in the presence of chlorine ions prevented the nucleation of Co_xO_y phase and constrained the Co incorporation to a self-limited partial cation exchange reaction.

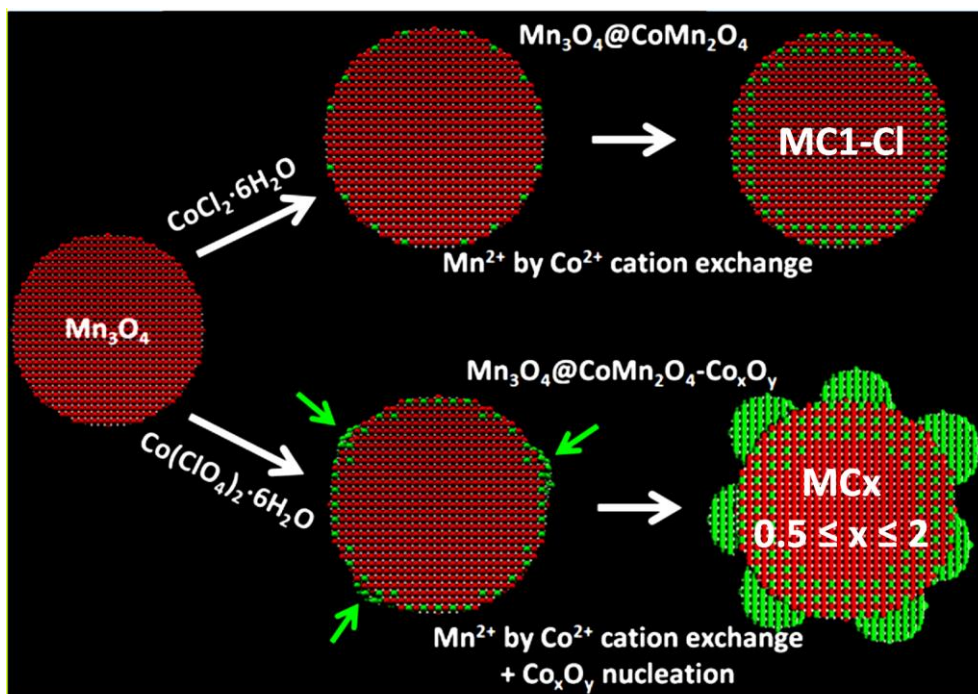


Figure 5-3. Scheme of the formation of the Mn₃O₄@CoMn₂O₄ and Mn₃O₄@CoMn₂O₄-Co_xO_y nano-heterostructures when using either a cobalt chloride or a cobalt perchlorate solution. Green arrows in the bottom point at Co_xO_y nanocrystal nucleation sites.

5.2.3 Rotating disk electrode analysis of NPs for ORR & OER

To study their electrocatalytic properties toward ORR and OER, NPs were mixed with carbon powder (Vulcan XC-72) with a weight ratio of 30% through sonication of NPs and carbon in chloroform and ethanol^{xiv}. NP/VC nanocomposites were then thermal treated under air atmosphere at 180 °C for 5 h to remove organic ligands. The carbon additive was mixed before thermal treatment to avoid NPs agglomeration after the removal of ligands. Otherwise ligand-free NPs would collapse into each other and would not be accessible for carbon additive to create an unbroken network of electronic conduction.

X-ray photoelectron spectroscopy (XPS) showed the presence of a main Co^{2+} component (purple and blue lines) and an additional Co^{3+} contribution (green lines), Figure 5-4(a), which evidenced partial oxidation of CoO crystallites to Co_3O_4 during the thermal treatment. For different chemical state of Co atoms, the binding energies in vacuum (E_b^v) strongly overlap to each other such as in Co_3O_4 and CoO which are both observable at ~ 779 and ~ 797 eV for $\text{Co}2p_{3/2}$ and $\text{Co}2p_{1/2}$, respectively¹³⁹.

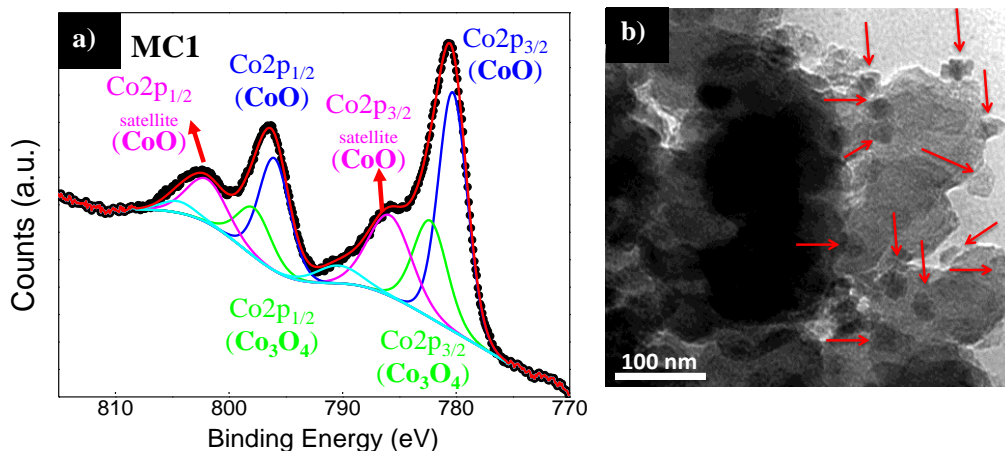


Figure 5-4. (a) XPS spectra of Co-oxide crystallites on MC1 NPs and (b) TEM micrograph MC1 NPs which was supported on carbon black (red arrows point at some of the NPs)

Yet, it is possible to distinguish Co oxidation states using *satellite features* of $\text{Co}2p_{1/2}$ spectrum because a single valence state (Co^{+2}O) gives a *stronger* satellite feature than a mixed state. In addition, commercial CoO samples often display an

^{xiv} Further details are given in Chapter 2.

oxidized Co_3O_4 surface in XPS even though powder XRD spectrum showed only CoO diffraction peaks. This appears to be a common surface activity of Co showing Co_3O_4 oxidized surfaces for CoO. TEM micrograph of the MC1/VC composite was given in Figure 5-4(b) revealing MC1 NPs were uniformly dispersed around carbon additive in the loading-annealing process. The red arrows show the individual MC1 particles that preserved their heterostructured morphology that their agglomeration was prevented as a result of carbon additive before the ligand removal.

Analysis of Kinetic Parameters

Electrochemical activity of the NPs was studied using linear sweep voltammetry (LSV) in a three-electrode cell coupled with a RDE configuration (see Chapter 2, Rotating disk electrode for further details). The initial sweep was performed without rotating (0rpm) and O_2 bubbling caused a noisy current density signal, grey plot in Figure 5-5(a). Consecutive sweeps were performed with six different rotating speeds – from 400 to 2000 rpm.

Figure 5-5(a-d) could be considered as a step-by-step guideline in order to perform a kinetic study for ORR. The given plots were for MC1/VC sample for clarity and this protocol was applied for each sample rigorously^{xv}. The initial step was to perform LSVs for a sample immobilized on CFS, as illustrated previously in Figure 2-4, Chapter 2. LSVs recorded for MC1/VC can be seen in Figure 5-5(a). The first feature observed was the overpotential (~ 0.3 V) respect to redox potential of ORR, $1.23 V_{\text{RHE}}$. The initial rise of the disk current (i_{disk}) at this overvoltage (between dashed lines) was almost independent of the electrode rotation rate, e.g. potential range of $0.85\text{--}1.0 V_{\text{RHE}}$. This suggested that the current density in this narrow potential range was under pure kinetic control. In these conditions, the electron-transfer rate at the electrode surface was much smaller than that of the diffusion-convection limiting rate ($i_{\text{k}} \ll i_{\text{diff}}$) and therefore, the disk current density was almost equal to kinetic current density, ($i_{\text{k}} = i_{\text{disk}}$)¹⁴⁰. Meaning that, if the kinetic rate of a catalyst would be fast ($k_0 \gg 0.02 \text{ cm}\cdot\text{s}^{-1}$); one could observe a very steep rise of the current until all the ions at the boundary layer are depleted (like a current jump of a capacitor under polarization). With further polarisation, the current would either

^{xv} In the next section, figures would show the comparison of all samples extracted from this step-by-step protocol.

remain stable or fall back to a lower value – due to the mass transfer from the bulk towards the vicinity of electrode, where the ions were depleted. In fact such behaviour could be seen in 0 rpm LSV scan (grey plot in Figure 5-5(a)) that the current density tends to fall slightly but O₂ bubbling improved mass transfer keeping the current relatively constant.

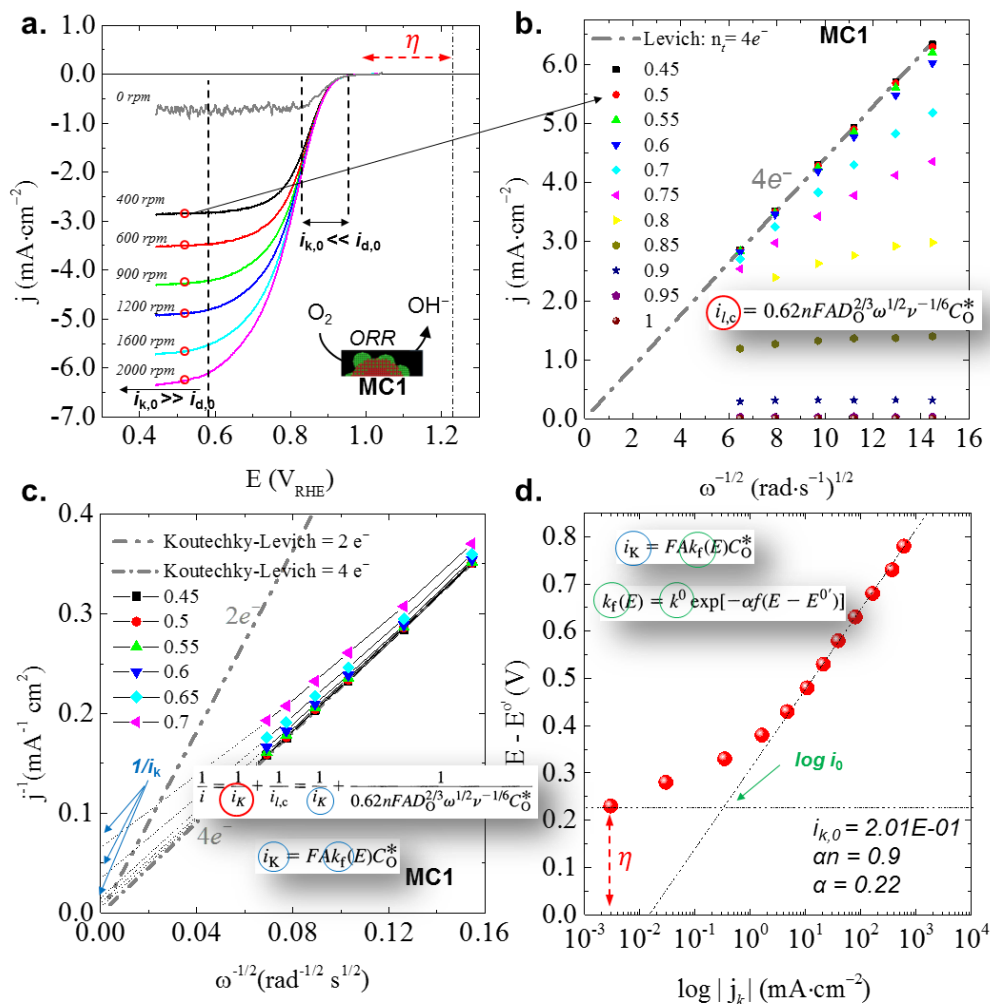


Figure 5-5. (a) Current-potential curves at different electrode rotating rates, recorded for MC1/VC on glassy carbon disk electrode (0.196 cm^2) using a potential scan rate of $5 \text{ mV}\cdot\text{s}^{-1}$ in O₂-saturated 0.1 M KOH aqueous solution; (b) the Levich plot and its equation; (c) the Koutecky-Levich plots at different electrode potentials and corresponding equations for find kinetic current (j_k) and electro-transfer rate constant (k_c); and (d) plot of E vs $\log(j_k)$. The measurement was carried out at 25C and 1.0 atm oxygen pressure

When the potential was beyond $0.85 \text{ V}_{\text{RHE}}$, disk current (i_{disk}) would be dependent on the rotating speed of the electrode. Here, the disk current was limited to a certain value ($i_{\text{disk,l}}$) by both electrochemical kinetic current and O₂ diffusion ($i_k \gg i_{\text{diff}}$). At

potentials lower than $0.85 V_{\text{RHE}}$, the kinetics were faster but the limiting factor on the current was the diffusion determined by rotating rate ($i_{\text{diff}}=i_{\text{disk,l}}$), so the total flux of current was under convection and diffusion control. If $i_{\text{disk,l}}$ of a fixed potential was taken from each LSV such as red circles in Figure 5-5(a) and plotted vs. the rotating speed as in Figure 5-5(b), $i_{\text{disk,l}}$ would be proportional to two parameters: O_2 concentration (C_O^*) and rotating speed ($\omega^{1/2}$), formulated by Levich equation,

$$i_{l,c} = 0.62 \cdot n \cdot F \cdot A \cdot D_O^{2/3} \cdot \omega^{1/2} \cdot \nu^{-1/6} \cdot C_O^* \quad (5.1)$$

where “ $i_{l,c}$ ” is the limiting current (A), “ n ” as the number of electrons transferred, “ F ” as Faraday’s constant (96485 C), “ D_O ” is the diffusion coefficient^{xvi} ($\text{cm}^2 \cdot \text{s}^{-1}$), ω as rotating speed ($\text{rad} \cdot \text{s}^{-1}$), “ ν ” as kinetic viscosity of the electrolyte) and “ C_O^* ”, is the concentration of the species “ O ” ($O_{2,\text{dissolved}} = 1.2 \times 10^{-6}$). Figure 5-5(b) shows that slope of the plots used to determine the electron transference number, “ n_t ”, which was the number of electrons transferred under steady-state conditions ($0.4 - 0.85 V_{\text{RHE}}$). The theoretical value, exchange of 4 electrons to reduce O_2 into OH^- , was plotted as well for clarity. For potentials between 0.6 and $1 V_{\text{RHE}}$, there were large deviations from the theoretical 4 electron path, suggesting the steady-state condition was not applicable for all potentials. Therefore, we needed to look for n_t value between 0.4 and $0.6 V_{\text{RHE}}$ by either taking the average of n_t values or considering the best fitting slope compared to Levich theory. Those values for MC1/VC are 3.95, 3.91, 3.82 and 3.63 for 0.45 , 0.5 , 0.55 and $0.6 V_{\text{RHE}}$, respectively. We can initially say that MC1/VC favoured $4e^-$ path for ORR at large overpotentials and a small portion of the reaction would undergo to $2e^-$ reduction to H_2O_2 which would be explained later on.

A key question in Figure 5-5(b) could simply be, “Why at the potentials between 0.6 and $1.0 V_{\text{RHE}}$ do not follow the Levich formulation?” To remind that, the reversible reactions provide very fast kinetics, j - E wave for a reversible reaction is independent of ω at the activation region. Thus, when $i_{\text{disk,l}}$ varies with $\omega^{1/2}$, it must be valid at any potential contrary to points at higher potentials in Figure 5-5(b). So, the deviation of the plots between 0.6 and $1.0 V_{\text{RHE}}$ from the straight Levich line

^{xvi} $D_{O_2} = 1.9 \times 10^{-5} \text{ cm}^2 \cdot \text{s}^{-1}$ and $\nu_{0.1M \text{ KOH}} = 0.01 \text{ cm}^2 \cdot \text{s}^{-1}$

intersecting the origin would suggest that a kinetic limitation (rate determining step) was involved in the electron-transfer reaction. This required further interpretation by using Koutechky-Levich equation and plot (Figure 5-5(c)) dedicated for quasi-reversible and irreversible reactions given by,

$$\frac{1}{i_{\text{disk}}} = \left(\frac{1}{i_k} + \frac{1}{i_{l,c}} \right) = \left(\frac{1}{n \cdot F \cdot A \cdot k^* \cdot C_0^*} + \frac{1}{0.62 \cdot n \cdot F \cdot A \cdot D_0^{\frac{2}{3}} \cdot \omega^{\frac{1}{2}} \cdot \nu^{-\frac{1}{6}} \cdot C_0^*} \right) \quad (5.2)$$

$$\frac{1}{i_{\text{disk}}} = \left(\frac{1}{n \cdot F \cdot A \cdot k^* \cdot C_0^*} \right) + \left(\frac{1}{0.62 \cdot n \cdot F \cdot A \cdot D_0^{\frac{2}{3}} \cdot \nu^{-\frac{1}{6}} \cdot C_0^*} \cdot \frac{1}{\omega^{\frac{1}{2}}} \right) \quad (5.3)$$

where i_k and k^* are the kinetic current and kinetic rate constant, respectively and rest of the symbols stand the same as Levich equation. Here the kinetic current, i_k resembles the reaction mechanism in the absence of any mass-transfer effects, that was, the current would flow under the pure kinetic control if the mass transfer were efficient enough to keep the concentration at the electrode surface equal to the bulk value, regardless of the electrode reaction²⁶. As a result, a plot of $1/i_{\text{disk},l}$ vs. $1/\omega^{1/2}$ (Figure 5-5(c)) should be linear and can be extrapolated to find the kinetic current from the intercept by $\omega^{1/2} = 0$ yielding $1/i_k$. The change of current is related exponentially to the applied overpotential explained by Tafel^{28a}. Thus, corresponding potential of each i_k could be used to plot $\log i_k$ vs. η to evaluate the kinetic parameters, Figure 5-5(d). The transfer coefficient, α could be found from Tafel slope and its intercept would give $\log(i^0)$. The standard rate constant of the reaction, k^0 could be estimated from Butler¹⁴¹-Volmer^{28b} equation,

$$i_k = i^0 \left[e^{\frac{(-\alpha) \cdot n \cdot F}{R \cdot T} \cdot \eta} \right] \quad (5.4)$$

$$\log(i_k) = \log(i^0) + \left(\frac{-\alpha \cdot n \cdot F}{2.3 \cdot R \cdot T} \right) \cdot \eta \quad (5.5)$$

$$i^0 = n \cdot F \cdot A \cdot k^0 \cdot C_0^* \quad (5.6)$$

Comparison of ORR Activity

The comparison of NPs activity vs. ORR was conducted for 1600 rpm rotation, shown in Figure 5-6(a). The kinetic and diffusion controlled region between mixed-Co/Mn NPs were significantly different than their forming oxides (Mn_3O_4 and Co_3O_4). This region corresponded to the voltage range of 0.95–0.7 V_{RHE} for MCx NPs

($0.5 < x < 2$) and $0.85-0.5 V_{\text{RHE}}$ for Mn_3O_4 and Co_3O_4 , respectively. When the electrodes were polarized to higher overpotentials, the reaction was under mass diffusion control determined by the rate of O_2 transport to the diffusion layer.

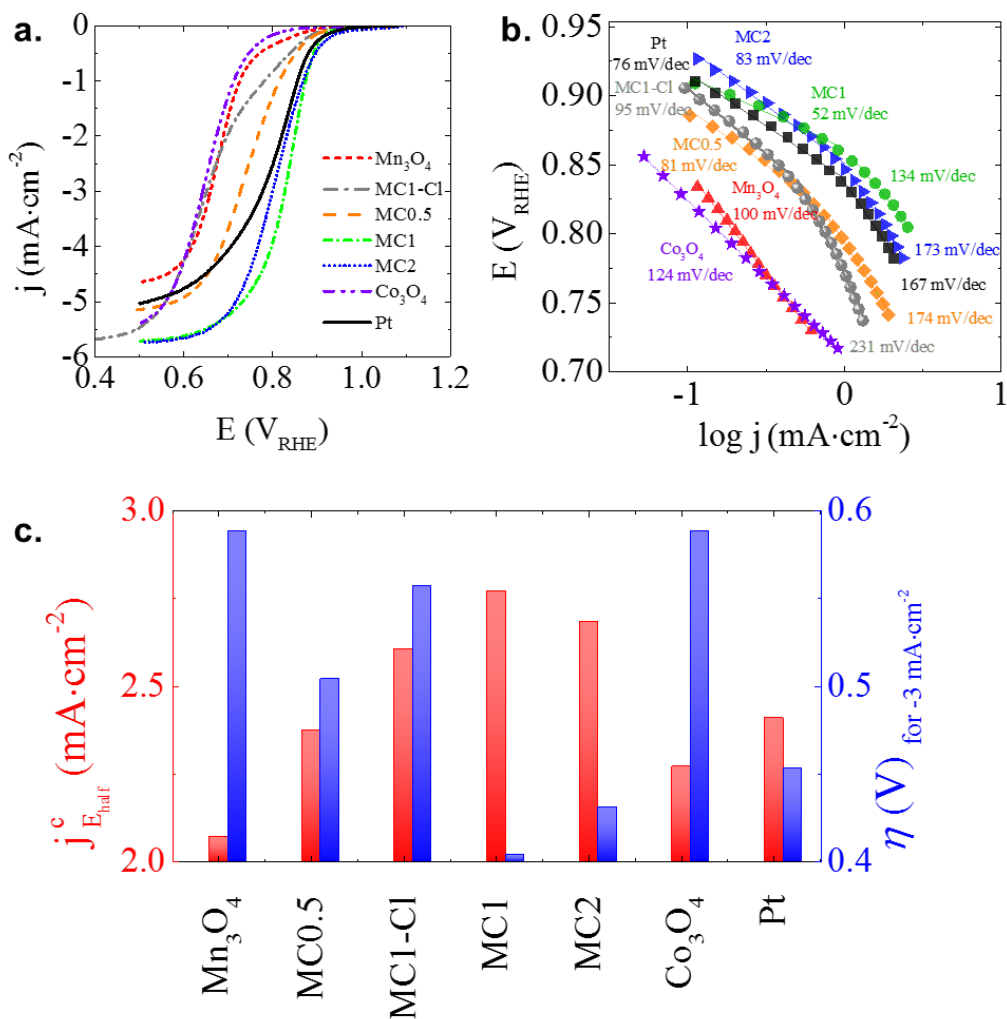


Figure 5-6. (a) ORR polarization curves of MC/C, $\text{Mn}_3\text{O}_4/\text{C}$, $\text{Co}_3\text{O}_4/\text{C}$ and Pt/C in O_2 -saturated 0.1 M KOH at 1600 rpm using a scan rate of $5 \text{ mV}\cdot\text{s}^{-1}$. (b) Corresponding Tafel plots derived of ORR polarization curves (c) Kinetic current densities at half-wave potential (red) and overpotentials (blue)

The diffusion limited current ($i_{\text{disk},l}$) of Co_3O_4 ($-5.5 \text{ mA}\cdot\text{cm}^{-2}$) was relatively higher than Mn_3O_4 ($-4.5 \text{ mA}\cdot\text{cm}^{-2}$) but with an expense of extra 0.2 V compared to MC1 and MC2. We might conclude that Co-cation exchange improved the kinetics of the ORR reaction, according to the improvement of on-set voltage and steep current rise in the mixed-region, $\text{MC0.5} > \text{MC2} > \text{MC1}$.^{xvii} Further investigation of electrochemical

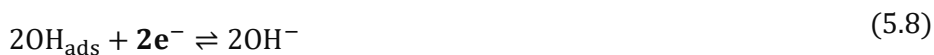
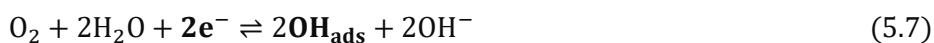
^{xvii} LSVs of all samples at different rotation speeds are given in Annex 5.1

kinetics were assessed from Tafel slopes, shown in Figure 5-6(b) obtained from the region closer to their on-set potentials, where the limitation by O_2 diffusion in the active layer was negligible. Two different Tafel behaviour between 0.95 and 0.7 V_{RHE} would imply similar reaction mechanism for spinel nanoparticles (MCx) and commercial Pt. MC1 exhibited favourable kinetics than MC1-Cl and even benchmark Pt (52, 95 and 76 $mV \cdot dec^{-1}$, respectively). Their forming oxides showed a stronger irreversible behaviour due to their high Tafel slope values; Mn_3O_4 (100 $mV \cdot dec^{-1}$) and Co_3O_4 (124 $mV \cdot dec^{-1}$).

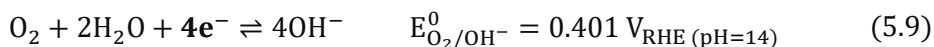
Figure 5-6(c) displays two ORR figures of merit, the current density at half-wave potential and the required overpotentials to reach $-3 \text{ mA} \cdot \text{cm}^{-2}$. When compared with Mn_3O_4 and Co_3O_4 , ORR current densities and overpotentials clearly improved with the presence of $CoMn_2O_4$ shell (MC1-Cl), but an additional enhancement was observed in presence of the Co_xO_y crystallites on MCx ($0.5 < x < 2$). In particular, the MC1 catalyst outperformed the rest, showing the highest half-wave current densities, $-2.77 \text{ mA} \cdot \text{cm}^{-2}$, and the lowest overpotential, 0.4 V_{RHE} . Higher Co_xO_y concentrations (MC2) maintained the large current density in the diffusion limited region with a slightly higher overpotential. MC0.5 required even larger overpotential to reduce oxygen suggesting sluggish reaction kinetics for ORR. Firstly, these observations indicated a trend between amounts of cation exchanged vs. ORR activity. Secondly, interaction of core/shell embodiment would influence ORR reaction path between 2 and 4 e^- .

In alkaline solution, the oxygen reduction reaction (ORR) can follow (i) a direct four electron pathway, (ii) a two electron pathway, or (iii) a sequential four electron pathway.¹⁴⁰

- i. The direct $4e^-$ pathway entails conversion of O_2 to OH^- via two electron transfer in two steps,



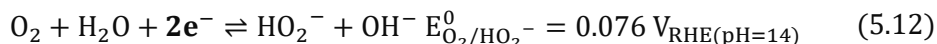
and overall reaction would be,



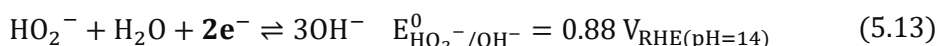
- ii. The $2e^-$ pathway converts O_2 to HO_2^- and OH^- via single electron transfer path in two steps,



and overall reaction would be,



- iii. The peroxide ion (HO_2^-) may either desorb from the catalyst surface (Eq. 5.12), or it may persist enabling a further $2e^-$ reduction to OH^- . This second step completes $4e^-$ transfer (Eq. 5.9) of the sequential mechanism,



For an electrochemical cell, $4e^-$ transfer of O_2/OH^- redox couple is preferable to prevent catalyst corrosion by oxidative peroxide ion¹⁴² so it would be useful to compare electrons transference number (n_t) of different catalysts by Levich equation²⁰ described previously in Eq. (5.1).

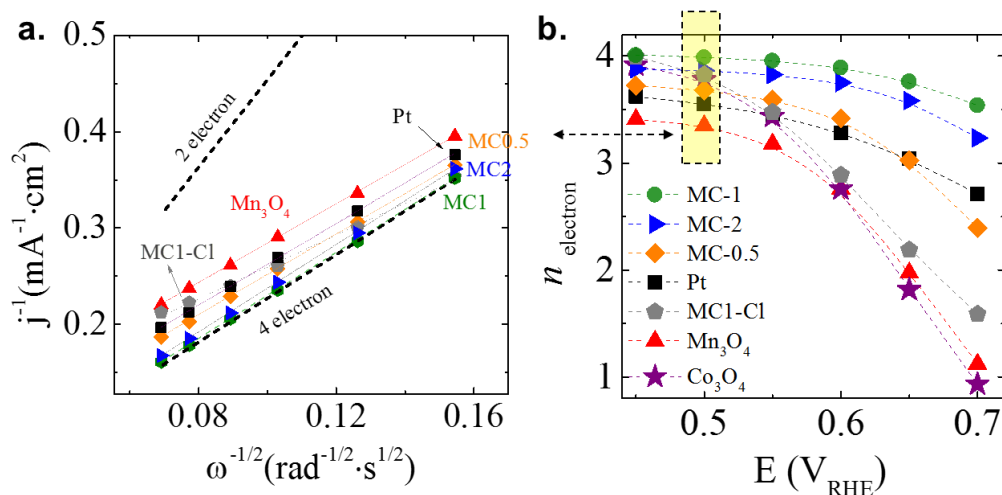


Figure 5-7. (a) K-L plots at $0.5 V_{RHE}$. The standard lines for 2 and 4 electron pathways are also plotted as a guideline (b) n_t at different potentials.

Figure 5-7 (b) shows Levich slopes and n_t as a function of electrode potential from the slope at potentials from 0.45 to $0.7 V_{RHE}$. The presence of $CoMn_2O_4$ shell around Mn_3O_4 surface (MC1-Cl) had a minor influence on n_t , which increased from 3.35 for bare Mn_3O_4/C to 3.43 for MC1-Cl/C at $0.5 V_{RHE}$.

The observation that n_t for MC1-Cl and its constituent oxides were neither exactly $2e^-$ nor $4e^-$ suggesting a simultaneous reduction of oxygen through both pathways. MC_x ($0.5 < x < 2$) catalysts with Co_xO_y crystallites displayed higher n_t than others. It was plausible that the presence of Co_xO_y at the $Mn_3O_4@CoMn_2O_4$ surface facilitated a rapid electron transfer, clearly shifting the ORR mechanism toward $4e^-$ path as evidenced by the increase of n_t values for $MC0.5/C < MC2/C < MC1/C$, respectively. To expand further, depending on the mode of adsorption of oxygen molecule on metal surface, different mechanistic steps can occur as proposed by various authors¹⁴³. A modified scheme proposed by Wroblowa et al.¹⁴⁴ has been very much accepted in the literature given in Figure 5-8.

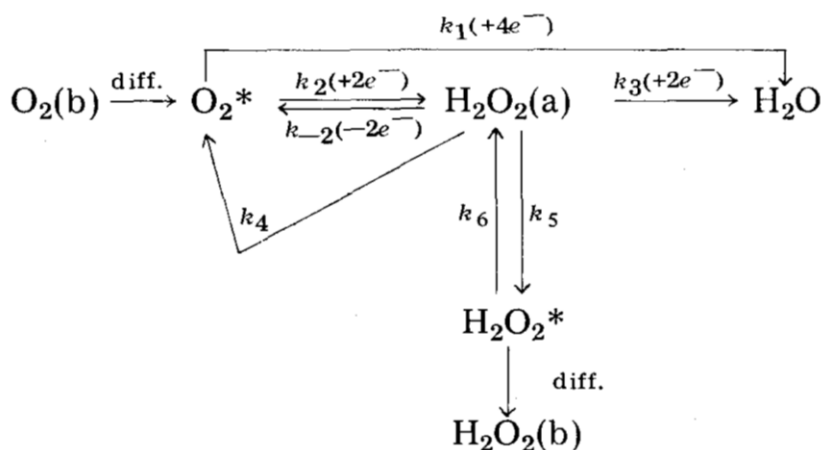


Figure 5-8. The proposed scheme of ORR pathway by Wroblowa et. al., (Image obtained from Ref. [144], with permission J. Electroanal. Chem., Elsevier)

In this scheme, at high potentials, $k_1 > k_2$, the portion of direct $4e^-$ reduction of oxygen to water will be more than $2e^-$ reduction to peroxide; at intermediate potentials, the decrease in k_1/k_2 ratio will indicate an increase in the portion of $2e^-$ reduction to peroxide; and at lower potentials k_1/k_2 becomes lower than 1. However, if k_3 increases, a further reduction of peroxide to water will happen before it desorbs to solution. This observation proposes the formation and stabilization of high-energy intermediate at the surface, peroxide, would be very critical for further reduction to H_2O . This is often related to the high stability of the O–O bond, which has a dissociation energy of $494 \text{ kJ}\cdot\text{mol}^{-1}$, while this value is only $146 \text{ kJ}\cdot\text{mol}^{-1}$ for H_2O_2 (peroxide). According to increment of n_t values upon Co cation exchange with Mn indicated an improvement for the adsorption of O_2 molecule and stabilization of H_2O_2 intermediate if a sequential $2e^-$ was the reaction path, Eq. (5.13). After careful

characterization of nanoparticle catalysts by ADF-STEM image and EELS elemental mapping and XPS analysis of the surface, we proposed a generally accepted mode of O_2 adsorption which was either “end-on” or “bridge” model of interaction, illustrated in Figure 5-9(a). The charge transfer for the end-on interaction of O_2 with the metal has been related to electron donating ability created by multivalent metal cations⁸⁴. Table 5.1 shows the valence state of the nanoparticle catalysts calculated by the stoichiometry obtained by XRD spectra and relative comparison of cations in EELS elemental mapping. The coexistence of multivalent Mn states (+2 to +4) is due to $Co_xMn_{2-x}O_4$ shell layer. It could be difficult to assign one “x” value even with high resolution microscopy, we assumed that values from 0.5 to 2 can generate a mixed valence state at the crystal lattice of the shell.

Table 5.1. The valence state of nanoparticle metal cations

Core	Mn_3O_4	$Mn_1^{+2} Mn_2^{+3} O_4^{-2}$
Shell	$Co_xMn_{2-x}O_4$	$Co_x^{+2} Mn_{1-x}^{+2/+3} Mn_{2-x}^{+3/+4} O_4^{-2}$
Crystallites	CoO	$Co^{+2} O^{-2}$
	Co_3O_4	$Co^{+2} Co_2^{+3} O_4^{-2}$

Nevertheless, all Co-doped Mn_3O_4 nanoparticles exhibited a shell layer found from HR-TEM and XRD studies. This brought up the second question about the intrinsic activity of the crystallites formed on the shell layer, $Co_xMn_{2-x}O_4$. This intrinsic activity, in fact, would be a result of the kinetic properties which could be studied by a comparison of their standard rate constants (k^0) and electron transfer coefficients (α). The values obtained from K-L plots and Tafel/Butler-Volmer equations were plotted in Figure 5-9(b-c). The first indication, in Figure 5-9(b) was k^0 of MCx NPs that lie in the quasi-reversible region, as well as Pt benchmark catalyst. The fastest rate of ORR reaction would belong to MC1 catalyst, $1.74 \times 10^{-3} \text{ cm}\cdot\text{s}^{-1}$ followed by Pt, $9.46 \times 10^{-4} \text{ cm}\cdot\text{s}^{-1}$, indicating an improved stabilization of peroxide. This would also linked to the mode of adsorption that a bridge bonding would be favoured at MC1 NPs because earlier studies¹⁴⁵ indicated that the bridge interaction would likely to occur on noble metals such as Pt, where O_2 was reduced to water with little or no peroxide formed.

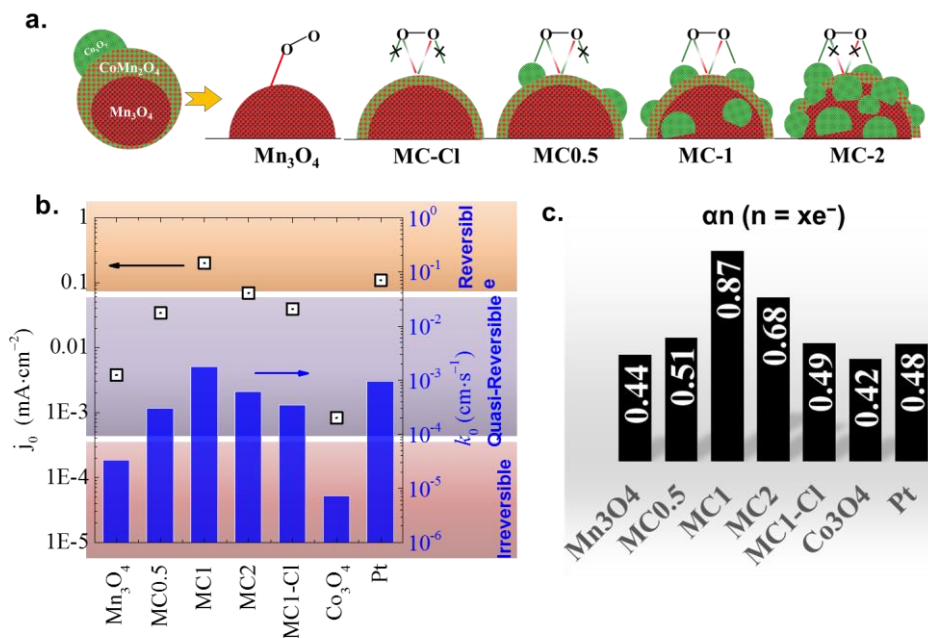


Figure 5-9. (a) Possible configurations of dioxygen interaction with NPs (b) limiting current density and kinetic rate constants of ORR for NPs extracted from the intercept of K-L plots and Butler-Volmer equations – different regions of reversibility for heterogeneous electrochemical reactions are highlighted (c) transfer coefficient (α) of catalyst NPs extracted from their slope of Tafel plots, “n” is the number electrons exchanged per mole of O_2

Moreover, their limiting current density showed a similar trend confirming that calculations were accurate. The second indication about the reaction mechanism was the values of electron transfer coefficients (α) given in Figure 5-9(c). Generally, electrochemical systems exhibit a value of $0.3 < \alpha \cdot n < 0.7$ for one-step one-electron transfer reactions ($n = 1$). The higher α value corresponds to a faster reaction kinetics and $\alpha = 1$ considered for a totally reversible reaction. Nevertheless, this would not be the case in many heterogeneous reactions due to the fact that catalysis reactions usually require the stabilization of the reductant (chemical step), not only a charge transfer (electrochemical step). For “ αn ” in catalysis of O_2 to OH^- , this n is different from that of the electron transference number (n_t). Here n is the number of electrons that could be transferred in the **rate-determining step (RDS)**. As highlighted previously in Eq. (5.7) to (5.13) for ORR, n has been recognized to have a value of $2e^-$ for RDS involving peroxide intermediate¹⁴⁵ therefore, $\alpha n = 0.87$ and α would be 0.43 whereas $n = 2$ for MC1 suggesting $2e^- + 2e^-$ path giving Eq. (5.9).

Catalyst stability is a critical requirement for practical applications. MC1 and MC2 catalysts showed current retention above 95% of the initial current after 20 hours, displayed in Figure 5-10(a). Mn_3O_4 , Co_3O_4 , MC1-Cl and Pt catalyst lost nearly half of their current density within the first 20 hours while MC0.5 preserved nearly 80% of the initial current after 2 ½ days, Figure 5-10(b). The direct O_2 reduction path (k_1 in Figure 5-8) implied a progressive decomposition activity against deteriorating peroxide species (contrary to k_2 , k_3 and k_5 in Figure 5-8) which was beneficial for holding a stable catalytic activity. n_t values of MC1 and MC2 were close to 4 and transfer coefficients of $0.5 < \alpha_n < 1.0$ revealed that ORR mechanism would be mostly (but not totally, see Figure 5-9 (c)) oriented toward k_1 path, direct $4e^-$ path again giving Eq. (5.9).

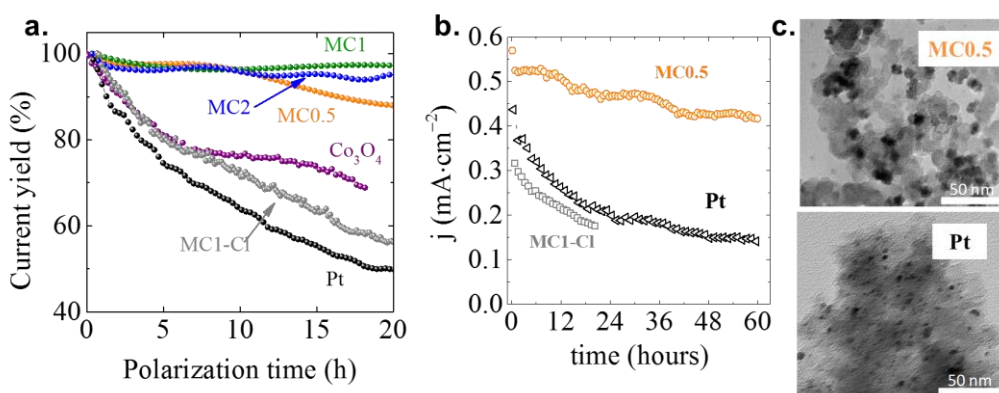


Figure 5-10. (a) Constant potential test performed at 0.8 V in O_2 -saturated 0.1 M KOH for all the nanoparticles for 20 hours and (b) MC0.5, MC-Cl and Pt for 60 hours (c) TEM images of MC0.5 and Pt NPs after 60 hours stability test. MC0.5 NPs were stable showing as dark spots covered with Vulcan carbon and Pt NPs were pulverized with Vulcan carbon additive due to oxidizing species formed during ORR.

On the contrary, for Pt catalysts, O_2 reduction into OH^- by direct $4e^-$ competed with $2e^-$ path yielding HO_2^- species which was proven to induce electrode corrosion^{21,22} Figure 5-10(c) displays TEM images taken after 60 hours ORR test. A strong pulverization of carbon support of Pt catalyst, along with an increment of its amorphous structure, verified a deformation of the catalyst particles by strong oxidizing character of peroxide species.

Comparison of OER Activity

OER activities of NPs are given in Figure 5-11(a-b), showing LSVs and Tafel plots. The amount the active ion (OH^-) in alkaline solution (0.1 M KOH) for OER is near infinite compared to low solubility of O_2 (1.2×10^{-3} M) in ORR. Therefore, the

diffusion limitation was much less of a factor and it was relatively simpler to evaluate Tafel slop in low overpotential region.

Co₃O₄ showed state-of-art values, with an excellent catalytic activity, clearly outperforming that of Mn₃O₄, Figure 5-11(a). Pt catalyst was not stable in OER²³ due to severe oxidation evident from the broad peak in LSV following its dissolution with carbon support. For that reason, IrO₂-based commercial anode was tested as OER benchmark catalyst. As expected, this material showed exceptionally a low overvoltage (0.25 V) and high current density. On the other hand, all MCx catalysts showed similar OER performances close to the Co₃O₄ and IrO₂ references, with low overpotentials (e.g. 0.31 and 0.41 V for MC1/C and Co₃O₄). In particular, MC1 exhibited the faster OER kinetics^{xviii} with a Tafel value of 95.2 mV·dec⁻¹, clearly below that of Mn₃O₄, but also of Co₃O₄ and even IrO₂-DSA.

The presence of Co_xO_y crystallites facilitated a faster reaction kinetics according to the improvement of the on-set potential. Similar to ORR catalysis, the degree of adsorption/desorption of O₂/OH⁻ is of importance in OER. The improvement of catalytic activity proven in ORR (4e⁻ path via OH⁻) would in parallel provide available active sites that have stronger affinity for both molecules O₂ and OH⁻. Surface metal cations (M) are usually the active sites which proceeds via a series of intermediates by the adsorbed oxygen atom (M–O) in OER, e.g. M–OH bond → M–O → M–OOH → M–OO^{69b}. Therefore, a synergy of both Mn- and Co- atoms at the surface layer might be the active sites for M–O bond. In that respect, activity trends of mixed metal oxides were often explained by the Sabatier principle⁷¹. It states that, the interactions between the catalyst and the substrate should be just right; that is, neither too strong nor too weak. Hence, “volcano” plots have often been employed to resemble the relationship between OER activities vs. M–O bond strength. Those studies usually suggested that an optimal M–O bond interaction would lie at the top of the volcano. If M–O bond strength would be too strong or too weak, OER ability would be at the bottom sides of the volcano, meaning a lesser extend of catalytic activity.

^{xviii} An extended summary of the electrochemical data is presented with a table in **Annex 5.1**.

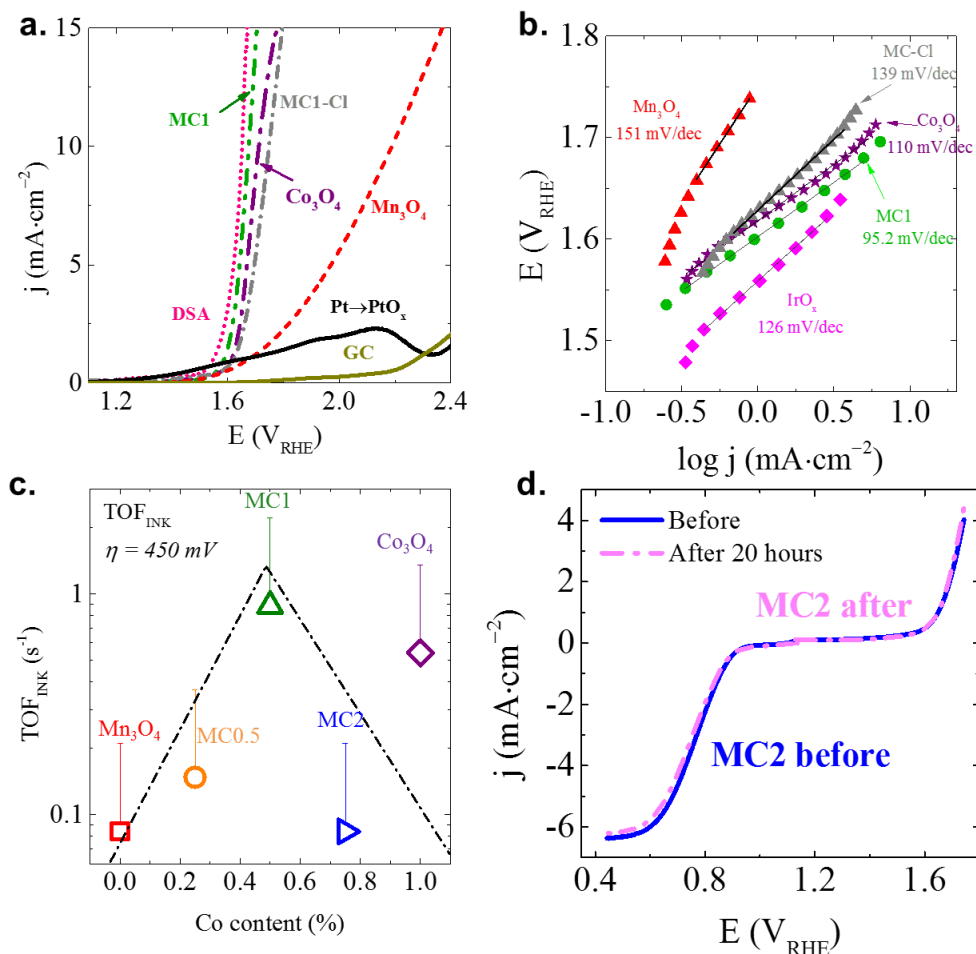


Figure 5-11. (a) OER polarization curves of Mn₃O₄/C, Co₃O₄/C, MC/C, Pt/C, DSA and glassy carbon (GC) in O₂-saturated 0.1 M KOH at a scan rate of 5 mV/s. (b) Tafel plots derived from OER polarization curves. (c) Linear polynomial regression of the LSV scans with a scale zoomed to onset potentials (d) Comparison of ORR and OER activities of MC2 NPs before and after 20 hours durability test in 0.1 M KOH solution. The rotation rate is 1600 rpm during ORR & OER

For instance, initial works of Delahay et.al and Hickling et. al.¹⁴⁶ showed a decreasing OER trend of Co \approx Fe > Cu > Ni correlated to M–OH bond strength. Later Trassati et. al.^{69a, 147} proposed a unified approach to determine OER activity trend of RuO₂ > IrO₂ > MnO₂ > NiO > Co₃O₄ > Fe₃O₄, correlated with the oxygen uptake of the active surface site of the metal, in accordance with M–O bond strength. If Mn-site presented the enhanced affinity to M-OH adsorption, then a decrease of OER activity was not surprising at MC2 due to the shielding of Mn-surface sites by Co_xO_y crystallites. A correlation between Co content and turn-over-frequency (TOF) at an overpotential of 450 mV was shown the support this explanation, Figure 5-11(c). 1:1 ratio of Mn to Co was at the top of the volcano and both ends gave a trend for

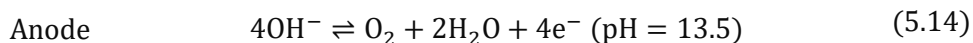
high Mn or Co content. Only Co_3O_4 did not fit exactly to the right end of the volcano plot and displayed significantly higher OER activity than Mn_3O_4 . Higher electrical conductivity of Co-oxides are well known and widely studied in energy storage systems, i.e. batteries^{9a, 148}. Its high intrinsic activity could be seen from the low on-set potential and Tafel value ($110 \text{ mV}\cdot\text{dec}^{-1}$) proposing faster kinetics compared to Mn_3O_4 . In a recent study, Burke et. al. presented the effective conductivity of first-row transition metals using an interdigitated array electrode in 1 M KOH solution. The results showed a dramatic decrease of electrical conductivity from $\text{CoO}_x\text{H}_y \gg \text{NiFeO}_x\text{H}_y > \text{NiO}_x\text{H}_y \gg \text{MnO}_x\text{H}_y$ which could also be correlated to the difference in kinetics between Mn- and Co-oxide NPs.^{70, 149} LSV scans before and after a 20 hours test, Figure 5-11(d), showed no significant change either in the on-set voltage or in current density of both ORR and OER for MC_x ($0 < x < 2$). Even a slight improvement of OER current density was observed, probably due to the penetration of electrolyte into the film nano-pores.

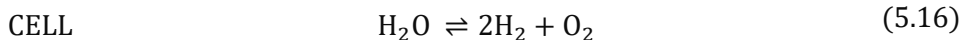
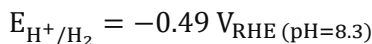
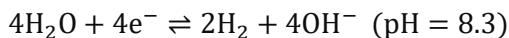
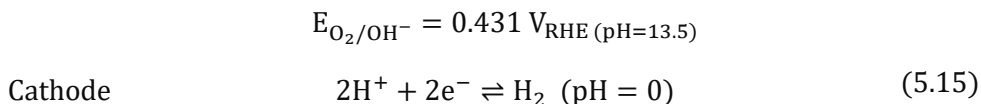
Eventually, MC1 catalyst was chosen as the only candidate to employ at the anode side of ECf-cell. In order to realize this test, we first had to form a catalyst-electrode assembly by spin coating method which would be explained in the next section.

5.2.4 DSA vs. NPs/CFS in ECf-cell

Nanoparticle immobilization on carbon fibre substrate

After rotating disk experiments MC1 catalyst were tested in ECf-cell set-up by immobilizing nanoparticles on carbon fibre substrate (CFS size: 1.5 cm x 1.5 cm) by spin coating method. An ink containing MC1 NPs was deposited on CFS by spin-coating method in two steps as illustrated in Figure 5-13(a). After drying in Ar vacuumed oven at 80°C for a night to completely remove the organic solution in the nano-pore cavities, MC1-CFS assembly was placed in the anode supporting plate. In the counterpart (cathode), a Pt coated Ti-plate was used for hydrogen evolution reaction (HER). 0.1 M KOH and 0.1 M KHCO_3 was used as anolyte and catholyte, respectively, and the cell was separated by a Nafion® membrane enabling the transfer of protons or potassium ions for ionic balance of the water splitting reaction. According to pH adjustment, cell reactions occurred according to,





$$E_{\text{CELL}} = -0.92 \text{ V}$$

Three different catalyst loading were applied on CFS by spin coating, Figure 5-12(a-b). MC1 NPs presented a fair distribution on CFS, immobilizing mostly at the cross-sections of the carbon fibres. Figure 5-13 shows FE-SEM image of MC1-CFS with 2 layers of spin coating.

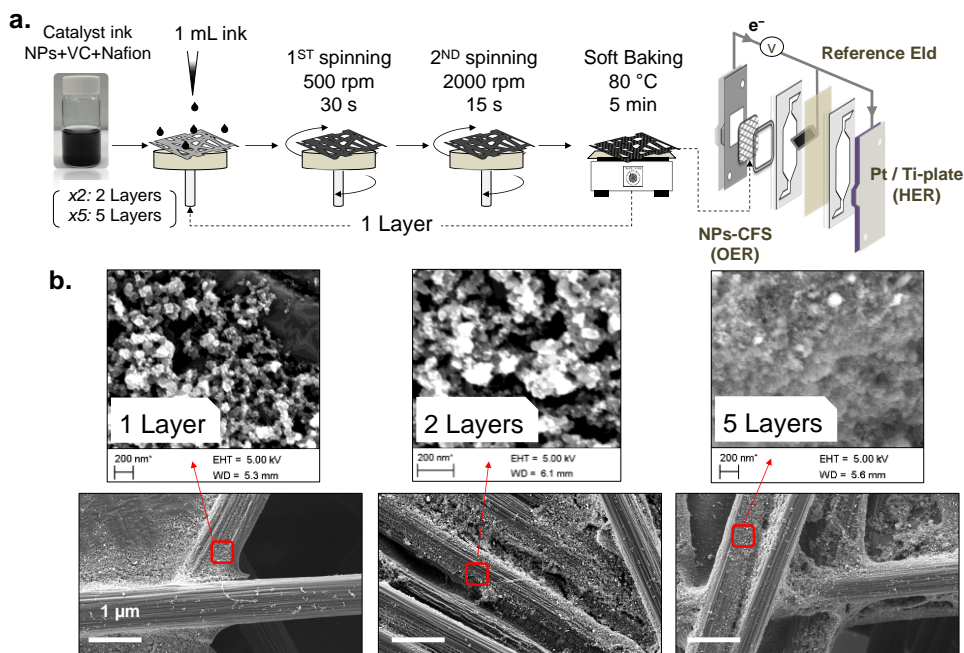


Figure 5-12. (a) Schematic illustration of [NPs:VC:Nafion] ink preparation and two step spin coating on carbon fibre substrate (CFS) following EC-flow cell assembling (b) FE-SEM images of MC1-CFS/1L, 2L and 5L electrodes. Magnified areas are shown by red squares.

Agglomerates of NPs varying from 20 to 60 nm were formed after 2nd layer which could be due to Nafion ionomer used as a binder additive in the catalyst ink formulation. The mass loading of spin coated samples have been calculated as 0.6, 1.3 and 3.2 mg·cm⁻² for MC1-CFS/1L, MC1-CFS/2L and MC1-CFS/5L, respectively.

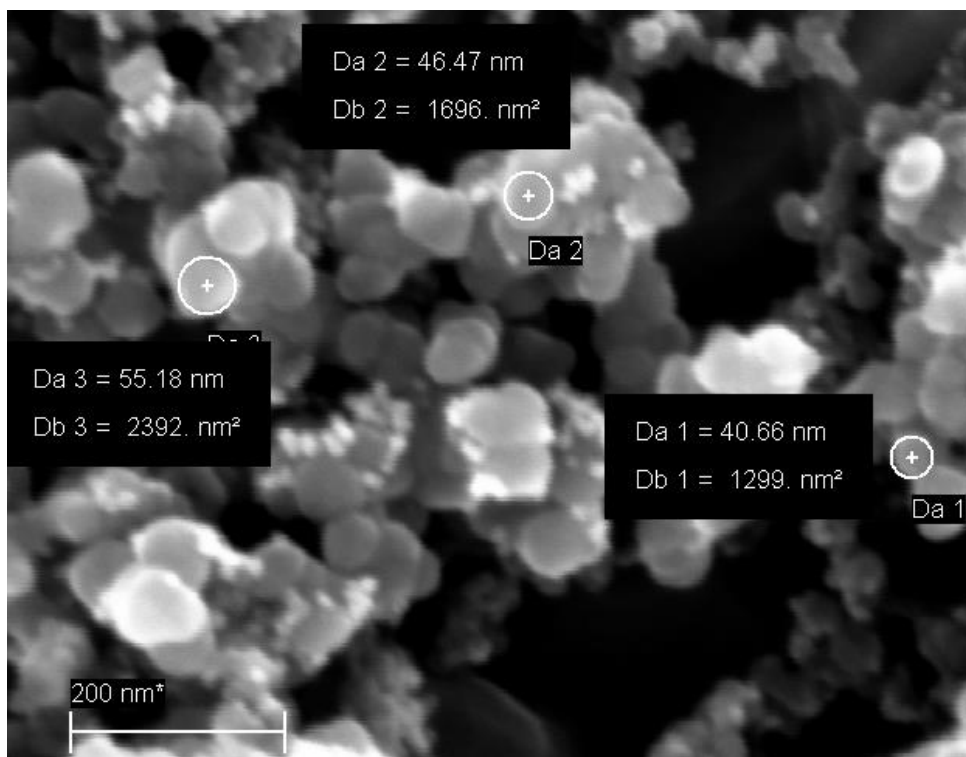


Figure 5-13. FE-SEM coupled with Charge Compensation method to investigate agglomerated nanoparticles of MC1-CFS/2L

OER activity of MC1-CFS in EC-flow Cell

Figure 5-14(a-d) presents OER activity of benchmark DSA ($\text{Ta}_2\text{O}_5\text{-IrO}_2/\text{Ti-plate}$) electrode under two different electrolyte modes. Initially, the liquid electrolyte (0.1M KOH) was pumped to the cell for almost 1 minute, until a steady flow is maintained. Then the pump was stopped and a CV was recorded at $5 \text{ mV}\cdot\text{s}^{-1}$ scan speed (black lines). This mode was referred as static mode “s” due to the electrolyte residing still in the anode (0.1 M KOH) and cathode parts (0.1 M KHCO_3). After these tests, liquid pump was fixed to a flow rate of $10 \text{ ml}\cdot\text{min}^{-1}$ and kept flowing during a second CV test. This mode was referred as dynamic mode “d”. During the assembly of ECf-cell, the gaskets and flow channels defined an active area for anode and cathode. Therefore mass-transport properties could be manipulated by changing two pieces of the assembly (gaskets and flow channels) and work with same electrode but having different geometric active area with an easy modification of assembly. The effect of diffusion and convection on electrochemical reactions were broadly studied in the previous section, so the initial results of ECf-cell were not a

surprise in terms of electrochemical principles, but highly informative about the applicability of OER catalysts to industrial electrochemical cells.

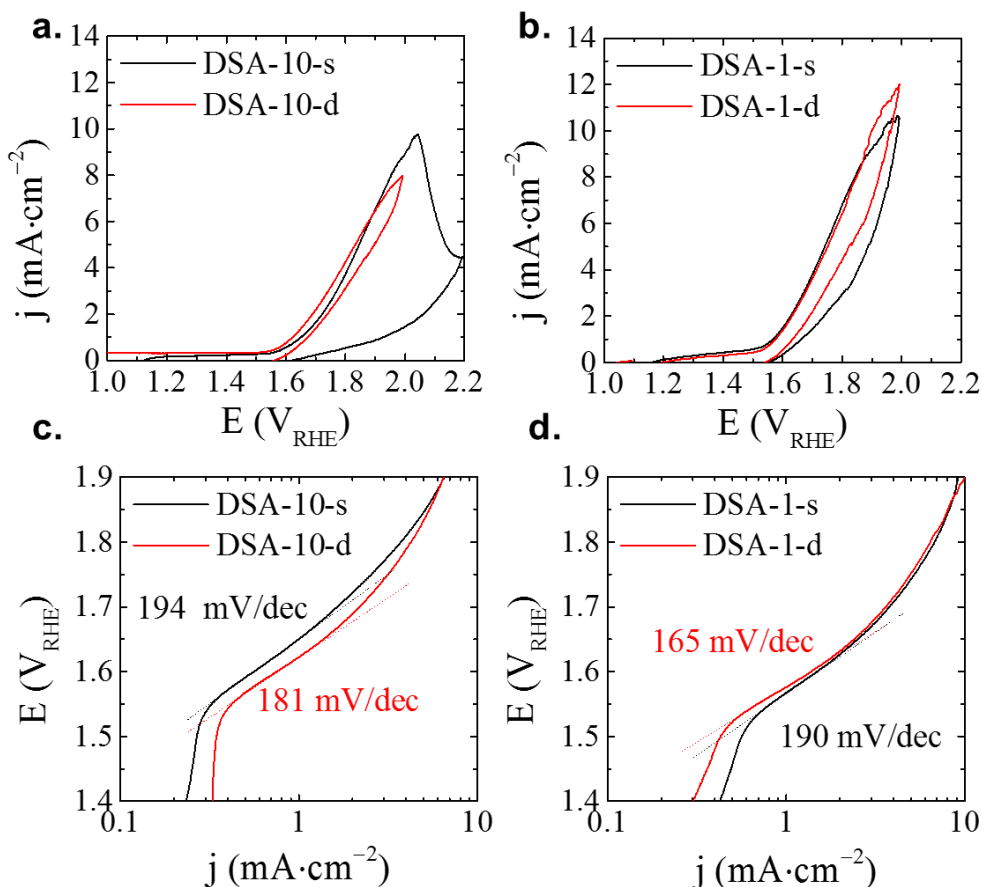


Figure 5-14. CV scans of DSA electrode with a defined geometrical area of (a) 10 cm² and (b) 1 cm² under static electrolyte mode “s” meaning no flow, and (b) dynamic mode “d” meaning 10 ml·min⁻¹ electrolyte flow (c) Tafel slopes of 10 cm² and (d) 1 cm² DSA electrode in static and dynamic modes

To start with s-mode (black lines) in Figure 5-14(a-b), the difference of CV shape between DSA-10 and 1 (black lines) was due to the mass-transport limitation. In the still solution, the concentration of OH⁻ species drastically decreased at the surface of 10 cm² electrode, evident from a maximum in OER current. Beyond this point, concentration of OH⁻ species at the electrode surface were almost zero and OER reaction was under diffusion control. For 1 cm² electrode area, this effect was still noticeable but less pronounced. In fact, the main reason was the small volume of the electrolyte reservoir at the anolyte compartment around 2 ml (10 cm x 10 cm x 0.2 cm). For instance, in rotating disk electrode tests, the geometrical area of glassy carbon electrode was 0.196 cm² while the volume of the liquid in beaker is ~80 ml.

This corresponds to a large difference between GCE/RDE tests and DSA/ECf-cell tests, shown in Table 5.2 in terms of volume to area ratio (ml electrolyte/cm² electrode) of 2-fold smaller for 1 cm² and 3-fold for 10 cm² DSA plate in s-mode. Nevertheless, this issue could easily be overcome by employing the d-mode and fixing a pump speed to increase the concentration of OH⁻ species by forced convection (e.g. 10 ml·min⁻¹ electrolyte flow), red lines in Figure 5-14(a-b).

Table 5.2. Dimensions of electrode area and anolyte volume inside the ECf-cell

	Electrodes		
	Glassy carbon	CFS (1 cm ²)	CFS (10 cm ²)
Anolyte volume (ml)	80	2	2
Electrode area (cm ²)	0.196	1	10
Ratio (ml/cm ²)	408	2	0.2

It is also important to mention that Tafel slope value significantly improved when cell was working under d-mode, Figure 5-14(c-d). The Tafel value is a factor of electrode kinetics and independent of diffusion control, therefore some explanation for electrolyte flow influence on Tafel parameter would be required. This could be related to an enhancement of local pH at the electrode surface. OER consumes OH⁻ species to produce O₂ which eventually increases the local H⁺ concentration at the surface. Since OER is a pH dependent reaction, evident from Pourbaix diagram,¹⁵⁰ it would require extra energy in terms of overpotential for O₂ evolution with the shift of local pH. Besides, the desorption H⁺ species from the surface to bulk of the electrolyte and their migration towards counter electrode to complement the counter reaction (HER) could be reasonably slow in a still solution. The constant flow of electrolyte would be expected to enhance the overall current, and could be associated to lower Tafel values in Figure 5-14(c-d).

Figure 5-15(a-b) shows CVs and corresponding Tafel slopes of CFS, MC1-CFS vs. DSA-1 electrode for OER activity under d-mode (10 ml·min⁻¹ flow of 0.1 M KOH). The overpotential required for 10 mA·cm⁻² along with the current density normalized to geometrical area and catalyst loading amount were given in Table 5.3. The results showed that a lower amount of catalyst loading on CFS immediately shifted OER on-set potential from 1.8 to 1.55 V_{RHE}. Moreover, current density

increased nearly 50 times thanks to faster kinetics of MC catalyst. In comparison of loadings, an improvement in Tafel value was observed at lower catalyst loadings, MC1-CFS 1L > 2L > 5L. This could be correlated to the accessibility of active sites around a single NP at low loadings compared to agglomerated particles at higher loadings.

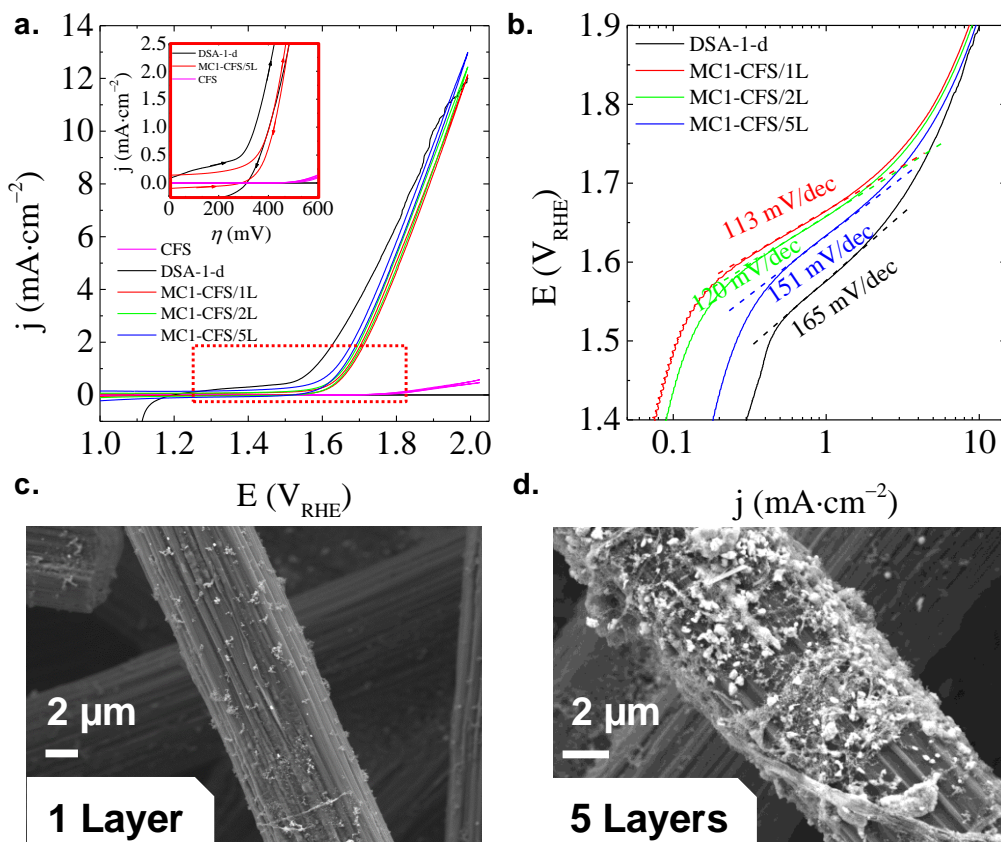


Figure 5-15. (a) CV scans of benchmark DSA electrode and MC1/CFS with different loadings; 1, 2 and 5 layers. In-set image shows necessary OER overpotential for DSA and MC1/CFS/5L (b) Corresponding Tafel slopes and FE-SEM images of MC1 NPs covering carbon fibres after (c) 1 layer and (d) 5 layers obtained by spin coating protocol.

In Figure 5-15(c-d), FE-SEM images of 1 and 5 layers of spin coating indicated that the coverage around carbon fibres were improved at 5L but we found coarser particles bundled with amorphous Nafion ionomer. There were two main roles of Nafion as ink additive in catalysis. First role was to act as a binder to sustain the particles on the support and the second role was to promote ion transport (desorption of H^+ or enhancing H_2O transport in the boundary layer¹⁵¹) forming a triple phase interface. Nafion is electronically insulating and it was possible to cause

an electrical resistance between NPs and carbon fibres if a large amount of Nafion ionomer would cover the fibre surface (or even block the electron path between NP and Vulcan® carbon additive)¹⁵².

Yet, according to the data in Table 5.3, at a higher potential such as 2.0 V_{RHE} (or larger current density, 10 $\text{mA}\cdot\text{cm}^{-2}$), MC1-CFS/5L performed better towards OER compared to lower loadings. At higher polarizations, the electrical charge at the anode surface could attract more OH^- species that requires extra amount of catalyst for O_2 evolution.

Table 5.3. OER parameters of MC1-CFS electrodes and benchmark DSA electrode in 0.1 M KOH under 10 $\text{ml}\cdot\text{min}^{-1}$ liquid flow

Sample	η mV †	Tafel mV $\cdot\text{dec}^{-1}$	j_{geo} mA $\cdot\text{cm}^{-2}$ Δ	j_{gravm} mA $\cdot\text{mg}^{-1}$	catalyst mg $\cdot\text{cm}^{-2}$
MC1-CFS/1L	707	113	12.02	18.49	0.65
MC1-CFS/2L	697	120	12.33	9.41	1.31
MC1-CFS/5L	683	151	12.85	3.91	3.28
DSA-1-d	668	165	11.83	n/a	n/a

† for 10 $\text{mA}\cdot\text{cm}^{-2}$, Δ at 2.0 V_{RHE}

As long as NPs are electrochemically accessible, higher catalyst mass loadings could sustain a larger current density at a given overpotential. Another significant value in Table 5.3 is the gravimetric current density which was obtained by normalizing the OER currents with the corresponding catalyst loading on CFS. It is clear that nearly ~ 5 x larger OER activity in terms of current could be obtained by applying a single layer of spin coating on CFS.

After CV tests, MC1-CFS/5L electrode was tested for long term stability (5 hours) at 2.0 V_{RHE} in ECf-cell under d-mode, Figure 5-16. The initial current density (12.51 $\text{mA}\cdot\text{cm}^{-2}$) under constant potential was well correlated to the value in CV experiments (12.85 $\text{mA}\cdot\text{cm}^{-2}$). However, a rapid decay of current density over time was observed. Nearly $\sim 70\%$ retention of the initial current density has been shown at the end of the first hour, Figure 5-16(b). One reason could be the poor attachment of NPs on CFS that was evident from periodic decay of the current density for 5

hours electrolysis. This appears to be a significant parameter that needs to be evaluated further considering that a constant OER activity is necessary if MC1-CFS electrodes would be used to complement CO₂RR in the future. CO₂RR is a potential-sensitive reaction, contrary to OER which can only undergo to O₂ evolution in aqueous solutions. However in CO₂RR experiments, for instance employing a working electrode with Cu catalyst, 3 or 4 different products can be produced for overpotentials between 0.2 – 1.0 V (at low overpotentials, CO and HCOO⁻ and high overpotentials, mainly C₂H₄ and CH₄).

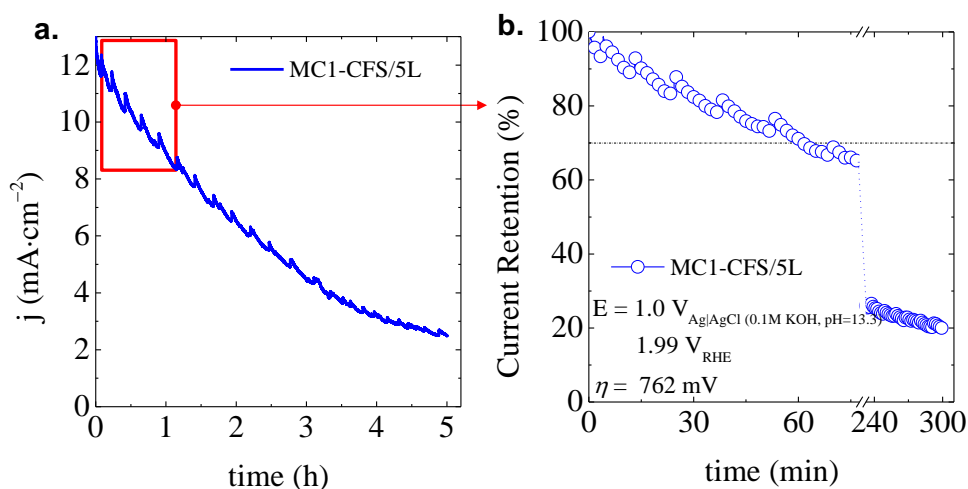


Figure 5-16. (a) Stability test of MC1-CFS/5L under constant potential ($\sim 2.0V_{\text{RHE}}$) during 5 hours in 0.1 M KOH under $10 \text{ ml}\cdot\text{min}^{-1}$ liquid flow (b) Normalized OER current activity with an emphasis on the first hour of electrolysis. Dash-dotted line represents 70% current retention.

5.3 Conclusion

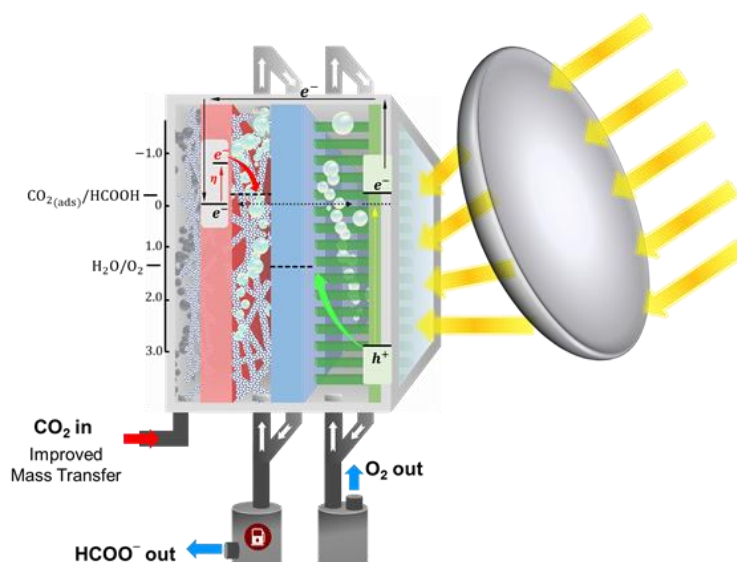
It was found that cation ion doping and nano-crystallite surface decoration have provided relatively low onset potentials and faster kinetics for spinel structures by increasing the availability of catalytically active sites³ providing higher affinity for O_2/OH^- absorption.¹⁰ In particular, the electrocatalytic activity of Co-Mn-O spinel particles were correlated with the oxygen binding ability on the catalyst surface³. The kinetic study of ORR mechanism suggested a $4e^-$ pathway via an initial $2e^-$ transfer to $O_{2(ads)}$ giving two $OH_{(ads)}$ proceeding with another $2e^-$ uptake thanks to enhancement of OH_{ads} adsorption on multivalent Co-Mn oxide sites (1:1 ratio with transfer coefficient value $\alpha_n = 0.87$ and $\alpha = 0.4$). These findings indicate that, in such complex catalyst, composition should be carefully adjusted to optimize performance in the both reactions, ORR/OER, in agreement with the state-of-the art⁹.

The presence of Co_xO_y crystallites allowed reaching OER performances above those of Co_3O_4 . Clearly, both $MnCo_2O_4$ and Co_xO_y played a key role in the overall performance as demonstrated by the weakening of the synergetic effect of the composite catalyst at high Co_xO_y loadings displayed with a volcano plot. We would postulate these improvements to i) a higher active site density after Co_xO_y nucleation; ii) enhanced charge transfer by highly conductive Co_xO_y phase⁷⁰; and iii) modified adsorption affinity for O_2/OH^- which could be supported with computational modelling.

Although $Mn_3O_4@CoMn_2O_4-CoO$ nanoparticles were promising in terms of their low cost, abundance and good catalytic activity, further work will be required to improve the immobilization method compared to benchmark DSA. This is a main drawback for their practical use in industrial electrochemical flow cells because the selectivity of CO_2RR is highly effected by current – voltage changes. For instance, in the previous sections (Chapter 3 and 4), the selectivity of Sn-GDE and Cu-GDE catalysts changed depending on the applied overvoltage. If anode compartment led to continues changes in its potential (and current) value, it would greatly influence the cathodic reaction and eventually the overall cell performance. Therefore, benchmark DSA will be used as the anode in the following studies until the stability of the NPs would be attained which could be the subject of another investigation.

CHAPTER 6

Light-CO₂RR & OER in PECf-cell



In this chapter, O₂ treated TiO₂ nanorods and electrodeposited Sn on gas diffusion electrode (GDE) have been studied in a photoelectrochemical flow cell (PECf-cell) under visible light irradiation. 1.2 V extra voltage was required for CO₂RR and OER overpotentials, yielding to very low CO₂ to formate (HCOO⁻) efficiencies, ca. 15 %. Two strategies were proposed to boost the efficiency which were (i) adjustment of cathode dimensions and (ii) concentration of solar light on photoanode. The former method gave above ~40 % faradaic and energy efficiency for HCOO⁻ near 6 hours while those values were increased beyond 65 % by introducing the second approach. Using H₂ treated TiO₂ nanorods as photoanode, same HCOO⁻ efficiency was accomplished at a lower bias potential, 0.95 V. The strategies followed here exhibit a maximum of 0.16 % applied bias photo-conversion and 0.25 % solar-to-fuel efficiency for HCOO⁻ beyond 5 hours. Those results prove that a decent system efficiency could be realized in industrial solar fuel synthesis.

6.1 Experimental Remarks

Titania nanorods (TiO_2 NRs) have been directly grown over a conductive substrate ($35 \times 40 \text{ mm}^2$ FTO-glass pieces) by using a hydrothermal process explained in Chapter 2. TiO_2 nanorods with different post annealing (under O_2 or H_2) were employed as photoanode in PECf-cell.

The engineering of photoanode assembly such as electrical wiring of the contacts, mechanical constraints of FTO glass substrate, isolation layers for electrolyte leakage, full stacking of PECf-cell and solar light concentration method were explained in detail in Chapter 2.

CO_2RR electrode was Sn-GDE so the main products of the reaction were formic acid, HCOOH (or formate, HCOO^- , according to pH) and carbon monoxide (CO) according to our previous results in Chapter 3. HPLC method was used to analyse the total amount of HCOO^- in the catholyte beaker after long electrolysis tests. The efficiency calculations (faradaic, energy and applied bias photo-conversion) were made from the number of moles and total number of coulombs at the end of the electrolysis, which was described in Chapter 2.

6.2 Results and Discussion

Among the different metal oxide photoanodes, as seen in Figure 6-1, compared to DSA anodes working in dark-conditions, TiO_2 photoanode could have the largest shift of the onset potential of oxygen evolution reaction (OER) under illumination thanks to titania large band gap and appropriate band edge positions^{97b} which would enable a lower cell potential. Besides, BiVO_4 photoanodes can be a good alternative for having higher conversion efficiencies than TiO_2 but its chemical stability limits the pH range of the electrolyte.¹⁵³ Thus, TiO_2 was selected for this study due to its robustness and photo-corrosion resistance.

One method that has been widely studied^{8, 87, 154} to improve charge collection efficiency is through the high aspect ratio structuring. Figure 6-2(a) shows the light absorption and separation of photoinduced free charge carriers in a photoelectrode.

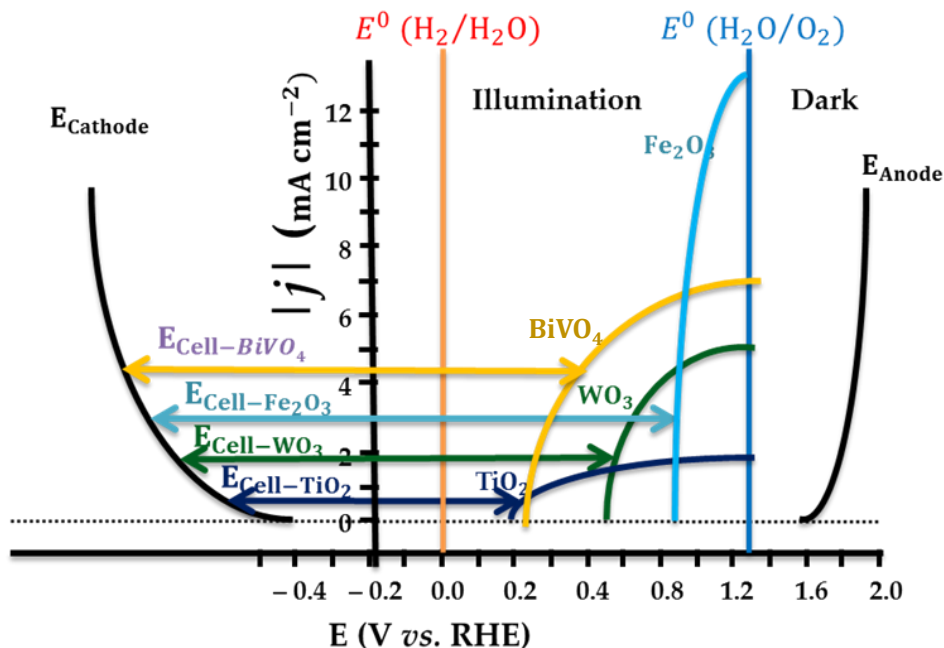


Figure 6-1. The standard redox potentials of HER (0 V_{RHE}) and OER (1.23 V_{RHE}) are given with straight lines. The y-axis were set at standard redox potential for CO₂R to HCOO⁻ (-0.225 V_{RHE}) The illustration of theoretical current - potential plots of a cathode performing CO₂R, > 400 mV overvoltage and a series of metal oxide type photoanodes performing OER under light irradiation. The illustration of an OER anode (DSA) is also given envisaging that >300 mV overvoltage is required.

Several studies of modelling and experimental demonstrations showed that¹⁵⁵ rod array like semiconductor structures were able to reduce the distance that minority carriers need to travel regardless of their short diffusion lengths (L_D). TiO₂ is an n-type semiconductor where the minority carriers are the holes which have short diffusion lengths. They must travel to electrode/solution interface to be collected by water molecules for OER. Vertically oriented 1-dimensional (1D) rutile titania nanorods can be obtained by hydrothermal synthesis which is shown in Figure 6-2(c-d). The cross-section FE-SEM images shows titania nanorods (TiO₂ NRs) grown by the hydrothermal process onto FTO covered glass substrates. The nanorods grew to a final rod length around 2.5 – 3 μm in a tetrahedral shape with a square tip. Higher magnification SEM images showed that each nanorod (150 \pm 50 nm) was formed by a bundle of smaller nanorods.

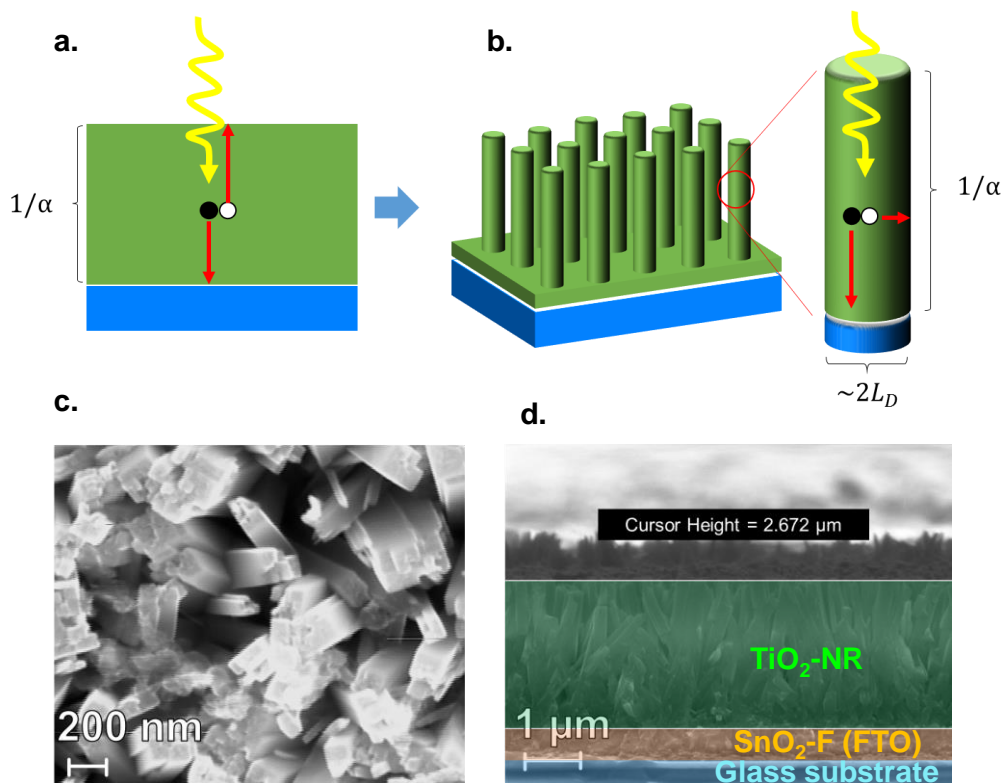


Figure 6-2. (a) In a planar device, photogenerated carriers must traverse the entire thickness of the cell, $\sim 1/\alpha$ (where α is the absorption coefficient), before collection. (b) In a rod-array cell, carriers must only reach the rod surface before recombination. L_D is the diffusion length of the photogenerated minority carrier (open circle). (c) Top and (d) cross-section image of TiO_2 -NRs synthesized by hydrothermal method.

6.2.1 Reaction at the anode side: OER

Figure 6-3(a) shows the OER activity of DSA and TiO_2 -NRs to compare by using LSV and CV techniques. DSA electrode gave $1.47 V_{\text{RHE}}$ on-set voltage under dark condition which corresponds to $0.24 V$ overvoltage given by,



Under light conditions, n-type behaviour of TiO_2 electrodes was revealed with anodic photocurrent starting at ~ 0.21 and $\sim 0.26 V_{\text{RHE}}$ for $\text{TiO}_2\text{-O}_2$ and $\text{TiO}_2\text{-H}_2$, respectively. Compared to DSA on-set voltage, illuminated TiO_2 photoanodes were able to shift OER on-set by $1.0 V$ to the negative direction thanks to its large band gap^{97b}, $\sim 3.0 \text{ eV}$. The maximum photocurrent detected was $0.83 \text{ mA}\cdot\text{cm}^{-2}$ for H_2 treated TiO_2 photoanode in front illumination condition. Additionally, H_2 treatment improved the fill factor (FF) in front (0.44 to 0.50) and back (0.52 to 0.64) illumination conditions.

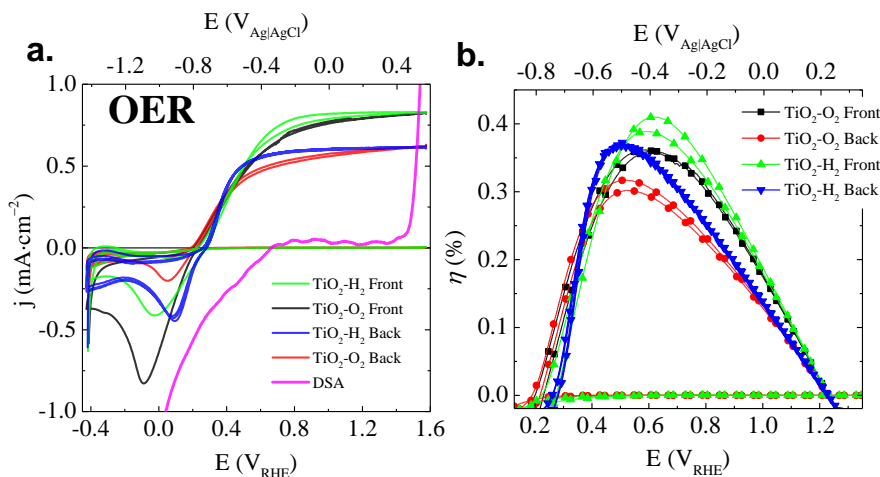


Figure 6-3. (a) OER analysis by linear sweep voltammetry of DSA/OER ($IrO_2-Ta_2O_5/Ti$) along with cyclic voltammograms of TiO_2 electrodes with O_2 and H_2 post-annealing treatment under EE (front) and SE (back) illumination. (b) Assisted photocurrent efficiency (η %) of TiO_2-O_2 and TiO_2-H_2 electrodes Electrolyte: 0.5 M NaOH, AM 1.5G, ca. 1 sun and potential sweep rate is 20 mV/s.

Post-annealing of TiO_2 NRs have showed that the density of oxygen vacancies (donor density) would increase under reducing gas atmosphere such as H_2 ⁹³ or ammonia^{97b} (NH_3). So, the improvement of FF and j_p would be correlated to the enhancement of the electrical conductivity and charge separation.

Table 6.1. Electrochemical activity of Dimensionally Stable Anode (DSA) under dark conditions and, TiO_2-O_2 and H_2 photoelectrodes at a sun intensity of $100 \text{ mW} \cdot \text{cm}^{-2}$ AM 1.5 G towards OER in 0.5 M NaOH

	Illum.	j_p $\text{mA} \cdot \text{cm}^{-2}$	$E_{\text{on-set}}$ V_{RHE}	η %	j_{mp} $\text{mA} \cdot \text{cm}^{-2}$	E_{mp} V_{RHE}	FF
TiO_2-O_2	Front	0.79	0.215	0.36	0.56	0.59	0.44
TiO_2-H_2	Front	0.83	0.254	0.41	0.67	0.62	0.50
TiO_2-O_2	Back	0.59	0.203	0.32	0.45	0.52	0.52
TiO_2-H_2	Back	0.60	0.269	0.37	0.51	0.50	0.64
Anode		j $\text{mA} \cdot \text{cm}^{-2}$	$E_{\text{on-set}}$ V_{RHE}			E^Δ V_{RHE}	
DSA		0.02	1.46			1.52	

Illum. is illumination condition; j_p (or j) is photocurrent and current density at $1.23 V_{RHE}$ respectively; η is the assisted photocurrent efficiency; j_{mp} and E_{mp} are the photocurrent and voltage at max η , respectively; FF is the fill factor of the photo-electrode. E^Δ is the voltage of DSA at $0.6 \text{ mA} \cdot \text{cm}^{-2}$

Figure 6-3(b) shows the increase in photocurrent efficiency, η %, from 0.36 to 0.41 % after the H_2 annealing. Nearly ~ 20 % of change in photocurrent at maximum

power (j_{mp}) between front and back illuminated electrodes were due to the light absorption at the FTO coated silicate glass. A summary of OER parameters are given in Table 6.1. In PECf assembly, TiO_2 photoelectrode would be placed in back-illuminated arrangement due to its interaction with the electrolyte-membrane-cathode parts for ionic charge transfer. Therefore, we would take back illuminated values into consideration for overall current and potential values in the full cell assembly.

6.2.2 Energy balance of full cell: Sn-GDE vs. Ti_2O -NR

Same area ratio

In a CV experiment, a lesser amount of the product would be generated near the vicinity of the electrode which would be consumed in the reverse scan. However, the dynamic flow disturbs the reactant to product ratio. This might lead to misinterpretation for a steady-state mode, because several $mV \cdot s^{-1}$ scan rate would be relatively short period to evaluate electrode potential values. Therefore, the voltage-step tests were conducted by taking the average of electrode potential values during 5 minutes under a fixed cell bias by using two channels in master & slave configuration. Briefly, the master channel (2-electrode mode) was responsible for overall cell current between the anode and cathode, while slave channel (3-electrode mode) would only follow the electrode potentials respect to reference electrode.

Once assembled, with the TiO_2 photoanode (10 cm^2) in the anodic compartment and Sn-GDE (10 cm^2) at the cathodic one, the cell was polarized for 5 min at different cell potentials from 0.4 to 2.4 V. As can be observed in Figure 6-4, contrary to what occurs in the process under dark conditions, under irradiation of the photoanode, cathode polarized at applied cell voltages lower than 1.8 V. When the cell voltage increased, then photoanode polarization increased. Nevertheless, contrary to what it is observed in the process under dark conditions, wherein increasing the cell voltage, then higher cathode polarization occurs, in the photoelectrochemical process, it is observed that between 1.2 V and 1.6 V, the cell voltage increase is invested in polarizing the photoanode while the cathode polarization remains constant. Therefore, working with this photoelectrode and the Sn cathode above 1.2 V (E_{cell}) will not be translated into an improvement of the faradaic efficiency of the

photoelectrochemical process. Above 1.8 V (outside the working range of the photoelectrochemical cell), the photoanode no longer limits the process and again the cathode polarization increases with increasing the cell voltage.

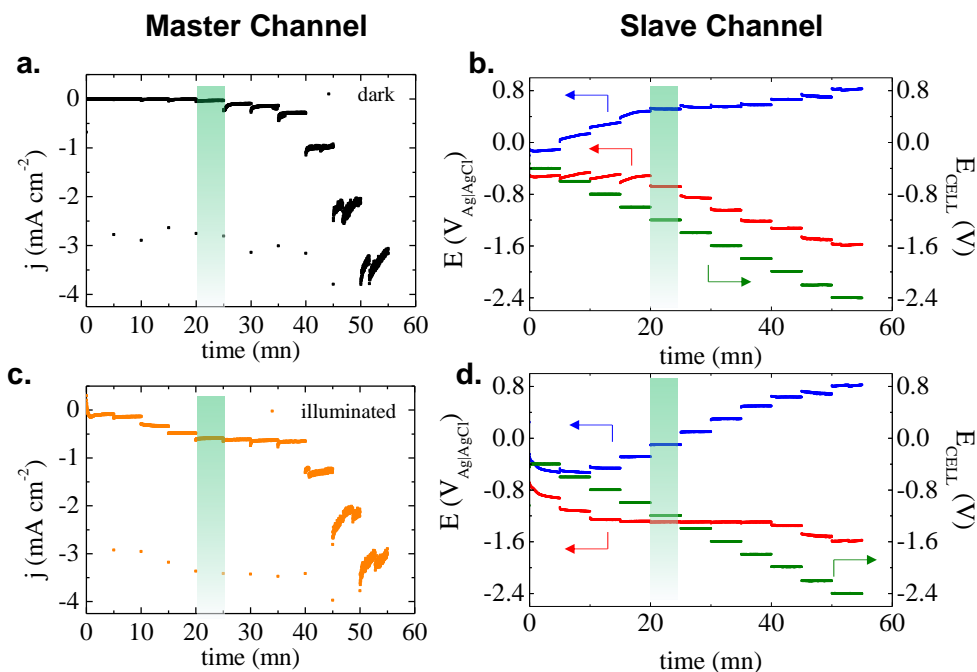


Figure 6-4. Voltage step tests in master-slave configuration under (a-b) dark condition and (c-d) AM 1.5 G solar light illumination condition.

A photoelectrolysis test was done at an applied cell voltage of 1.2 V for quantification of formate by HPLC and a faradaic efficiency to formate of around 16 % was obtained.

Different area ratio and sunlight concentration

In photo-assisted electrochemical cells, energy balance was obtained by maintaining the optimum operation potentials of both electrodes. For OER, the maximum photocurrent efficiency using the TiO₂ NRs will be achieved between -0.5 and -0.3 V_{Ag|AgCl} providing 0.5 mA·cm⁻². This corresponds to an intensity of ca. 5 mA respect to TiO₂ for an electrode of 10 cm². On the other hand, the most suitable potential for CO₂R over HER would be between -1.4 and -1.6 V_{Ag|AgCl} providing from 3 to 5 mA·cm⁻². Thus, this potential range would provide 30 – 50 mA on the 10 cm² cathode (Sn-GDE10) in PEC_f assembly. These calculations indicate that net currents at both electrodes must be balanced, which could be achieved with the

selected electrodes by two strategies, (i) decreasing the Sn-GDE geometrical area to confine a higher energy density at the cathode or (ii) increasing solar flux on TiO₂ photoanode by solar concentrators to uplift the photocurrent.

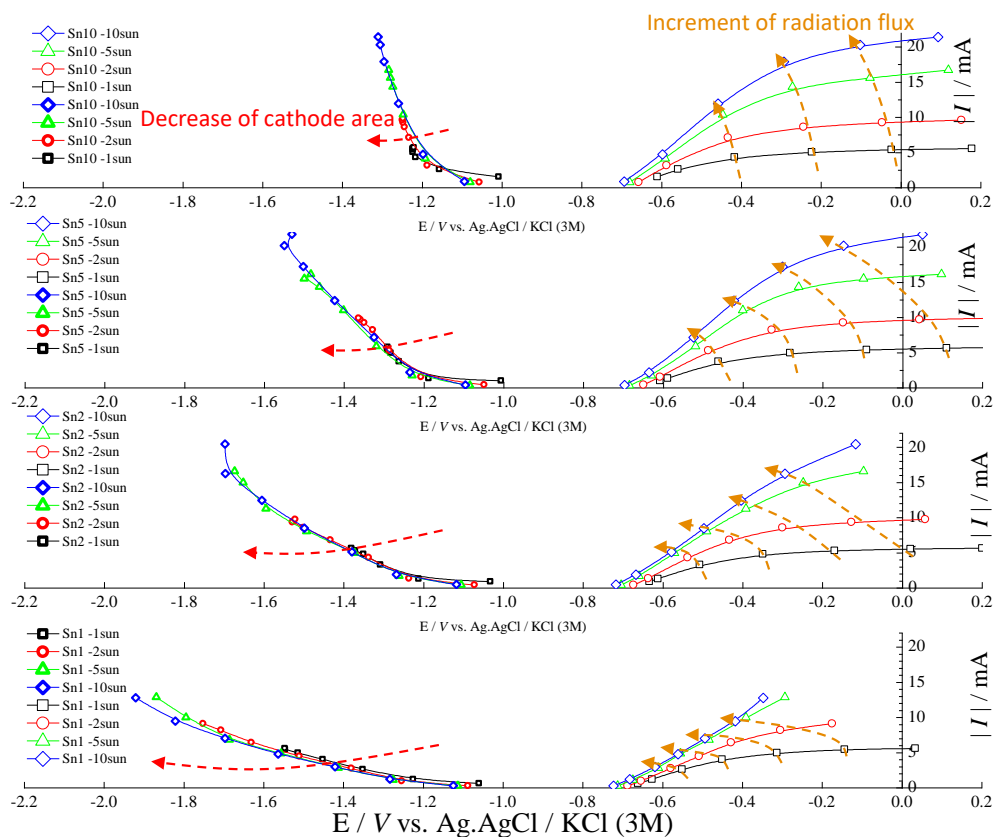


Figure 6-5. Electrode potentials and current value of voltage step tests collected from slave and master channels, respectively. Sn-GDE area was decreased from 10 to 1 cm² whereas the sunlight illumination was changed from 10 to 1 sun intensity (1 sun intensity = 100 mW·cm⁻² AM. 1.5G)

Therefore, the photoelectrochemical cell was adapted to accommodate different cathode sizes (10, 5, 2, and 1 cm²) while maintaining the photoanode size fixed at 10 cm². Figure 6-5 shows the evolution of the individual cathode and photoanode potentials at different radiation fluxes from 100 mW·cm⁻² (1 sun) to 1000 mW·cm⁻² (10 suns) and for an anode-to-cathode area ratio of 1, 2, 5 and 10 cm². It was observed that in all cases increasing the radiation flux increased the photoanode polarization, as seen also for the current intensity (photocurrent) and cathode polarization; besides cathode polarization increased as with smaller cathode area and thus higher cathode potentials were obtained. Since the absolute value of

applied voltage is the difference of both electrode polarizations, Sn-GDE potential could be shifted to more negative potentials by either increasing the radiation flux or adjusting the geometrical area of the cathode, to avoid the drawback of reaching the limiting photocurrent of TiO₂ where further polarization lies just at the photoanode and not at the cathode. Considering the results of dark electrolysis, the correlation between the cathode polarization values and the cathode current intensity ranges required to obtain different faradaic efficiencies allow us to estimate the faradaic efficiency range that could be expected in each case.

The individual values of current and potential values of each step was plotted for SnGDE10 and SnGDE1 vs. TiO₂-O₂. Figure 6-6 shows the first strategy which was the decrease of Sn-GDE geometrical area from 10 to 1 cm² in order to localize the energy density given by,

$$\text{Energy Density (mW} \cdot \text{cm}^{-2}) = \frac{I \text{ (mA)}}{\text{area (cm}^{-2})} \cdot E \text{ (V)} \quad (6.2)$$

By doing so, the photo-current at TiO₂ photoanode provided by 1 sun solar flux (AM 1.5G, 100 mW·cm⁻²) shifted the cathode potential to an energetically more favourable potential range for CO₂RR. The photocurrent density of TiO₂ gave earlier on-set potentials at lower cell bias values but the saturation current was similar in both systems at larger bias values. It appears that Sn-GDE cathode dimension could not be larger than 1 cm², otherwise FE% would substantially fall. Besides, larger bias values (beyond 1.2 V) were not beneficial because all the polarization voltage have spent by TiO₂-O₂ photoanode's current under saturation until the dark current would prevail.

The cell currents were obtained by a chronoamperometry method at 1.2 V cell bias at the master channel and current values were normalized respect to geometrical area of Sn-GDE (left y-axis in Figure 6-6 (b)) in order to highlight the effect of energy localization between two systems.

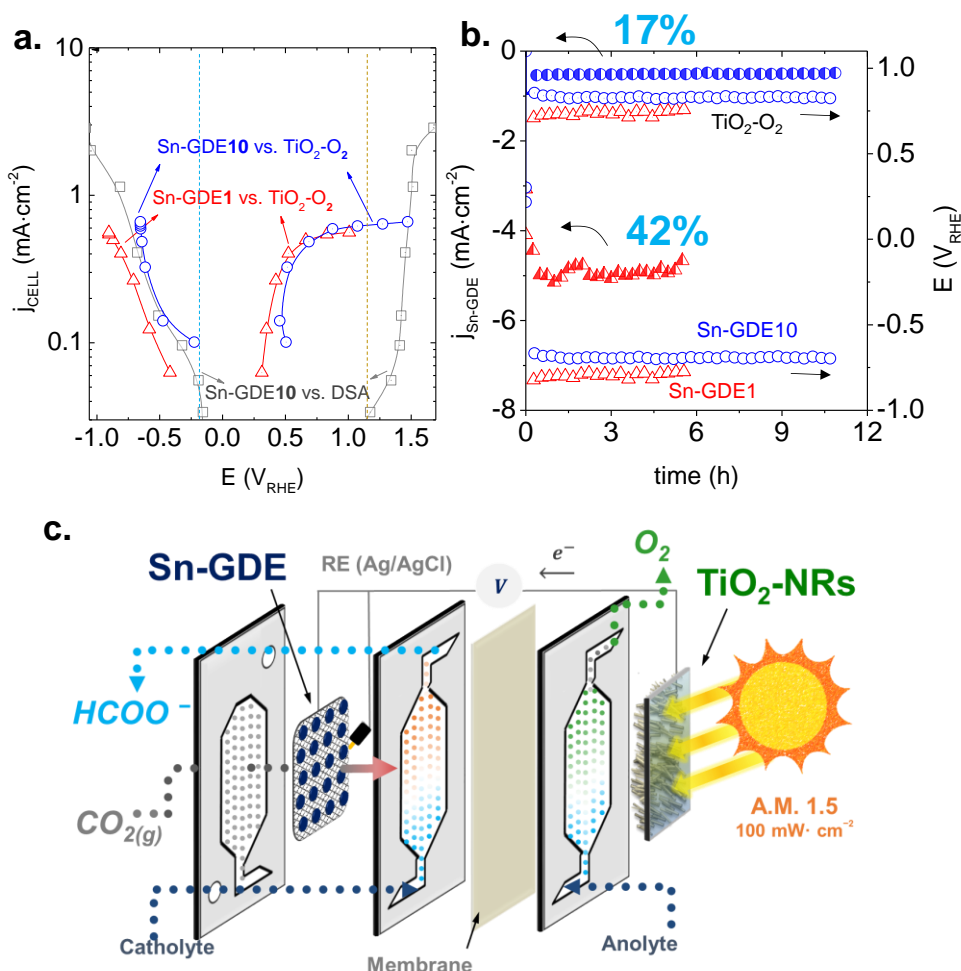


Figure 6-6. (a) j and E points recorded by voltage-steps test of Sn-GDE (1 or 10 cm^2) vs. $\text{TiO}_2\text{-NRs}$ under 1 sun (AM 1.5 G) solar illumination, including the points recorded from Sn-GDE10 vs DSA/OER voltage-steps test (b) Long term stability test under the same conditions but at fixed cell potential of -1.2 V (c) Schematic image of the stack assembly for cathode and anode parts showing the flow directions of gas and liquid. $\text{TiO}_2\text{-NRs}$ are illuminated from back (glass) side.

The individual electrode potential values were followed with a leak free micro-reference electrode and recorded by the slave channel (right y-axis in Figure 6-6 (b)). At the end of the tests, HPLC analysis over the electrolytes samples showed that F.E. % for HCOO^- was increased nearly 2.5 times (from 17 to 42 %). The current and potential values remained constant during the entire stability test (~ 11 and ~ 6 hours for Sn-GDE10 and Sn-GDE1).

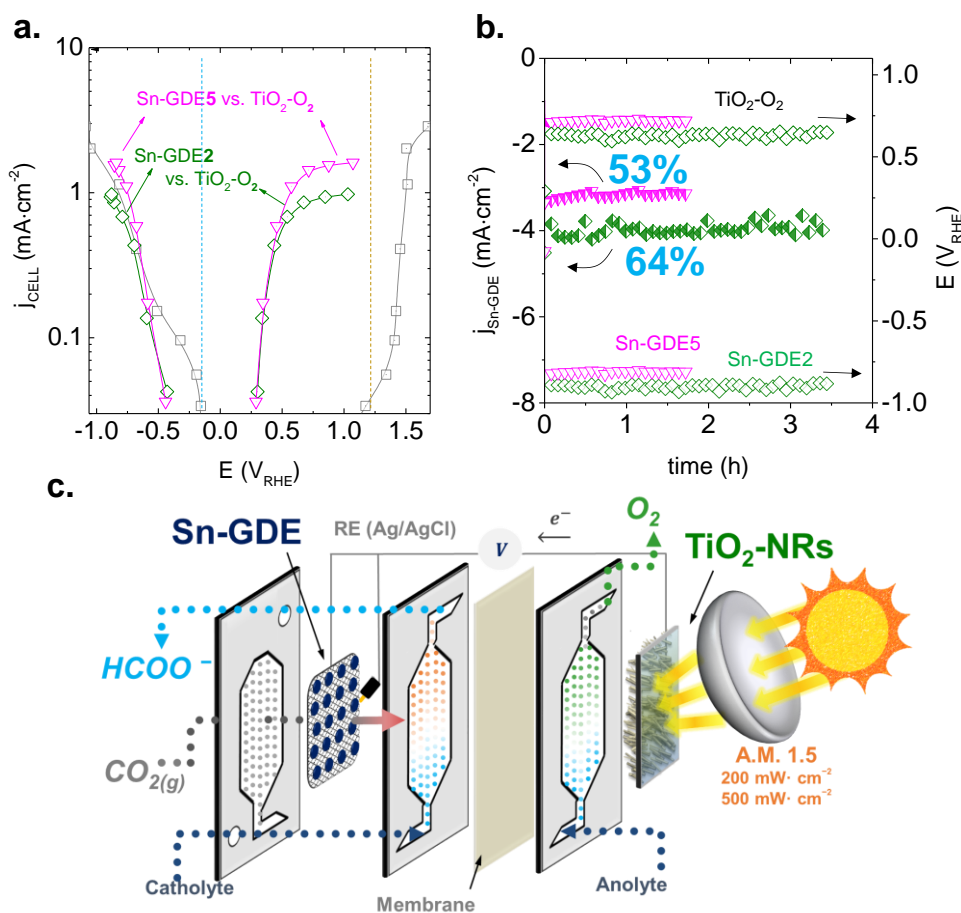


Figure 6-7. (a) j and E points recorded by voltage-steps test of Sn-GDE(2 or 5 cm²) vs. TiO₂-NRs under 2 or 5 suns (AM 1.5 G) solar illumination, respectively, including the points recorded from Sn-GDE vs DSA/OER voltage-steps test (b) Long term stability test under the same conditions but at fixed cell potential of -1.2 V (c) Schematic image of the stack assembly for cathode and anode parts showing the flow directions of gas and liquid. TiO₂-NRs are illuminated from SE (back) side with 2 or 5 suns (AM 1.5 G) by solar concentration.

As outlined previously, the net current requirement of a larger cathode would be as high as 30 mA to obtain an efficient reduction of CO₂ at SnGDE ~ 10 cm². Besides, the increment of the cell bias would not provide higher current density owing to the limitation by photocurrent saturation. Figure 6-7 shows the *second strategy* for further increment of faradaic efficiency in parallel with the solar light power. Our measurement on voltage steps tests showed that, net photo-current of TiO₂ nanorods could be increase but up to a certain value of solar power. The maximum photocurrent cannot be increased to values beyond 30 mA even 10 times higher solar flux (1000 mW·cm⁻²) would be concentrated on the photoanode reaching to faradaic efficiency of 64 % and energy efficiency of 70 % which is discussed in the next section.

6.2.3 PECf system efficiency

In PEC cells, solar-to-fuel efficiency, STF^{xix} is the most used figure of merit to describe the overall system efficiency⁸⁸. In our system, this would be the ratio of output power (chemical energy stored in terms of formate) to input power (AM 1.5G solar light and applied bias) given by,

$$STF^* (\%) = \frac{(\text{mol HCOO}^-/\text{s}) \cdot (254,721 \text{ J/mol})}{[P_{\text{solar flux}} + P_{\text{bias}} (\text{W} \cdot \text{m}^{-2})] \cdot \text{Area} (\text{m}^2)} \quad (6.3)$$

where $P_{\text{solar flux}}$ is the power generated by the solar light simulator and P_{bias} is the bias produced by the potentiostat and pH difference. The advantage of Eq. (6.3) would be the reliability of the power output (at the numerator) based on the HCOO^- production rate detected by HPLC. The results of the calculations were given in Table 6.2 that both strategies provided similarly high STF efficiency, $\sim 0.25\%$.

Most of the results in the literature are based on half-cell reactions covering only CO_2R or OER under light illumination. Amongst a few studies on full cell configuration, a photoelectrochemical flow cell is first of its kind so far, that minimizes the electrolyte gap and optimizes solar to fuel conversion by adjusting the operational working conditions of the photoelectrochemical cell (irradiance and anode-to-cathode area ratio). Among the data, coupling of Sn-GDE – TiO_2 in PEC_f shows the highest faradaic efficiency (45-64 % HCOO^-) for reduction of CO_2 to HCOO^- with the lowest cell bias, such as in BiVO_4 coupled with Cu^{156} or WO_3 coupled Sn/ SnO_x ¹⁵⁷ where the faradaic efficiency was limited to 44.3% ($\text{CO} + \text{HCOO}^-$) since the cell was not rationally optimized. Moreover, 0.25% solar conversion is one of the highest efficiencies reported amongst the data obtained from full cell configurations (e.g. 0.14 % efficiency obtained with SrTiO_3 photoanodes²²)

Table 6.2 summarizes the system efficiencies after long term experiments ranging from 2 – 11 hours. The increment of final formate concentration and energy efficiency, demonstrate that solar light concentration could be a feasible strategy.

^{xix} STF is used for solar-to-fuel but in this section, produced fuel is formate, HCOO^- so STF^* would be solar-to-formate efficiency.

Table 6.2. PECf cell conditions and system efficiencies of discrete electrolysis (charge accumulated 4C/mL)

E _{cell} (V)	Area cathode (cm ²)	j _{cathode} (mA cm ⁻²)	Irradiance (mW·cm ⁻²)	F.E. (%)	E.E. (%)	STF* (%)
1.2	10	0.5	100	17	19	0.11
1.2	5	2.9	500	64	70	0.25
1.2	2	3.4	200	53	58	0.24
1.2	1	4.0	100	42	46	0.22
0.95	1	4.1	100	42	58	0.23

λ is solar flux of A.M. 1.5 in mW·cm⁻² and j is the cell current normalized for Sn-GDE geometrical area in mA·cm⁻², [M] is the molarity in mmol HCOO⁻ per litre. ABPE is applied bias photon-to-current efficiency and is a direct comparison of dark vs. light system. STF is solar-to-fuel efficiency and contains the chemical bias in the denominator in Eq. 6.10 (as input power).

The use of concentrated light for solar energy conversion is an extensively studied field, especially on high intensity photovoltaics and solar thermal electricity generation. For instance, commonly used solar concentrators in the industry include heliostats, parabolic reflectors and Fresnel lenses¹⁵⁸. This provides a wealth of experience available in the solar energy industry for the design and construction of concentrated solar systems for photoelectrochemical cells.

Another promising feature of this system would be the ease of different photoelectrodes implementation at the anode compartment. For instance, we have conducted several tests with TiO₂-H₂ nanorods which could provide slightly higher current density than conventional O₂ treated photoelectrodes. Under 1 sun illumination, faradaic and energy efficiency for formate production were enhanced at the same bias value, 1.2 V. Additionally, PECf system was able to operate at even lower bias values such as 0.95 V with TiO₂-H₂ photoanode, which provided highest ABPE with 0.16 %. This could be explained with the improvement of FF (0.52) after hydrogen treatment (0.64 given in Table 6.1). Most of the results in the literature have been based on half-cell reactions covering either CO₂RR or OER under light illumination. Amongst a few studies on full cell configuration, a photoelectrochemical flow cell is first of its kind so far. The cell potentials reported for a complete photoelectrochemical cell grasping CO₂RR and OER are given in Table 6.3.

Table 6.3. PECf cell conditions and system efficiencies shown in Fig. 6-6 and Fig. 6-7

Cathode (CO ₂ RR)	Anode (OER)	Cond.	HCOO ⁻		Ref.
			F.E. %	STF %	
p-InP/Ru complex ($\lambda > 400$ nm)	SrTiO ₃ (0.25 cm ²)	OCV	71	0.14	2013, Arai et. al., Energy Environ. Sci., 2013 (6) pp 1274 ²²
Sn/SnOx (1 cm ²)	WO ₃ (4 cm ²) ($\lambda > 420$ nm)	~0.7 V _(CELL)	27	-	2013, Magesh et. al., J. Mater. Chem. A, 2014 (2) pp 2044 ¹⁵⁷
Pt-rGO/Ni (7 cm ²)	TiO ₂ -NT/Pt (7 cm ²) (UV-Vis/Xe arc lamp)	2.0 V _(CELL)	~4.5	-	2015, Chen et. al., Solar Energy Materials and Solar Cells. 2015 (132) pp 606 ¹⁵⁹
Carbon cloth /Ru complex	IrO _x /SiGe-aSi-3jn (0.25 cm ²)	OCV	94	4.5	2015, Takeo et. al., Energy Environ. Sci., 2015 (8) pp 1998 ²³
Cu _x O nanowires	WO ₃ (0.25 cm ²)	~1.0 V _(CELL)	1.5	-	2016, Deb Nath et. al., Nano Energy 2016 (25) pp 51 ¹⁶⁰
H-Si-NW/Rh- mediator /NADH	3-jn-Si/ITO/CoPi ($\lambda > 420$ nm)	1.8 V _(CELL)	16	-	2016, Son et.al., Chem. Commun., 2016, (52), pp 9723 ¹⁶¹
Pd/C (0.04 cm ²) (2.8M KHC03)	GaAs/InGaP / TiO ₂ /Ni (0.03 cm ²) (1M KOH)	OCV	94	10	2016, Zhou & Lewis N., ACS Energy Lett., 2016, 1 (4), pp 764 ²⁴
Sn-GDE (5 cm ²)	TiO ₂ -O ₂ (10 cm ²) (500 mW/cm ²)	~1.2 V _(CELL)	64	0.25	This study
Sn-GDE (1 cm ²)	TiO ₂ -H ₂ (10 cm ²) (100 mW/cm ²)	~0.95 V _(CELL)	42	0.25	This study

λ is the solar flux and OCV is bias free condition where the cell is at open circuit voltage.

There are several examples listed which use UV light illumination at photoanode for OER or organic molecules at photocathode as CO₂RR promoters (i.e. Ru- or pyridine complexes). As highlighted in a recent study, relatively small active device area had to be used due to the instability of photoelectrodes by pinholes and other defects at large electrode areas which cause active dissolution and degradation²⁴, whereas our electrodes ensured more than 2-fold geometrical active area. This would be a critical parameter considering rate of conversion from a continuous flow of CO₂ gas into a solar fuel product. Amongst the data, coupling of [Sn-GDE vs. TiO₂-O₂/H₂] in

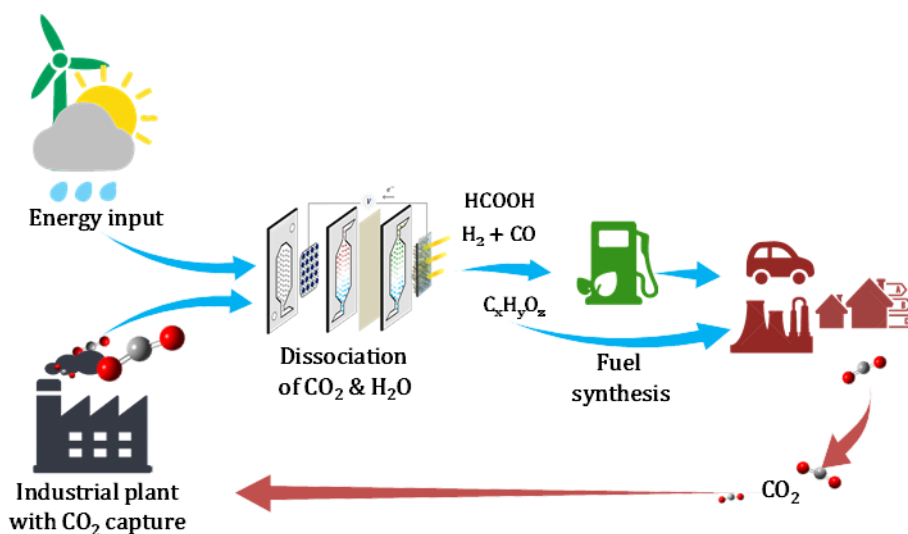
PECf shows an outstanding faradaic efficiency (45-64 % HCOO⁻) for reduction of CO₂ to HCOO⁻, including the lower bias potential (0.95 V) than that of [WO₃ vs. Sn/SnO_x]¹⁵⁷ (1.5 % HCOO⁻ 1.0 V).

6.3 Conclusions

A photoelectrochemical flow cell working under continuous flow of gas and liquid was constructed for simultaneous CO₂RR and OER. Under external bias of 1.2 V, Sn coated carbon fibres of GDE (Sn-GDE) exhibited a sturdy electrocatalytic activity for CO₂ conversion to HCOO⁻. Faradaic efficiencies of 45–65 % for HCOO⁻ production were obtained under a cell bias of 1.2 V when coupled with TiO₂-O₂ photoanodes, whereas Faradaic efficiencies of 42 % were achieved at a lower negative potential (0.95 V) for TiO₂-H₂ photoanodes. After long term stability tests, maximum HCOO⁻ production by assisted solar illumination reached 0.25 % STF were calculated after 5.5 h. PECf system demonstrated a stable rate of HCOO⁻ production from CO₂RR under prolonged solar illumination reaching 11 hours, despite a small change in the alkalinity of the anolyte. Those results prove that, even though the cathode and anode do not perfectly match in terms of current density or on-set potential to run in zero-bias mode, these results provide strategies for materials scientists to modify cell designs which provide comparable results for producing solar fuels.

CHAPTER 7

Conclusion & Perspectives



This chapter summarizes the results between Chapter 3 and 6. The main principles and key figures are underlined to complement experimental findings. The best results from each chapter are given with a table to compare the advantages and drawbacks of each system modification. Two cell configurations that work under dark and light conditions are compared in terms of the energy consumption vs. final product amount, formic acid (HCOOH). Finally, an outlook and future perspectives towards CO₂ reduction reaction are highlighted.

7.1 Conclusions

The main contribution of this work was to bring fundamental and functional understanding in domain of artificial photosynthesis at device level. One of the most important challenge in a solar-to-fuel conversion device is to confirm a positive monetary and net energy balance over their lifetimes to be viable for large scale deployment. In this line, catalyst materials ensuring high selectivity and stability for carbon dioxide (CO_2) reduction to formate (HCOO^-) in aqueous electrolytes have been implement and studied in a filter press photoelectrochemical cell. A special attention was devoted for HCOO^- production for its modest energy requirement and utilization in various applications (e.g., direct formic acid fuel cells¹²⁰; leather, textile, chemical and food industries). The parameters addressed and optimized for this system cover; gas and liquid flow rates (5 to 50 $\text{ml}\cdot\text{min}^{-1}$), electrocatalytic activity of different metal/metal oxides (Sn, Cu metals and MnCo-oxides), active area of electrodes (1 to 10 cm^2 for one site) and solar light concentration on the photoelectrode (100 to 500 $\text{mW}\cdot\text{cm}^{-2}$). Hence, effective coupling of electrodes and operational parameters allowed us to reach a maximum of 0.25 % solar-to-fuel (STF) efficiency for conversion of CO_2 into HCOO^- which is one of few prototype STF value to be reported at device level. The disclosed information in this thesis can be valuable for the future deployment of artificial photosynthesis from device level to industrial levels.

- Chapter 3

In comparison of bicarbonate electrolytes, catholyte with 0.5 M KHCO_3 showed 200 mV improvement over 0.5 M NaHCO_3 in overall cell voltage. Electrolyte cation size is known to influence the electrochemical reduction of CO_2 over metals which could either be attributed to specific adsorption and steric hindrance of increasing cation size¹⁶² or be related to higher buffering effect of larger cations maintaining a favourable pH and local CO_2 concentration.¹⁶³ The effect of hydrodynamic conditions (flow rate of CO_2 gas and liquid electrolytes) were also evaluated in this chapter by testing three different values (5, 10 and 50 $\text{mL}\cdot\text{min}^{-1}$) systematically. Our findings showed that the residence time of CO_2 molecule at the active site of the catalyst plays a key role in the initial adsorption and consecutive electron-proton uptake. This was supported with the increase of cathode potentials at higher flow

rates creating a local turbulence and hindering active sites. Nevertheless, 1:1 ratio of gas to liquid gave the highest faradaic efficiency (~71 and 74 %) and proved to be stable beyond 6 hours, therefore following tests were conducted with this ratio.

- Chapter 4

The same cell set-up but with CuGDE as cathode for CO₂RR and Selemion membrane which allows the diffusion of anions (OH⁻) instead of. This allowed us to maintain a pH balance (~6.8) utilizing bicarbonate electrolyte at both sites with a compromise of higher cell voltage value 3.2 V due to lower ionic conductivity and unfavourable OER kinetics in this electrolyte. The pulsed current electrodeposition (PCE) method employed in this chapter showed a remarkable particle nucleation & growth on the fibres inside GDE including a good control on the Cu-particles size creating Cu-islands. This was attributed to the improved Cu ion diffusion into the GDE pores during the OFF time of PCE. Moreover, a trend between Cu-island size and product selectivity was found. Smaller Cu-islands (~700 nm) promoted HCOOH while selectivity shifted to CO with larger Cu-islands (~1.5 – 2 μm). The defect sites were suggested to act as active sites in CO₂RR^{124, 128, 136, 164} thus increased amount of grain boundaries with smaller Cu-islands could be responsible for this improvement.

- Chapter 5

Mn₃O₄, Co₃O₄ and Mn₃O₄@CoMn₂O₄-Co_xO_y mixed oxides nanoparticles were studied to replace a commercial anode of Ta₂O₅-IrO₂. First, kinetic studies were conducted to gain an insight on the electron transfer mechanism. The result suggested a quasi-reversible 4e⁻ transfer pathway which was attributed to enhancement of OH_{ads} adsorption on multivalent Co-Mn oxide sites in the heterostructured nanoparticle (Mn:Co ratio 1, MC1). OER performance of MC1 also showed fast kinetics with a low Tafel slope value (95.2 mV·dec⁻¹) and overpotential (310 mV). Consequently an ink of MC1:Vulcan carbon:Nafion was deposited by spin coating on GDL and tested in ECf-cell under continuous flow of liquid electrolyte (0.1 M KOH). The initial Tafel slope and potential values were similar to RDE tests (113 mV·dec⁻¹ and ~350 mV) but a rapid activity decay of current density was observed. The initial conclusion was the particle detachment from GDL substrate however further work could be performed to find an alternative deposition method to improve longevity.

- Chapter 6

TiO₂ nanorods were grown with hydrothermal method on 10 cm² FTO glass substrate and used as photoanode to exploit solar energy input for PECf-cell. This photoanode could provide a low on-set potential around 0.6 V_{RHE} for OER, whereas cathode on-set potential was for ca. -0.6 V_{RHE} for CO₂RR corresponding to 1.2 V bias voltage and ca. 0.5 mA·cm⁻² under 1 sun illumination. The resulting faradaic efficiency (F.E.) was 17 % for CO₂ conversion to HCOO⁻. Two strategies were applied to increase this value. The decrease of SnGDE area from 10 to 1 cm² which tripled F.E. to 42 % HCOO⁻ while increase of solar flux from 1 to 5 sun quadrupled this value, 64 % HCOO⁻ along with 0.25 % solar-to-fuel conversion efficiency. The post-annealing of TiO₂ nanorods under reductive H₂ atmosphere offered 20 % enhancement of the fill factor playing a significant role on the lessening of overall cell voltage from 1.2 V to 0.95 V bringing 42 % F.E. and 0.23 % STH for HCOO⁻.

- Overview of economic analysis for ECf-cell vs. PECf-cell

In comparison of the best results^{xx}, there are several advantages and drawbacks in each one of them. For instance, ECf-cell system of Chapter 3 employing SnGDE provided the highest gas-to-fuel conversion yield at 4%, while this value decreased in other configurations due to the lower partial current density and electrode vs. electrolyte contact area. Gas-to-fuel yield is a very important figure for large scale deployment of this process so ECf design coupled to an array of solar collectors seems more feasible. On the other hand, PECf design offered a lower partial current density for HCOO⁻ but the energy efficiency (E.E.) of the system up increased from 33 % (ECf-cell in dark) to 70 % (PECf-cell under light). Considering energy efficiency, introduction of solar energy with PECf design seems more interesting. Meanwhile, in terms of energy consumption per unit of product, the evolution in this dissertation study shows a remarkable cost reduction for HCOOH synthesis from CO₂ gas. Using a solar light assisted flow cell system (PECf-cell design), HCOOH fuel cost was reduced by half (ca. 234 to 100 Wh·mol⁻¹) close to its combustion energy, 70.7 Wh·mol⁻¹.

^{xx} See Table 9.2 in Annex

7.2 Future Perspectives

The three main targets of any catalytic reaction are the selectivity, stability and cost. Unfortunately, CO₂RR cannot provide all at the same time. Expensive metal catalyst such as Au or Ag can provide high selectivity towards CO above 90 % whereas Hg metal can produce HCOOH beyond 95 % faradaic efficiency. The cost (\$/g) and stability of such metals remains to be solved. Cu is the unique catalyst that forms higher carbon derivatives from electroreduction of CO₂ and Cu metal is relatively cheaper than former metals but its selectivity for one product (> 90 %) has not been demonstrated yet. Apart from metal catalysts, organic compounds such as pyridine and Ru/Re(bipy)-complexes could offer high selectivity for CO but their low current density and high cost is another challenge. In this respect, research and development should focus on specific aspects of electrocatalytic reactions by dividing the concepts into four categories:

1. Electrode – catalyst formation
2. Electrolyte – additives effect
3. Cell – reactor design
4. Reaction mechanism – in-situ methods and computational analysis

In the first category, there are plenty rooms to study from nano-materials (e.g. graphene supported metals) to nano-alloys (e.g. bottom-up synthesis of two different metals with low and high CO bonding) and mixed metal oxides (e.g. perovskite family with oxygen or carbon end-group). Apart from the catalyst material, the immobilization methods are also important. Deposits with a high roughness factor and good mechanical resistance are of particular interest. Gas diffusion electrodes are vital for flow reactors, therefore firm attachment of the catalyst on GDE under dynamic flow conditions are required. Electrodeposition or chemical vapour deposition methods could be optimized to form mixed metal/metal oxides with precise stoichiometry.

The aqueous electrolytes limit CO₂ reduction to a lower current density due to competitive HER but the solubility of most organic electrolytes is much higher than water. CO₂ solubility in dimethyl sulfoxide (DMSO) and acetonitrile (CH₃CN) is 4 times; propylene carbonate (PC) is 8 times; and dimethylformamide (DMF) is 20 times that in water. Additionally, the additives such as pyridine is a hot topic that it

can provide coordination sites for the fixation of CO₂ intermediates. The challenge here is to overcome low ionic conductivity of those solvents and finding suitable agents to the complementary anode reaction to realize a full cell configuration.

The third category must be the optimization of the full cell. Our approach was to increase electrolyte vs. electrode contact area and maximize gas-liquid-catalyst junction sites. This approach could be developed by altering the reactor design further. Micro-fluidic reactors or nano-porous catalyst supports with the space between two walls of a few micron apart, so-called nano-space effect can exist where the reaction conditions mimic high pressure. Enhanced CO₂ adsorption can be obtained with the deposition of metal catalyst on those micro/nano channels to realize higher efficiencies.

Additionally, fundamental research for mechanistic aspects of CO₂RR with in-situ analysis methods is needed. The electroreduction of intermediate species (formate, glyoxal, formaldehyde, oxalic acid etc.) can be conducted to understand the reaction mechanism (e.g. recent works of Koper group working with on-line electrochemical mass spectrometer on Cu metal). On the other hand, computational methods needs progress to elucidate kinetic limitations of CO₂RR. (e.g. the computational hydrogen electrode model developed by Norskov group)

To conclude, a gas- and liquid-tight photoelectrochemical cell needs attentive study on its components i.e. electrodes, membranes and electrolytes. To address those challenges, we proposed this special designed flow cell integrated with a light harvesting semiconductor electrode as photoanode. Further work towards the design of PECf-cell could use a different candidate as photoanode which can supply a large enough photovoltage and photocurrent that CO₂R cathode could work at short circuit voltage. This approach could mimic photosynthesis in plants and realize a concrete solar-to-fuel conversion device which is under development in our group.

Secondment Reports

8.1 INRS, Montreal – CANADA

2015

8.1.1 Introduction

This research stay was done under the framework of WIROX project in partnership with INRS (Institut National de la Recherche Scientifique – Canada). Nano(meter)-Femto(second) Lab (NFL) group led by Prof. Federico Rosei performed studies on TiO₂ electrodes for solar hydrogen production¹⁶⁵. Particularly they had experience on the synthesis of nanoparticles and quantum dots of metal chalcogenides, i.e. PbS, CdS, CdSe. As indicated in their first email (from Dr. Haiguang Zhao), they supported TiO₂ photo-electrodes with “Giant Quantum Dots” (core/shell nanoparticles of CdS/CdSe) to obtain higher quantum efficiency. We had expertise on 1-D TiO₂ structures, i.e. nanorods and nanotubes, which have several advantages over granular-TiO₂ structures. Therefore, TiO₂ nanorods from IREC were taken to INRS Canada to be supported by quantum dots to obtain higher quantum efficiency thanks to their improved charge separation compared to granular TiO₂ particle films.

8.1.2 Objective

The objective was to increase the photocurrent density of TiO₂ nanorods (TiO₂-NRs) under A.M. 1.5 solar light. Due to the wide band gap of TiO₂ (3.2 eV), it only absorbs UV radiation (wavelength range of 400-320 nm for UVA and 320-290 nm for UVB). In order to utilize this photocatalyst and at the same time exploit visible light, TiO₂ must be combined with appropriate sensitizers active in visible region of the light spectrum (wavelength range of 700-400 nm). In the meantime, the choice of a photo-catalyst should be dictated by the position of its conduction and valence band levels, while determining its oxidation and reduction capacities. The control on the nanorod growth, higher specific surface area and the effective charge separation are some main advantages of TiO₂-NRs, despite of its known disadvantage; wavelength absorption range. Therefore, the objective of the secondment was to demonstrate an approach to use visible-light-absorbing

sensitizers (CdS, CdSe or ZnS) on TiO₂-NRs with two methods; electrophoretic deposition (EPD) and successive ionic layer adsorption and reaction (SILAR) method.

8.1.3 Experimental Activities

Initially, TiO₂-NRs were produced in IREC by hydrothermal reaction synthesis and afterwards calcination step as explained previously in Figure 2-5. Table 8.1 shows the method and properties of the electrodes transferred to INRS. The current-voltage values were measured in 0.1 M KOH electrolyte under A.M. 1.5 solar.

Table 8.1. TiO₂ nanorods produced by hydrothermal reaction at IREC.

Type	ID	Size	Reactants	Hydrothermal Condition	Annealing Condition	Rod Size Length/Width	Current Density at Voltage *
NR	TiO ₂ -NRs	15 cm ² FTO	3mL TiBu, 50mL HCl, 50mL DI (100mL)	200°C 2h	450°C 1h	3.5µm / ~200nm	^f 0.82 mA·cm ⁻² at 0.2 V _{Ag AgCl} ^b 0.7 mA·cm ⁻² at 0.2 V _{Ag AgCl}

* "f" is donated as front illumination which is the electrolyte-electrode side and "b" is when the substrate-electrode side was illuminated.

The following experimental methods and results from this part forward were conducted in INRS laboratories. Electrophoretic deposition process (EPD) is a deposition technique performed with a suspension of particles in a solvent. Under high electric field, the charged colloidal particles move toward and deposit onto the oppositely charged electrodes.

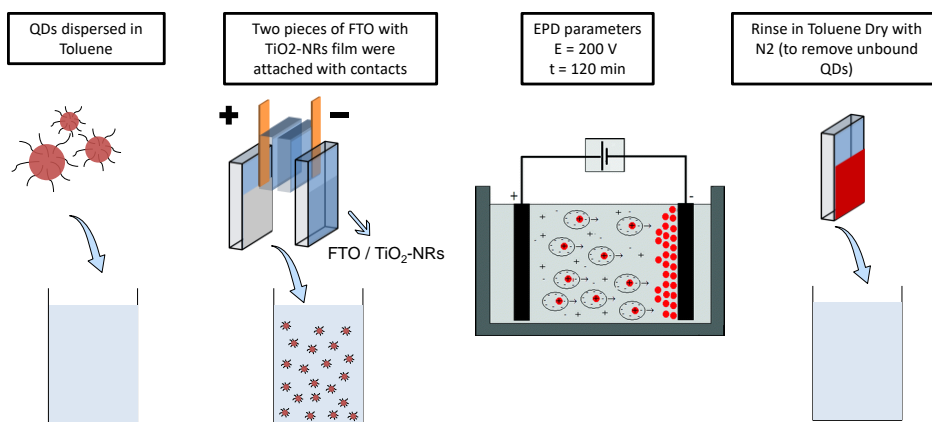


Figure 8-1. The illustration of electrophoretic deposition (EPD) process to immobilize CdSe/CdS core/shell quantum dots on TiO₂-NRs

As schematized in Figure 8-1, giant quantum dots (QDs) were dispersed in toluene and vertically aligned pair of TiO_2 -NRs / FTO slides were immersed in the QDs solution with nanorod sites facing each other. The distance in between them was adjusted to 1 cm. A direct voltage of 200 V was applied for 120 min¹⁶⁶. To wash off unbound QDs after EPD process, samples were rinsed several times with toluene and dried with N_2 at room temperature. The SILAR deposition cycle is shown in Figure 8-2. Initial cycle for Cd^{2+} ions have been deposited from an ethanoic solution of 0.05 M $\text{Cd}(\text{NO}_3)_2 \cdot 4\text{H}_2\text{O}$. The sulphide source was 0.05 M solution of $\text{Na}_2\text{S} \cdot 9\text{H}_2\text{O}$ in methanol/water (50/50 in vol.). An aqueous solution of 0.1 M $\text{Zn}(\text{NO}_3)_2$ ($\text{Zn}(\text{NO}_3)_2 \cdot 6\text{H}_2\text{O}$, 98%, Sigma-Aldrich) was used as Zn^{2+} source. The sulphide source was 0.1 M solution of $\text{Na}_2\text{S} \cdot 9\text{H}_2\text{O}$ in DI water. A single SILAR cycle consisted of 5 min of dip-coating of TiO_2 -NRs / FTO slides into the metal precursors (Cd^{2+} or Zn^{2+}) and subsequently into the sulphide solutions¹⁶⁷.

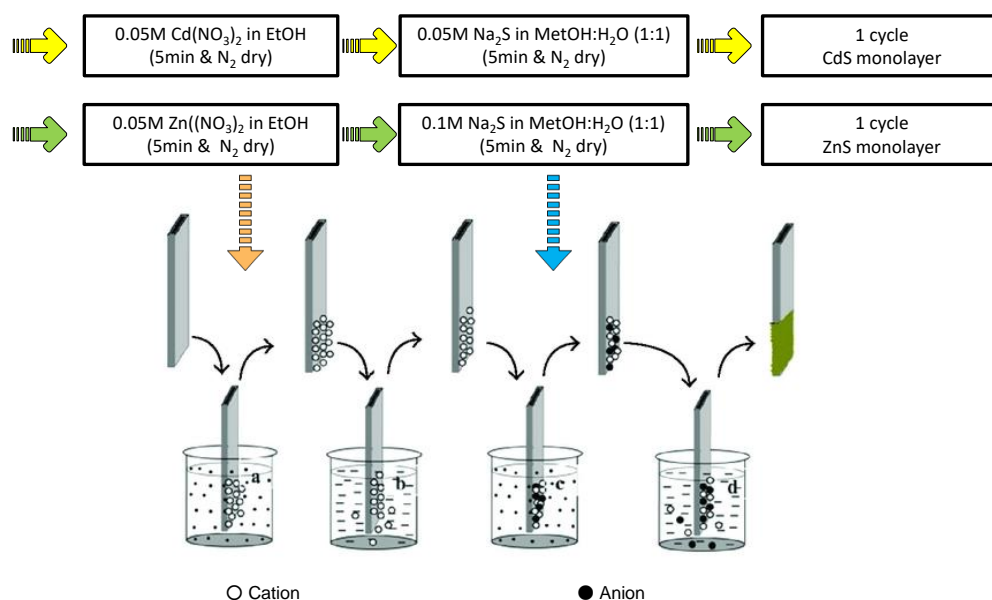


Figure 8-2. Successive ionic layer adsorption and reaction (SILAR) conducted for CdS and ZnS immobilization on TiO_2 -NRs film grown on FTO glass slides.

After each bath, the photoanode was thoroughly rinsed by immersion in the corresponding solvent to remove the chemical residuals from the surface and then drying with a nitrogen gun. A single repetition of SILAR cycle would correspond to a single layer so each sample was successively dipped to immobilize 4 layers of CdS and 2 layers of ZnS, illustrated in Figure 8-2. Three out of four TiO_2 -NRs were sensitized:

- Sample #1 was left untreated to be used as pristine electrode for comparison.
- Sample #2 was sensitized with 4 layers of CdS and 2 layers of ZnS by SILAR method. Four successive cycle of CdS were applied to obtain a good distribution of CdS quantum dots (QDs) on the nanorods to gain absorbance in the visible spectrum.
- Sample #3 had 2 more ZnS layers to inspect if ZnS would provide a stable photocurrent by preventing charge recombination.
- Sample #4 was first sensitized with Giant Quantum Dot particles which had a CdSe-core and CdS shell layer by EDP method. Then, 4 layers of CdS and 2 layers of ZnS were immobilized by SILAR method.

All the samples were tested in three-electrode configurations in an aqueous solution containing 0.25 M Na₂S and 0.35 M Na₂SO₃ (pH = 13) serving as the sacrificial hole scavenger. A platinum wire and Ag/AgCl electrode encapsulated in 3.5 M KCl solution were used as a counter and reference electrode, respectively. The cyclic voltammetry was conducted between -1.4 and 0 V vs Ag/AgCl with a scan rate of 20 mV s⁻¹. The experimental methods and theoretical energy levels of the semiconductor materials are shown in Figure 8-3(a-b). The difference of the film colour after EDP or SILAR deposition can be seen in Figure 8-3(c). The deposition of more layers gave darker films, where TiO₂ was white-grey and 4CdS/2ZnS was bright yellow and 4CdS/4ZnS was getting pale yellow. This was the initial evidence that CdS and ZnS deposition by SILAR was successful that the visible light absorption must be improved. The cyclic voltammetry results were tested in a Na₂S/Na₂SO₃ sacrificial electrolyte. In the absence of a sacrificial agent, CdS and ZnS would undergo oxidation because photogenerated holes were trapped by Cd⁺² or Zn⁺² metals, called as photocorrosion by self-oxidation¹⁶⁸.

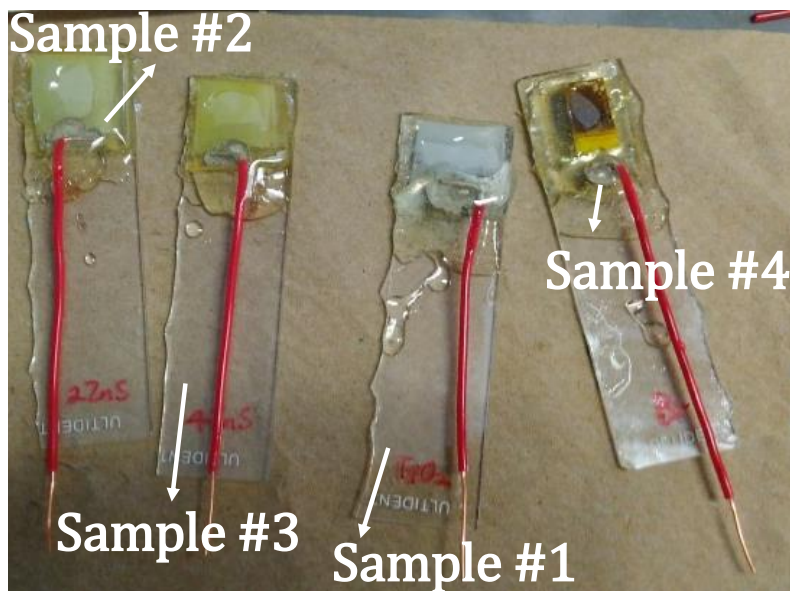
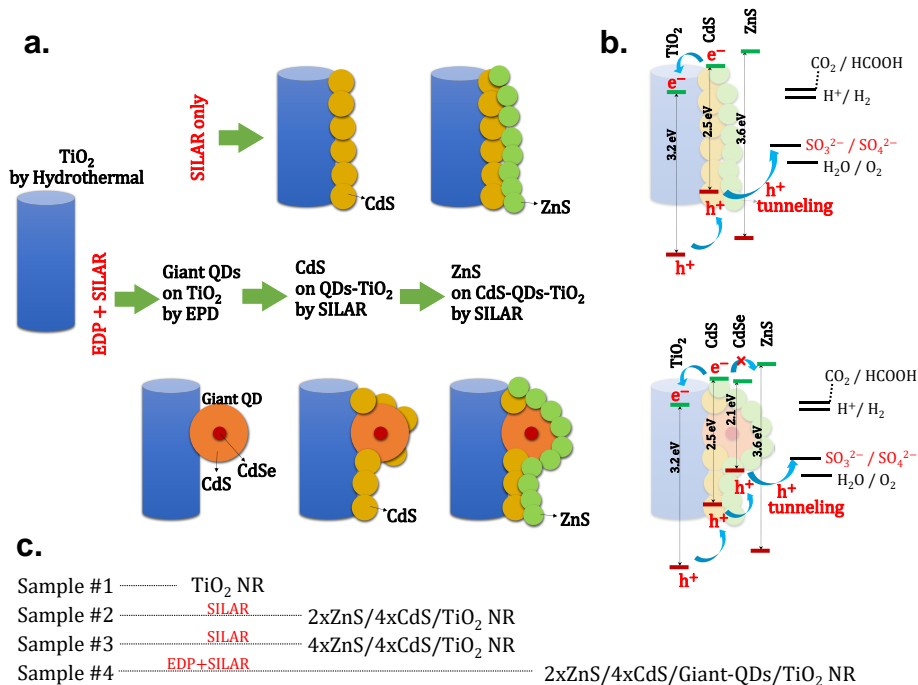


Figure 8-3. (a) Experimental method to produce sensitized electrodes (b) Energy levels of semiconductors and redox potentials of the electrolytes. CdS and CdSe are shown as sensitizers by Fermi level alignment with TiO₂ and ZnS layer acts as a coating layer to improve the stability. The band gap values correspond to quantum dot nanoparticles and are larger than in bulk semiconductors. (c) the digital pictures of the samples to highlight the colour change

8.1.4 Results & Discussion

All the experiments have been performed with the illumination from the front (EE = electrode - electrolyte side) and back (SE = substrate - electrolyte side) part of

the electrode. The photocurrent from the back illumination was lower than the front site in all tests (Figure 8-4(a)) suggesting that some part of the light spectra was absorbed by 500 nm thick FTO layer + 3 mm thick silica glass. Compared to the results in our laboratory at IREC in 0.1 M KOH electrolyte (0.7 and $0.82 \text{ mA}\cdot\text{cm}^{-2}$), the maximum photocurrent of pristine TiO_2 -NRs was lower; 0.15 and $0.22 \text{ mA}\cdot\text{cm}^{-2}$ at $0.2 \text{ V}_{\text{Ag|AgCl}}$ from back and front side, respectively. TiO_2 is well-known to produce an hydroxide layer facilitating water oxidation reaction.

A slight increase was obtained after deposition of CdS – ZnS layer by SILAR method Figure 8-4(b-c). Several consecutive scans were performed in the front illumination mode to inspect the charge transfer and surface stability by time. In Figure 8-4(b), Sample #2 gave a few large current peaks between $1 - 2 \text{ mA}\cdot\text{cm}^{-2}$ at the 1st and 3rd cycle of the front illumination mode. However, those values were not stable and did not appear in the reverse scan. In Figure 8-4(c), noisy current signals were obtained in the 1st cycle of Sample #3 which did not appear in the reverse scan and consecutive scans.

Table 8.2. TiO_2 nanorods results for photocurrent under AM 1.5 illumination in $0.25 \text{ M Na}_2\text{S}$ and $0.35 \text{ M Na}_2\text{SO}_3$ (pH = 13) at 20 mV s^{-1} scan rate

Sample	Active area cm^{-2}	Front mA cm^{-2}	Back mA cm^{-2}
TiO ₂ - NRs – pristine (IREC)	1.5	0.82	0.70
Sample # 1 TiO ₂ - NRs – pristine (INRS)	0.5	0.24	0.17
Sample # 2 TiO ₂ -NRs / 4CdS / 2ZnS	0.5	0.35	0.19
Sample # 3 TiO ₂ -NRs / 4CdS / 4ZnS	0.5	0.29	0.17
Sample # 4 TiO ₂ -NRs + CdSe-CdS QDs / 4CdS / 2ZnS	0.5	0.14	0.17

On the other hand, EDP method did not show any enhancement in the photocurrent density as seen from Figure 8-4(d). These observations suggest a poor charge separation or transfer throughout all the electrodes. A summary of the data is given in Table 8.2.

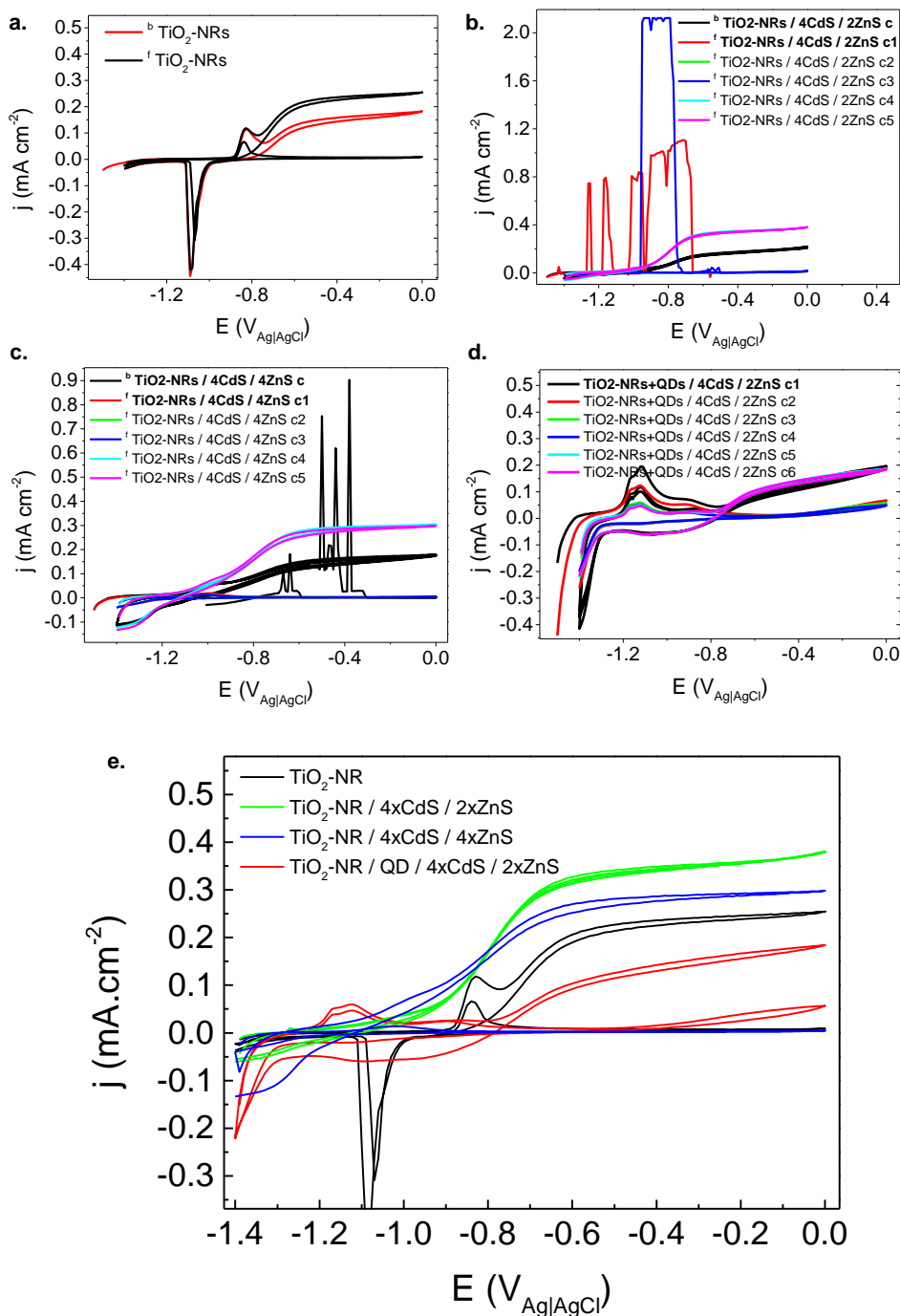


Figure 8-4. TiO₂-NR samples; **(a)** pristine TiO₂-NRs; **(b)** SILAR deposited 4 cycles of CdS and 2 cycles of ZnS; **(c)** SILAR deposited 4 cycles of CdS and 4 cycles of ZnS; **(d)** EPD+SILAR deposited core/shell CdSe-CdS Quantum Dots and 4 CdS+2 ZnS. The consecutive scans were obtained in an aqueous solution containing 0.25 M Na₂S and 0.35 M Na₂SO₃ (pH = 13) while sample was illuminated from front “f” and back “b” side **(e)** comparison of photocurrent densities in front illumination mode.

Further investigation would be necessary to understand the poor charge separation problem. Due to the short time span of the secondment, we have managed to

perform only a single characterization method on the samples after CV scans. The initial suspicion was perhaps CdS, ZnS layers were not well attached to the rods at the SILAR method and they fall off during electrochemical tests. Hence, high resolution transmission electron microscope (HR-TEM) was used to inspect some scratched samples from the surface of the electrode; Figure 8-5 (a) TiO₂-NRs pristine vs. (b) TiO₂-NRs + QDs + 4CdS/2ZnS. The high-resolution images of the rods showed that pristine sample has a good crystalline structure with well-aligned lattice growth along [001] direction whereas core/shell quantum dot (CdSe/CdS) sensitized sample by EPD method showed a very poor crystallinity and also an amorphous surface layer. Most probably the high voltage applied during EPD process (200 V during 2 hours) caused lattice distortions and decrease the crystallinity of the rods creating in trap states as suspected in the CV scans.

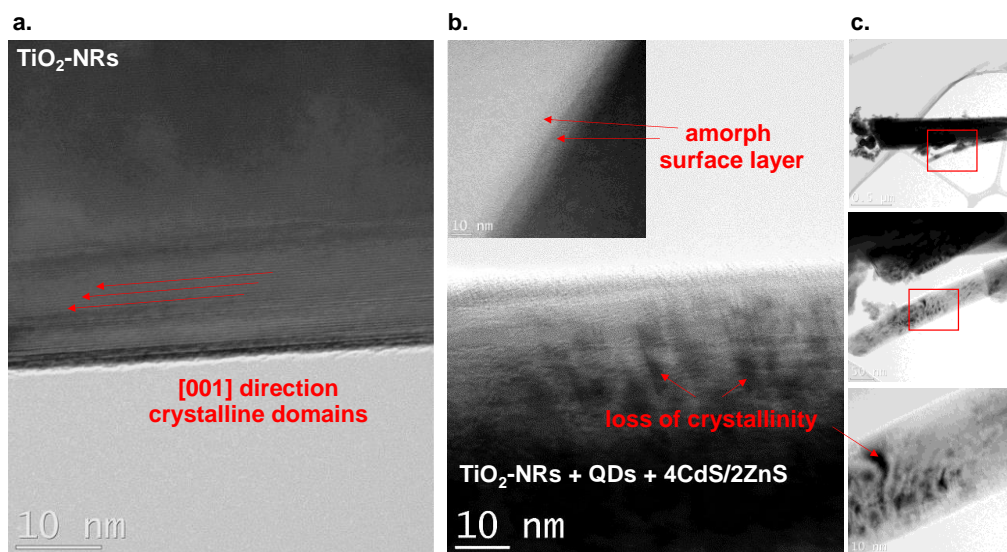


Figure 8-5. (a) (sample #1) pristine TiO₂-NRs and (b-c) (sample #4) TiO₂-NRs sample sensitized with EPD and SILAR

A stability test of half an hour was performed on Sample #4 under a fixed potential of 0.2 V_{Ag|AgCl}. As mentioned before, the electrolyte contains sacrificial agent Na₂S and Na₂SO₃ therefore we did not apply a longer time to change the concentration of the agent. The current retention was above 90%, with an initial current of 0.13 and final point at 0.11 mA·cm⁻².

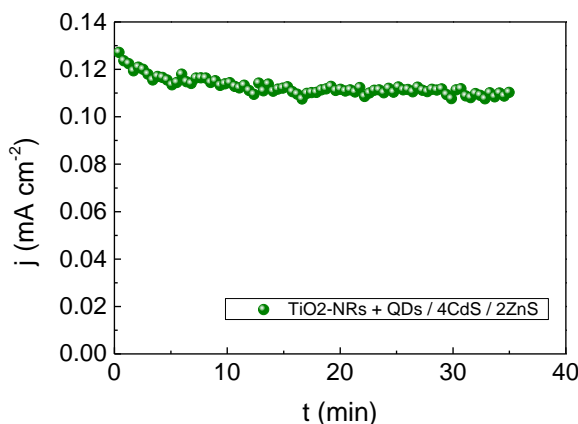


Figure 8-6. The stability test of Sample #4 which has been sensitized with CdSe/CdS (core/shell) quantum dots and SILAR method.

8.1.5 Conclusions

In summary, TiO₂-NRs were fabricated by hydrothermal synthesis at IREC. The core/shell CdSe/CdS giant quantum dots were deposited via electrophoretic deposition and CdS/ZnS nanoparticles were deposited on TiO₂-NRs via successive ion layer adsorption. These formed heterojunctions of TiO₂-NRs/(CdSe)/CdS/ZnS and TiO₂-NRs/CdS/ZnS NPs. Pristine TiO₂-NRs exhibited both good visible light photoelectrochemical properties in 0.1 MKOH but gave lower photocurrent density in Na₂S/Na₂SO₃ electrolyte. This might be due to excited electrons injected into TiO₂ which would be trapped at the hydroxide layer formed in KOH tests. Also, TEM images showed an amorphous layer which could be the evidence of the hydroxyl layer. EDP method to attach giant quantum dots would impaired an efficient electron-hole separation due to the high voltage giving rise to defect sites in oxide lattice (Sample #4). However, CdS/ZnS nanoparticles deposited by SILAR method doubled the photocurrent (Sample #2) of the pristine electrode (Sample #1). Meanwhile, a shift of the on-set potential was achieved to more negative values (Sample #3), around $-1.1 V_{Ag|AgCl}$. This performance was attributed to electron-hole separation with increasing the SILAR cycles of ZnS layers.

A significant experience was gained on two different methods (SILAR and EPD) on nanoparticles deposition. This work provided insights for forming heterojunctions of CdS NPs and TiO₂-NRs which is a promising way to fabricate material applied in the solar energy conversion.

8.2 ETH Zurich, Hönggerberg - SWITZERLAND

2016

8.2.1 Introduction

This research stay was conducted in Advanced Catalysis Engineering (aCe) group in Institute for Chemical and Bioengineering, ETH Zurich. aCe group led by Prof. Pérez-Ramírez who holds a solid expertise on heterogeneous catalysis and reactor concepts including carbon dioxide valorization with sustainable technologies. In this line, our institute (IREC) had proven and disclosed its expertise on photo/electrochemical reduction of CO₂ via journal articles and international patents. Following the research activities and expertise of both groups, a period of three months visiting stay was agreed to conduct research on a family of Cu-based materials for electrochemical reduction of CO₂.

8.2.2 Objective

The propose of this visiting stay has been focused on testing a family of Cu-based materials for electrochemical reduction of CO₂ (CO₂RR) in aqueous electrolyte to produce syngas (CO/H₂). A recent discovery on a unique equilibration process was unveiled in one of the members of the Cu-based material family by aCE group. Accordingly, the objective was to explore other similar compounds to check whether the findings could be a general phenomenon. The work was primarily focused on determining catalytic performances, with further emphasis on deep non-electrochemical characterization in case of promising results.

8.2.3 Experimental Activities

The experimental methods used during this visiting stay was described by Gaston et.al.¹⁶⁹ Briefly, the electrodes were prepared by airbrushing a catalyst ink (50 mg catalyst, 5 ml DI-H₂O, 5 ml 2-propanol, 50 µl, 5 wt.%, Nafion) on a gas diffusion layer (GDL) until 1 to 2 mg·cm⁻² of loading was achieved (a geometric area of 2.25 cm²).

Two compartments gastight glass cell separated by a Nafion® 212 membrane was used for all electrochemical experiments. The measurements were carried out at room temperature with an Autolab PGSTAT302N potentiostat, using a Pt wire as the counter electrode and a Ag/AgCl reference electrode. The electrochemical techniques such as cyclic voltammetry, galvanostatic and/or potentiostatic

experiments have been applied to evaluate CO₂RR. The on-line analysis of gaseous products was conducted with a SRI 8610C gas chromatograph (GC) equipped with packed HayeSep D and Molecular Sieve 13X columns, a methanizer, and thermal conductivity and flame ionization detectors. An automated sample injection was initiated every 15 min into the GC column from the headspace of the electrochemical cell. At the end of the electrolysis, a liquid sample was collected and the formate concentration was determined by high-performance liquid chromatography (HPLC) in a Merck LaChrom system equipped with a Bio-Rad Aminex HPX-87H column and a refractive index detector. A schematic illustration of the set-up was given in Figure 1-9(b) in Chapter 1.

8.2.4 Results and Discussion

Delafossites have the general chemical formula ABO₂ where A is metal cation with +1 valence (such as Na, Cu, and Ag) and B is a Group III metal (e.g. Fe, Al, and In). Figure 8-7(a) shows structure model of the delafossite structure where each Cu atom (A site) is linearly coordinated with two O atoms, forming O—Cu—O dumbbells parallel; while the cation at the B site (Al, Cr, Ga, Fe, Mn) forms distorted edge-shared MO₆ octahedra with M in the central position. Alternative layer stackings are possible, resulting in a hexagonal (space group P6₃/mmc) or rhombohedral (space group R-3m) unit cell.

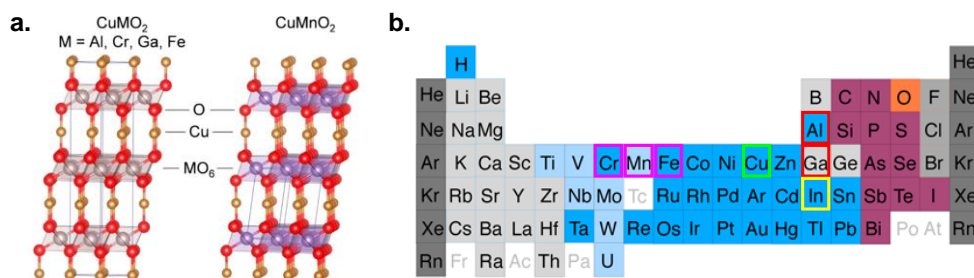


Figure 8-7. (a) The rhombohedral structure of CuAlO₂, CuCrO₂, CuGaO₂, and CuFeO₂ and the monoclinic structure of CuMnO₂. (b) The periodic table where the elements used in this part of the study is highlighted.

Due to the excellent p-type mobility, resistance to oxidative corrosion, stability in aqueous solution and potential application in catalysis; the delafossite family is a subject of recent interest in the literature¹⁷⁰. For that reason, a study on the CO₂R activity of selected delafossite materials as a function of the nature of B site (M⁺³ cations of Al, Cr, Ga, Fe, Mn) have been conducted in a two-compartment

electrochemical cell. Figure 8-7(b) shows the selected B site metals which could be divided into two categories that are;

1. Iron (^{26}Fe), manganese (^{25}Mn) and chromium (^{24}Cr) are elements that lie in the same period (4th period) but different groups (VIII, VIIA and VIA group, respectively).
2. Indium (^{49}In), gallium (^{31}Ga) and aluminium (^{13}Al) are elements that lie in the same group (IIIB) but in different periods (5th, 4th and 3rd period).

The consecutive two-hour electrolysis tests of cuprous delafossite catalysts; CuFeO_2 , CuCrO_2 and CuMnO_2 from the 1st category and their ex-situ XRD scans after the test are given in Figure 8-8(a-b), (c-d) and (e-f), respectively. The XRD spectra of gas diffusion layer (GDL) to support the delafossite catalysts were also included (in grey colour). The fresh electrodes first underwent a potentiostatic run of electrochemical reduction at $-0.6 V_{\text{RHE}}$ in CO_2 -saturated 0.1M KHCO_3 electrolyte solution during 2 h. The closed symbols represent the total current of the cell (j) that was stable for CuCrO_2 and CuMnO_2 whereas a sharp decrease has been observed for CuFeO_2 in the first run. A significant change in the peak intensity of CuFeO_2 phase can be seen in Figure 8-8(b). Nearly 1-fold decrease of the current density during Run1 was attributed to the transformation of CuFeO_2 structure that most of the charge was spent for its reduction to Cu and Fe metal, as well as Fe_2O_3 and CuO phases evidenced by ex-situ XRD scans. When the current of CuFeO_2 was merely stabilized around $3 \text{ mA}\cdot\text{cm}^{-2}$, carbon monoxide current density (j_{CO}) started to increase which could be due to creation of active sites such as Cu and CuO during the reduction of the delafossite phase. Most of the current efficiency has been spent on H_2 evolution reaction (faradaic efficiency of $\geq 85 \%$) which could be due to Cu and Fe sites that was stable and active in the consecutive runs as well. Contrary to CuFeO_2 phase which have almost disappeared after 1st run, CuCrO_2 and CuMnO_2 delafossites have showed outstanding stability owing to their XRD peak positions and intensity. Between the latter two, CuCrO_2 seemed to be the most stable delafossite providing a stable j_{CO} of 0.005, 0.17 and $0.54 \text{ mA}\cdot\text{cm}^{-2}$ at each potentiostatic run from -0.6 , -0.8 and $-1.0 V_{\text{RHE}}$, respectively, even though the rise of the overall current in Run4 only contributed to the efficiency of H_2 evolution. On

the other hand, CuMnO_2 exhibited a partial reduction giving a mixed phase of Cu-Mn alloy after the initial run and following the appearance of Cu metal after Run2.

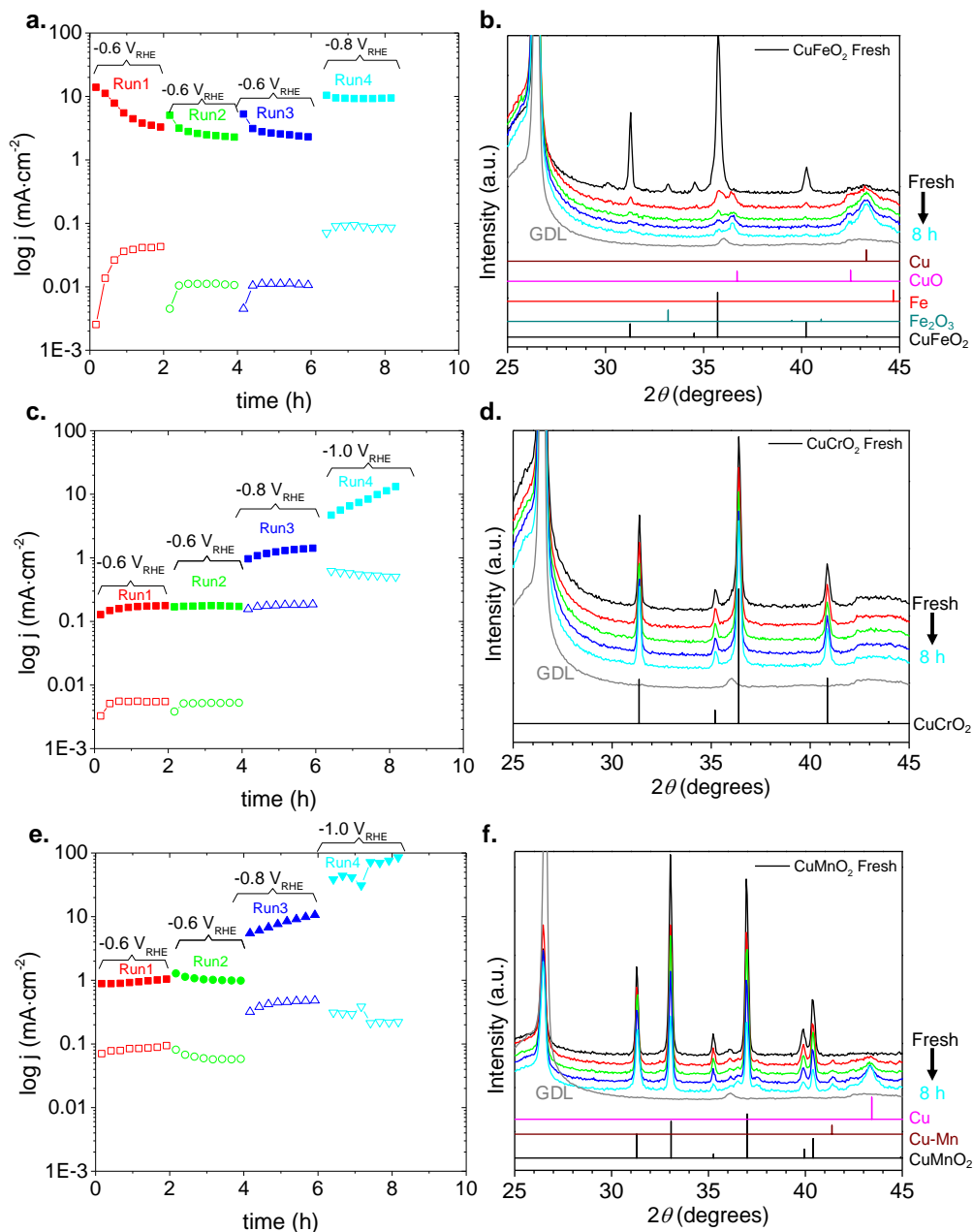


Figure 8-8. Total current density of the electrode (closed symbols) and partial current density of CO (open symbols) during CO_2 electrolysis under constant potential with (a) CuFeO_2 (c) CuCrO_2 (d) CuMnO_2 sprayed on GDL (Conditions: 0.1 M KHCO_3 saturated with CO_2 , pH=6.75) along with their XRD scans at the end of each potentiostatic run for (b) CuFeO_2 (d) CuCrO_2 (e) CuMnO_2 . The colour of each XRD scan corresponds to the spectra obtained at the end of that potentiostatic “Run”

These results confirm that delafossite structures alone do not provide a high faradaic efficiency for CO_2 reduction into CO (or even formate ion HCOO^-) however

in-situ reduction of the delafossite phase give rise to active sites towards CO₂R in line with their XRD analysis.

The delafossite catalyst of the second category had their B site metal (in ABO₂) in the same group (IIIB). CuAlO₂ and CuGaO₂ phases were stable throughout the potentiostatic runs for CO₂R except for CuInO₂ which have shown some distinct evolution of different phases given in Figure 8-9. The increase of the applied potential on CuAlO₂ was in line with j and j_{CO} in favour of CO production reaching up to 28 % at -1.0 V_{RHE}. The stability of the main delafossite phase may confirm that a synergy between Cu and Al in this type of delafossite could favour higher conversion efficiencies for CO₂R. Several post-treatments on the powder of CuAlO₂ were applied to evolve a mixed alloy of Cu and Al. However, the extraordinary stability of aluminium oxide (Al₂O₃) phase did not yield to Cu-Al mixed alloy, even though we have applied a temperature-programmed reduction under H₂ or CO (1 atm) atmosphere (TPR at 900°C for 8 h). Further treatment of CuAlO₂ with high pressure (50 bars) H₂ treatment at 300°C for 72 h also resulted in formation of Cu metal and Al₂O₃ phases. At this point, we would presume that for CuAlO₂ delafossite, the stabilizing influence of Al on Cu⁺ species would be ascribed to steady activity versus CO formation throughout the potentiostatic runs¹⁶⁹. The fresh electrode of CuGaO₂ catalyst exhibited oxides of gallium and copper which did not present a gradual change in their peak intensity in their XRD scans. The potentiostatic runs from 1 to 3 at -0.6 V_{RHE} showed gave 0.02 mA·cm⁻² for j_{CO} with a decrease to nearly half of this value, suggesting the poisoning of active sites by CO. As the potential step increased, partial current of CO increased to 0.16 mA·cm⁻² which corresponds to 11.6 % faradaic efficiency for CO₂R to CO. In the following runs (Run5 and Run6) where higher potentials were applied, faradaic efficiency of CO decreased to 8.7 and 7.7 %. The effect of CO poisoning is unclear since the potentiostatic run at -1.2 V_{RHE} did not alter the peak reflections of secondary phases so it was elusive to assign CO₂R activity to delafossite phase solely. Contrary to the former delafossite structures, CuInO₂ underwent major structural changes and gave promising CO partial current at low overvoltage. The current density of Run1 was around 3.4 mA·cm⁻² following a decrease to 2.9 mA·cm⁻² at Run5 after 8 hours. This was also corresponding to the transformation CuInO₂ delafossite phase into a mixed CuIn and Cu₂In alloys along with evolution of In(OH)₃ phase. These results confirmed that the interaction

between copper and indium phases have led to the suppression of HER from 70 % to 25 % faradaic efficiency of H₂ between Run1 and Run 6, respectively.

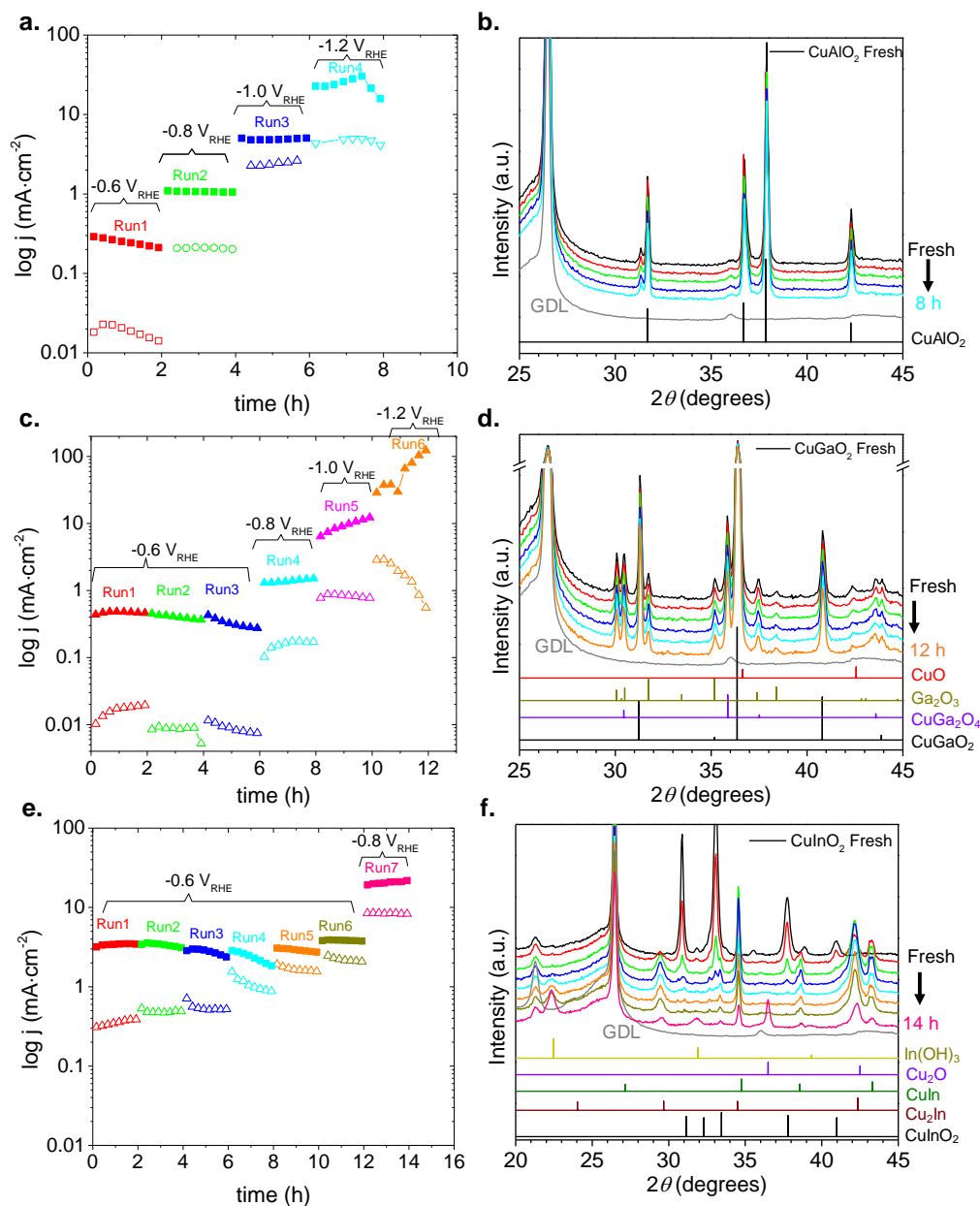


Figure 8-9. Total current density of the electrode (closed symbols) and partial current density of CO (open symbols) during CO₂ electrolysis under constant potential with (a) CuAlO₂ (c) CuGaO₂ (d) CuInO₂ sprayed on GDL (Conditions: 0.1 M KHCO₃ saturated with CO₂, pH=6.75) along with their XRD scans at the end of each potentiostatic run for (b) CuFeO₂ (d) CuCrO₂ (e) CuMnO₂. The colour of each XRD scan corresponds to the spectra obtained at the end of that potentiostatic “Run”

The last electrolysis at -0.8 V_{RHE} (Run7) gave rise to evolution of CuO phase and a slight decrease of CO faradaic efficiency from 55 % to 40 % whereas formate

(HCOO⁻) efficiency had increased from ca. 20 % to 33 %. The faradaic efficiency of HCOO⁻ was measured by HPLC from the aliquots taken between each potentiostatic run for all the samples. The faradaic efficiencies of CO, HCOO⁻ and H₂ after CO₂R in aqueous electrolyte for all delafossite catalysts tested at -0.6 and -0.8 V_{RHE} are given Figure 8-10(a) and (b), respectively. The values of total faradaic efficiencies did not converge exactly to 100 % because of the standard deviation in the average current density of each run (5 % and higher at larger applied potentials) and peak area estimation from the gas chromatograms (maximum ca. 2 % for CO and ca. 7 % for H₂). At first glance, the faradaic efficiency of CO was in an increasing trend moving from CuFeO₂ to CuInO₂ except for CuCrO₂ which could provide 14 % CO efficiency at -0.8 V_{RHE} with a compromise of a lower current density than the rest.

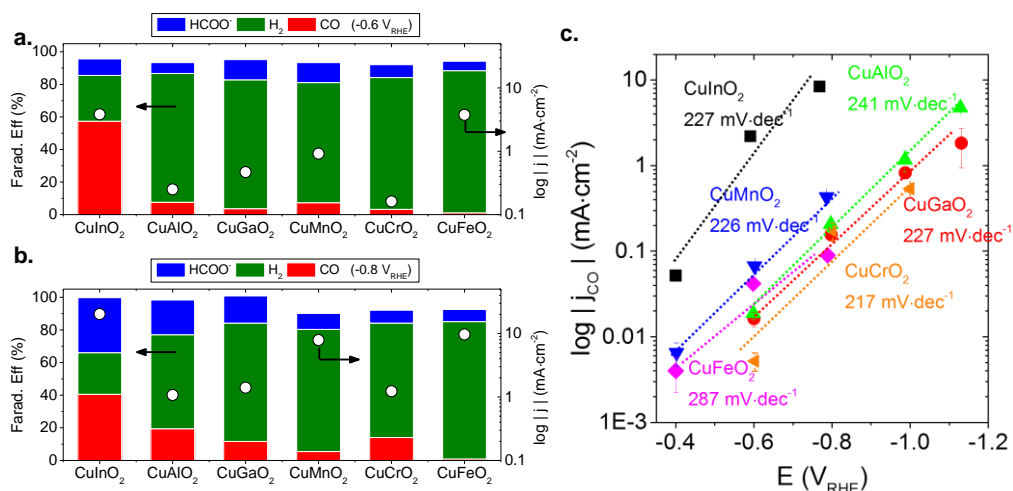


Figure 8-10. The comparison chart of faradaic efficiency (columns) and total current density (circles) at (a) -0.6 V_{RHE} and (b) -0.8 V_{RHE} along with (c) Tafel slopes of CO for delafossites catalysts

Figure 8-10(c) shows the Tafel slopes of cuprous delafossite structures. In the 1st category elements where B site metals lie at the same period (4th), the increase of CO efficiency would be present in an order of Fe < Cr < Mn for potentiostatic run under -0.6 V_{RHE}. In line with this, 2nd category elements where B site metals lie at the same group (IIIB), an order of Ga < Al < In elements would be evident at both potentials. However, in terms of catalytic performance, CuInO₂ outperformed rest of the catalyst both in total current density and faradaic efficiencies. On course of the electroreduction, most of the delafossite structures either showed some minor transformations resulting in the formation of metals prone to poisoning such as Cu, Fe and Mn. On the other hand, the delafossites which do not reduce or evolve,

exhibited a decreasing efficiency towards CO_2R . At this point, it was only CuInO_2 which could evolve and pursue an efficient catalytic property. These results suggest in-situ formation of active sites (by the gradual segregation of Cu and In)¹⁷¹ do not bind CO too strongly so that poisoning of those sites could be inhibited. Meanwhile, undue H_2 evolution seemed to be retarded by the formation of indium oxide phase showing a synergetic effect between In(OH)_3 and the metallic phases.

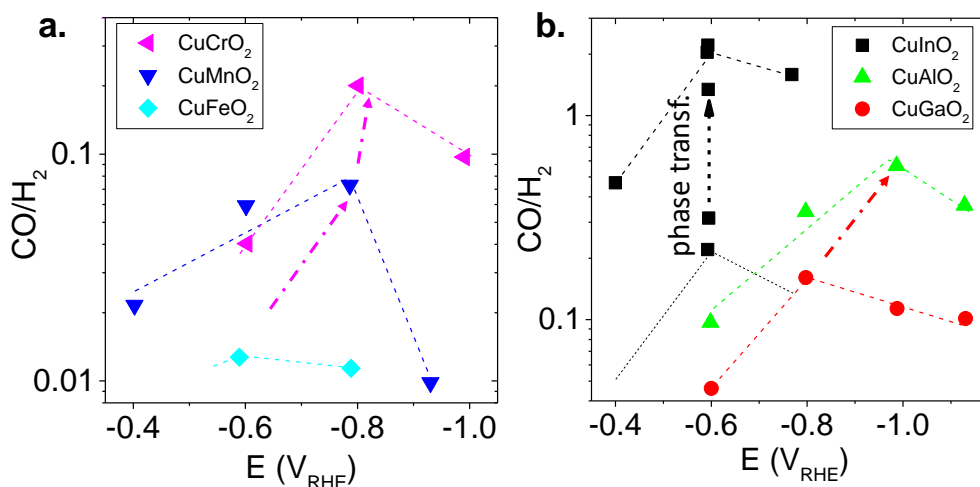


Figure 8-11. The selectivity plot for CO to H_2 ratio as a function of the working electrode potential of delafossites with B-site element (ABO_2) in the (a) same period and (b) in the same group

Figure 8-11(a) and (b) shows the selectivity of CO versus H_2 for the delafossites which were in the 1st and 2nd category as indicated previously. In line with the previous findings from consecutive potentiostatic runs and ex-situ XRD patterns, the selectivity and the nature of the B site element are connected. In the 1st category, moving from right to left side of the periodic table, the B site elements that lie at the 4th period presented the tendency to give higher CO selectivity over H_2 evolution. A similar tendency was more prominent between fresh-In, Ga and Al derived delafossites of the 2nd category. Nevertheless, CuInO_2 where its B site element is below the other two delafossites in IIIB group, underwent a phase transformation. It exhibited the highest CO selectivity over H_2 therefore its evolved form does not follow that trend of selectivity.

8.2.5 Conclusion

A family of cuprous delafossite materials (ABO_2) were studied as a potential catalyst for electrochemical reduction of CO_2 into C1 group molecules. Three of the delafossite had their B-site elements in 4th period ($CuFeO_2$, $CuCrO_2$ and $CuMnO_2$) while the other three were in the same group, IIIB ($CuAlO_2$, $CuGaO_2$ and $CuInO_2$). The consecutive two-hour electrolysis tests and ex-situ XRD analysis provided structural insights such as importance of the catalyst evolution during CO_2R tests. Amongst the six delafossite catalyst, only $CuFeO_2$ and $CuInO_2$ underwent a major reduction where the former showed comparatively low performance for CO_2R . Only the selectivity of $CuInO_2$ shifted from H_2 to CO and increased upon successive potentiostatic electrolysis tests, forming a highly active and stable Cu_xIn ($x = 1$ or 2) and $In(OH)_3$ phase.

The other delafossite catalysts which do not reduce or evolve into a different phase, have shown a trend in the selectivity of CO over H_2 in line with their order in the periodic table – considering the initial run of fresh- $CuInO_2$ only.

A significant experience was gained on a new class of materials such as cuprous delafossites. This work provided insights for the development of transition metal-oxide based electrocatalysts for CO_2 reduction and provided extensive experience on experimental methods (ex-situ) for studying the evolution of CO_2R .

Bibliography

1. Hansen, J.; Ruedy, R.; Sato, M.; Lo, K., Global surface temperature change. *Reviews of Geophysics* **2010**, *48* (4).
2. McGlade, C.; Ekins, P., The geographical distribution of fossil fuels unused when limiting global warming to 2 [deg]C. *Nature* **2015**, *517* (7533), 187-190.
3. United Nations Framework Convention on Climate Change (UNFCCC). Report of the Conference of the Parties on its Fifteenth Session, held in Copenhagen from 7 to 19 December 2009. Part Two: Action taken by the Conference of the Parties at its Fifteenth Session. United Nations Climate Change Conf. Report 43 <http://unfccc.int/resource/docs/2009/cop15/eng/11a01.pdf> (UNFCCC, 2009).
4. Paris climate conference (COP21) in December 2015 https://ec.europa.eu/clima/policies/international/negotiations/paris/index_en.htm
5. "Key World Energy Statistics 2015" (PDF). www.iea.org. IEA. 2015. pp. 8, 37. Archived from the original on 13 March 2015.
6. (a) Gielen, D.; Boshell, F.; Saygin, D., Climate and energy challenges for materials science. *Nat Mater* **2016**, *15* (2), 117-120; (b) Gallo, A. B.; Simões-Moreira, J. R.; Costa, H. K. M.; Santos, M. M.; Moutinho dos Santos, E., Energy storage in the energy transition context: A technology review. *Renewable and Sustainable Energy Reviews* **2016**, *65*, 800-822.
7. (a) Olah, G. A.; Prakash, G. K. S.; Goepfert, A., Anthropogenic Chemical Carbon Cycle for a Sustainable Future. *Journal of the American Chemical Society* **2011**, *133* (33), 12881-12898; (b) Aresta, M.; Dibenedetto, A.; Angelini, A., Catalysis for the Valorization of Exhaust Carbon: from CO₂ to Chemicals, Materials, and Fuels. Technological Use of CO₂. *Chemical Reviews* **2013**; (c) Centi, G.; Quadrelli, E. A.; Perathoner, S., Catalysis for CO₂ conversion: a key technology for rapid introduction of renewable energy in the value chain of chemical industries. *Energy & Environmental Science* **2013**, *6* (6), 1711-1731.
8. Walter, M. G.; Warren, E. L.; McKone, J. R.; Boettcher, S. W.; Mi, Q.; Santori, E. A.; Lewis, N. S., Solar Water Splitting Cells. *Chemical Reviews* **2010**, *110* (11), 6446-6473.
9. (a) Tarascon, J.-M.; Armand, M., Issues and challenges facing rechargeable lithium batteries. *Nature* **2001**, *414* (6861), 359-367; (b) Arico, A. S.; Bruce, P.; Scrosati, B.; Tarascon, J.-M.; van Schalkwijk, W., Nanostructured materials for advanced energy conversion and storage devices. *Nat Mater* **2005**, *4* (5), 366-377; (c) Larcher, D.; Tarascon, J. M., Towards greener and more sustainable batteries for electrical energy storage. *Nat Chem* **2015**, *7* (1), 19-29.
10. Barnham, K.; Knorr, K.; Mazzer, M., Recent progress towards all-renewable electricity supplies. *Nat Mater* **2016**, *15* (2), 115-116.
11. USA and EU CO₂ conversion projects, accessed on May 2016 <http://www.briangwilliams.us/methanol-economy/references.html>
12. Turner, J. A., A Realizable Renewable Energy Future. *Science* **1999**, *285* (5428), 687-689.
13. Soloveichik, G. L., Flow batteries: current status and trends. *Chemical reviews* **2015**, *115* (20), 11533-11558.
14. (a) Shibata, T.; Kumamoto, T.; Nagaoka, Y.; Kawase, K.; Yano, K., Redox flow batteries for the stable supply of renewable energy. *SEI Technical Review* **2013**, *76*, 14; (b) Aneke, M.; Wang, M., Energy storage technologies and real life applications – A state of the art review. *Applied Energy* **2016**, *179*, 350-377.
15. Metz, B.; Davidson, O.; De Coninck, H.; Loos, M.; Meyer, L., Carbon dioxide capture and storage. **2005**.
16. Zhu, D. D.; Liu, J. L.; Qiao, S. Z., Recent Advances in Inorganic Heterogeneous Electrocatalysts for Reduction of Carbon Dioxide. *Advanced Materials* **2016**, *28* (18), 3423-3452.

17. Herron, J. A.; Kim, J.; Upadhye, A. A.; Huber, G. W.; Maravelias, C. T., A general framework for the assessment of solar fuel technologies. *Energy & Environmental Science* **2015**, *8*(1), 126-157.
18. (a) Hou, X.; Hou, H. J. M., Roles of manganese in photosystem II dynamics to irradiations and temperatures. *Frontiers in Biology* **2013**, *8*(3), 312-322; (b) Meyer, T. J., Chemical approaches to artificial photosynthesis. *Accounts of Chemical Research* **1989**, *22*(5), 163-170.
19. Bensaid, S.; Centi, G.; Garrone, E.; Perathoner, S.; Saracco, G., Towards Artificial Leaves for Solar Hydrogen and Fuels from Carbon Dioxide. *ChemSusChem* **2012**, *5*(3), 500-521.
20. (a) Jia, J.; Seitz, L. C.; Benck, J. D.; Huo, Y.; Chen, Y.; Ng, J. W. D.; Bilir, T.; Harris, J. S.; Jaramillo, T. F., Solar water splitting by photovoltaic-electrolysis with a solar-to-hydrogen efficiency over 30%. *Nature Communications* **2016**, *7*; (b) Moniz, S. J. A.; Shevlin, S. A.; Martin, D. J.; Guo, Z.-X.; Tang, J., Visible-light driven heterojunction photocatalysts for water splitting - a critical review. *Energy & Environmental Science* **2015**, *8*(3), 731-759; (c) Peerakiatkhajohn, P.; Yun, J.-H.; Wang, S.; Wang, L., Review of recent progress in unassisted photoelectrochemical water splitting: from material modification to configuration design. *Journal of Photonics for Energy* **2017**, *7*(1), 012006-012006.
21. Xie, S.; Zhang, Q.; Liu, G.; Wang, Y., Photocatalytic and photoelectrocatalytic reduction of CO₂ using heterogeneous catalysts with controlled nanostructures. *Chemical Communications* **2016**, *52*(1), 35-59.
22. Arai, T.; Sato, S.; Kajino, T.; Morikawa, T., Solar CO₂ reduction using H₂O by a semiconductor/metal-complex hybrid photocatalyst: enhanced efficiency and demonstration of a wireless system using SrTiO₃ photoanodes. *Energy & Environmental Science* **2013**, *6*(4), 1274-1282.
23. Arai, T.; Sato, S.; Morikawa, T., A monolithic device for CO₂ photoreduction to generate liquid organic substances in a single-compartment reactor. *Energy & Environmental Science* **2015**, *8*(7), 1998-2002.
24. Zhou, X.; Liu, R.; Sun, K.; Chen, Y.; Verlage, E.; Francis, S. A.; Lewis, N. S.; Xiang, C., Solar-Driven Reduction of 1 atm of CO₂ to Formate at 10% Energy-Conversion Efficiency by Use of a TiO₂-Protected III-V Tandem Photoanode in Conjunction with a Bipolar Membrane and a Pd/C Cathode. *ACS Energy Letters* **2016**, *1*(4), 764-770.
25. Schreier, M.; Curvat, L.; Giordano, F.; Steier, L.; Abate, A.; Zakeeruddin, S. M.; Luo, J.; Mayer, M. T.; Grätzel, M., Efficient photosynthesis of carbon monoxide from CO₂ using perovskite photovoltaics. *Nature communications* **2015**, *6*.
26. Bard, A. J.; Faulkner, L. R., *Electrochemical methods: fundamentals and applications*. Wiley New York: 1980; Vol. 2.
27. Urbain, F.; Rau, U.; Jaegermann, W. Light induced water splitting using multijunction thin film silicon solar cells. Dissertation / PhD Thesis, RWTH Aachen, Jülich, 2016.
28. (a) Tafel, J., Über die Polarisation bei kathodischer Wasserstoffentwicklung. *Z. phys. Chem* **1905**, *50*, 641; (b) Erdey-Gruz, T.; Volmer, M., The theory of hydrogen high tension. *Z. Physik. Chem* **1930**, *150*, 203-213.
29. Singh, M. R.; Clark, E. L.; Bell, A. T., Effects of electrolyte, catalyst, and membrane composition and operating conditions on the performance of solar-driven electrochemical reduction of carbon dioxide. *Physical Chemistry Chemical Physics* **2015**, *17*(29), 18924-18936.
30. Newman, J.; Thomas-Alyea, K. E., *Electrochemical systems*. John Wiley & Sons: 2012.
31. Brett, C. M.; Brett, A. M. O., *Electrochemistry: principles, methods, and applications*. Oxford university press Oxford: 1993; Vol. 4.
32. Tanaka, Y., *Ion exchange membranes: fundamentals and applications*. Elsevier: 2015.
33. Kondratenko, E. V.; Mul, G.; Baltrusaitis, J.; Larrazabal, G. O.; Perez-Ramirez, J., Status and perspectives of CO₂ conversion into fuels and chemicals by catalytic, photocatalytic and electrocatalytic processes. *Energy & Environmental Science* **2013**, *6*(11), 3112-3135.

34. (a) Hori, Y.; Murata, A.; Takahashi, R.; Suzuki, S., Electroreduction of carbon monoxide to methane and ethylene at a copper electrode in aqueous solutions at ambient temperature and pressure. *Journal of the American Chemical Society* **1987**, *109* (16), 5022-5023; (b) Hori, Y.; Wakebe, H.; Tsukamoto, T.; Koga, O., Electrocatalytic process of CO selectivity in electrochemical reduction of CO₂ at metal electrodes in aqueous media. *Electrochimica Acta* **1994**, *39* (11-12), 1833-1839; (c) Hori, Y., Electrochemical CO₂ Reduction on Metal Electrodes. In *Modern Aspects of Electrochemistry*, Vayenas, C.; White, R.; Gamboa-Aldeco, M., Eds. Springer New York: 2008; Vol. 42, pp 89-189; (d) Hori, Y., CO₂ Reduction Using Electrochemical Approach. In *Solar to Chemical Energy Conversion: Theory and Application*, Sugiyama, M.; Fujii, K.; Nakamura, S., Eds. Springer International Publishing: Cham, 2016; pp 191-211.
35. Wenzhen, L., Electrocatalytic Reduction of CO₂ to Small Organic Molecule Fuels on Metal Catalysts. In *Advances in CO₂ Conversion and Utilization*, American Chemical Society: 2010; Vol. 1056, pp 55-76.
36. Sanchez-Sanchez, C.; Montiel, V.; Tryk, D.; Aldaz, A.; Fujishima, A., Electrochemical approaches to alleviation of the problem of carbon dioxide accumulation. *Pure and Applied Chemistry* **2001**, *73* (12), 1917-1927.
37. Lu, X.; Leung, D. Y. C.; Wang, H.; Leung, M. K. H.; Xuan, J., Electrochemical Reduction of Carbon Dioxide to Formic Acid. *ChemElectroChem* **2014**, *1* (5), 836-849.
38. Lee, J.; Kwon, Y.; Machunda, R. L.; Lee, H. J., Electrocatalytic Recycling of CO₂ and Small Organic Molecules. *Chemistry – An Asian Journal* **2009**, *4* (10), 1516-1523.
39. (a) Kortlever, R.; Balemans, C.; Kwon, Y.; Koper, M. T. M., Electrochemical CO₂ reduction to formic acid on a Pd-based formic acid oxidation catalyst. *Catalysis Today* **2015**, *244* (0), 58-62; (b) Del Castillo, A.; Alvarez-Guerra, M.; Solla-Gullón, J.; Sáez, A.; Montiel, V.; Irabien, A., Electrocatalytic reduction of CO₂ to formate using particulate Sn electrodes: Effect of metal loading and particle size. *Applied Energy* **2015**, *157*, 165-173; (c) Alvarez-Guerra, M.; Del Castillo, A.; Irabien, A., Continuous electrochemical reduction of carbon dioxide into formate using a tin cathode: Comparison with lead cathode. *Chemical Engineering Research and Design* **2013**, (0); (d) Machunda, R. L.; Lee, J.; Lee, J., Microstructural surface changes of electrodeposited Pb on gas diffusion electrode during electroreduction of gas-phase CO₂. *Surface and Interface Analysis* **2010**, *42* (6-7), 564-567; (e) Innocent, B.; Liaigre, D.; Pasquier, D.; Ropital, F.; Léger, J. M.; Kokoh, K. B., Electroreduction of carbon dioxide to formate on lead electrode in aqueous medium. *J Appl Electrochem* **2009**, *39* (2), 227-232; (f) Noda, H.; Ikeda, S.; Oda, Y.; Imai, K.; Maeda, M.; Ito, K., Electrochemical Reduction of Carbon Dioxide at Various Metal Electrodes in Aqueous Potassium Hydrogen Carbonate Solution. *Bulletin of the Chemical Society of Japan* **1990**, *63* (9), 2459-2462; (g) Azuma, M.; Hashimoto, K.; Hiramoto, M.; Watanabe, M.; Sakata, T., Carbon dioxide reduction at low temperature on various metal electrodes. *Journal of Electroanalytical Chemistry and Interfacial Electrochemistry* **1989**, *260* (2), 441-445; (h) Mahmood, M. N.; Masheder, D.; Harty, C. J., Use of gas-diffusion electrodes for high-rate electrochemical reduction of carbon dioxide. I. Reduction at lead, indium- and tin-impregnated electrodes. *J Appl Electrochem* **1987**, *17* (6), 1159-1170.
40. Irtem, E.; Andreu, T.; Parra, A.; Hernandez-Alonso, M. D.; Garcia-Rodriguez, S.; Riesco-Garcia, J. M.; Penelas-Perez, G.; Morante, J. R., Low-energy formate production from CO₂ electroreduction using electrodeposited tin on GDE. *Journal of Materials Chemistry A* **2016**, *4* (35), 13582-13588.
41. (a) Köleli, F.; Atilan, T.; Palamut, N.; Gizir, A. M.; Aydin, R.; Hamann, C. H., Electrochemical reduction of CO₂ at Pb- and Sn-electrodes in a fixed-bed reactor in aqueous K₂CO₃ and KHCO₃ media. *J Appl Electrochem* **2003**, *33* (5), 447-450; (b) Lv, W.; Zhang, R.; Gao, P.; Lei, L., Studies on the faradaic efficiency for electrochemical reduction of carbon dioxide to formate on tin electrode. *Journal of Power Sources* **2014**, *253* (0), 276-281.
42. (a) Li, H.; Oloman, C., The Electro-Reduction of Carbon Dioxide in a Continuous Reactor. *J Appl Electrochem* **2005**, *35* (10), 955-965; (b) Li, H.; Oloman, C., Development of a continuous reactor for the electro-reduction of carbon dioxide to formate – Part 2: Scale-up. *J Appl Electrochem* **2007**, *37* (10), 1107-1117.

43. (a) Wu, J.; Sharma, P. P.; Harris, B. H.; Zhou, X.-D., Electrochemical reduction of carbon dioxide: IV dependence of the Faradaic efficiency and current density on the microstructure and thickness of tin electrode. *Journal of Power Sources* **2014**, *258* (0), 189-194; (b) Wu, J.; Risalvato, F. G.; Shuguo, M.; Zhou, X.-D., Electrochemical Reduction of Carbon Dioxide: III. The Role of Oxide Layer Thickness on the Performance of Sn Electrode in a Full Electrochemical Cell. *Journal of The Electrochemical Society* **2013**; (c) Wu, J.; Risalvato, F. G.; Sharma, P. P.; Pellechia, P. J.; Ke, F.-S.; Zhou, X.-D., Electrochemical Reduction of Carbon Dioxide: II. Design, Assembly, and Performance of Low Temperature Full Electrochemical Cells. *Journal of The Electrochemical Society* **2013**, *160* (9), F953-F957; (d) Wu, J.; Risalvato, F. G.; Ke, F.-S.; Pellechia, P. J.; Zhou, X.-D., Electrochemical Reduction of Carbon Dioxide I. Effects of the Electrolyte on the Selectivity and Activity with Sn Electrode. *Journal of The Electrochemical Society* **2012**, *159* (7), F353-F359.
44. Del Castillo, A.; Alvarez-Guerra, M.; Irabien, A., Continuous electroreduction of CO₂ to formate using Sn gas diffusion electrodes. *AIChE Journal* **2014**, *60* (10), 3557-3564.
45. Wang, Q.; Dong, H.; Yu, H., Fabrication of a novel tin gas diffusion electrode for electrochemical reduction of carbon dioxide to formic acid. *RSC Advances* **2014**, *4* (104), 59970-59976.
46. (a) Gattrell, M.; Gupta, N.; Co, A., A review of the aqueous electrochemical reduction of CO₂ to hydrocarbons at copper. *Journal of Electroanalytical Chemistry* **2006**, *594* (1), 1-19; (b) Peterson, A. A.; Abild-Pedersen, F.; Studt, F.; Rossmeisl, J.; Nørskov, J. K., How copper catalyzes the electroreduction of carbon dioxide into hydrocarbon fuels. *Energy and Environmental Science* **2010**, *3* (9), 1311-1315; (c) Durand, W. J.; Peterson, A. A.; Studt, F.; Abild-Pedersen, F.; Nørskov, J. K., Structure effects on the energetics of the electrochemical reduction of CO₂ by copper surfaces. *Surface Science* **2011**, *605* (15-16), 1354-1359; (d) Schouten, K. J. P.; Kwon, Y.; van der Ham, C. J. M.; Qin, Z.; Koper, M. T. M., A new mechanism for the selectivity to C₁ and C₂ species in the electrochemical reduction of carbon dioxide on copper electrodes. *Chemical Science* **2011**, *2* (10), 1902-1909; (e) Kuhl, K. P.; Cave, E. R.; Abram, D. N.; Jaramillo, T. F., New insights into the electrochemical reduction of carbon dioxide on metallic copper surfaces. *Energy & Environmental Science* **2012**, *5* (5), 7050-7059; (f) Kortlever, R.; Shen, J.; Schouten, K. J. P.; Calle-Vallejo, F.; Koper, M. T. M., Catalysts and Reaction Pathways for the Electrochemical Reduction of Carbon Dioxide. *The Journal of Physical Chemistry Letters* **2015**, *6* (20), 4073-4082; (g) Back, S.; Kim, J.-H.; Kim, Y.-T.; Jung, Y., On the mechanism of high product selectivity for HCOOH using Pb in CO₂ electroreduction. *Physical Chemistry Chemical Physics* **2016**, *18* (14), 9652-9657.
47. (a) Hori, Y.; Takahashi, R.; Yoshinami, Y.; Murata, A., Electrochemical Reduction of CO at a Copper Electrode. *The Journal of Physical Chemistry B* **1997**, *101* (36), 7075-7081; (b) Hori, Y.; Murata, A.; Tsukamoto, T.; Wakebe, H.; Koga, O.; Yamazaki, H., Adsorption of carbon monoxide at a copper electrode accompanied by electron transfer observed by voltammetry and IR spectroscopy. *Electrochimica Acta* **1994**, *39* (17), 2495-2500.
48. Hori, Y.; Murata, A.; Takahashi, R., Formation of hydrocarbons in the electrochemical reduction of carbon dioxide at a copper electrode in aqueous solution. *Journal of the Chemical Society, Faraday Transactions 1: Physical Chemistry in Condensed Phases* **1989**, *85* (8), 2309-2326.
49. (a) Hori, Y.; Takahashi, I.; Koga, O.; Hoshi, N., Selective Formation of C₂ Compounds from Electrochemical Reduction of CO₂ at a Series of Copper Single Crystal Electrodes. *The Journal of Physical Chemistry B* **2002**, *106* (1), 15-17; (b) Hori, Y.; Takahashi, I.; Koga, O.; Hoshi, N., Electrochemical reduction of carbon dioxide at various series of copper single crystal electrodes. *Journal of Molecular Catalysis A: Chemical* **2003**, *199* (1-2), 39-47.
50. (a) Schouten, K. J. P.; Qin, Z.; Gallent, E. P.; Koper, M. T. M., Two Pathways for the Formation of Ethylene in CO Reduction on Single-Crystal Copper Electrodes. *Journal of the American Chemical Society* **2012**, *134* (24), 9864-9867; (b) Schouten, K. J. P.; Pérez Gallent, E.; Koper, M. T. M., Structure Sensitivity of the Electrochemical Reduction of Carbon Monoxide on Copper Single Crystals. *ACS Catalysis* **2013**, *3* (6), 1292-1295.
51. Tang, W.; Peterson, A. A.; Varela, A. S.; Jovanov, Z. P.; Bech, L.; Durand, W. J.; Dahl, S.; Nørskov, J. K.; Chorkendorff, I., The importance of surface morphology in controlling the

- selectivity of polycrystalline copper for CO₂ electroreduction. *Physical Chemistry Chemical Physics* **2012**, *14* (1), 76-81.
52. Chen, C. S.; Handoko, A. D.; Wan, J. H.; Ma, L.; Ren, D.; Yeo, B. S., Stable and selective electrochemical reduction of carbon dioxide to ethylene on copper mesocrystals. *Catalysis Science & Technology* **2015**, *5* (1), 161-168.
53. Jhong, H.-R. M.; Brushett, F. R.; Kenis, P. J. A., The Effects of Catalyst Layer Deposition Methodology on Electrode Performance. *Advanced Energy Materials* **2013**, *3* (5), 589-599.
54. Schlesinger, M.; Paunovic, M., *Modern electroplating*. John Wiley & Sons: 2011; Vol. 55.
55. Bidault, F.; Brett, D.; Middleton, P.; Brandon, N., Review of gas diffusion cathodes for alkaline fuel cells. *Journal of Power Sources* **2009**, *187* (1), 39-48.
56. Wang, G.; Zhang, L.; Zhang, J., A review of electrode materials for electrochemical supercapacitors. *Chemical Society Reviews* **2012**, *41* (2), 797-828.
57. Weber, A. Z.; Mench, M. M.; Meyers, J. P.; Ross, P. N.; Gostick, J. T.; Liu, Q., Redox flow batteries: a review. *J Appl Electrochem* **2011**, *41* (10), 1137-1164.
58. (a) Alvarez-Guerra, M.; Quintanilla, S.; Irabien, A., Conversion of carbon dioxide into formate using a continuous electrochemical reduction process in a lead cathode. *Chemical Engineering Journal* **2012**, *207-208* (0), 278-284; (b) Wang, Q.; Dong, H.; Yu, H., Development of rolling tin gas diffusion electrode for carbon dioxide electrochemical reduction to produce formate in aqueous electrolyte. *Journal of Power Sources* **2014**, *271*, 278-284.
59. Chen, Y.; Kanan, M. W., Tin Oxide Dependence of the CO₂ Reduction Efficiency on Tin Electrodes and Enhanced Activity for Tin/Tin Oxide Thin-Film Catalysts. *Journal of the American Chemical Society* **2012**, *134* (4), 1986-1989.
60. (a) Lee, S.; Ocon, J. D.; Son, Y. I.; Lee, J., Alkaline CO₂ electrolysis toward selective and continuous HCOO⁻ production over SnO₂ nanocatalysts. *Journal of Physical Chemistry C* **2015**, *119* (9), 4884-4890; (b) Fu, Y.; Liu, Y.; Li, Y.; Qiao, J.; Zhou, X. D. In *Electrochemical CO₂ reduction to formic acid on crystalline SnO₂ nanosphere catalyst*, ECS Transactions, 2015; pp 53-59.
61. Zhao, C.; Wang, J.; Goodenough, J. B., Comparison of electrocatalytic reduction of CO₂ to HCOOH with different tin oxides on carbon nanotubes. *Electrochemistry Communications* **2016**, *65*, 9-13.
62. Zhang, S.; Kang, P.; Meyer, T. J., Nanostructured Tin Catalysts for Selective Electrochemical Reduction of Carbon Dioxide to Formate. *Journal of the American Chemical Society* **2014**, *136* (5), 1734-1737.
63. Hori, Y.; Konishi, H.; Futamura, T.; Murata, A.; Koga, O.; Sakurai, H.; Oguma, K., "Deactivation of copper electrode" in electrochemical reduction of CO₂. *Electrochimica Acta* **2005**, *50* (27), 5354-5369.
64. P. Millet, R. Ngameni, S. A. Grigoriev, N. Mbemba, F. Brisset, A. Ranjbari and C. Etiévant, *Int. J. Hydrogen Energy*, 2010, *35*, 5043-5052.
65. Fabbri, E.; Haberer, A.; Waltar, K.; Kotz, R.; Schmidt, T. J., Developments and perspectives of oxide-based catalysts for the oxygen evolution reaction. *Catalysis Science & Technology* **2014**, *4* (11), 3800-3821.
66. Pourbaix, M., *Atlas of Electrochemical Equilibria in Aqueous Solutions*. **1974**.
67. (a) Hirai, S.; Yagi, S.; Seno, A.; Fujioka, M.; Ohno, T.; Matsuda, T., Enhancement of the oxygen evolution reaction in Mn³⁺-based electrocatalysts: correlation between Jahn-Teller distortion and catalytic activity. *RSC Advances* **2016**, *6* (3), 2019-2023; (b) Menezes, P. W.; Indra, A.; Sahraie, N. R.; Bergmann, A.; Strasser, P.; Driess, M., Cobalt-Manganese-Based Spinel as Multifunctional Materials that Unify Catalytic Water Oxidation and Oxygen Reduction Reactions. *ChemSusChem* **2015**, *8* (1), 164-171; (c) Li, J.; Wang, Y.; Zhou, T.; Zhang, H.; Sun, X.; Tang, J.; Zhang, L.; Al-Enizi, A. M.; Yang, Z.; Zheng, G., Nanoparticle Superlattices as Efficient Bifunctional Electrocatalysts for Water Splitting. *Journal of the American Chemical Society* **2015**, *137* (45), 14305-14312; (d) Meng, Y.; Song, W.; Huang, H.; Ren, Z.; Chen, S.-Y.; Suib, S. L., Structure-Property Relationship of Bifunctional MnO₂ Nanostructures: Highly Efficient, Ultra-Stable Electrochemical Water Oxidation and Oxygen

- Reduction Reaction Catalysts Identified in Alkaline Media. *Journal of the American Chemical Society* **2014**, *136* (32), 11452-11464; (e) Ma, T. Y.; Dai, S.; Jaroniec, M.; Qiao, S. Z., Synthesis of Highly Active and Stable Spinel-Type Oxygen Evolution Electrocatalysts by a Rapid Inorganic Self-Templating Method. *Chemistry – A European Journal* **2014**, *20* (39), 12669-12676; (f) Suntivich, J.; May, K. J.; Gasteiger, H. A.; Goodenough, J. B.; Shao-Horn, Y., A Perovskite Oxide Optimized for Oxygen Evolution Catalysis from Molecular Orbital Principles. *Science* **2011**, *334* (6061), 1383-1385; (g) Cheng, F.; Shen, J.; Peng, B.; Pan, Y.; Tao, Z.; Chen, J., Rapid room-temperature synthesis of nanocrystalline spinels as oxygen reduction and evolution electrocatalysts. *Nat Chem* **2011**, *3* (1), 79-84; (h) Cheng, F.; Shen, J.; Ji, W.; Tao, Z.; Chen, J., Selective Synthesis of Manganese Oxide Nanostructures for Electrocatalytic Oxygen Reduction. *ACS Applied Materials & Interfaces* **2009**, *1* (2), 460-466.
68. I. C. Man, H.-Y. Su, F. Calle-Vallejo, H. A. Hansen, J. I. Martínez, N. G. Inoglu, J. Kitchin, T. F. Jaramillo, J. K. Nørskov and J. Rossmeisl, *ChemCatChem*, 2011, *3*, 1159–1165.
69. (a) Trasatti, S., Electrocatalysis by oxides—attempt at a unifying approach. *Journal of Electroanalytical Chemistry and Interfacial Electrochemistry* **1980**, *111* (1), 125-131; (b) Rossmeisl, J.; Qu, Z.-W.; Zhu, H.; Kroes, G.-J.; Nørskov, J. K., Electrolysis of water on oxide surfaces. *Journal of Electroanalytical Chemistry* **2007**, *607* (1), 83-89.
70. Burke, M. S.; Enman, L. J.; Batchellor, A. S.; Zou, S.; Boettcher, S. W., Oxygen evolution reaction electrocatalysis on transition metal oxides and (oxy) hydroxides: Activity trends and design principles. *Chemistry of Materials* **2015**, *27* (22), 7549-7558.
71. Sabatier, P., *La Catalyse en chimie organique* 1913, Paris, Bøøanger; b) P. Sabatier, M.J. Nye, *Chem. World* **2004**, *1* (12), 46-49.
72. I. C. Man, H.-Y. Su, F. Calle-Vallejo, H. A. Hansen, J. I. Martínez, N. G. Inoglu, J. Kitchin, T. F. Jaramillo, J. K. Nørskov and J. Rossmeisl, *ChemCatChem*, 2011, *3*, 1159–1165.
73. I. C. Man, H.-Y. Su, F. Calle-Vallejo, H. A. Hansen, J. I. Martínez, N. G. Inoglu, J. Kitchin, T. F. Jaramillo, J. K. Nørskov and J. Rossmeisl, *ChemCatChem*, 2011, *3*, 1159–1165.
74. Yang, X.; Wang, D., "Enabling practical electrocatalyst-assisted photoelectrochemical water splitting with earth abundant materials", *Nano Research* **2015**, *8*(1): 56–81
75. M. E. G. Lyons and M. P. Brandon, *J. Electroanal. Chem.*, 2010, *641*, 119–130.
76. P. W. T. Lu and S. Srinivasan, *J. Electrochem. Soc.*, 1978, *125*, 1416–1422.
77. D. Cibrev, M. Jankulovska, T. Lana-Villarreal and R. Gomez, *Int. J. Hydrogen Energy*, 2013, *38*, 2746–2753.
78. S. Joiret, M. Keddani, X. R. Nóvoa, M. C. Pérez, C. Rangel and H. Takenouti, *Cem. Concr. Compos.*, 2002, *24*, 7–15.
79. R. N. Singh, N. K. Singh and J. P. Singh, *Electrochim. Acta*, 2002, *47*, 3873–3879.
80. Zaharieva, I.; Chernev, P.; Risch, M.; Klingan, K.; Kohlhoff, M.; Fischer, A.; Dau, H. *Energy Environ. Sci.* 2012, *5*, 7081–7089
81. Gorlin, Y.; Lassalle-Kaiser, B.; Benck, J. D.; Gul, S.; Webb, S. M.; Yachandra, V. K.; Yano, J.; Jaramillo, T. F. *J. Am. Chem. Soc.* 2013, *135*, 8525–8534.
82. Robinson, D. M.; Go, Y. B.; Mui, M.; Gardner, G.; Zhang, Z.; Mastrogiovanni, D.; Garfunkel, E.; Li, J.; Greenblatt, M.; Dismukes, G. C. *J. Am. Chem. Soc.* 2013, *135*, 3494–3501.
83. Huynh, M.; Bediako, D. K.; Nocera, D. G., A Functionally Stable Manganese Oxide Oxygen Evolution Catalyst in Acid. *Journal of the American Chemical Society* **2014**, *136* (16), 6002-6010.
84. Hasan, M. A.; Zaki, M. I.; Pasupulety, L.; Kumari, K., Promotion of the hydrogen peroxide decomposition activity of manganese oxide catalysts. *Applied Catalysis A: General* **1999**, *181* (1), 171-179.
85. Luo, Z.; Irtem, E.; Ibáñez, M.; Nafria, R.; Martí-Sánchez, S.; Genç, A.; de la Mata, M.; Liu, Y.; Cadavid, D.; Llorca, J.; Arbiol, J.; Andreu, T.; Morante, J. R.; Cabot, A., Mn₃O₄@CoMn₂O₄-CoxOy Nanoparticles: Partial Cation Exchange Synthesis and Electrocatalytic Properties toward the Oxygen Reduction and Evolution Reactions. *ACS Applied Materials & Interfaces* **2016**, *8* (27), 17435-17444.
86. Kittel, C., *Introduction to solid state*. John Wiley & Sons: 1966.

87. Kudo, A.; Miseki, Y., Heterogeneous photocatalyst materials for water splitting. *Chemical Society Reviews* **2009**, *38*(1), 253-278.
88. Chen, Z.; Dinh, H. N.; Miller, E., Photoelectrochemical water splitting. *SpringerBriefs in Energy, New York* **2013**, 49-61.
89. White, J. L.; Baruch, M. F.; Pander III, J. E.; Hu, Y.; Fortmeyer, I. C.; Park, J. E.; Zhang, T.; Liao, K.; Gu, J.; Yan, Y., Light-driven heterogeneous reduction of carbon dioxide: Photocatalysts and photoelectrodes. *Chemical reviews* **2015**, *115*(23), 12888-12935.
90. Boddy, P. J., Oxygen Evolution on Semiconducting TiO₂. *Journal of The Electrochemical Society* **1968**, *115*(2), 199-203.
91. Fujishima, A.; Honda, K., Electrochemical Photolysis of Water at a Semiconductor Electrode. *Nature* **1972**, *238*(5358), 37-38.
92. Chen, X.; Mao, S. S., Titanium Dioxide Nanomaterials: Synthesis, Properties, Modifications, and Applications. *Chemical Reviews* **2007**, *107*(7), 2891-2959.
93. Wang, G.; Wang, H.; Ling, Y.; Tang, Y.; Yang, X.; Fitzmorris, R. C.; Wang, C.; Zhang, J. Z.; Li, Y., Hydrogen-Treated TiO₂ Nanowire Arrays for Photoelectrochemical Water Splitting. *Nano Letters* **2011**, *11*(7), 3026-3033.
94. Liu, B.; Aydil, E. S., Growth of Oriented Single-Crystalline Rutile TiO₂ Nanorods on Transparent Conducting Substrates for Dye-Sensitized Solar Cells. *Journal of the American Chemical Society* **2009**, *131*(11), 3985-3990.
95. Grätzel, M., Photoelectrochemical cells. *Nature* **2001**, *414*(6861), 338-344.
96. Shafiei, M.; Alpas, A. T., Electrochemical performance of a tin-coated carbon fibre electrode for rechargeable lithium-ion batteries. *J. Power Sources* **2011**, *196*(18), 7771-7778.
97. (a) Fàbrega, C.; Andreu, T.; Tarancón, A.; Flox, C.; Morata, A.; Calvo-Barrio, L.; Morante, J. R., Optimization of surface charge transfer processes on rutile TiO₂ nanorods photoanodes for water splitting. *International Journal of Hydrogen Energy* **2013**, *38*(7), 2979-2985; (b) Fàbrega, C.; Monllor-Satoca, D.; Ampudia, S.; Parra, A.; Andreu, T.; Morante, J. R., Tuning the Fermi Level and the Kinetics of Surface States of TiO₂ Nanorods by Means of Ammonia Treatments. *The Journal of Physical Chemistry C* **2013**, *117*(40), 20517-20524.
98. Lefrou, C.; Fabry, P.; Poignet, J.-C., *Electrochemistry: the basics, with examples*. Springer Science & Business Media: 2012.
99. Genctec-EO manufacturer whitepaper on "How It Works: Power Detectors" obtained from <https://gentec-eo.com/> on May, 2016.
100. Bich, E.; Millat, J.; Vogel, E., The viscosity and thermal conductivity of pure monatomic gases from their normal boiling point up to 5000 K in the limit of zero density and at 0.101325 MPa. *Journal of physical and chemical reference data* **1990**, *19*(6), 1289-1305.
101. Jia, F.; Yu, C.; Ai, Z.; Zhang, L., Fabrication of nanoporous gold film electrodes with ultrahigh surface area and electrochemical activity. *Chemistry of Materials* **2007**, *19*(15), 3648-3653.
102. Uribe, F.; Mason, E. A.; Kestin, J., Thermal conductivity of nine polyatomic gases at low density. *Journal of physical and chemical reference data* **1990**, *19*(5), 1123-1136.
103. Skoog, D. A., *Fundamentals of analytical chemistry*. Grupo Editorial Norma: 2004.
104. Skoog, D. A.; West, D. M., *Principles of instrumental analysis*. Saunders College Philadelphia: 1980; Vol. 158.
105. Hadad, G. M.; Emara, S.; Mahmoud, W. M., Development and validation of a stability-indicating RP-HPLC method for the determination of paracetamol with dantrolene or/and cetirizine and pseudoephedrine in two pharmaceutical dosage forms. *Talanta* **2009**, *79*(5), 1360-1367.
106. The images are taken from <http://www.mhhe.com/>
107. Hornak, J. P., *The Basics of NMR*. 1997.
108. Shafiei, M.; Alpas, A. T., Electrochemical performance of a tin-coated carbon fibre electrode for rechargeable lithium-ion batteries. *Journal of Power Sources* **2011**, *196*(18), 7771-7778.

109. Bard, A. J.; Parsons, R.; Jordan, J., *Standard potentials in aqueous solution*. CRC press: 1985; Vol. 6.
110. Sullivan, B. P.; Krist, K.; Guard, H., *Electrochemical and electrocatalytic reactions of carbon dioxide*. Elsevier: 1992.
111. Sapountzi, F. M.; Gracia, J. M.; Weststrate, C. J.; Fredriksson, H. O. A.; Niemantsverdriet, J. W., Electrocatalysts for the generation of hydrogen, oxygen and synthesis gas. *Progress in Energy and Combustion Science* **2017**, *58*, 1-35.
112. Hernández, R. M.; Márquez, J.; Márquez, O. P.; Choy, M.; Ovalles, C.; Garcia, J. J.; Scharifker, B., Reduction of Carbon Dioxide on Modified Glassy Carbon Electrodes. *Journal of The Electrochemical Society* **1999**, *146* (11), 4131-4136.
113. Jitaru, M.; Lowy, D.; Toma, M.; Toma, B.; Oniciu, L., Electrochemical reduction of carbon dioxide on flat metallic cathodes. *J Appl Electrochem* **1997**, *27* (8), 875-889.
114. Chaplin, R. P. S.; Wragg, A. A., Effects of process conditions and electrode material on reaction pathways for carbon dioxide electroreduction with particular reference to formate formation. *J Appl Electrochem* **2003**, *33* (12), 1107-1123.
115. (a) Lee, S.; Ju, H.; Machunda, R.; Uhm, S.; Lee, J. K.; Lee, H. J.; Lee, J., Sustainable production of formic acid by electrolytic reduction of gaseous carbon dioxide. *Journal of Materials Chemistry A* **2015**, *3* (6), 3029-3034; (b) Prakash, G. K. S.; Viva, F. A.; Olah, G. A., Electrochemical reduction of CO₂ over Sn-Nafion® coated electrode for a fuel-cell-like device. *Journal of Power Sources* **2013**, *223* (0), 68-73.
116. Chen, Y.; Li, C. W.; Kanan, M. W., Aqueous CO₂ Reduction at Very Low Overpotential on Oxide-Derived Au Nanoparticles. *Journal of the American Chemical Society* **2012**, *134* (49), 19969-19972.
117. (a) Cui, C.; Han, J.; Zhu, X.; Liu, X.; Wang, H.; Mei, D.; Ge, Q., Promotional effect of surface hydroxyls on electrochemical reduction of CO₂ over SnO_x/Sn electrode. *Journal of Catalysis*; (b) Cui, C.; Wang, H.; Zhu, X.; Han, J.; Ge, Q., A DFT study of CO₂ electrochemical reduction on Pb(211) and Sn(112). *Sci. China Chem.* **2015**, *58* (4), 607-613.
118. Subramanian, K.; Asokan, K.; Jeevarathinam, D.; Chandrasekaran, M., Electrochemical membrane reactor for the reduction of carbondioxide to formate. *J Appl Electrochem* **2007**, *37* (2), 255-260.
119. Garsany, Y.; Gould, B. D.; Baturina, O. A.; Swider-Lyons, K. E., Comparison of the sulfur poisoning of PBI and Nafion PEMFC cathodes. *Electrochemical and Solid-State Letters* **2009**, *12* (9), B138-B140.
120. Steele, B. C. H.; Heinzl, A., Materials for fuel-cell technologies. *Nature* **2001**, *414* (6861), 345-352.
121. Kieboom, A. P. G., Purification of Laboratory Chemicals, 3rd edition. D.D. Perrin and W. L. F. Armarego. Pergamon Press, Oxford, 1988, X + 392 pp. ISBN 0-08-034714-2, Flexicover, Price £37.50. ISBN 0-08-034715-0, Hardcover, Price £75.00. *Recueil des Travaux Chimiques des Pays-Bas* **1988**, *107* (12), 685-685.
122. (a) Del Castillo, A.; Alvarez-Guerra, M.; Irabien, A., Continuous electroreduction of CO₂ to formate using Sn gas diffusion electrodes. *AIChEJ.* **2014**, *60* (10), 3557-3564; (b) Del Castillo, A.; Alvarez-Guerra, M.; Solla-Gullón, J.; Sáez, A.; Montiel, V.; Irabien, A., Electrocatalytic reduction of CO₂ to formate using particulate Sn electrodes: Effect of metal loading and particle size. *Appl. Energy* **2015**, *157*, 165-173.
123. Bard, A. J.; Faulkner, L. R.; Leddy, J.; Zoski, C. G., *Electrochemical methods: fundamentals and applications*. Wiley New York: 1980; Vol. 2.
124. Sen, S.; Liu, D.; Palmore, G. T. R., Electrochemical Reduction of CO₂ at Copper Nanofoams. *ACS Catalysis* **2014**, *4* (9), 3091-3095.
125. Radisic, A.; Vereecken, P. M.; Searson, P. C.; Ross, F. M., The morphology and nucleation kinetics of copper islands during electrodeposition. *Surface Science* **2006**, *600* (9), 1817-1826.
126. Lian, G.; Gerko, O.; Aleksandar, R.; Peter, M. H.; Peter, C. S., Island growth in electrodeposition. *Journal of Physics D: Applied Physics* **2011**, *44* (44), 443001.
127. Larson, C.; Farr*, J. P. G., Current research and potential applications for pulsed current electrodeposition – a review. *Transactions of the IMF* **2012**, *90* (1), 20-29.

128. Ren, D.; Wong, N. T.; Handoko, A. D.; Huang, Y.; Yeo, B. S., Mechanistic Insights into the Enhanced Activity and Stability of Agglomerated Cu Nanocrystals for the Electrochemical Reduction of Carbon Dioxide to n-Propanol. *Journal of Physical Chemistry Letters* **2016**, *7*(1), 20-24.
129. Chung, J.; Won, D. H.; Koh, J.; Kim, E.-H.; Woo, S. I., Hierarchical Cu pillar electrodes for electrochemical CO₂ reduction to formic acid with low overpotential. *Physical Chemistry Chemical Physics* **2016**, *18*(8), 6252-6258.
130. Natter, H.; Hempelmann, R., Nanocrystalline Copper by Pulsed Electrodeposition: The Effects of Organic Additives, Bath Temperature, and pH. *The Journal of Physical Chemistry* **1996**, *100*(50), 19525-19532.
131. Despic, A.; Popov, K., The effect of pulsating potential on the morphology of metal deposits obtained by mass-transport controlled electrodeposition. *J Appl Electrochem* **1971**, *1*(4), 275-278.
132. (a) DeWulf, D. W.; Jin, T.; Bard, A. J., Electrochemical and surface studies of carbon dioxide reduction to methane and ethylene at copper electrodes in aqueous solutions. *Journal of The Electrochemical Society* **1989**, *136*(6), 1686-1691; (b) Xie, J.; Huang, Y.; Yu, H., Tuning the catalytic selectivity in electrochemical CO₂ reduction on copper oxide-derived nanomaterials. *Frontiers of Environmental Science & Engineering* **2015**, *9*(5), 861-866.
133. Scherrer, P., Göttinger Nachrichten Math. Phys **1918**, *2*, 98-100.
134. Singh, A., *Advanced x-ray techniques in research and industry*. IOS Press: 2005.
135. Li, C. W.; Kanan, M. W., CO₂ Reduction at Low Overpotential on Cu Electrodes Resulting from the Reduction of Thick Cu₂O Films. *Journal of the American Chemical Society* **2012**, *134*(17), 7231-7234.
136. Verdaguer-Casadevall, A.; Li, C. W.; Johansson, T. P.; Scott, S. B.; McKeown, J. T.; Kumar, M.; Stephens, I. E. L.; Kanan, M. W.; Chorkendorff, I., Probing the Active Surface Sites for CO Reduction on Oxide-Derived Copper Electrocatalysts. *Journal of the American Chemical Society* **2015**, *137*(31), 9808-9811.
137. Hara, K.; Tsuneto, A.; Kudo, A.; Sakata, T., Electrochemical Reduction of CO₂ on a Cu Electrode under High Pressure: Factors that Determine the Product Selectivity. *Journal of The Electrochemical Society* **1994**, *141*(8), 2097-2103.
138. Ma, M.; Djanashvili, K.; Smith, W. A., Selective electrochemical reduction of CO₂ to CO on CuO-derived Cu nanowires. *Physical Chemistry Chemical Physics* **2015**, *17*(32), 20861-20867.
139. M.C. Biesinger, B.P. Payne, A.P. Grosvenor, L.W.M. Lau, A.R. Gerson, R.St.C. Smart, *Appl. Surf. Sci.* **257** (2011) 2717.
140. Xing, W.; Yin, G.; Zhang, J., *Rotating electrode methods and oxygen reduction electrocatalysts*. Elsevier: 2014.
141. Butler, J., Studies in heterogeneous equilibria. Part II.—The kinetic interpretation of the nernst theory of electromotive force. *Transactions of the Faraday Society* **1924**, *19* (March), 729-733.
142. Roche, I.; Chaînet, E.; Chatenet, M.; Vondrák, J., Carbon-Supported Manganese Oxide Nanoparticles as Electrocatalysts for the Oxygen Reduction Reaction (ORR) in Alkaline Medium: Physical Characterizations and ORR Mechanism. *The Journal of Physical Chemistry C* **2007**, *111*(3), 1434-1443.
143. Tarasevich, M.; Sadkowski, A.; Yeager, E., Oxygen electrochemistry. In *Comprehensive treatise of electrochemistry*, Springer: 1983; pp 301-398.
144. Wroblowa, H. S.; Razumney, G., Electroreduction of oxygen: A new mechanistic criterion. *Journal of Electroanalytical Chemistry and Interfacial Electrochemistry* **1976**, *69*(2), 195-201.
145. Yedger, E. *Recent Advances in the Sciences of Electrocatalysis*; DTIC Document: 1980.
146. (a) Hickling, A.; Hill, S., Oxygen overvoltage. Part I. The influence of electrode material, current density, and time in aqueous solution. *Discussions of the Faraday Society* **1947**, *1*, 236-246; (b) Rüetschi, P.; Delahay, P., Influence of electrode material on oxygen overvoltage: A theoretical analysis. *The Journal of Chemical Physics* **1955**, *23*(3), 556-560.

147. Trasatti, S., Electrocatalysis in the anodic evolution of oxygen and chlorine. *Electrochimica Acta* **1984**, *29* (11), 1503-1512.
148. Li, L.; Wu, Z.; Yuan, S.; Zhang, X., Advances and Challenges for Flexible Energy Storage and Conversion Devices and Systems. *Energy & Environmental Science* **2014**.
149. Burke, M. S.; Kast, M. G.; Trotochaud, L.; Smith, A. M.; Boettcher, S. W., Cobalt-Iron (Oxy)hydroxide Oxygen Evolution Electrocatalysts: The Role of Structure and Composition on Activity, Stability, and Mechanism. *Journal of the American Chemical Society* **2015**, *137* (10), 3638-3648.
150. Pourbaix, M., Potential-pH Diagram of Lead and its Applications to the Study of Lead Corrosion and to the Lead Storage Battery. **1951**.
151. Rao, D. B., *Electrochemistry for environmental protection*. Discovery Publishing House: 2001.
152. Bessarabov, D.; Wang, H.; Li, H.; Zhao, N., *PEM electrolysis for hydrogen production: principles and applications*. CRC Press: 2016.
153. Murcia-López, S.; Fàbrega, C.; Monllor-Satoca, D.; Hernández-Alonso, M. D.; Penelas-Pérez, G.; Morata, A.; Morante, J. R.; Andreu, T., Tailoring multilayered BiVO₄ photoanodes by pulsed laser deposition for water splitting. *ACS applied materials & interfaces* **2016**, *8* (6), 4076-4085.
154. Sivula, K.; van de Krol, R., Semiconducting materials for photoelectrochemical energy conversion. *Nature Reviews Materials* **2016**, *1*, 15010.
155. (a) Spurgeon, J. M.; Atwater, H. A.; Lewis, N. S. J. *Phys. Chem. C* **2008**, *112*, 6186. (b) Erne, B. H.; Vanmaekelbergh, D.; Kelly, J. J. *Adv. Mater.* **1995**, *7*, 739. (c) Erne, B. H.; Vanmaekelbergh, D.; Kelly, J. J. *J. Electrochem. Soc.* **1996**, *143*, 305. (d) Maiolo, J. R.; Atwater, H. A.; Lewis, N. S. J. *Phys. Chem. C* **2008**, *112*, 6194. (e) Maiolo, J. R.; Kayes, B. M.; Filler, M. A.; Putnam, M. C.; Kelzenberg, M. D.; Atwater, H. A.; Lewis, N. S. J. *Am. Chem. Soc.* **2007**, *129*, 12346.
156. Kim, J. H.; Magesh, G.; Kang, H. J.; Banu, M.; Kim, J. H.; Lee, J.; Lee, J. S., Carbonate-coordinated cobalt co-catalyzed BiVO₄/WO₃ composite photoanode tailored for CO₂ reduction to fuels. *Nano Energy* **2015**, *15*, 153-163.
157. Magesh, G.; Kim, E. S.; Kang, H. J.; Banu, M.; Kim, J. Y.; Kim, J. H.; Lee, J. S., A versatile photoanode-driven photoelectrochemical system for conversion of CO₂ to fuels with high faradaic efficiencies at low bias potentials. *Journal of Materials Chemistry A* **2013**.
158. (a) Alpert, D. J.; Mancini, T. R.; Houser, R. M.; Grossman, J. W.; Schissel, P.; Carasso, M.; Jorgensen, G.; Scheve, M., Solar concentrator development in the United States. *Solar energy materials* **1991**, *24* (1), 307-319; (b) Yamaguchi, M.; Takamoto, T.; Araki, K., Super high-efficiency multi-junction and concentrator solar cells. *Solar Energy Materials and Solar Cells* **2006**, *90* (18), 3068-3077; (c) Zubi, G.; Bernal-Agustín, J. L.; Fracastoro, G. V., High concentration photovoltaic systems applying III-V cells. *Renewable and Sustainable Energy Reviews* **2009**, *13* (9), 2645-2652.
159. Cheng, J.; Zhang, M.; Wu, G.; Wang, X.; Zhou, J.; Cen, K., Optimizing CO₂ reduction conditions to increase carbon atom conversion using a Pt-RGO||Pt-TNT photoelectrochemical cell. *Solar Energy Materials and Solar Cells* **2015**, *132*, 606-614.
160. Deb Nath, N. C.; Choi, S. Y.; Jeong, H. W.; Lee, J.-J.; Park, H., Stand-alone photoconversion of carbon dioxide on copper oxide wire arrays powered by tungsten trioxide/dye-sensitized solar cell dual absorbers. *Nano Energy* **2016**, *25*, 51-59.
161. Son, E. J.; Ko, J. W.; Kuk, S. K.; Choe, H.; Lee, S.; Kim, J. H.; Nam, D. H.; Ryu, G. M.; Kim, Y. H.; Park, C. B., Sunlight-assisted, biocatalytic formate synthesis from CO₂ and water using silicon-based photoelectrochemical cells. *Chemical Communications* **2016**, *52* (62), 9723-9726.
162. (a) Kyriacou, G. Z.; Anagnostopoulos, A. K., Influence CO₂ partial pressure and the supporting electrolyte cation on the product distribution in CO₂ electroreduction. *J Appl Electrochem* **1993**, *23* (5), 483-486; (b) Thorson, M. R.; Siil, K. I.; Kenis, P. J., Effect of Cations on the Electrochemical Conversion of CO₂ to CO. *Journal of the Electrochemical Society* **2013**, *160* (1), F69-F74.

163. Singh, M. R.; Kwon, Y.; Lum, Y.; Ager, J. W.; Bell, A. T., Hydrolysis of Electrolyte Cations Enhances the Electrochemical Reduction of CO₂ over Ag and Cu. *Journal of the American Chemical Society* **2016**.
164. Mistry, H.; Varela, A. S.; Bonifacio, C. S.; Zegkinoglou, I.; Sinev, I.; Choi, Y.-W.; Kisslinger, K.; Stach, E. A.; Yang, J. C.; Strasser, P., Highly selective plasma-activated copper catalysts for carbon dioxide reduction to ethylene. *Nature Communications* **2016**, *7*.
165. Jin, L.; Zhao, H.; Ma, D.; Vomiero, A.; Rosei, F., Dynamics of semiconducting nanocrystal uptake into mesoporous TiO₂ thick films by electrophoretic deposition. *Journal of Materials Chemistry A* **2015**, *3* (2), 847-856.
166. L. Jin, H. Zhao, D. Ma, A. Vomiero and F. Rosei, *J. Mater. Chem. A* **2014**, *3*, 847-856.
167. H. Jun, M. Careem and A. Arof, *International Journal of Photoenergy* **2014**, *2014*. and Y.-L. Lee, C.-F. Chi and S.-Y. Liao, *Chemistry of materials* **2009**, *22*, 922-927.
168. Sfaelou, S.; Sygellou, L.; Dracopoulos, V.; Travlos, A.; Lianos, J. *Phys. Chem. C* **2014**, *118*, 22873–22880.
169. Larrazábal, G. O.; Martín, A. J.; Krumeich, F.; Hauert, R.; Pérez-Ramírez, J., Solvothermally-Prepared Cu₂O Electrocatalysts for CO₂ Reduction with Tunable Selectivity by the Introduction of p-Block Elements. *ChemSusChem* **2016**, n/a-n/a.
170. Haycock, B. J.; Kylee Rice, M.; Lewis, J. P., High-throughput calculations of alloyed delafossite materials: Application to CuGa_{1-x}Fe_xO₂. *Computational Materials Science* **2014**, *86*, 155-164.
171. Larrazábal, G. O.; Martín, A. J.; Mitchell, S.; Hauert, R.; Pérez-Ramírez, J., Enhanced Reduction of CO₂ to CO over Cu-In Electrocatalysts: Catalyst Evolution Is the Key. *ACS Catalysis* **2016**, *6* (9), 6265-6274.
172. (a) Levich, V. G., *Physicochemical hydrodynamics*. Prentice Hall: 1962; (b) Levich, V., Present state of the theory of oxidation-reduction in solution (bulk and electrode reactions). *Advances in electrochemistry and electrochemical engineering* **1966**, *4*, 249-371.
173. Bezemer, G. L.; Bitter, J. H.; Kuipers, H. P.; Oosterbeek, H.; Holewijn, J. E.; Xu, X.; Kapteijn, F.; van Dillen, A. J.; de Jong, K. P., Cobalt particle size effects in the Fischer–Tropsch reaction studied with carbon nanofiber supported catalysts. *Journal of the American Chemical Society* **2006**, *128* (12), 3956-3964.

Annexes

Annex 1. Surface Area Calculation

At first, the fluorine doped tin oxide coated silicate glass (FTO) was cut into 35 x 40 mm dimensions. The edges are isolated with Teflon tape to wire an electrical contact via FTO layer. Next, the digital pictures of the samples were taken with a mobile phone (SONY Z5) having a 10 MP high definition camera that could make a macro-focus for close-up photo shooting. The digital picture of FTO before and after hydrothermal synthesis of TiO₂ Nanorods is given in Figure 9-1.

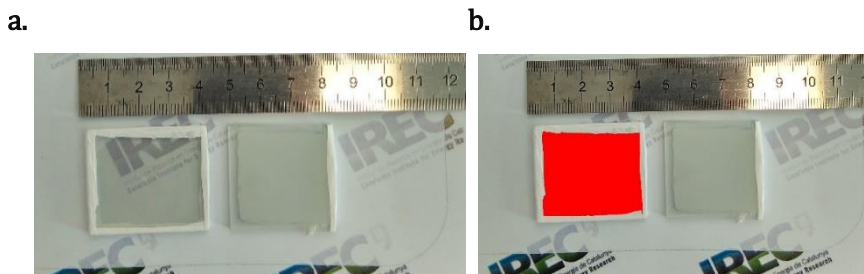


Figure 9-1. (a) Digital image of FTO/Silicate Glass before and after hydrothermal synthesis of TiO₂ nanorods, the metal ruler is for scale. (b) The highlighted active surface area of FTO is where TiO₂ nanorods would be grown by hydrothermal method, the metal ruler is for scale.

Once the digital picture was transferred to the computer, the geometrical surface area of a sample was found by using two different software: Paint.net and Image J. The active surface of an electrode was highlighted with red colour by using Paint.net, “Magic Wand” tool. The highlighted image was saved with a different nomenclature and opened by using Image-J analysis software. After the adjustment of the pixel-to-mm scale and tuning colour threshold, the active surface area was determined by selected area vs. pixel analysis. Finally, the active surface area of FTO that will be used in hydrothermal synthesis was found to be 10.478 cm². The total surface area was found to be 14.230 cm², so nearly an area of 3.75 cm² from the edges was isolated by Teflon tape. The place to install the FTO inside the PECf set-up is 35 x 40 mm (14 cm). The plastic gasket is placed on top of the electrode-holder assembly and limits the surface area to 30 x 34 mm (10.2). The dimensions after cutting of the FTO glass and Teflon lining for isolation seems to fit well to the cell-assembly dimensions.

Annex 2. Equations used for rotating disk electrode tests

Solution of the Convective-Diffusion Equation. Now we consider a situation where an electroactive species such as “O” transported by convective-diffusion to an electrode surface where it undergoes an electrode reaction:



where n is the number of electrons transferred, k_f and k_b are the forward and backward kinetic rate constants. When a forced convection is imposed to such system in RDE experiment, the diffusion layer has a time-independent thickness which was explained by Levich et. al¹⁷². This theory formulates the simplified model of the Nernst layer and provides a mathematical equation to express the thickness of that layer as a function of the system parameters. Accordingly, the thickness of the diffusion-layer (δ_o) can be found from,

$$\delta_o = 1.61 \cdot D_o^{1/3} \cdot \omega^{-1/2} \cdot \nu^{1/6} \quad (9.2)$$

where δ_o stands for diffusion layer thickness (cm), D_o is the diffusion coefficient ($\text{cm}^2 \cdot \text{s}^{-1}$), ω as rotating speed ($\text{rad} \cdot \text{s}^{-1}$), ν as kinematic viscosity of the electrolyte ($\text{cm}^2 \cdot \text{s}^{-1}$).

According to this model, the concentration of O at the diffusion layer is equal to the initial concentration until the Nernst layer, δ_{Nernst} shown in Figure 9-2. At δ_{Nernst} , a reversible reaction would follow the Nernst equation (blue line in Figure 9-2) which is given in Eq.(1.11) previously in Fundamentals of electrochemistry section. When the real profile (red line) shows a deviation from the Nernst model, it indicates a limiting step in the reaction kinetics, i.e. irreversible reaction.

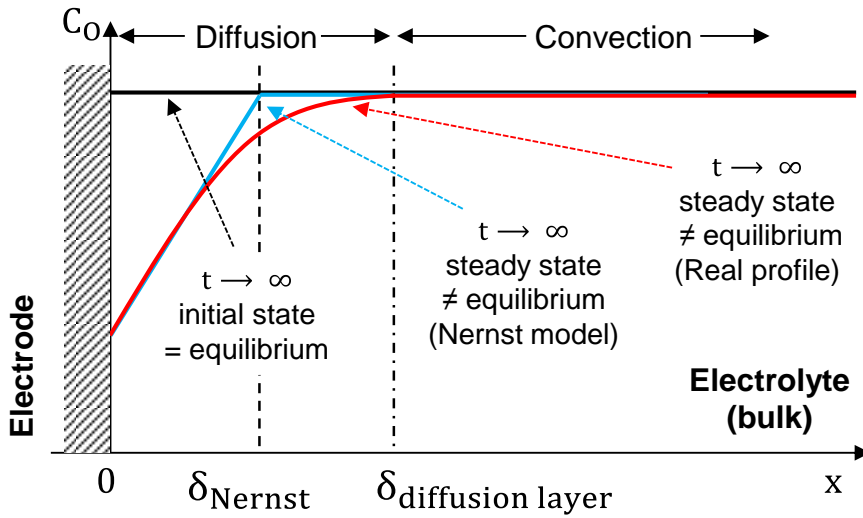


Figure 9-2. Concentration profile of species “O” consumed in a system under convective-diffusion

The number of electrons transferred at the kinetic step can be found under convective-diffusion conditions. This could be realized by the relationship between the measured limiting currents ($i_{lim,c}$) at various rotating speeds (ω) under fixed potentials and can be expressed on the basis of Levich equation,

$$i_{lim,c} = 0.62 \cdot n \cdot F \cdot A \cdot D_O^{2/3} \cdot \omega^{1/2} \cdot \nu^{-1/6} \cdot C_O^* \quad (9.3)$$

where $i_{lim,c}$ is the limiting current in amperes, n is the number of electrons transferred, F as Faraday’s constant (96485 C), and C_O^* , is the concentration of the species “O” ($O_{2,dissolved} = 1.2 \times 10^{-6}$). This equation applies to the total mass-transfer-limited condition at the RDE and predicts that $i_{lim,c}$ is proportional to C_O^* and $\omega^{1/2}$. By plotting $i_{lim,c} = f(\omega^{1/2})$, the slope of this plot would provide the electron transference number, “ n_t ” if the diffusion coefficient of species “O” and kinetic viscosity of the solution are known^{xxi}. The slope of this plot would be,

$$\text{slope} = 0.62 \cdot n_t \cdot F \cdot A \cdot D_O^{2/3} \cdot \nu^{-1/6} \cdot C_O^* \quad (9.4)$$

A deviation of a plot of $i_{lim,c} = f(\omega^{1/2})$ from a straight line intersecting the origin suggests that a kinetic limitation is involved in the electron-transfer reaction.

^{xxi} For ORR, those parameters are, $D_{O_2} = 1.9 \times 10^{-5} \text{ cm}^2 \cdot \text{s}^{-1}$ and $\nu_{0.1M \text{ KOH}} = 0.01 \text{ cm}^2 \cdot \text{s}^{-1}$

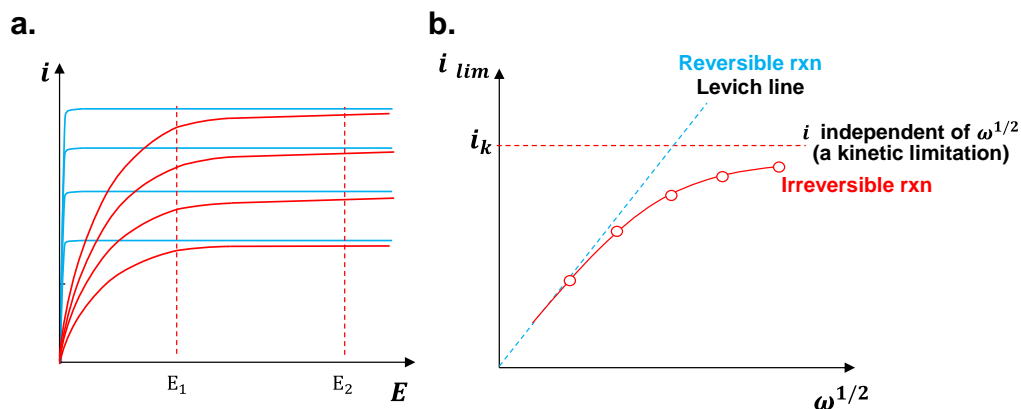


Figure 9-3. (a) Linear sweep voltammograms of a RDE experiment for a reversible (blue line) and irreversible (red line) reactions (b) Variation of i with $\omega^{1/2}$ for an electrode reaction with fast kinetics (blue dashed line) and slow kinetics (red line) due to the deviation from Levich line.

Koutecky-Levich equations. C_O^* in Eq.(9.3) and (9.4) stands for fixed concentration at δ_{Nernst} layer. According to this model, the concentration at the bulk of the electrolyte is equal to the initial concentration till the border of δ_{Nernst} . At quasi-steady state this model leads to a mathematical discontinuity in the concentration profile at this δ_{Nernst} distance from the electrode, shown in Figure 9-3. This implies that apart from the diffusion, there is another phenomena such as a kinetic limitation and Levich equation alone is not sufficient to model. After the arrangement of Levich equation to define two separate regions, one can obtain the Koutecky-Levich equation,

$$\frac{1}{i} = \left(\frac{1}{i_k} + \frac{1}{i_{l,c}} \right) = \left(\frac{1}{n \cdot F \cdot A \cdot k_f \cdot C_O^*} + \frac{1}{0.62 \cdot n \cdot F \cdot A \cdot D_O^{\frac{2}{3}} \cdot \omega^{\frac{1}{2}} \cdot \nu^{-\frac{1}{6}} C_O^*} \right) \quad (9.5)$$

Here, i_k represents the current in the absence of any mass-transfer effects, that is, the current that would flow under pure kinetic limitation of that individual potential-current point.

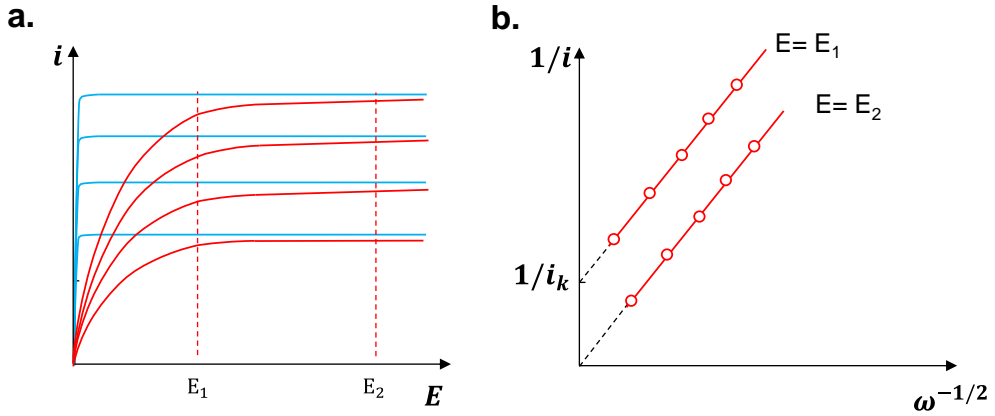


Figure 9-4. (a) Concentration profile of species “O” consumed in a system with forced convection **(b)** Koutecky-Levich plots at potential E_1 where electron transfer is a limiting factor and at E_2 where the electron transfer is fast

The slope of the plot would be similar to Levich line in Eq.(9.3). The intersection of the plot would be used to calculate the kinetic parameters e.g. kinetic rate constant (k_f), standard rate constant (k_0) and electron transfer coefficient at the rate determining step (α). Considering the irreversible one-step, “n” electron transfer reaction, the disk current is given by,

$$i = n \cdot F \cdot A \cdot \mathbf{k}_f(\mathbf{E}) \cdot C_0^{x=0} \quad (9.6)$$

and

$$\mathbf{k}_f(\mathbf{E}) = k^0 \cdot \exp\left[\frac{-\alpha \cdot F}{R \cdot T} \cdot (E - E^{0'})\right] \quad (9.7)$$

where R stands for ideal gas constant. Eq.(9.6) and Eq.(9.7) can be used together to find kinetic rate constant (k^0) where the concentration of species “O” at $x=0$, is so small that we can neglect C_0^* . Also “ η ” can be used for overpotential term instead of $(E - E^{0'})$ given by,

$$i_k = \left[n \cdot F \cdot A \cdot k^0 \cdot \exp\left(\frac{-\alpha \cdot F}{R \cdot T} \cdot \eta\right) \cdot C_0^* \right]_{\Delta x=0} \quad (9.8)$$

Once k^0 is found from Eq.(9.8), one can derive a Tafel plot where the system is under pure kinetic limitation given by,

$$\mathbf{k}_f = k^0 \cdot \exp\left[\left(\frac{-\alpha \cdot F}{R \cdot T}\right) \cdot \eta\right] \quad (9.9)$$

by taking the logarithm, a plot of k_f vs. η would give the intrinsic rate constant, k^0 and transfer rate coefficient, α given by,

$$\mathbf{\log(k_f) = \log(k^0) + \left(\frac{-\alpha \cdot F}{2.3 \cdot R \cdot T}\right) \eta} \quad (9.10)$$

These calculation models offer a brief description of the theory used for RDE experiments. The application of the models to O_2 reduction reaction (ORR) and O_2 evolution reaction (OER) kinetics are elucidated in Chapter 5, which may provide a profound understanding on the use RDE technique.

Annex 3. Analysis of copper oxide phases with in-situ XRD

HCOO⁻ selectivity vs. CO between different duty cycles suggested that Cu-island size and its GDE coverage might play a critical role on the reaction pathway of CO₂. First at all, we must consider the concept of activity to evaluate the behavior of a catalyst like copper. This concept gives us the produced quantity of final product normalized to the time unit and total available quantity of catalyst. This unit can be summarized by partial current density of each product. Different duty cycles of PCE using offered Cu-island radius ranging from few hundred of nanometers to a few microns. Assuming semispherical islands, we can estimate the number of particles considering the total area of the electrode divided by the cross section of the grain as “ πR^2 ”,

$$N_{\text{particles}} = \text{Electrode area} / \pi R^2 \quad (9.11)$$

If the catalysis process takes place in the perimeter of the grain where there are triple phase points, then the total perimeter would be given by “ $2\pi R \times N_{\text{particles}}$ ”. Then the activity would be inversely related to the radius of the particles,

$$\text{Activity} \sim R^{-1} \quad (9.12)$$

This situation is highly probable when we need to combine different active sites which occurs in the Fischer-Tropsch processes¹⁷³. If the catalysis process takes place in the surface of the Cu-island, then available total area would be given by “ $\pi R^2 \times N_{\text{particles}}$ ”. In this case the activity would be constant,

$$\text{Activity} \sim R^0 = \text{constant} \quad (9.13)$$

It should be noted that two different situations can happen depending whether there are or not competition between CO₂ and H₂O molecules for absorption site. If there is one, then we should consider the total activity for the active sites at the surface area of the Cu-islands instead of the perimeter that should be given by the overall absorption of water molecules plus that of CO₂ molecules.

The initial observation to support this phenomenon was presented in Figure 4-9(a). At first, it is important to mention that the first step in electrochemical reduction of CO₂ is to form CO₂^{•-} radical which occurs at more negative voltages than the onset potential of CO₂ reduction. This could explain the requirement of a moderate

potential ($-1.0 V_{\text{RHE}}$). The electrocatalytic reaction for HCOO^- showed a slight dependence to the Cu-island perimeter. Additionally, CO selectivity was decreased when the Cu-island perimeter was superior to its surface area. Hence, a significant insight into this catalytic process could be outlined by their electrocatalysis undergoing at two different sites of the catalyst. Importance of the perimeter of Cu-islands for the catalyst process of HCOO^- would be the triple phase points where CO_2 -electron-proton would meet each other.

Annex 4. Particle size analysis with Image-J

ImageJ is a very powerful software especially for researchers working on analysis related to microscopy. It not only counts the number of particles, it can also analyse the size of each particle. The software can also analyse if the particle is a semi-circle, full circle or rocky particles and so it can eventually provide additional information such as diameter. The two features are very critical and it mainly depends on the resolution (quality) of the image; (i) particle separation and (ii) segmentation.

- i. Automatic particle counting can be done if the image does not have too many individual particles touching. In order to prevent misinterpretation, we also counted the particles one-by-one from FE-SEM images. Nearly ~20 manual particle counting was done using software that comes with the SEM machine, Bruker particle size analysis.
- ii. Segmentation, or the ability to distinguish an object from its background, can be a difficult issue to deal with. Once this has been done, however, the object can then be analysed as shown below.

Let's say that we want to take the following image and gather information about the dark inclusions. The first step is to duplicate the image, then Threshold the duplicated image. We duplicated the image so that the Binary Mask we create from the copy can be used to sample the original for pixel intensities.

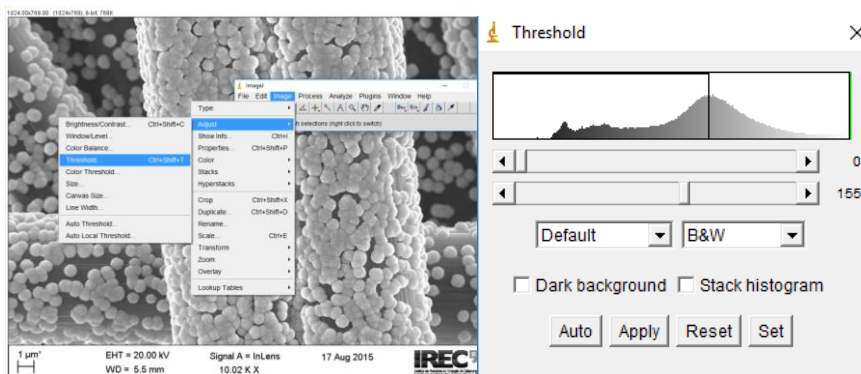
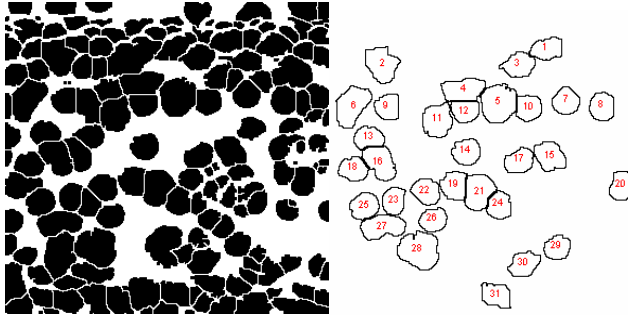


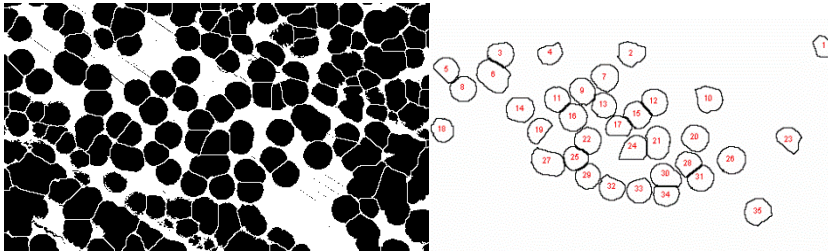
Figure 9-5. Image J analysis for contrast threshold

This creates region of interest (ROIs) based on pixel intensity. In this example dark pixels will be selected: Thresholding results in a "binary" image. Black pixels are the ROIs; white pixels are background.

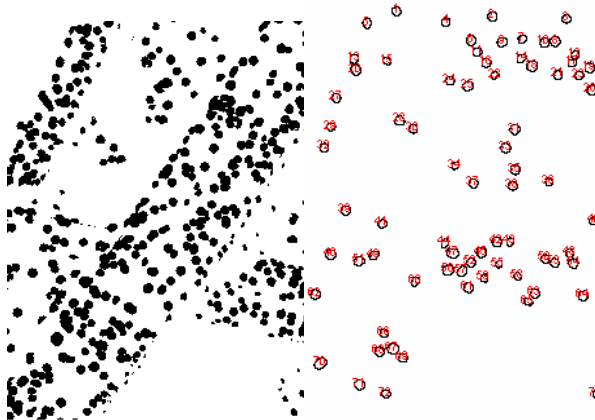
a.



b.



c.



d.



Figure 9-6. (a-d) Binary ROI - B&W images and corresponding particle analysis of Cu-PCE1, 2, 4 and 7, respectively.

Selecting Set Measurements tells ImageJ what data to collect. In this case we want the ROI area and average pixel intensity. Selecting "Redirect To" instructs ImageJ uses the ROI data from the binary image, but gathers intensity values from a

different window. This analysis was performed on 4 different sites of the GDE to obtain a homogenous size distribution and neglect the diffusion effect occurred during electrodeposition process. **Table 9.1** shows an example of a data report obtained by Image J for only one single site. Therefore minimum 100 particles were counted for size distribution analysis.

Table 9.1. Example of particle analysis obtained from several binary B&W images of Cu-PCE1

	Area	r ² , radius (μm)	r, radius (μm)	diameter (μm)
1	0.442	0.140693	0.375091	0.750181
2	0.426	0.1356	0.368239	0.736478
3	0.484	0.154062	0.392507	0.785015
4	0.433	0.137828	0.371252	0.742504
5	0.436	0.138783	0.372536	0.745072
6	0.426	0.1356	0.368239	0.736478
7	0.535	0.170296	0.412669	0.825338
8	0.478	0.152152	0.390067	0.780134
9	0.464	0.147696	0.384312	0.768624
10	0.46	0.146423	0.382652	0.765304
11	0.484	0.154062	0.392507	0.785015
12	0.433	0.137828	0.371252	0.742504
13	0.488	0.155335	0.394126	0.788252
14	0.543	0.172842	0.415743	0.831486
15	0.439	0.139738	0.373816	0.747631
16	0.407	0.129552	0.359933	0.719867
17	0.47	0.149606	0.386789	0.773578
18	0.402	0.127961	0.357716	0.715432
19	0.571	0.181755	0.426327	0.852655
20	0.438	0.13942	0.37339	0.746779
21	0.474	0.150879	0.388431	0.776863
22	0.428	0.136237	0.369102	0.738205
23	0.43	0.136873	0.369964	0.739928
24	0.47	0.149606	0.386789	0.773578
25	0.477	0.151834	0.389659	0.779317
26	0.434	0.138146	0.371681	0.743361
27	0.401	0.127642	0.357271	0.714541
28	0.434	0.138146	0.371681	0.743361
29	0.458	0.145786	0.381819	0.763638
30	0.431	0.137192	0.370394	0.740788

Annex 5. Verification of Image-J analysis by Bruker-SEM

Besides Image-J particle size analysis, manual size operation was performed in scanning electron microscope (SEM) software. Bruker-SEM software can provide the necessary measurement to verify the obtained results, presented in Figure 9-7.

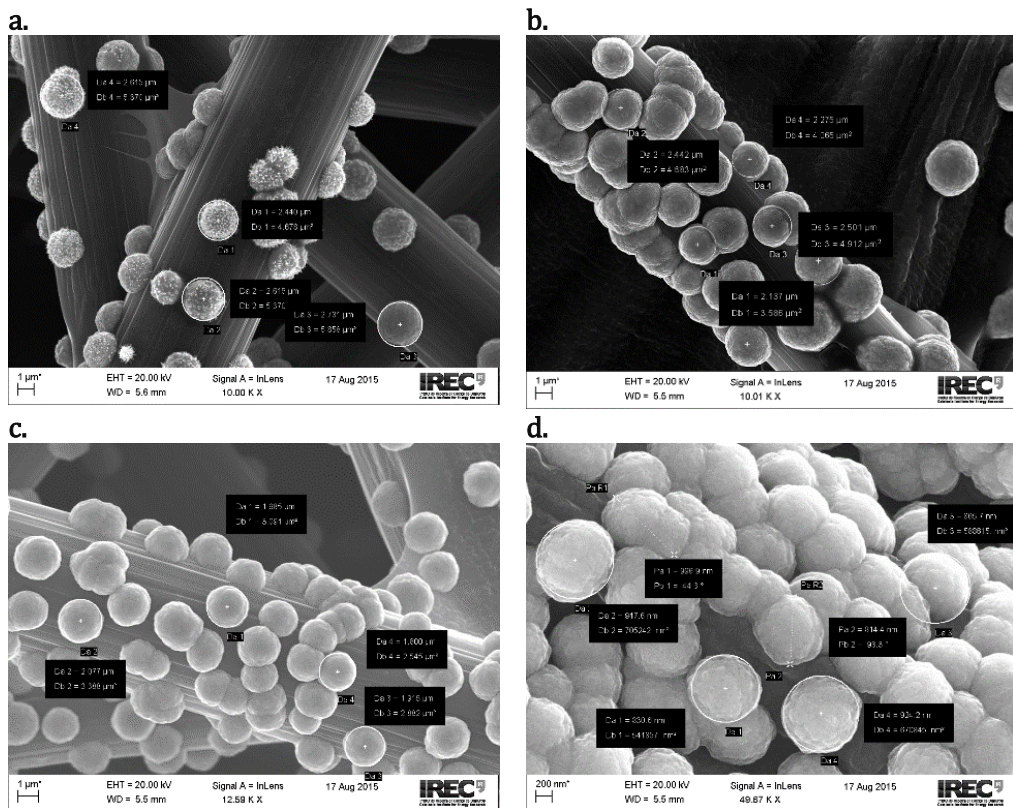


Figure 9-7. (a-d) FE-SEM image of Cu-PCE1, 2, 4 and 7, respectively.

Annex 6. Linear sweep voltammetry scans and K-L plots

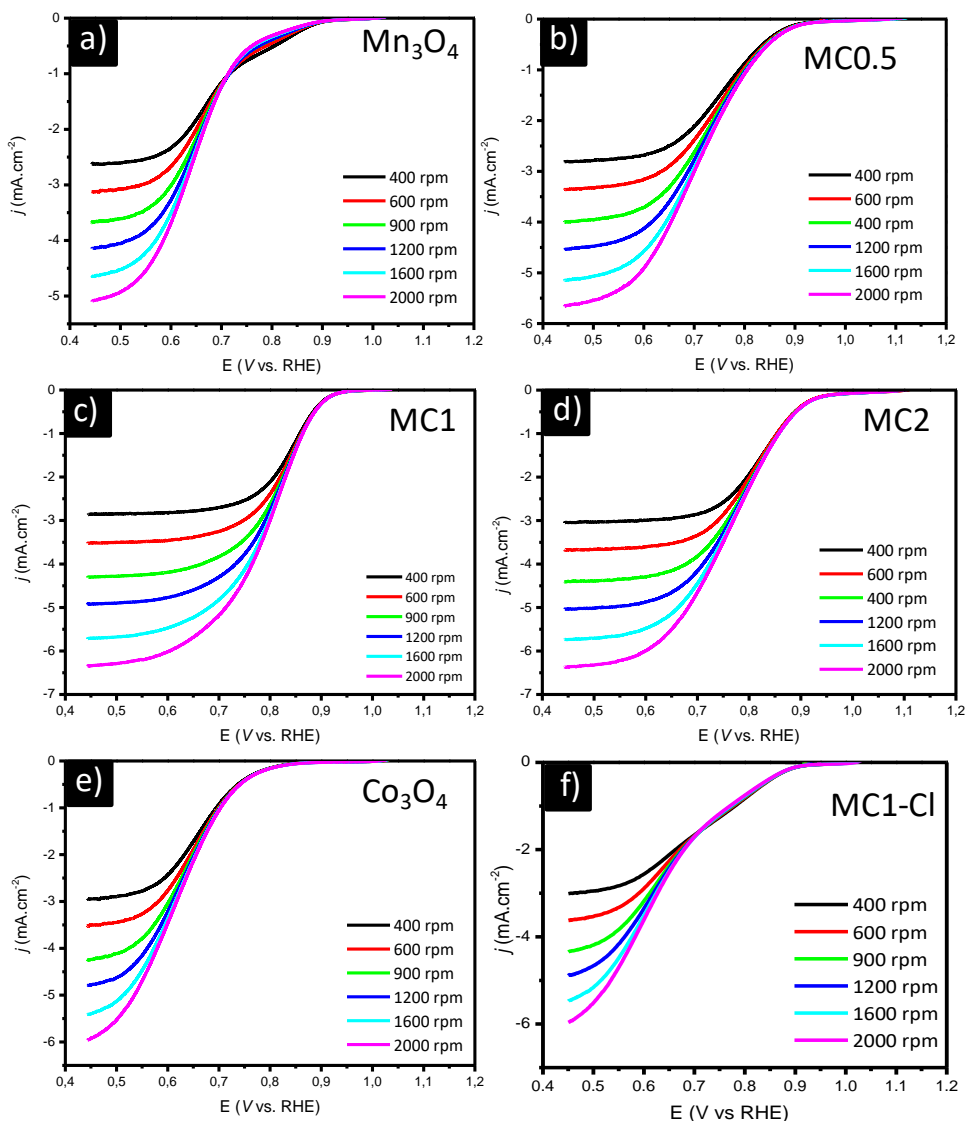


Figure 9-8. Rotating-disk voltammograms recorded on different catalyst-modified electrodes in O₂-saturated 0.1 M KOH solution at different rotation rates as indicated: (a) Mn₃O₄/C, (b) MC0.5/C, (c) MC1/C, (d) MC2/C, (e) Co₃O₄/C, (f) MC1-Cl/C. All those values for ORR and OER were calculated by interpolation and analysis of the wave form at both ends. The wave analysis was made according to two straight lines, defined using a linear regression fit. The software (EC Lab, Biologic Instruments) automatically finds the two parts of the curve with the shallowest slope for the fit.

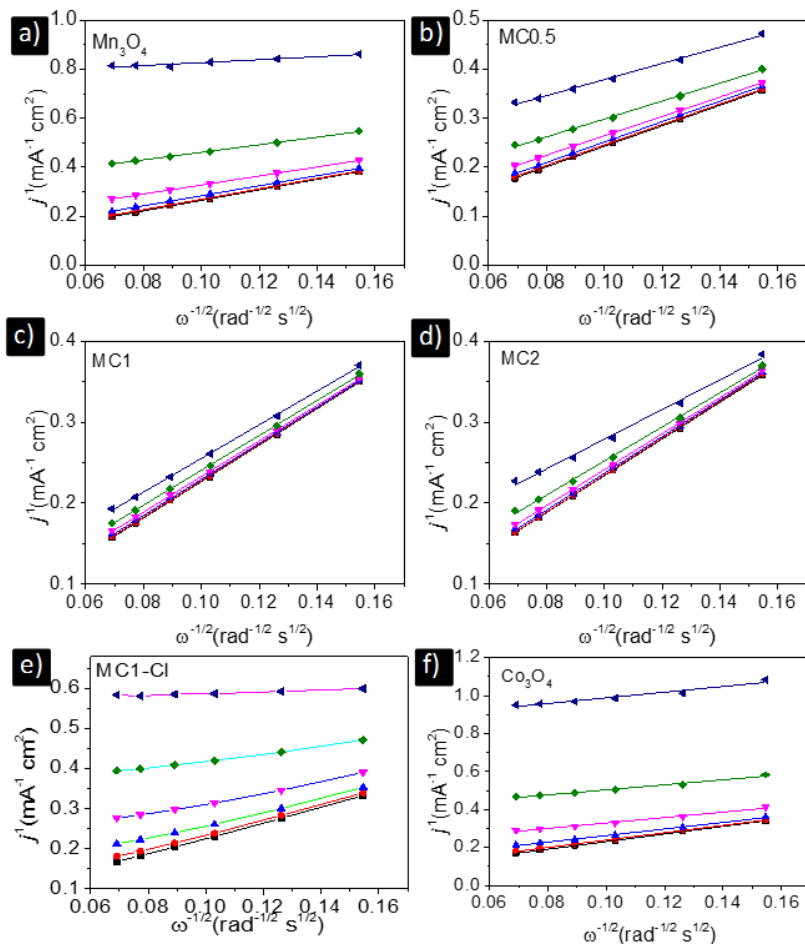


Figure 9-9. K-L plots of different HNPs samples at 0.5 V *vs* RHE: (a) $\text{Mn}_3\text{O}_4/\text{C}$, (b) $\text{MC0.5}/\text{C}$, (c) $\text{MC1}/\text{C}$, (d) $\text{MC2}/\text{C}$, (e) $\text{MC1-Cl}/\text{C}$, (f) $\text{Co}_3\text{O}_4/\text{C}$.

Summary of the ORR/OER catalytic performance revealed from Tafel Plots and Koutechky-Levich plots.

	ORR				OER			ORR-OER
	$\eta_{E-E_{eq}}$ V	$j_{L,c}$ mA $\cdot \text{cm}^{-2}$	n_t	Tafel mV $\cdot \text{dec}^{-1}$	$\eta_{E-E_{eq}}$ V	$E_{j=-10\text{mA}\cdot\text{cm}^{-2}}$ V	Tafel mV $\cdot \text{dec}^{-1}$	E^\ddagger V
Mn_3O_4	0.35	-4.64	3.2	100	0.43	2.19 Δ	151	1.53
MC1-Cl	0.34	-5.50	3.5	95	0.43	1.75	106	1.10
MC0.5	0.38	-5.14	3.6	81	0.38	1.72 Δ	95	0.99
MC1	0.31	-5.71	4.0	52	0.31	1.68	81	0.85
MC2	0.34	-5.73	3.8	83	0.35	2.01	83	1.21
Co_3O_4	0.41	-5.40	3.4	124	0.39	1.71	110	1.07
$\text{Pt}/\text{DSA}\dagger$	0.34	-5.25	3.5	76	0.25	1.65	104	Ω 0.88

Δ Values extrapolated from Tafel slopes;

\clubsuit Difference between the potential at ORR current density of $-3 \text{ mA}\cdot\text{cm}^{-2}$ and that at OER current density of $10 \text{ mA}\cdot\text{cm}^{-2}$;

\dagger ORR values for Pt and OER values for DSA;

Ω Potentials difference of Pt ORR and DSA OER performance.

Annex 7. Overview of the general data obtained in each section of this thesis work

Table 9.2. Selected results according to the highest faradaic efficiency for conversion of CO₂ into HCOOH (FE % HCOOH). The results are taken from chapters where CO₂ reduction reaction were studied using full cell set-up, ECf and PECf.

Thesis	Cathode vs. Anode (Ely)	E _{cell}	I _{cell}	time	VE	FE	EE	Rate	Concentration in beaker		CO ₂ flow rate		Gas-to-fuel yield HCOOH/CO ₂	Rate turnover % · h ⁻¹ · g ⁻¹	Energy Consumption Wh · mol ⁻¹
		V	mA						mol · h ⁻¹	mol · L ⁻¹	%	mL · min ⁻¹			
Chapter 3	SnGDE:10 vs. DSA:10 (Na ⁺)	2.8	87.5	0.7	47	71	33	0.0010	0.021	0.08%	10	0.027	3.9%	3.4%	234
Chapter 3	SnGDE:10 vs. DSA:10 (K ⁺)	2.6	79.2	0.7	51	74	37	0.0011	0.022	0.08%	10	0.027	4.0%	3.5%	190
Chapter 4	CuGDE:2 vs. DSA:10 (K ⁺)	3.2	15.4	2	41	47	20	0.0001	0.005	0.02%	2	0.005	2.5%	1.5%	361
Chapter 6	SnGDE:1 vs. TiO ₂ -O ₂ :10 (Na ⁺)	1.2	4.0	5.7	110	42	46	0.00004	0.009	0.03%	1	0.003	1.4%	1.8%	125
Chapter 6	SnGDE:2 vs. TiO ₂ -O ₂ :10 (Na ⁺)	1.2	6.8	3.5	110	53	58	0.00008	0.011	0.04%	2	0.005	1.5%	1.8%	104
Chapter 6	SnGDE:5 vs. TiO ₂ -O ₂ :10 (Na ⁺)	1.2	15.0	1.8	110	64	70	0.00018	0.013	0.05%	5	0.013	1.4%	1.7%	98
Chapter 6	SnGDE:1 vs. TiO ₂ -H ₂ :10 (Na ⁺)	0.95	4.1	5.5	139	42	58	0.00004	0.009	0.03%	1	0.003	1.5%	1.8%	100

E_{cell} and I_{cell} is cell voltage and current; VE, FE and EE is voltage, faradaic and energy efficiency, respectively; 1, 2, 5 and 10 are the geometrical area of the electrodes in cm²; 1 mL · min⁻¹ is equal to 0.06 L · h⁻¹ which is equal to 0.026 mol · h⁻¹ for an ideal gas (according to 22.4 L · mol⁻¹ at standard temperature and pressure); molecular weight and density of HCOOH is 46.0254 g · mol⁻¹ and 1.22 g · mL⁻¹, respectively.

Glossary

Common abbreviations

Acronym	Meaning
ABPE	Applied Bias Photon-to-Current Efficiency
AC	Alternating current
a.k.a.	as known as
AM	Air mass
ca.	circa (approximately)
CE	Counter electrode (Secondary electrode)
CO ₂ RR	Carbon dioxide reduction reaction
CV	Cyclic voltammetry
DC	Direct current
EC	Electrochemical cell
ECf	Electrochemical flow cell
et. al.	et alios (and others)
FTO	Fluorine doped tin oxide
HER	Hydrogen evolution reaction
HPLC	High pressure liquid chromatography
IREC	Institute Recerca Energia de Cataluna
LSV	Linear sweep voltammetry
OER	Oxygen evolution reaction
PEC	Photoelectrochemical cell
PECf	Photoelectrochemical flow cell
RE	Reference electrode (Auxiliary electrode)
RHE	Reversible hydrogen electrode
RT	Room temperature (~25 °C or 298 °K)
SHE	Standard hydrogen electrode
STH	Solar to hydrogen
UV	Ultra violet
UV-Vis	Ultra violet visible light spectroscopy
WE	Working electrode

Formula abbreviations

Symbol	Description	Unit
<i>b</i>	Tafel slope	mV
E	Potential of an electrode versus a reference or electromotive force of a reaction	V

E_{eq}^0	Standard potential at equilibrium	
E_{dep}	Potential of electrodeposition of a metal ion	V
$E_{j_{\text{peak}}}^c$	Cathodic peak potential	V
FF	Fill factor	
I	Current	mA or A
j	Current density	$\text{mA}\cdot\text{cm}^{-2}$
j_0	Exchange current density	$\text{mA}\cdot\text{cm}^{-2}$
ΔG^0	Standard Gibbs free energy	$\text{kJ}\cdot\text{mol}^{-1}$
Q	Coulombic charge of electricity	C
R	Resistance	Ω
t	Time	S (or min or h)
T	Absolute temperature	K or $^{\circ}\text{C}$
z	Charge number (of transferred electrons)	
z_1	Charge number (of transferred electrons) for species i	

Greek symbols

Symbol	Spelling (EN UK)	Description	Unit
α	alpha	Cathodic charge transfer coefficient	
β	beta	Anodic charge transfer coefficient	
ϕ	phi	electric field	
$\eta_{\text{anode}}(j)$	itha	Anodic overpotential for a current density of j	mV
$\eta_{\text{cathode}}(j)$	itha	Cathodic overpotential for a current density of j	mV
Ω	ohms	unit of electrical resistance	
ν		Scan rate of a CV test	$\text{mV}\cdot\text{s}^{-1}$

Chemical symbols

Symbol	IUPAC name
H_2	Hydrogen
O_2	Oxygen
H_2O	Water

CO ₂	Carbon dioxide
HCO ₃ ⁻	Bicarbonate ion
CO ₃ ⁻²	Carbonate ion
CO	Carbon monoxide
HCOOH	Formic acid
HCOO ⁻	Formate ion
CH ₄	Methane
CH ₃ OH	Methanol
C ₂ H ₂	Acetylene
C ₂ H ₄	Ethylene (Ethene)
C ₂ H ₆	Ethane
C ₂ H ₅ OH	Ethanol
C ₃ H ₅ OH	Propionaldehyde
C ₃ H ₇ OH	1-propanol
C ₄ H ₉ OH	n-butanol
C ₄ H ₁₀	Butane
C ₈ H ₁₈	Octane

Constants

Molar constant	$R = 8.314\ 462\ 1(75)$	J·mol ⁻¹ ·K ⁻¹
Elementary charge	$e = 1.602\ 176\ 565(35) \times 10^{-19}$	C
Faraday constant	$F = 96\ 485.3365(21)$	C·mol ⁻¹

List of Figures

Figure 1-1. The shifting distribution of summer temperature anomalies adopted from Ref [1].....	15
Figure 1-2. (a) Shares of world total primary energy supply till 2014. 100 % corresponds to 13,699 Mtoe (million tonnes of oil equivalent) (b) Shares of world electricity generation till 2014. 100 % corresponds to 23,816 TWh (terawatt hour) *Other includes geothermal, solar, wind, heat and etc. Adopted from “2016 Key world energy statistics” report pg. 6, from International Energy Agency (IEA) Ref.[5].....	16
Figure 1-3. Volume energy density of batteries compared to that of different classes of chemicals. Image reproduced from Ref [7 ^b] Copyright 2013, American Chemical Society.....	18
Figure 1-4. Schematic overview of the CO ₂ conversion routes to including renewable energy routes. Image taken from Ref [7 ^c] Copyright 2013, Royal Society of Chemistry.....	20
Figure 1-5. Schematic that illustrates the constitution and operation of a solar refinery for on-site capturing and transformation of solar fuel feedstocks (CO ₂ , H ₂ O, sunlight) into conventional fuels by: (1) Solar utilities, (2) CO ₂ capturing, (3) Direct CO ₂ reduction, (4) CO ₂ & H ₂ O activation, (5) Catalytic conversion. The approximate temperature requirements for the solar-driven conversion processes are color-coded with red and yellow for high and ambient temperature, respectively. Reproduced with permission of Ref [17] Copyright 2015, Royal Society of Chemistry.....	22
Figure 1-6. Free energy of redox system at the electrode-electrolyte interface where the redox system is at equilibrium (black) and at polarized state (red curve). ΔG_{eq-} and ΔG_{eq+} denote the activation energies for the cathodic and anodic reactions, respectively under equilibrium. ΔG_{-*} and ΔG_{+*} denote the activation energies for the cathodic and anodic reactions, respectively, for applied bias conditions. α is the transfer coefficient and η_{ct} is the overpotential for charge transfer. The figure is adapted from Ref. [27].....	25
Figure 1-7. Representative Tafel plots for anodic and cathodic branches of a logarithmic current versus potential curve.....	27
Figure 1-8. (a) Current versus applied voltage modelled ²⁹ for half-cell reactions: an ideal anode for OER in a 0.1 M KOH solution ($\alpha = 1.0$ or $60 \text{ mV}\cdot\text{dec}^{-1}$ and $i_0 = 0.1 \text{ mA}$) versus a hypothetical cathode with 100 % CO ₂ RR conversion efficiency in 0.1 M KHCO ₃ solution ($\alpha = 0.29$ or $200 \text{ mV}\cdot\text{dec}^{-1}$ and $i_0 = 0.1 \text{ mA}$) (b) Electrochemical load curve of the full-cell showing the contributions of ionic and electronic losses; 5 and 2 Ω , respectively.....	28
Figure 1-9. (a) Two electrode cell separated with a proton exchange membrane. HER and OER occurs at cathode and anode, respectively. (b) Three electrode cell separated with either cation or anion exchange membrane. CO ₂ RR and OER occurs at cathode and anode, respectively. Electrons flow from anode to cathode direction and “V” is the symbolic voltage reading at the potentiostat that controls the direction and rate of electron transfer. CO ₂ is continuously bubbled before and during the electrocatalysis reactions.....	32
Figure 1-10. (a) Electrode materials and their selectivity in accordance to reaction products of CO ₂ reduction ^{36 37 34d 35 38} († semi-inert because modified conditions such as high pressure or in ionic	

liquids showed CO ₂ RR activity ³⁶ †inert because even if the reactions conditions are modified no CO ₂ RR activity was found.) (b) Schematic illustration of metal and surface bound CO ₂ and CO interactions. The first one is weak CO bonding leading to desorption before its further reaction, second is strong CO adsorption leading to surface poisoning and the last figure is the optimum CO adsorption for further electron and proton uptake to form intermediates species.	34
Figure 1-11. Schematic diagram of a gas-diffusion electrode active layer adapted from Ref[³⁶] Copyright 2001, International Union of Pure and Applied Chemistry.	38
Figure 1-12. Volcano plot; Theoretical overpotential for OER vs. the difference between the standard free energy of two subsequent intermediates ($\Delta GO^* - \Delta GHO^*$) in electron volts for various binary oxides adapted from Ref[⁶⁸] Copyright 2014, Royal Society of Chemistry.	40
Figure 1-13. The schematic electron occupancy of allowed energy bands for a conductor, semiconductor and insulator. The shaded areas indicate the regions filled with electrons. The upper edge of the valence band is marked by E_v and lower edge of the conduction band by E_c . E_{bg} , is the bandgap energy expressed in electron volts (eV).....	43
Figure 1-14. Schematic illustration of (a) energy levels in an intrinsic semiconductor and an electrolyte containing a redox couple shown on a vacuum reference scale. (b) The position of band levels for an n-type semiconductor before contacting an electrolyte, in contact at equilibrium under dark and light conditions (c) same as in (b) but for a p-type semiconductor.....	45
Figure 1-15. Schematic illustration of photoelectrochemical cell with a photoanode for OER against a metal cathode used for CO ₂ RR. The reference electrode is placed near metal cathode and CO ₂ was bubbled through the solution during the tests.	47
Figure 1-16. (a) j-E plot of a hypothetical n- and p-type semiconductor under AM 1.5G solar light illumination in an aqueous electrolyte to catalyse OER and CO ₂ RR. Rest of the curves are plotted with the parameters of Figure 1-8. (b) j-E plot and photoconversion efficiency of n-type semiconductor (TiO ₂ nanorods in 0.1 M KOH) under AM 1.5G solar light illumination employed for OER.	48
Figure 1-17. The band positions of several semiconductor materials in contact with aqueous electrolyte respect to pH ~0. The red and green lines represent the upper edge of the valence band and lower edge of the conduction band, respectively. The standard potentials of CO ₂ RR, HER and OER are adjusted to RHE scale.....	51
Figure 1-18. (a) In a planar device, photogenerated carriers must traverse the entire thickness of the cell $\sim 1/\alpha$ (where α is the absorption coefficient), before collection. (b) In a 2D-array structure, carriers must only reach the rod surface before recombination. L_D is the diffusion length of the photogenerated minority carrier (open circle).....	52
Figure 2-1. (a) 3-electrode set-up of tin pyrophosphate batch, Toray® carbon paper (GDE) is working electrode (WE), two short-circuited pieces of graphite foils are counter electrodes (CE) and Ag/AgCl/KCl(3M) is the reference electrode (RE) (b) Different GDE dimensions (10, 5, 2 and 1 cm ²) before and after (10 cm ²) electrodeposition of tin catalyst.	58
Figure 2-2. Different GDE dimensions (10 and 2 cm ²) before and after electrodeposition of copper catalyst. 3-electrode set-up is similar to Figure 2-1 (a) except that counter electrode (CE) was a copper foil.....	59

- Figure 2-3. (a) Schematic illustration of the controlled synthesis of Mn_3O_4 , and Co_3O_4 in 1st step, MC_x and $MC-Cl$ NPs synthesized in the 2nd step (b) Digital pictures of the NPs dissolved in xylene, oleylamine, oleic acid mixture at the end of 300 minutes aging. 60
- Figure 2-4. Protocol for the (a) two steps of ink [NPs:VC:Nafion] preparation of NPs (b) Schematic illustration of drops casting on GCE and RDE experiments (c) two steps of spin coating of ink on carbon fibre substrate (CFS) following its assembly in EC-flow cell. 62
- Figure 2-5. (a) Digital pictures of FTO-glass with Teflon[®] sealing at the edges, before (left) and after (right) the hydrothermal synthesis. (b) Schematic illustration of the protocol for the hydrothermal synthesis (c) Digital pictures of the Teflon[®] beaker, stainless steel autoclave and electrical furnace. 63
- Figure 2-6. (a) Three electrode cell to study CO_2RR of cathodes and (b) photoelectrochemical three electrode cell to study OER of TiO_2 photoanodes. The counter electrode for both cells is a Pt wire and the reference electrode is a silver-silver chloride electrode ($Ag/AgCl/KCl$ (3M)). Both cells have a separate inlet for gas bubbling during the test, e.g. CO_2 , Ar or O_2 66
- Figure 2-7. Main steps for an electrochemical study with Rotating Disk Electrode set-up; (i) Ink Preparation (ii) Drop casting of the ink to the glassy carbon (iii) Rotating disk electrode testing (iv) Data to be exploited for an electrochemical reaction such as O_2 reduction reaction (ORR) and O_2 evolution reaction (OER)..... 67
- Figure 2-8. Digital pictures showing the stacking of the filter-press photo/electrochemical cell end to end order from cathode to anode compartments. CO_2RR occurs at the cathode compartment and OER at the anode. ECf cell employs a DSA as anode whereas PECf cell operates with TiO_2 nanorods as a photoanode. 68
- Figure 2-9. Scheme of ECf cell where cathode is a porous gas diffusion electrode with an electrodeposited metal (M-GDE) for CO_2RR and anode is a Dimensionally Stable Anode for OER. Anode and cathode compartments were separated with an ion exchange membrane. The liquid electrolyte was continuously circulated with electrical pumps at a flow rate of $10\text{ mL}\cdot\text{min}^{-1}$. CO_2 gas flow was controlled with a mass flow controller at a flow rate of $10\text{ mL}\cdot\text{min}^{-1}$ unless otherwise specified. 69
- Figure 2-10. Scheme of PECf cell where cathode is a porous gas diffusion electrode with an electrodeposited metal (M-GDE) for CO_2RR and anode is an n-type semiconductor (TiO_2 nanorods) for OER. Anode and cathode compartments were separated with an ion exchange membrane. The liquid electrolyte was continuously circulated with electrical pumps at a flow rate of $10\text{ mL}\cdot\text{min}^{-1}$. CO_2 gas flow was controlled with a mass flow controller at a flow rate of $10\text{ mL}\cdot\text{min}^{-1}$ unless otherwise specified. 70
- Figure 2-11. PECf flow cell set-up under continuous flow and illumination. The flow directions of the gas, catholyte and anolyte are highlighted. The experiment run with two channels of the potentiostat in master-slave configuration. 72
- Figure 2-12. (a) Solar light simulator, XPS power supply and bench set-up during PECf cell test under illumination. The positions to increase the solar light power (1 sun to 10 suns) was calibrated with power detector before each test. (b) The digital picture of the power detector used to calibrate the intensity of the solar light for the exact position of PECf-cell..... 74
- Figure 2-13. (a) Digital picture of Micro-GC 490 from Varian Instruments (b) The segments of the gas chromatogram in working order (c) Digital picture of PECf cell coupled to Gas Chromatogram for on-

line product analysis from CO ₂ reduction reaction. (d) The examples of gas chromatograms presents the peaks detected for H ₂ , CO ₂ , CO in the first GC machine (shown in the picture), CH ₄ and C ₂ H ₄ in the second GC machine (not shown here).	76
Figure 2-14. (a) Transitions between the bonding and anti-bonding electronic states when light energy is absorbed in UV-Visible Spectroscopy. Vibrational energy levels cause ultraviolet-visible spectra to be smooth and not sharp peaks. (b) Digital pictures of UV-Visible Spectroscopy machine, sample and reference cuvettes (c) Illustration of working principle for UV-Visible Spectroscopy analysis.....	80
Figure 2-15. Quantification procedure of formic acid by UV-Vis spectroscopy. (a) UV-Vis absorption spectra for samples taken from Cu-GDE after 2 hours of electrolysis (b) UV-Vis absorption spectra for different concentrations of commercial formic acid and (c) its calibration curve for three different representative wavelength (d) for calculation of the standard deviation (220, 215 and 210 nm)	82
Figure 2-16. (a) An electron microscope image of silica particles and depiction of species retention due to the particle size vs. pore size relation (b) Illustration of the species entering the column with the flow of the mobile phase at time zero and after 10 minutes (c) The scheme of working principle for HPLC system. The images are taken from Ref [105].....	83
Figure 2-17. HPLC product analysis results of liquid phase samples generated from electrochemical CO ₂ reduction. Carbonic acid and HCOOH were observed with retention time of 7.86 and 14.9 respectively.....	84
Figure 2-18. (a) The illustration of NMR system (b) spin polarization of nuclei under an applied magnetic field (c) sample position between the magnetic coils. The images are taken from Ref[106]	85
Figure 2-19. NMR spectra of known amount of commercial samples in 0.1 M KHCO ₃ and internal standard solution containing Phenol and DMSO. Due to the shift in the baseline, Phenol and DMSO standards are used for left and right part of the water peak in the NMR spectra, respectively.	87
Figure 3-1 Sketch of the electrochemical flow cell and experimental setup used in CO ₂ RR tests, using a cathode formed by Sn electrodeposition on gas diffusion electrode. DSA is a commercial dimensionally stable anode for O ₂ evolution reaction, IrO ₂ -Ta ₂ O ₅ catalyst immobilized on Ti plate.	90
Figure 3-2 (a) Cyclic voltammogram recorded for Sn deposition and stripping on gas diffusion electrode in the pyrophosphate bath (pH 8.3) at a scan rate of 20 mV·s ⁻¹ and (a)-(in-set) is the chronoamperometry test of Sn deposition at 15 mA·cm ⁻² (b – f) FE-SEM images at different current densities from 1 – 30 mA cm ⁻² , respectively. Scale bars; (b – c) 20 μm, (d) 40 μm and (e – f) 100 μm.	91
Figure 3-3. (a-b) FE-SEM images of carbon toray fibres of Sn-GDE. Images taken from different sites of Sn-GDE cross-section which shows a granular deposit with a thickness around 1 μm. (c) Top view of a fibre with Sn deposit displaying a compact and pore-free Sn grains (d) corresponding XRD pattern of β-Sn and graphite peaks –from the GDE support.....	93
Figure 3-4. 3D Optical Profiler – Line Profile Scanning presenting the profile depth of (a) pristine GDE and (b) Sn-GDE and corresponding top view. Arrows indicate the direction of the line scan (c) Cross-section views of GDE and Sn-GDE (d) FE-SEM of Sn-GDE cross-section, mean GDE thickness was 150 ± 15 μm and Sn coverage from top to bottom, 50 ± 5 μm.	94
Figure 3-5. (a) Cyclic voltammogram on glassy carbon (GC), GDE and Sn-GDE under 10 mL·min ⁻¹ Ar and CO ₂ gas flow at scan rate 20 mV·s ⁻¹ in 0.5 M NaHCO ₃ electrolyte (only GC electrode was tested vs.	

Pt mesh in a glass beaker with 0.5 M NaHCO ₃ electrolyte), (b) Current vs. potential curves for Sn-GDE compared to nanostructured SnO _x ¹⁹ and Sn (5 nm) catalyst ⁴⁶	95
Figure 3-6. Chronoamperometry tests conducted at $-0.85 V_{RHE}$ to check the inertness of (a) GDE towards CO ₂ RR and (b) to verify that the CO ₂ gas is the main product that is reduced.....	96
Figure 3-7. (a) Total faradaic efficiency of CO ₂ reduction products at the end of 200 C charge passed from the external circuit and (b) corresponding Tafel plots for production of HCOO ⁻ , CO and H ₂ (c) HPLC formic acid analysis: formic acid peak retention starts at 15 th minute (d) CO and H ₂ peak retention is after 0.3 and 1.15 minutes, respectively. In half an hour, accumulation of the gaseous products reaches to an equilibrium	97
Figure 3-8. Conversion efficiency of CO ₂ and H ₂ O into syngas (CO : H ₂) in 0.5 M NaHCO ₃ electrolyte solution and 10 mL·min ⁻¹ CO ₂ and electrolyte flow rate.	98
Figure 3-9. (a) Increasing the amount of gas by CO ₂ percentage in Ar gas flow (total flow 50 mL·min ⁻¹). For G/L 2 and 4, 100 and 200 mL·min ⁻¹ of gas flow was used. Each CV scan was recorded at 20 mV·s ⁻¹ in ECf-cell in 0.5 M NaHCO ₃ (electrolyte flow fixed at 50 mL·min ⁻¹) (b) Histogram of net current density for CO ₂ reduction obtained by subtracting the current density value of Ar from CO ₂ at $-1.1 V_{RHE}$ in the CV scans.	100
Figure 3-10. Faradaic efficiency of formate against Sn-GDE electrode potential in a full cell experiments for g/L ratio (a) higher and (b) lower than 1 – conducted under current densities of 1, 5 and 10 mA cm ⁻² in 0.5 M NaHCO ₃ for 200 C (c) CO ₂ gas to 0.5M NaHCO ₃ electrolyte flow ratio effect on Sn-GDE voltage (d) Schematic of gas and liquid flow through Sn-GDE, at flow ratio lower and higher than 1, left and right parts respectively.	101
Figure 3-11. (a) Long term catalytic activity of SnGDE conducted under different current densities: 10, 5 and 1 mA·cm ⁻² (b) EDX scan and FE-SEM; images of Sn-GDE before and after electroreduction of CO ₂ in EC flow cell at $-1.1 V_{RHE}$ in 0.5 M NaHCO ₃ electrolyte while both gas and liquid were flowing at 10 mL·min ⁻¹	102
Figure 3-12. (a) Energy consumption of CO ₂ reduction to HCOO ⁻ using Sn-GDE in ECf-cell at different production rates. Data from this work and Ref. [39c, 58a].....	103
Figure 4-1. Cyclic voltammetry of glassy carbon and GDE in 0.16 M CuSO ₄ , 0.15 M citric acid and 0.38 M ammonium sulphate solution. Scan rate is 20 mV·s ⁻¹	111
Figure 4-2. (a) Continuous electrodeposition of Cu at different potentials applied as a function of time – chronoamperometry. Total charge per unit area is 2.7 C·cm ⁻² . In contrast to CV experiments, mild stirring (100 rpm) was applied during plating experiments to improve Cu ion diffusion into the GDE pores by convection. Additionally, N ₂ gas was bubbled into the electrolyte beaker to eliminate the O ₂ bubbles generated at the counter electrode. (b) FE-SEM images of Cu deposits formed on GDE at the end of the chronoamperometry tests	112
Figure 4-3. Illustration of the nuclei formation and grain growth of the deposits under (a) higher rate of surface diffusion at low deposition potentials and (b) higher rate of nucleation at higher deposition potentials.....	113
Figure 4-4. (a) Effect of electrodeposition potential on the particle distribution (analysed by FE-SEM) of deposited Cu at potentials from -0.2 to $-0.8 V_{Ag AgCl}$. Solution conditions: 0.16 M CuSO ₄ , 0.15 M citric acid and 0.38 M ammonium sulphate; pH 2.1. Copper deposition equivalent to 2.7 C·cm ⁻² (b) Schematic	

presentation of phenomena involved during Cu nucleation and growth on GDE by DE at a potential (Edep) lower or higher than the peak potential (EjpeakCu) (c) Representation of the boundary layer on the carbon fibres (dashed line) and concentration gradient of Cu particles between carbon fibre surface and bulk of solution. Red and blue curves represent the concentration gradient of Cu ⁺² ions and Cu adatoms/deposited metal, respectively.....	114
Figure 4-5. (a – b) Potential vs. time plot of the pulsed electrodeposition of copper at different duty cycles; 7, 4, 2 and 1 % respectively. The in-set picture is FE-SEM of a carbon fibre decorated with Cu–islands. (e) Potential vs. time plots of PD are overlapped in a single graph to highlight the increment of relaxation time, <i>tOFF</i> in accordance to deposition potential driven by peak current density during <i>tON</i> period. (f) Particle diameter plotted as a function of duty cycle applied during pulsed electrodeposition. The effect of duty cycle shows an exponential profile on the Cu–island diameter.....	117
Figure 4-6. (a-d) FE-SEM images of copper deposit formed on carbon fibres at 1, 2, 4 and 7% duty cycle, respectively (all scale bars are 50 µm); (e) Particle size distribution calculated from FE-SEM images.	118
Figure 4-7. Schematic illustration of the phenomena during steady state, ON and OFF states and corresponding boundary condition between carbon fibre surface and bulk of the solution.....	119
Figure 4-8. Faradaic efficiency of CO ₂ RR products for (a) Cu-CE samples tested at different potentials and (b) Cu-PCE tested at -1.0 V _{RHE} during 2 hours with 0.1M KHCO ₃ electrolyte flow at 10 ml·min ⁻¹ and 2 ml·min ⁻¹ CO ₂ gas bubbling through GDE (d) X-ray diffraction patterns (220-reflections) of Cu-CE and Cu-PCE samples.....	120
Figure 4-9 Faradaic efficiency of formate (a) and carbon monoxide (b) as a function of Cu-island diameter, and related pathways occurring on PCE1 and PCE7 for CO ₂ RR (c) through formate (F) intermediate and (d) carboxyl (C) intermediate.....	122
Figure 4-10. (a) Schematic illustration of the continuous electrochemical flow cell with the individual stacks of the cathode, membrane and anode parts are displayed from left to right, (RE: Reference Electrode, AEM: Anion Exchange Membrane, DSA: Dimensionally Stable Anode) (b) Digital image of pristine GDE and Cu-PCE1 sample (scale bar length is 20 mm). (c) The comparison of partial current density of HCOO ⁻ (formate) obtained from this work vs. state-of-the-art for Cu-modified catalyst electrodes to reduce CO ₂ into formate, 0.1M KHCO ₃ (d) Amount of formate concentration accumulated at the catholyte per hour and same data taking into account the Cu-loading on GDE on the left axis. The dashed line corresponds to 80 % in vol. formate concentration. The right axis is the energy cost per hour for one mole of formate and dashed green line represents formic acid formation energy; 76.6 Wh·mol ⁻¹	124
Figure 5-1. (a-b) TEM micrographs of Mn ₃ O ₄ NPs (a) and MC1-Cl NPs (b). (c) ADF-STEM image and EELS elemental mapping of MC1-Cl NPs and compositional line profile of Mn, Co and O elements recorded along the arrow in the STEM images. (d) HRTEM micrograph of a MC1-Cl NP, power spectra of the blue squared region and colourful structural map showing the distribution of Mn ₃ O ₄ (red) and CoMn ₂ O ₄ (green) phases.	129
Figure 5-2. (a-c) HRTEM micrographs of MC0.5 (a), MC1 (b) and MC2 (c) NPs. TEM (scale bar = 100 nm) (d) ADF-STEM image and EELS elemental mapping of MC2 NPs and compositional line profile of	

Mn, Co and O elements recorded along the arrow in the STEM image. (e) HRTEM micrographs of a MC1 NP, details of the red and green squared regions with the corresponding power spectra, and colourful structural map showing the distribution of body centered tetragonal Mn_3O_4 (red) and face centered cubic CoO (green) phases.....	130
Figure 5-3. Scheme of the formation of the $Mn_3O_4@CoMn_2O_4$ and $Mn_3O_4@CoMn_2O_4-Co_xO_y$ nano-heterostructures when using either a cobalt chloride or a cobalt perchlorate solution. Green arrows in the bottom point at Co_xO_y nanocrystal nucleation sites.....	131
Figure 5-4. (a) XPS spectra of Co-oxide crystallites on MC1 NPs and (b) TEM micrograph MC1 NPs which was supported on carbon black (red arrows point at some of the NPs).....	132
Figure 5-5. (a) Current-potential curves at different electrode rotating rates, recorded for MC1/VC on glassy carbon disk electrode (0.196 cm ²) using a potential scan rate of 5 mV·s ⁻¹ in O ₂ -saturated 0.1 M KOH aqueous solution; (b) the Levich plot and it's equation; (c) the Koutechky-Levich plots at different electrode potentials and corresponding equations for find kinetic current(j_k) and electro-transfer rate constant (k_c); and (d) plot of E vs log(j_k). The measurement was carried out at 25C and 1.0 atm oxygen pressure	134
Figure 5-6. (a) ORR polarization curves of MC/C, Mn_3O_4/C , Co_3O_4/C and Pt/C in O ₂ -saturated 0.1 M KOH at 1600 rpm using a scan rate of 5 mV·s ⁻¹ . (b) Corresponding Tafel plots derived of ORR polarization curves (c) Kinetic current densities at half-wave potential (red) and overpotentials (blue)	137
Figure 5-7.(a) K-L plots at 0.5 V _{RHE} . The standard lines for 2 and 4 electron pathways are also plotted as a guideline (b) n_t at different potentials.....	139
Figure 5-8. The proposed scheme of ORR pathway by Wroblawa et. al., (Image obtained from Ref. [144], with permission J. Electroanal. Chem., Elsevier)	140
Figure 5-9. (a) Possible configurations of dioxygen interaction with NPs (b) limiting current density and kinetic rate constants of ORR for NPs extracted from the intercept of K-L plots and Butler-Volmer equations – different regions of reversibility for heterogeneous electrochemical reactions are highlighted (c) transfer coefficient (α) of catalyst NPs extracted from their slope of Tafel plots, “n” is the number electrons exchanged per mole of O ₂	142
Figure 5-10. (a) Constant potential test performed at 0.8 V in O ₂ -saturated 0.1 M KOH for all the nanoparticles for 20 hours and (b) MC0.5, MC-Cl and Pt for 60 hours (c) TEM images of MC0.5 and Pt NPs after 60 hours stability test. MC0.5 NPs were stable showing as dark spots covered with Vulcan carbon and Pt NPs were pulverized with Vulcan carbon additive due to oxidizing species formed during ORR.....	143
Figure 5-11. (a) OER polarization curves of Mn_3O_4/C , Co_3O_4/C , MC/C, Pt/C, DSA and glassy carbon (GC) in O ₂ -saturated 0.1 M KOH at a scan rate of 5 mV/s. (b) Tafel plots derived from OER polarization curves. (c) Linear polynomial regression of the LSV scans with a scale zoomed to on-set potentials (d) Comparison of ORR and OER activities of MC2 NPs before and after 20 hours durability test in 0.1 M KOH solution. The rotation rate is 1600 rpm during ORR & OER	145
Figure 5-12. (a) Schematic illustration of [NPs:VC:Nafion] ink preparation and two step spin coating on carbon fibre substrate (CFS) following EC-flow cell assembling (b) FE-SEM images of MC1-CFS/1L, 2L and 5L electrodes. Magnified areas are shown by red squares.....	147

Figure 5-13. FE-SEM coupled with Charge Compensation method to investigate agglomerated nanoparticles of MC1-CFS/2L	148
Figure 5-14. CV scans of DSA electrode with a defined geometrical area of (a) 10 cm ² and (b) 1 cm ² under static electrolyte mode “s” meaning no flow, and (b) dynamic mode “d” meaning 10 ml·min ⁻¹ electrolyte flow (c) Tafel slopes of 10 cm ² and (d) 1 cm ² DSA electrode in static and dynamic modes	149
Figure 5-15. (a) CV scans of benchmark DSA electrode and MC1/CFS with different loadings; 1, 2 and 5 layers. In-set image shows necessary OER overpotential for DSA and MC1/CFS/5L (b) Corresponding Tafel slopes and FE-SEM images of MC1 NPs covering carbon fibres after (c) 1 layer and (d) 5 layers obtained by spin coating protocol.....	151
Figure 5-16. (a) Stability test of MC1-CFS/5L under constant potential (~2.0V _{RHE}) during 5 hours in 0.1 M KOH under 10 ml·min ⁻¹ liquid flow (b) Normalized OER current activity with an emphasis on the first hour of electrolysis. Dash-dotted line represents 70% current retention.	153
Figure 6-1. The standard redox potentials of HER (0 V _{RHE}) and OER (1.23 V _{RHE}) are given with straight lines. The y-axis were set at standard redox potential for CO ₂ R to HCOO ⁻ (-0.225 V _{RHE}) The illustration of theoretical current – potential plots of a cathode performing CO ₂ R, > 400 mV overvoltage and a series of metal oxide type photoanodes performing OER under light irradiation. The illustration of an OER anode (DSA) is also given envisaging that >300 mV overvoltage is required.	157
Figure 6-2. (a) In a planar device, photogenerated carriers must traverse the entire thickness of the cell, ~1/α (where α is the absorption coefficient), before collection. (b) In a rod-array cell, carriers must only reach the rod surface before recombination. L _D is the diffusion length of the photogenerated minority carrier (open circle). (c) Top and (d) cross-section image of TiO ₂ -NRs synthesized by hydrothermal method.....	158
Figure 6-3. (a) OER analysis by linear sweep voltammetry of DSA/OER (IrO ₂ -Ta ₂ O ₅ /Ti) along with cyclic voltammograms of TiO ₂ electrodes with O ₂ and H ₂ post-annealing treatment under EE (front) and SE (back) illumination. (b) Assisted photocurrent efficiency (η %) of TiO ₂ -O ₂ and TiO ₂ -H ₂ electrodes Electrolyte: 0.5 M NaOH, AM 1.5G, ca. 1 sun and potential sweep rate is 20 mV/s.....	159
Figure 6-4. Voltage step tests in master-slave configuration under (a-b) dark condition and (c-d) AM 1.5 G solar light illumination condition.	161
Figure 6-5. Electrode potentials and current value of voltage step tests collected from slave and master channels, respectively. Sn-GDE area was decreased from 10 to 1 cm ² whereas the sunlight illumination was changed from 10 to 1 sun intensity (1 sun intensity = 100 mW·cm ⁻² AM. 1.5G)	162
Figure 6-6. (a) j and E points recorded by voltage–steps test of Sn-GDE (1 or 10 cm ²) vs. TiO ₂ -NRs under 1 sun (AM 1.5 G) solar illumination, including the points recorded from Sn-GDE10 vs DSA/OER voltage–steps test (b) Long term stability test under the same conditions but at fixed cell potential of -1.2 V (c) Schematic image of the stack assembly for cathode and anode parts showing the flow directions of gas and liquid. TiO ₂ -NRs are illuminated from back (glass) side.	164
Figure 6-7. (a) j and E points recorded by voltage–steps test of Sn-GDE(2 or 5 cm ²) vs. TiO ₂ -NRs under 2 or 5 suns (AM 1.5 G) solar illumination, respectively, including the points recorded from Sn-GDE vs DSA/OER voltage–steps test (b) Long term stability test under the same conditions but at fixed cell	

potential of -1.2 V (c) Schematic image of the stack assembly for cathode and anode parts showing the flow directions of gas and liquid. TiO ₂ -NRs are illuminated from SE (back) side with 2 or 5 suns (AM 1.5 G) by solar concentration.....	165
Figure 8-1. The illustration of electrophoretic deposition (EPD) process to immobilize CdSe/CdS core/shell quantum dots on TiO ₂ -NRs.....	178
Figure 8-2. Successive ionic layer adsorption and reaction (SILAR) conducted for CdS and ZnS immobilization on TiO ₂ -NRs film grown on FTO glass slides.....	179
Figure 8-3. (a) Experimental method to produce sensitized electrodes (b) Energy levels of semiconductors and redox potentials of the electrolytes. CdS and CdSe are shown as sensitizers by Fermi level alignment with TiO ₂ and ZnS layer acts as a coating layer to improve the stability. The band gap values correspond to quantum dot nanoparticles and are larger than in bulk semiconductors. (c) the digital pictures of the samples to highlight the colour change.....	181
Figure 8-4. TiO ₂ -NR samples; (a) pristine TiO ₂ -NRs; (b) SILAR deposited 4 cycles of CdS and 2 cycles of ZnS; (c) SILAR deposited 4 cycles of CdS and 4 cycles of ZnS; (d) EPD+SILAR deposited core/shell CdSe-CdS Quantum Dots and 4 CdS+2 ZnS. The consecutive scans were obtained in an aqueous solution containing 0.25 M Na ₂ S and 0.35 M Na ₂ SO ₃ (pH = 13) while sample was illuminated from front “f” and back “b” side (e) comparison of photocurrent densities in front illumination mode..	183
Figure 8-5. (a) (sample #1) pristine TiO ₂ -NRs and (b-c) (sample #4) TiO ₂ -NRs sample sensitized with EPD and SILAR.....	184
Figure 8-6. The stability test of Sample #4 which has been sensitized with CdSe/CdS (core/shell) quantum dots and SILAR method.....	185
Figure 8-7. (a) The rhombohedral structure of CuAlO ₂ , CuCrO ₂ , CuGaO ₂ , and CuFeO ₂ and the monoclinic structure of CuMnO ₂ . (b) The periodic table where the elements used in this part of the study is highlighted.....	187
Figure 8-8. Total current density of the electrode (closed symbols) and partial current density of CO (open symbols) during CO ₂ electrolysis under constant potential with (a) CuFeO ₂ (c) CuCrO ₂ (d) CuMnO ₂ sprayed on GDL (Conditions: 0.1 M KHCO ₃ saturated with CO ₂ , pH=6.75) along with their XRD scans at the end of each potentiostatic run for (b) CuFeO ₂ (d) CuCrO ₂ (e) CuMnO ₂ . The colour of each XRD scan corresponds to the spectra obtained at the end of that potentiostatic “Run”	189
Figure 8-9. Total current density of the electrode (closed symbols) and partial current density of CO (open symbols) during CO ₂ electrolysis under constant potential with (a) CuAlO ₂ (c) CuGaO ₂ (d) CuInO ₂ sprayed on GDL (Conditions: 0.1 M KHCO ₃ saturated with CO ₂ , pH=6.75) along with their XRD scans at the end of each potentiostatic run for (b) CuFeO ₂ (d) CuCrO ₂ (e) CuMnO ₂ . The colour of each XRD scan corresponds to the spectra obtained at the end of that potentiostatic “Run”	191
Figure 8-10. The comparison chart of faradaic efficiency (coloumns) and total current density (circles) at (a) -0.6 V _{RHE} and (b) -0.8 V _{RHE} along with (c) Tafel slopes of CO for delafossites catalysts	192
Figure 8-11. The selectivity plot for CO to H ₂ ratio as a function of the working electrode potential of delafossites with B-site element (ABO ₂) in the (a) same period and (b) in the same group.....	193
Figure 9-1. (a) Digital image of FTO/Silicate Glass before and after hydrothermal synthesis of TiO ₂ nanorods, the metal ruler is for scale. (b) The highlighted active surface area of FTO is where TiO ₂ nanorods would be grown by hydrothermal method, the metal ruler is for scale.....	I

Figure 9-2. Concentration profile of species “O” consumed in a system under convective-diffusion III

Figure 9-3. (a) Linear sweep voltammograms of a RDE experiment for a reversible (blue line) and irreversible (red line) reactions (b) Variation of i with $\omega^{1/2}$ for an electrode reaction with fast kinetics (blue dashed line) and slow kinetics (red line) due to the deviation from Levich line.IV

Figure 9-4. (a) Concentration profile of species “O” consumed in a system with forced convection (b) Koutechky-Levich plots at potential E1 where electron transfer is a limiting factor and at E2 where the electron transfer is fast.....V

Figure 9-5. Image J analysis for contrast threshold IX

Figure 9-6. (a-d) Binary ROI - B&W images and corresponding particle analysis of Cu-PCE1, 2, 4 and 7, respectively.X

Figure 9-7. (a-d) FE-SEM image of Cu-PCE1, 2, 4 and 7 , respectively.XII

Figure 9-8. Rotating-disk voltammograms recorded on different catalyst-modified electrodes in O₂-saturated 0.1 M KOH solution at different rotation rates as indicated: (a) Mn₃O₄/C, (b) MC0.5/C, (c) MC1/C, (d) MC2/C, (e) Co₃O₄/C, (f) MC1-Cl/C. All those values for ORR and OER were calculated by interpolation and analysis of the wave form at both ends. The wave analysis was made according to two straight lines, defined using a linear regression fit. The software (EC Lab, Biologic Instruments) automatically finds the two parts of the curve with the shallowest slope for the fit.XIII

Figure 9-9. K-L plots of different HNPs samples at 0.5 V vs RHE: (a) Mn₃O₄/C, (b) MC0.5/C, (c) MC1/C, (d) MC2/C, (e) MC1-Cl/C, (f) Co₃O₄/C..... XIV

List of Tables

Table 1.1. Profile of worldwide large CO ₂ stationary sources emitting more than 0.1 Mt CO ₂ per year, adapted from Ref [15 7b]	19
Table 1.2. Selected Tafel slope values calculated from Eq.(1.8) for a direct 1, 2 and 4 electron transfer at the rate determining step (RDS), $R = 8.314 \text{ J mol}^{-1} \text{ K}^{-1}$ and $T = 298 \text{ K}$	27
Table 1.3. Selected properties of some post-transition metals with high H ₂ overpotential	35
Table 1.4. Mechanistic pathway for CO ₂ RR /CORR on Cu proposed by different authors. The asterisk “*” indicates that this compound is adsorbed at the surface. Underlined arrows (→) indicates the RDS – rate determining step.	37
Table 1.5. Charge carriers in intrinsic and extrinsic semiconductors	44
Table 2.1. Thermal conductivity (κ) of selected gases at 400° Kelvin.....	77
Table 2.2. Selected parameters of CO ₂ RR products and internal standards used in NMR measurements	88
Table 4.1. Summary of experimental data for electrolyte used to deposit copper catalyst.....	108
Table 4.2. Experimental data for pulsed electrodeposition of copper for CO ₂ RR in the this study .	109
Table 4.3. Experimental data of the selected literature with pulsed current electrodeposition of Cu for CO ₂ RR.....	116
Table 5.1. The valence state of nanoparticle metal cations	141
Table 5.2. Dimensions of electrode area and anolyte volume inside the ECf-cell.....	150
Table 5.3. OER parameters of MC1-CFS electrodes and benchmark DSA electrode in 0.1 M KOH under 10 ml·min ⁻¹ liquid flow	152
Table 6.1. Electrochemical activity of Dimensionally Stable Anode (DSA) under dark conditions and, TiO ₂ -O ₂ and H ₂ photoelectrodes at a sun intensity of 100 mW·cm ⁻² AM 1.5 G towards OER in 0.5 M NaOH.....	159
Table 6.2. PECf cell conditions and system efficiencies of discrete electrolysis (charge accumulated 4C/mL)	167
Table 6.3. PECf cell conditions and system efficiencies shown in Fig. 6-6 and Fig. 6-7	168
Table 8.1. TiO ₂ nanorods produced by hydrothermal reaction at IREC.	178
Table 8.2. TiO ₂ nanorods results for photocurrent under AM 1.5 illumination in 0.25 M Na ₂ S and 0.35 M Na ₂ SO ₃ (pH = 13) at 20 mV s ⁻¹ scan rate.....	182
Table 9.1. Example of particle analysis obtained from several binary B&W images of Cu-PCE1.....	XI
Table 9.2. Selected results according to the highest faradaic efficiency for conversion of CO ₂ into HCOOH (FE % HCOOH). The results are taken from chapters where CO ₂ reduction reaction were studied using full cell set-up, ECf and PECf.....	XV

List of Scientific Activities

Patents

1. M.D. Hernandez-Alonso; G. Penelas; T. Andreu; **E. Irtem**; A. Parra; C. Fàbrega; J. R. Morante. "Photoelectrochemical cell" European Patent Application. EP14382541.2. 2014 PCT European Patent

Journal Publications as first author

1. **E. Irtem**, J.R. Morante, T. Andreu* "Pulsed electrodeposition of nanocrystalline Cu-islands on Gas Diffusion Electrodes for selective electroreduction of CO₂ to formate in a continuous flow electrochemical cell." ACS Catalysis, to be submitted.
2. **E. Irtem**, M.D. Hernandez-Alonso^c, S. García-Rodríguez^c, J.M. Riesco-García^c, G. Penelas-Pérez^c, J.R. Morante, T. Andreu* "Towards an efficient photoelectrochemical reduction of CO₂". Electrochimica Acta, under revision.
3. **Irtem E**, Andreu T, Parra A, Hernandez-Alonso MD, Garcia-Rodriguez S, Riesco-Garcia JM, et al. "Low-energy formate production from CO₂ electroreduction using electrodeposited tin on GDE." Journal of Materials Chemistry A. 2016; 4(35):13582-8.
4. Luo Z †, **Irtem E. †**, Andreu T., Morante J. R., Cabot A., "Mn₃O₄@CoMn₂O₄-CoxOy Nanoparticles: Partial Cation Exchange Synthesis and Electrocatalytic Properties toward the Oxygen Reduction and Evolution Reactions." †equal contribution, ACS Applied Materials & Interfaces. 2016;8(27):17435-44.

Conference Presentations

1. **Irtem E.**, Parra, A., Fàbrega, C., Hernandez-Alonso, M., Penelas, G., Morante, J. R. & Andreu, T., "An additive free architecture of gas diffusion electrode for efficient conversion of CO₂ into sustainable fuels", Oral presentation, Symp. FF, E-MRS 2015 Spring Meeting, Belgium
2. **Irtem E.**, Parra, A., Fàbrega, C., Hernandez-Alonso, M., Penelas, G., Andreu, T. & Morante, J. R., "Strategies towards artificial photosynthesis: Assisted solarlight driven CO₂ reduction for sustainable fuel production", Oral presentation, Symp. A, E-MRS 2015 Spring Meeting, Belgium
3. **Irtem E.**, Parra A., Andreu T. & Morante J. R., "Highly robust Sn gas diffusion electrodes for the electrochemical reduction of CO₂", Oral presentation,

XXXV Meeting of the Electrochemistry Group of the Spanish Royal Society of Chemistry, Spain, 2014 RESQ Oral Talk

Visiting Stays

1. ETH Zurich, Prof. Javier Pérez-Ramírez – Advanced Catalysis Engineering Group in ETH Hönggerberg, Switzerland (May – August, 2^{1/2} months) 2016
2. INRS Montreal, Prof. Federico ROSEI Center for Energy Materials and Telecommunications of Institut National de la Recherche Scientifique in the framework of our “WIROX Project” Canada (December, 1 month) 2015

Acknowledgments

I want to thank Prof. Dr. Joan Ramon Morante and Dra. Teresa Andreu for giving me the opportunity to come to Spain to work in this exciting project of IREC. I also appreciate a lot the opportunity they have given me to present my work in international conferences where I had the chance to improve my communicational skills and professional network. Being the first student with a dedicated doctoral work on the photo/electrochemical CO₂ reduction brought some challenges while developing a robust set-up and it was frustrating from a results perspective. However, through the entire time, both of my supervisors managed to stay upbeat and excited.

The guidance and critical analysis of Prof. Dr. Joan Ramon Morante helped me to improve my personal skills, my publications, and allowed me to grow as a researcher. He also made my first secondment to INRS, Canada possible which I am grateful for that experience.

Dra. Teresa Andreu has always been a supporting leader with her practical inputs and encouragements that provided me the sense of thinking beyond, which has been so beneficial to not only my research but also my future career. Teresa's openness to trying new ideas and taking scientific risks was paramount to my own development as an independent researcher and the success of this project.

It has been great pleasure to share the work with all the people in the electrochemistry lab of ESEH, in the facilities of IREC, from R&D division of Repsol S.A. and University of Barcelona that I have learnt from each one of you. I thank my colleague, Dr. Andres Parra who helped me during CO₂ electroreduction project and donated me with his practical skills on experimental set-up. I thank David Pou for his assistance in HPLC measurements, Dr. Cristian Fàbrega, Dra. Doris Cadavid and Dra. Diouldé Sylla for their technical assistance in several characterization methods, and group of Prof. Miguel Feliz, from University of Barcelona for their help to quantify my samples with nuclear magnetic resonance spectroscopy. I am grateful to María D. Hernández Alonso from Repsol S.A. for the value she brought into this project and for carrying out my research to an outstanding international patent. I

also thank to Prof. Dr. Andreu Cabot, Dra. Maria Ibáñez Sabaté and Dr. Zhishan Luo that I had the chance to work with and produce my second paper as a first author. This opportunity gave me the chance to grasp some electrochemical methods in a fundamental level.

I thank to Prof. Federico Rosei, Dr. Haiguang Zhao and Lei Jin for their guidance during my first visiting stay in Institut National de la Recherche Scientifique (INRS) in Montreal, Canada which provided me a deeper understanding in quantum dots and their application in photoelectrochemistry. I was also part of Advanced Catalysis Engineering Group in ETH Hönggerberg lead by Prof. Dr. Javier Pérez-Ramírez for my second short stay. Prof. Dr. Javier Pérez-Ramírez was an extremely dedicated scientist who demonstrated a level of scientific thoroughness that will inspire me for the rest of my career. I also would like to thank Gastón Larrazábal and Dr. Antonio Martín Fernández guiding me during my stay, which has been invaluable on both an academic and a personal level.

During my thesis, Barcelona, Montreal and Zurich offered me great friends who supported me in good and bad days. I have been lucky to work and be friends with those remarkable people so I want to thank for: Cristina Flox, Jordi Jacas, Sebastián Murcia, Carles Ros, Javier Vazquez (Mr. B), my junior Hemesh Avireddy (Mr. J), Nina Magali Carretero (our queen), Antonio Bazzo (chuti-knee warrior), Silvia Ortega (my cheerful friend), Maria Companyà (my devoted assistance during her master internship), Javier Rubio and Edgar Ventosa (my fruitful tête-à-tête Doyens), Francesc Torregrosa (for his support with administrative work), Gerard Gadea Díez (my climbing and ex-swing partner), Ersan and Ilker (my Turkish team), Elena Papalabrou and Stavros Samouilidis (my Greek family), Grace Gudgeon (for her moral support in my last year), Esen Sokullu (my half Canadian half-sister), Felix Urbain (my bodypump bru), and my friends in aCe group in Zurich.

I want to thank my (extended) family Esen and Hilmi Karagoz that regardless of the distance they helped keep me on track and be a part of my life. Above all, my greatest thanks to my father, Ömer Irtem and my mother Şükran Irtem for their endless support and love. I could not have done this without your encouragement. I love you and dedicate this thesis to you!

Erdem IRTEM

Financial Support

I am thankful to AGAUR for my PhD grant (FI-2013-B-00769) that made this doctoral project possible. The work was partially supported by MINECO project ENE2012-3651, the European Regional Development Funds (FEDER) and Repsol, SA. I am also thankful to WIROX project under the framework of FP7 call PEOPLE-2011-IRSES for the support of my visiting stay in INRS Montreal, Canada.

Curriculum vitae

Information



Turkish

Born in North Cyprus - Turkey on October 7, 1985

+34 673 51 33 26

erdemirtem@gmail.com

<https://ch.linkedin.com/in/erdemirtem/en>

Barcelona 08003 | Spain

Education

- 2013 – 2016 Postgraduate studies on Nanotechnology at University of Barcelona (UB) and Catalonia Institute for Energy Research (IREC), SPAIN
Degree: Doctorate in Nanoscience (cont.)
- 2010 – 2012 Graduate studies in Erasmus Mundus Master Frame Materials for Energy Storage and Conversion (MESC) at UPJV-FRANCE, WUT-POLAND and UCO-SPAIN
Degree: Master of Science
- 2005 – 2009 Undergraduate studies on Materials Science and Engineering (MSE) at Anadolu University and Istanbul Technical University, TURKEY
Degree: Bachelor of Engineering
- 2001 – 2005 Secondary school education on Science Major at Izmir Bornova Anatolian High School (BAL), TURKEY
Degree: Lyceum Diploma with Science Major

Professional Experience

- 2016 Visiting Scientist in Advanced Catalysis Engineering, ETH Zurich, SWITZERLAND (May – August)
- 2015 Visiting Scientist in Institut National de la Recherche Scientifique, INRS-Montreal, CANADA (December-January)
- 2013 Junior Researcher in Catalonia Institute for Energy Research, Barcelona, SPAIN

- 2012 Industrial Intern in Renault–Nissan Alliance, Guyancourt, FRANCE
- 2009 Research Intern in SAM (Ceramic Research Center), Anadolu University, Eskisehir, TURKEY [□](#)

Awards and Accomplishments

- 2013 Full Ph.D. Grant FI Grant from Generalitat de Catalunya, 1st in IREC grant listing - 2013-2016 – no G64946387 [□](#)
- 2010 Full Master Scholarship, E.U. Erasmus Mundus Joint Master Program [□](#) 2010-2012 Top 5% in 21K candidate in the world listing [□](#)
- 2009 Honour certificate in the last two semesters of bachelor degree [□](#)



UNIVERSITAT_{DE}
BARCELONA